Title

Novel Magnetic Resonance Imaging Tools to Characterize Molecular Subtypes and Malignant Transformation of Human IDH-Mutant Gliomas

Author

Cho, Nicholas

Publication Date

2024

Peer reviewed|Thesis/dissertation

UNIVERSITY OF CALIFORNIA

Los Angeles

Novel Magnetic Resonance Imaging Tools to Characterize Molecular Subtypes and Malignant Transformation of Human IDH-Mutant Gliomas

A dissertation submitted in partial satisfaction of the

requirements for the degree

Doctor of Philosophy in Bioengineering

by

Nicholas Sung Jin Cho

2024

ABSTRACT OF THE DISSERTATION

Novel Magnetic Resonance Imaging Tools
to Characterize Molecular Subtypes and Malignant Transformation
of Human IDH-Mutant Gliomas

by

Nicholas Sung Jin Cho
Doctor of Philosophy in Bioengineering
University of California, Los Angeles, 2024
Professor Benjamin M. Ellingson, Chair

Magnetic resonance imaging (MRI) is a valuable tool for the clinical management and scientific investigation of patients diagnosed with brain tumors. Continued efforts in brain tumor imaging research are critical because of the ever-evolving landscape of MRI technological advancements and new insights into brain tumor biology. For example, while historically, tumor tissue diagnoses relied on histopathological features, today, tumor molecular genetic features are the foundational component of tumor classification and patient management. Isocitrate dehydrogenase (IDH)-mutant gliomas are a specific brain tumor molecular subtype that particularly impact younger adults and remain incurable. Within IDH-mutant gliomas, there are also now molecularly defined IDH-mutant astrocytomas (1p/19q intact) and IDH-mutant oligodendrogliomas (1p/19q-codeleted). Although IDH-mutant gliomas often present as indolent,

low-grade tumors, these tumors eventually become more aggressive in a process clinically described as “malignant transformation” into high-grade tumors, which are more resistant to therapy and have worse prognosis.

This dissertation focuses on developing novel MRI tools to characterize molecular subtypes of IDH-mutant gliomas and malignant transformation. Specifically, this dissertation introduces four new tools for IDH-mutant glioma imaging research and clinical care: (1) optimal normal appearing white matter-normalization for diffusion and perfusion MRI analyses, (2) T2-FLAIR subtraction maps for quantitative T2-FLAIR mismatch analyses, (3) pseudo-resting-state functional MRI for functional connectivity analyses using DSC perfusion MRI (provisional patent filed), and (4) digital flipbooks of patient MRI scans to visually assess brain tumors. This dissertation utilized these tools to study IDH-mutant gliomas, particularly focusing on classifying glioma molecular subtypes, assessing cognitive impairment in patients, characterizing IDH inhibitor targeted therapy treatment response, and identifying IDH-mutant glioma tumor progression, including malignant transformation.

The dissertation of Nicholas Sung Jin Cho is approved.

Corey Wells Arnold

Timothy F. Cloughesy

David A. Nathanson

Noriko Salamon

Benjamin M. Ellingson, Committee Chair

University of California, Los Angeles

2024

To my family, particularly my late Uncle Daniel Cho (1970–2018), a devoted MRI technologist at Memorial Sloan Kettering Cancer Center for over 15 years, whose love and compassion I aspire to emulate in my care for future patients.

TABLE OF CONTENTS

LIST OF FIGURES

LIST OF TABLES

ACKNOWLEDGEMENTS

There are numerous people to thank as part of this dissertation. First and foremost, thank you to my thesis mentor Dr. Benjamin Ellingson for your invaluable mentorship throughout my academic journey. Among so many great qualities, what I will treasure the most is how generous you were with your time to give me helpful project guidance and career advice. I hope to give my future trainees the same generosity, focused presence, empowerment, and career advancement opportunities that you have given me.

Thank you to my thesis committee, Dr. Corey Arnold, Dr. Timothy Cloughesy, Dr. Benjamin Ellingson, Dr. David Nathanson, and Dr. Noriko Salamon, who have generously given their time to mentor me during my graduate studies.

Thank you to my mentors in the lab, Dr. Francesco Sanvito, Dr. Chencai Wang, Dr. Akifumi Hagiwara, Dr. Sonoko Oshima, Dr. Jingwen Yao, Dr. Alfredo Lopez Kolkovsky, and Dr. Masanori Nakajo who have taught me so much over the years. I am so grateful for all of you, and I am so proud of the work we accomplished together.

Thank you to our lab staff members, Catalina Raymond, Ashley Teraishi, and Raksha Nagaraj, who tremendously helped in improving our workflow processes and recruiting patient volunteers for our projects.

Thank you to the fellow graduate students in the lab, Alex Kostiuk, Dr. Talia Oughourlian, and Guowen Shao, for supporting and helping me throughout these years.

Thank you to our MRI technologists, Lalageh Arezooian, Angela Clark, Francine Cobla, Sergio Godinez, Nicholas Haid, Brandon Johnson, Amy Nguyen, Glen Nyborg, Kelley O'Connor, and Mayssam Wehbe, who all play a vital role in our research studies and in the treatment journeys of our patients.

Thank you to our collaborators and co-authors across UCLA Neuroradiology, Neuro-oncology, Neurosurgery, Radiation Oncology, Psychiatry, and Molecular & Medical Pharmacology, who made key contributions to our multi-disciplinary projects.

Thank you to my current & former MSTP Co-Directors, Dr. Carlos Portera-Cailliau, Dr. Olujimi Ajijola, and Dr. David Dawson, who have provided me so much support and career guidance ever since my interview day.

Thank you to our lab's Administrative Assistants, Eloisa Rodriguez and Mercedes Valladarez, our Grant Manager Audrey Gallego, the Medical Scientist Training Program (MSTP) Administrative Office Staff, Susie Esquivel, Staci Chikami, Phuong Macadangdang, and Maleka Rasmussen, and Bioengineering Student Affairs Office Staff Member, Lili Bulhoes, who have supported me so much—both visibly and behind the scenes—to help ensure a smooth experience during my graduate studies.

Thank you to my lab volunteers, Viên Lam Le, Jianwen Lu, and Shurti Thakuria, who have worked hard balancing working in the lab with their undergraduate studies. I am proud of all of you, and you will accomplish so much.

Thank you to my undergraduate research mentors Dr. Andrei Holodny and Dr. Kyung Peck, who gave me my first opportunities in neuroradiology research. I hope I have taught my own undergraduate volunteers with the same kindness, encouragement, patience, and early opportunities for critical thinking that you provided me when I was their age.

Thank you to my family, my mother Hi Sun Choi, my father Steven Cho, my sibling Brian Lux Cho, my uncle Samuel Lee, my partner Olivia Man, and all my friends who have all supported me, encouraged me, and made me laugh every day.

Thank you to my late uncle and MRI technologist Daniel Cho, who I thought about every day during this Ph.D.

And thank you to all the patients and their families who make this work possible and for whom we do this work.

VITA

2018 B.S. in Biomedical Engineering, Summa Cum Laude
Columbia University, New York, NY

FELLOWSHIPS

2023-Present Ruth L. Kirschstein National Research Service Award F30CA284809-01
National Institutes of Health, National Cancer Institute

2021 Jack and Fay Netchin Medical Student Summer Fellowship MSSF2100033
American Brain Tumor Association

SELECTED ACHIEVEMENTS

2023-Present Editorial Fellow, *American Journal of Neuroradiology (AJNR)*

- First-ever student recipient, originally intended for fellows/junior faculty
- Spearheaded 3 new, diversity-based award initiatives at the *AJNR*:
  1. Early Career (Advocated for eligibility of students)
  2. Women in Neuroradiology (Advocated for eligibility of women at all levels)
  3. Global Neuroradiology (Advocated for eligibility of visiting scholars & international medical graduates in the US and international groups)

2023-2024 3 Journal Cover Image Selections as First-Author
AJNR, Journal of Neuro-Oncology, NMR in Biomedicine

2023 Conference Travel Award, American Society of Functional Neuroradiology

SELECTED FIRST-AUTHOR PUBLICATIONS

1. **Cho NS*,** Lam VL*, Sanvito F*, Oshima S, Harper J, Chun S, Raymond C, Lai A, Nghiemphu PL, Yao J, Everson R, Salamon N, Cloughesy TF, Ellingson BM. Digital "flipbooks" for enhanced visual assessment of simple and complex brain tumors. *Neuro-Oncology*. In Press. *Contributed equally

2. **Cho NS***, Wang C*, Van Dyk K, Sanvito F, Oshima S, Yao J, Lai A, Salamon N, Cloughesy TF, Nghiemphu PL, Ellingson BM. Pseudo-resting-state functional MRI derived from dynamic susceptibility contrast perfusion MRI can predict cognitive impairment in glioma. *AJNR Am J Neuroradiol.* In Press. *Contributed equally.

3. **Cho NS**, Sanvito F, Le VL, Oshima S, Teraishi A, Yao J, Telesca D, Raymond C, Pope WB, Nghiemphu PL, Lai A, Cloughesy TF, Salamon N, Ellingson BM. Quantification of T2-FLAIR Mismatch in Nonenhancing Diffuse Gliomas Using Digital Subtraction. *AJNR Am J Neuroradiol.* 2024 Feb 7;45(2):188-197. doi: 10.3174/ajnr.A8094. PMID: 38238098.
   a. Selected for *AJNR* cover image (Vol. 45, Issue 2) and "Editor's Choice" designation
   b. Nominated for the 2024 *AJNR* (1) Lucien Levy Best Research Article Award and (2) Early Career Award

4. **Cho NS**, Wong WK, Nghiemphu PL, Cloughesy TF, Ellingson BM. The Future Glioblastoma Clinical Trials Landscape: Early Phase 0, Window of Opportunity, and Adaptive Phase I-III

Studies. *Curr Oncol Rep*. 2023 Sep;25(9):1047-1055. doi: 10.1007/s11912-023-01433-1. Epub 2023 Jul 4. PMID: 37402043; PMCID: PMC10474988.

5. **Cho NS,** Sanvito F, Thakuria S, Wang C, Hagiwara A, Nagaraj R, Oshima S, Lopez Kolkovsky AL, Lu J, Raymond C, Liau LM, Everson RG, Patel KS, Kim W, Yang I, Bergsneider M, Nghiemphu PL, Lai A, Nathanson DA, Cloughesy TF, Ellingson BM. Multi-nuclear sodium, diffusion, and perfusion MRI in human gliomas. *J Neurooncol*. 2023 Jun;163(2):417-427. doi: 10.1007/s11060-023-04363-x. Epub 2023 Jun 9. PMID: 37294422; PMCID: PMC10322966.
    a. Selected for *Journal of Neuro-Oncology* cover image (Vol. 163, Issue 2)

6. **Cho NS,** Hagiwara A, Sanvito F, Ellingson BM. A multi-reader comparison of normal-appearing white matter normalization techniques for perfusion and diffusion MRI in brain tumors. *Neuroradiology.* 2023 Mar;65(3):559-568. doi: 10.1007/s00234-022-03072-y. Epub 2022 Oct 27. PMID: 36301349; PMCID: PMC9905164.

7. **Cho NS**, Hagiwara A, Eldred BSC, Raymond C, Wang C, Sanvito F, Lai A, Nghiemphu P, Salamon N, Steelman L, Hassan I, Cloughesy TF, Ellingson BM. Early volumetric, perfusion, and diffusion MRI changes after mutant isocitrate dehydrogenase (IDH) inhibitor treatment in IDH1-mutant gliomas. *Neurooncol Adv*. 2022 Aug 4;4(1):vdac124. doi: 10.1093/noajnl/vdac124. PMID: 36033919; PMCID: PMC9400453.

8. **Cho NS***, Hagiwara A*, Yao J, Nathanson DA, Prins RM, Wang C, Raymond C, Desousa BR, Divakaruni A, Morrow DH, Nghiemphu PL, Lai A, Liau LM, Everson RG, Salamon N, Pope WB, Cloughesy TF, Ellingson BM. Amine-weighted chemical exchange saturation transfer (CEST) MRI in brain tumors. *NMR Biomed.* 2023 Jun;36(6):e4785. doi: 10.1002/nbm.4785. Epub 2022 Jun 29. PMID: 35704275. *Contributed equally
    a. Selected for *NMR in Biomedicine* cover image (Vol. 36, Issue 6)

9. **Cho N,** Wang C, Raymond C, Kaprealian T, Ji M, Salamon N, Pope WB, Nghiemphu PL, Lai A, Cloughesy TF, Ellingson BM. Diffusion MRI Changes in the Anterior Subventricular Zone Following Chemoradiation in Glioblastoma with Posterior Ventricular Involvement. *J Neurooncol.* 2020 May;147(3):643-652. doi: 10.1007/s11060-020-03460-5. Epub 2020 Apr 1. PMID: 32239430; PMCID: PMC7769136.

EDITORIALS

1. **Cho NS**, Ozkara BB, Boutet A, Halm K, Wilhelm L, Shah L, Wintermark M. Introducing Our New AJNR Early Career, Women in Neuroradiology, and Global Neuroradiology Awards. *AJNR Am J Neuroradiol*. 2024 Apr 8;45(4):362. doi: 10.3174/ajnr.A8231. PMID: 38514092.

PROVISIONAL PATENTS

1. Ellingson BM, **Cho NS**, Wang C. Resting-state functional magnetic resonance imaging (MRI) derived from dynamic susceptibility contrast (DSC) perfusion MRI. Provisional U.S. Patent #63/570,544. Filed March 27, 2024.

Chapter 1. Introduction

Preface

This chapter includes excerpts adapted from the below publications:

Cho NS, Sanvito F, Le VL, Oshima S, Teraishi A, Yao J, Telesca D, Raymond C, Pope WB, Nghiemphu PL, Lai A, Cloughesy TF, Salamon N, Ellingson BM. Quantification of T2-FLAIR Mismatch in Nonenhancing Diffuse Gliomas Using Digital Subtraction. *AJNR Am J Neuroradiol.* 2024 Feb 7;45(2):188-197. doi: 10.3174/ajnr.A8094. PMID: 38238098.

Cho NS, Sanvito F, Thakuria S, Wang C, Hagiwara A, Nagaraj R, Oshima S, Lopez Kolkovsky AL, Lu J, Raymond C, Liau LM, Everson RG, Patel KS, Kim W, Yang I, Bergsneider M, Nghiemphu PL, Lai A, Nathanson DA, Cloughesy TF, Ellingson BM. Multi-nuclear sodium, diffusion, and perfusion MRI in human gliomas. *J Neurooncol*. 2023 Jun;163(2):417-427. doi: 10.1007/s11060-023-04363-x. Epub 2023 Jun 9. PMID: 37294422; PMCID: PMC10322966.

Cho NS, Hagiwara A, Eldred BSC, Raymond C, Wang C, Sanvito F, Lai A, Nghiemphu P, Salamon N, Steelman L, Hassan I, Cloughesy TF, Ellingson BM. Early volumetric, perfusion, and diffusion MRI changes after mutant isocitrate dehydrogenase (IDH) inhibitor treatment in IDH1-mutant gliomas. *Neurooncol Adv*. 2022 Aug 4;4(1):vdac124. doi: 10.1093/noajnl/vdac124. PMID: 36033919; PMCID: PMC9400453.

Background on Clinical and Molecular Features of Isocitrate Dehydrogenase (IDH)-Mutant Gliomas

Clinical Description and Molecular Classification

Gliomas are brain tumors of glial cells (e.g. astrocytes, oligodendrocytes, but not neurons) and unfortunately remain a uniformly fatal disease even with treatment.[1, 2] While historically, adult gliomas were classified based on *histopathological* features of tumor tissue samples, tumor *molecular* genetic features are now the basis of adult diffuse glioma classification in the current 2021 World Health Organization (WHO) Classification of Tumors of the Central Nervous System (CNS).[3] First, the isocitrate dehydrogenase (IDH)-mutation status, namely wild-type or mutant, is the most critical glioma molecular feature (**Figure 1.1**).[4] Next, IDH-mutant gliomas can also be further classified based on the 1p/19q-codeletion molecular status to be defined as IDH-mutant astrocytomas (1p/19q-intact) or IDH-mutant oligodendrogliomas (1p/19q-codeleted).[3] Lastly, within these molecular tumor entities, IDH-mutant gliomas are also classified by tumor grade, ranging from grade 2–4 for IDH-mutant astrocytomas or grade 2–3 for IDH-mutant oligodendrogliomas.[3] Higher tumor grades indicate more aggressive phenotypes and are determined using a combination of varying histologic and molecular features. For example, histologic markers like microvascular proliferation can indicate grade 4 for IDH-mutant astrocytoma, while molecular markers like homozygous CDKN2A/B co-deletion also signify grade 4 for IDH-mutant astrocytoma, regardless of histology.[3]

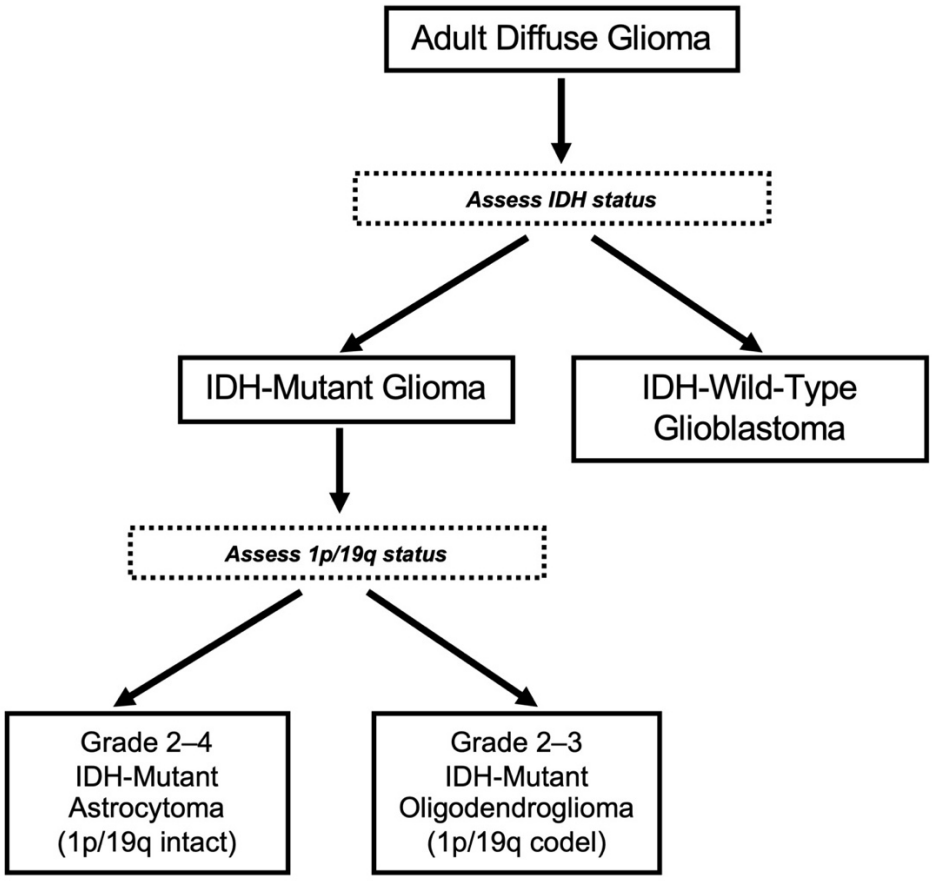

Figure 1.1 Schematic of 2021 WHO Molecular-Based Classification of Adult Diffuse Gliomas.

Determining the IDH-mutation status is critical for patient management because IDH-mutant gliomas have a markedly improved prognosis and a tendency to occur in younger adults compared to IDH-wild-type gliomas (glioblastomas) (**Table 1.1**).[5] Specifically, for IDH-mutant astrocytomas, the peak age of onset is 30–34 years and overall survival with standard treatment is 3.6–9.3 years; for IDH-mutant oligodendrogliomas, those values are 40–44 and 10–17.5 years, respectively; and for IDH-wild-type glioblastomas, those values are 75–84 and 1.2 years,

respectively.[5-9] IDH-mutant gliomas also tend to occur in the frontal lobe,[10] while IDH-wild-type glioblastomas tend to occur in posterior, periventricular regions.[11]

Tumor Type	Peak Age of Onset (Years)	Overall Survival (Years)	Age-Adjusted Incidence
IDH-Mutant Astrocytoma (1p/19q-intact)	30–34[5, 6]	3.6–9.3[7]	0.43/100,100[5, 6]
IDH-Mutant Oligodendroglioma (1p/19q-codeleted)	40–44[5, 6]	10–17.5[7, 8]	0.27/100,000[5, 6]
IDH-Wild Type Glioblastoma	75–84[9]	1.2[7]	3.23/100,000[9]

Table 1.1 Peak Age of Onset, Overall Survival, and Age-Adjusted Incidence of Patients with Gliomas. IDH = isocitrate dehydrogenase

While the standard of care for gliomas remains maximally safe surgical resection followed by adjuvant chemoradiation, IDH-mutant gliomas can be followed and managed more conservatively than IDH-wild-type glioblastomas.[5] Targeted therapies for patients with IDH-mutant gliomas are also currently under consideration for United States Food & Drug Administration (FDA) approval after mutant IDH inhibitor vorasidenib was recently shown to have significant benefit in progression-free survival in a multi-center Phase III clinical trial.[12]

Continued advancements in our knowledge of IDH-mutant gliomas remain critical to improve patient management and the therapeutic landscape for this fatal disease.

Tumor Molecular Biology and Malignant Transformation

Transcriptional studies have shown that IDH mutations occur early in tumorigenesis in neuroglial precursor cells.[13, 14] These mutations most commonly occur in cytosolic IDH1 enzymes (>95%) as IDH1 R132K mutations and less frequently in mitochondrial IDH2 enzymes[15] as IDH2 R172K mutations. IDH1/2 normally catalyzes the oxidative decarboxylation of isocitrate into α-ketoglutarate (α-KG).[16] Mutations in IDH1/2 result in a gain of function to catalyze the conversion of α-KG into the oncometabolite D-2-hydroxyglutarate (D-2-HG) (**Figure 1.2**).[17] Elevated D-2-HG levels cause many downstream effects, including inhibiting α-KG-dependent dioxygenases, which results in DNA hypermethylation and inhibited cellular differentiation,[18, 19] as well as decreasing levels of hypoxia inducible factor 1α (HIF-1α) that result in reduced hypoxic signaling, proangiogenic signaling, and glycolytic capacity.[20, 21] These downstream effects of the mutant IDH enzyme are the reasons driving the exploration of this feature as a potential therapeutic target through IDH inhibitors. Pre-clinical studies have shown that inhibition of mutant IDH enzymes reduced D-2-HG levels,[22] increased glutamate levels,[22] and promoted differentiation of glioma cells.[23] Clinical studies of IDH inhibitors have also demonstrated tumor shrinkage effects in glioma patients.[24, 25]

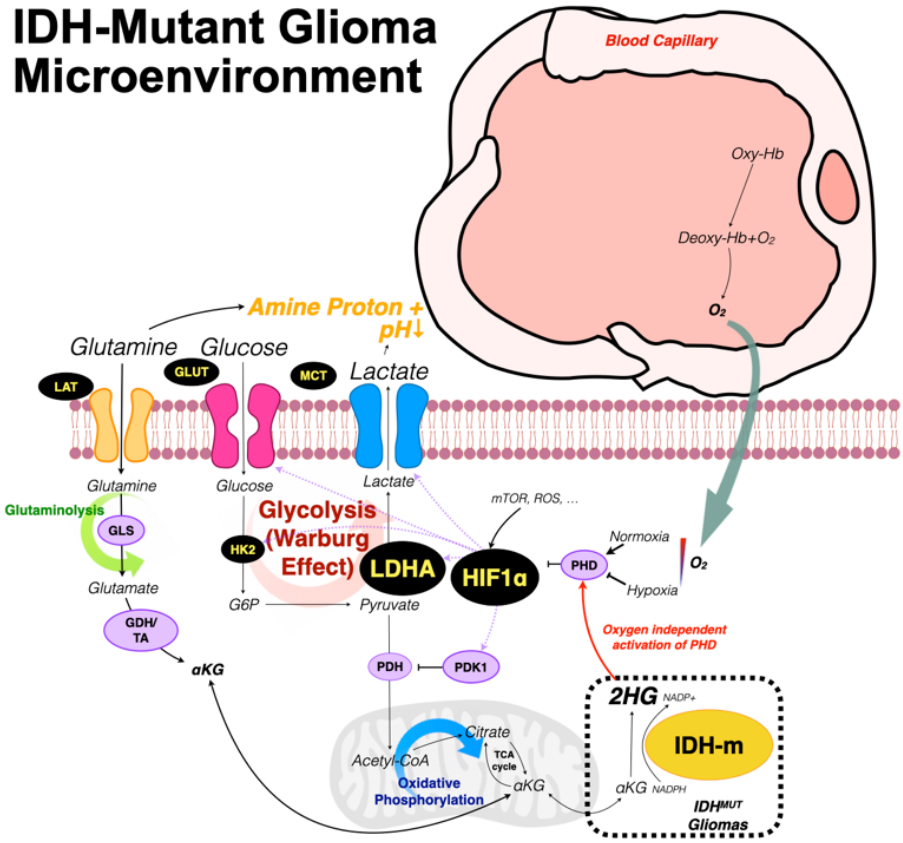

Figure 1.2. Schematic of Downstream Effects of IDH Mutation in Gliomas.

While the IDH mutation has a driver role early in glioma tumorigenesis, this mutation later assumes a passenger role[26] as the tumor progresses, becomes more aggressive, and gains resistance to therapy. In clinical contexts, this transition of an initial low grade 2 IDH-mutant glioma progresses into a higher grade 3 or 4 IDH-mutant glioma is defined as "malignant transformation". Interestingly, D-2-HG levels continue to rise as the tumor progresses.[27] However, even though IDH inhibition can still reduce D-2-HG levels in the transformed stage as evidenced in a study on human cell lines,[26] the same study also showed that this reduction in D-2-HG does not lead to tumor shrinkage upon transformation.[26] Similar observations were observed in a Phase I clinical trial of IDH inhibitor vorasidenib where there was minimal therapeutic effect on more-aggressive

(contrast-enhancing) IDH-mutant gliomas compared to less aggressive (non-enhancing) IDH-mutant gliomas.[25]

At the molecular level, many other key events of malignant transformation have been characterized. IDH-mutant gliomas originally present with a high glioma-CpG island methylator phenotype (G-CIMP) DNA hypermethylation state[28] but later transition to a low G-CIMP state.[29] The tumor also undergoes metabolic shifts from a low glycolytic phenotype to a high glycolytic phenotype, particularly from loss of promoter methylation of lactate dehydrogenase A (LDHA).[30] This metabolic change has also been shown to precede the transition of high G-CIMP to low G-CIMP states and lead to tumor aggressiveness.[30] Additionally, mTOR signaling pathway-related genes increase in activity after IDH-mutant glioma malignant transformation.[31] Further characterization of tumor genetics and metabolic processes—along with their non-invasive imaging biomarker correlates—will be valuable to identify more therapeutic vulnerabilities to treat patients with IDH-mutant gliomas in the future.

Background on Magnetic Resonance Imaging (MRI) Features of IDH-Mutant Gliomas

Brain Tumor MRI Techniques

Magnetic resonance imaging (MRI) is the gold standard for diagnosis and management of human gliomas. Notably, MRI is non-invasive and does *not* involve ionizing radiation. MRI can be used to generate various image contrasts (e.g. T1-weighted, T2-weighted) by selectively perturbing the magnetic properties of protons in the human body, particularly water protons, to image healthy and diseased tissue. Contrast enhancement on post-contrast, T1-weighted proton MRI can be used to define the contrast-enhancing component of the tumor, which contains the most aggressive high-grade features of the tumor,[32, 33] while T2-weighted proton images, including fluid-attenuated inversion recovery (FLAIR) sequences, are useful for defining non-enhancing tumor, which contains the bulk of the tumor in lower grade gliomas and a combination of infiltrative glioma cells and edema in higher grade tumors.[34]

In addition to these standard anatomic MRI sequences that are used to isolate areas of concern, advanced physiologic imaging techniques including diffusion and perfusion MRI are often used to explore cellularity and vascularity, respectively, within these tumor regions. The metric apparent diffusion coefficient (ADC) measured using diffusion weighted imaging has been shown to be inversely correlated to cell density and proliferation.[35] Dynamic susceptibility contrast (DSC) perfusion MRI is also frequently employed in human gliomas. This scanning modality involves imaging the brain during the administration of a gadolinium-based contrast agent to isolate areas of high vascular density,[36] identify highly aggressive areas of the tumor undergoing

angiogenesis,[34] and differentiating recurrent tumor from pseudoprogression[37] using the metric normalized relative cerebral blood volume (nrCBV).

Imaging of IDH-Mutant Gliomas

There is gaining interest in being able to use imaging features alone to molecularly classify gliomas for guiding patient management. Non-invasive, imaging-based molecular classification may be particularly valuable in the future in the context of targeted therapies like IDH inhibitors during situations where biopsy/surgery may be less feasible or necessary. Two representative patient MRI scans of a grade 2 IDH-mutant oligodendroglioma and a grade 4 IDH-wild-type glioblastoma are shown in **Figure 1.3.** These scans illustrate the typical imaging features that can be used to classify IDH status, as confirmed in a meta-analysis.[10] Specifically, IDH-mutant gliomas usually exhibit less concerning imaging features of less contrast-enhancement, higher ADC (lower cellular density), and lower nrCBV (lower tumor vascularity) compared to IDH-wild-type gliomas.[10] The recent discovery of the visual "T2-FLAIR Mismatch Sign" imaging feature has also gained much excitement in clinical neuroradiology because this feature is nearly 100% specific for IDH-mutant astrocytomas but with low sensitivity.[38]

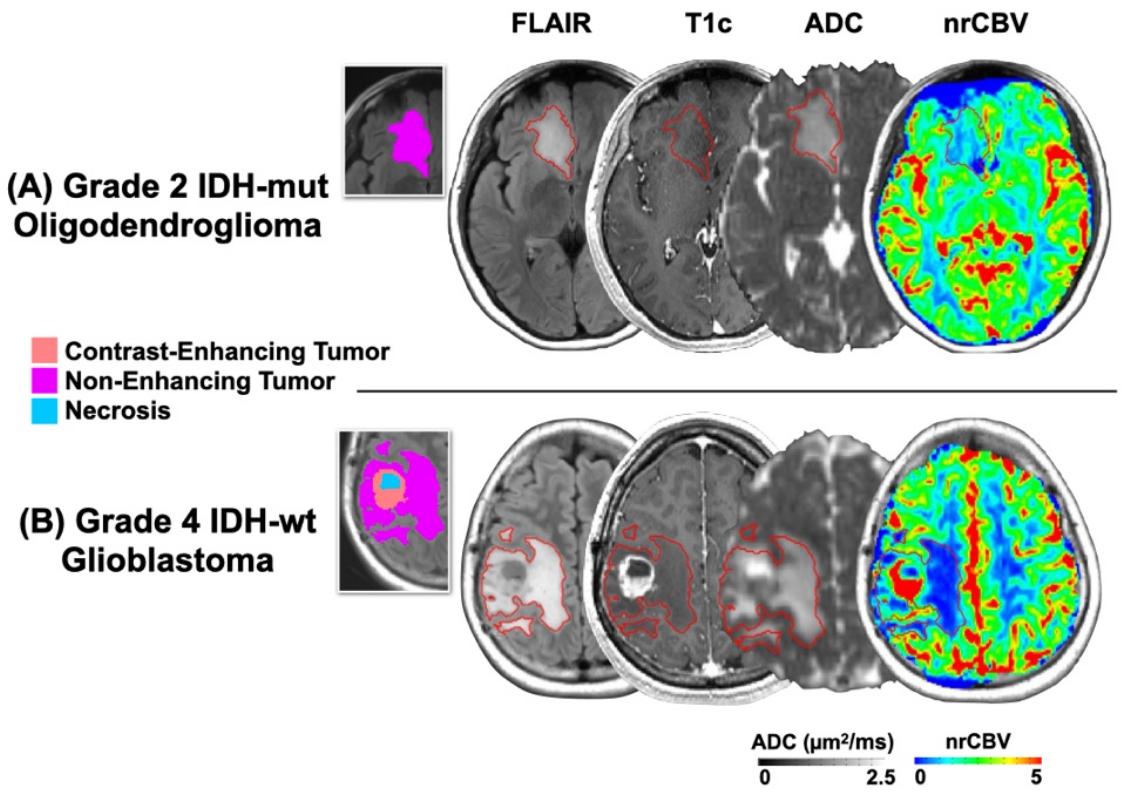

Figure 1.3. Representative Anatomical, Diffusion, and Perfusion MRI Scans of Patients with IDH-Mutant Glioma and IDH-Wild-Type Glioblastoma. Adapted from Cho *et al.*[39]

Purpose of this Dissertation

While the field of clinical neuroradiology has traditionally relied on mostly *qualitative* imaging assessments of brain tumors, advancements in computing capabilities have propelled the field towards an increased adoption of *quantitative* imaging assessments, along with long-term ambitions of readily utilizing artificial intelligence. Nevertheless, significant foundational research in developing and utilizing novel quantitative MRI methods remains needed to address crucial knowledge gaps in our understanding of IDH-mutant gliomas. Furthermore, prior to the 2021 WHO Classification of CNS Tumors, brain tumor imaging studies placed greater emphasis on

histologically-defined gliomas rather than molecularly-defined gliomas (IDH or 1p/19q codeletion). This approach involved grouping tumors by histologic features with different molecular characteristics due to our limited understanding of molecular features at the time (e.g. grouping IDH-wild-type astrocytomas and IDH-mutant astrocytomas as "astrocytomas"), including when studying low-grade glioma malignant transformation.[40] Consequently, there is a pressing need for contemporary brain tumor imaging studies to distinguish between distinct molecular tumor subtypes (IDH-mutant astrocytoma 1p/19q-intact, IDH-mutant oligodendroglioma 1p/19q-codeleted, IDH-wild-type glioblastoma) to improve glioma classification and to advance image-based phenotyping of gliomas.

The main goal of this dissertation is to address these needs by bridging the gap between qualitative and quantitative neuroradiology of brain tumors using contemporary definitions of glioma molecular subtypes through the following 2 aims:

Aim 1: Development of Novel MRI Tools for IDH-Mutant Glioma Analyses. (Chapters 2–5)

In **Chapter 2**, we develop an optimal normalization method for DSC perfusion MRI-derived normalized rCBV values and diffusion weighted MRI-derived normalized ADC values to study gliomas and differentiate IDH-mutational status.[41] In **Chapter 3**, we introduce T2-FLAIR subtraction maps and quantitatively validate the visual "T2-FLAIR Mismatch Sign" to classify IDH-mutant astrocytomas with 100% specificity using a novel metric percentage T2-FLAIR mismatch volume.[42] In **Chapter 4**, we utilize T2-FLAIR subtraction maps to further characterize the diffusion characteristics of mismatched and non-mismatched IDH-mutant astrocytomas as separate tumor entities and compare the classification performance of percentage T2-FLAIR mismatch volume with normalized ADC. In **Chapter 5**, we introduce a new MRI image contrast

called “pseudo-resting-state functional MRI” derived from DSC perfusion MRI to assess brain functional connectivity and cognitive impairment status in a predominately IDH-mutant glioma survivor cohort.

Aim 2: Contemporary Longitudinal Analyses of IDH-Mutant Gliomas. (Chapters 6–8)

In **Chapters 6 & 7**, we utilize anatomical, diffusion, and perfusion MRI (i) to characterize early imaging changes in patients diagnosed with IDH-mutant gliomas upon receiving IDH inhibitor therapy (**Chapter 6**)[43] and (ii) to assess histologically-confirmed malignant transformation via multiple biopsies in molecularly-defined IDH-mutant astrocytomas and IDH-mutant oligodendrogliomas (**Chapter 7**). Lastly, in **Chapter 8**, we introduce the concept of digital “flipbooks” of patient MRI scans, which may strike the balance between traditional, qualitative “side-by-side” reads and whole tumor quantitation to improve the clinical assessment of brain tumors.

The work in this dissertation aims to address clinical needs in brain tumor imaging and introduces new analysis methods that can be utilized by our field for further exploration of IDH-mutant gliomas beyond this dissertation.

Chapter 2. "Normal Appearing White Matter" Normalization Techniques for Perfusion and Diffusion MRI in Brain Tumors

Preface

This chapter is adapted from the following publication:

Cho NS, Hagiwara A, Sanvito F, Ellingson BM. A multi-reader comparison of normal-appearing white matter normalization techniques for perfusion and diffusion MRI in brain tumors. *Neuroradiology.* 2023 Mar;65(3):559-568. doi: 10.1007/s00234-022-03072-y. Epub 2022 Oct 27. PMID: 36301349; PMCID: PMC9905164.

Introduction

Relative cerebral blood volume (rCBV) values of brain tumors obtained from dynamic susceptibility contrast (DSC) perfusion MRI are routinely normalized (nrCBV) in both research and clinical settings to reduce variability across different MR protocols, scanners, and timepoints within the same patient. However, even though nrCBV values are affected by the chosen normalization technique itself,[44, 45] there remains no consensus normalization method. Common normalization methods include placing a reference region of interest (ROI) on the contralateral normal appearing white matter (NAWM), but numerous regions have been reported such as the white matter directly opposite to the tumor,[46-48] the posterior limb of the internal capsule,[49] the temporal lobe,[50] and the centrum semiovale[43, 51-54] along with variations in the placement of a single-ROI[52] or multiple-ROIs anteriorly-to-posteriorly.[43, 53, 55] Automated normalization methods, such as Gaussian-normalized nrCBV[44] and "standardized" nrCBV involving training-set data,[44, 56-58] have also been described, but these methods require advanced software that limit their clinical feasibility.

There has also been growing interest in normalizing apparent diffusion coefficient (ADC) values of brain tumors obtained from diffusion MRI.[48, 59-66] For example, although ADC is a quantity measured in units [e.g. mm^2/s], ADC values in a multi-center phase II trial of bevacizumab and chemotherapy in recurrent glioblastoma varied 7.3% in NAWM and 10.5% in cerebrospinal fluid across all sites.[67] Interestingly, ADC values of contralateral NAWM have also been shown to be significantly different across lobes in glioma patients,[68] yet various NAWM normalization methods for normalized ADC (nADC) have been reported, including ROIs directly opposite to the tumor,[48, 59] the posterior limb of the internal capsule,[64] and the centrum semiovale.[60, 61] To our

knowledge though, there remains no study comparing nADC normalization techniques in glioma patients.

The purpose of this reader study was to compare single-planar and multiple-spherical ROI NAWM normalization methods in the centrum semiovale and slice of the tumor center for nrCBV and nADC. In addition to assessing the impact of normalization methods on nrCBV and nADC values and reader variability, these normalization methods were validated by assessing their diagnostic performance when discriminating between IDH-wild-type gliomas and IDH-mutant 1p/19q-intact gliomas, since previous literature extensively showed the predictive value of ADC and nrCBV for this molecular profiling.[10, 63, 69] We hypothesized that there would be significantly different values for nrCBV and nADC based on the normalization method and that the centrum semiovale and multiple-spherical ROI methods would provide significant benefit in reduced time compared to the tumor slice and single-planar ROI methods, respectively.

Methods

Patient Selection

This study was conducted in compliance with the Health Insurance Portability and Accountability Act. All patients provided written informed consent to be part of our institutional review board approved clinical database (IRB#11-001427). In order to choose an adequate sample size for the present study, a power analysis based on previous findings[63] of nrCBV and nADC differences between IDH-wild-type and IDH-mutant 1p/19q intact gliomas was conducted using $\beta = 0.8$ and $\alpha = 0.05$. Based on their nrCBV findings, a Cohen's *d* effect size of 1.2 and a minimum number of 12 patients per group was determined; for their nADC findings, a Cohen's *d* effect size of 1.4 and minimum number of 10 patients per group was determined.

Based on the results of the power analysis, a total of 18 IDH-wild-type glioma patients and 17 IDH-mutant 1p/19q intact glioma patients with histologically-confirmed diagnoses and who obtained DSC-perfusion MRI, diffusion MRI, and anatomical MRI scans before treatment were retrospectively studied. Since the IDH-mutational status assessment was not the focus of the study but rather performed as a benchmark for the validation of the normalization methods, IDH-mutant 1p/19q co-deleted tumors (oligodendrogliomas) were not included since previous literature already showed that the usefulness of ADC and rCBV to detect this tumor type is limited because of their intermediate features between IDH-mutant 1p/19q intact gliomas and IDH-wild type gliomas.[69] IDH mutation was assessed by immunohistochemistry, genomic sequencing analysis, and/or polymerase chain reaction,[70] and 1p/19q codeletion status was determined using fluorescence in situ hybridization. Patient scans were conducted between August 2015 and October 2019. Patient data are summarized in **Table 2.1.**

Characteristic	Patients (n=35)
Average Age (Years) ± SD	48 ± 16
Sex (Male/Female)	24/11
Tumor Location:	
Hemisphere (Left/Right)	16/19
Frontal Lobe	9
Fronto-Temporal Lobes	2
Temporal Lobe	11
Temporo-Parietal Lobes	2
Parietal Lobe	7
Parieto-Occipital Lobes	1
Occipital Lobe	2
Thalamus	1
Tumor Grade (2/3/4)	9/13/13
IDH Mutation Status (Wild-type/Mutant)	18/17

Table 2.1. Clinical Data of Patients.

Image Acquisition and Processing

Anatomical, diffusion, and DSC perfusion MRI were obtained on 1.5T or 3T MRI scanners (Siemens Healthcare; Erlangen, Germany). Anatomical MRI and diffusion-weighted imaging (DWI) were collected according to the international standardized brain tumor imaging protocol (BTIP).[71] ADC maps were calculated from either DWI or diffusion tensor imaging (DTI) data with

b-values of 0 and 1000 s/mm^2. For DSC perfusion MRI, images were collected according to previously described single-echo and multi-echo imaging protocols.[36, 72, 73] DSC data were first motion-corrected using FSL (*mcflirt*; Functional Magnetic Resonance Imaging of the Brain Software Library; Oxford, England), and a bidirectional contrast agent leakage correction method was used to calculate rCBV maps.[74] All parameter maps were registered to the post-contrast T1-weighted images (1-mm isotropic resolution) using a six-degree-of-freedom rigid transformation and a mutual information cost function using FSL software (*flirt*).

Normal Appearing White Matter and Tumor Segmentation

The two readers in this study were a board-certified radiologist (AH) and a radiology resident (FS) with 10 and 6 years of experience in neuroimaging analysis, respectively. Both readers were blinded to patient information, and each reader segmented four contralateral NAWM ROIs using ITK-SNAP software (http://www.itksnap.org/)[75] that avoided cortex, large vessels, and ventricles with the following names and instructions: 1) CSOp: a planar ROI of 400-450 mm^2 drawn on a single slice in the contralateral centrum semiovale approximately 3 mm (~3 slices) superior to the lateral ventricles similar to Conte et al.[52] (**Figure 2.1A**) 2) CSOs: 3 intra-slice 3D spheres of 5 mm diameter (~5 slices) spanning anteriorly-to-posteriorly in the contralateral centrum semiovale approximately 3 mm superior to the lateral ventricles as done in prior studies[43, 60] and similar to Smits et al.[53] (**Figure 2.1B**) 3) TUMp: a planar ROI of 400-450 mm^2 drawn on a single slice in the slice of the center of the tumor as similarly suggested by the Quantitative Imaging Biomarkers Alliance's (QIBA's) Stage 2 Consensus Profile guidelines for nrCBV[46] (**Figure 2.1C**) 4) TUMs: 3 intra-slice 3D spheres of 5 mm diameter (~5 slices) spanning anteriorly-to-posteriorly in the slice of the center of the tumor (**Figure 2.1D**). If a contiguous single-slice

planar ROI was unable to be created, readers were allowed to create 2 planar ROIs on 2 consecutive slices (**Figure 2.1C**). One month later, the patient order was randomized, and each reader repeated NAWM ROI segmentations and recorded the time needed to segment each ROI. nrCBV and nADC maps were calculated by dividing the rCBV and ADC maps by the mean rCBV and ADC values of the NAWM ROIs. A volume of interest (VOI) was segmented on the FLAIR hyperintense tumor using an in-house, semi-automated thresholding method using the Analysis of Functional NeuroImages (AFNI) software (NIMH Scientific and Statistical Computing Core; Bethesda, MD, USA; https://afni.nimh.nih.gov).[76] Median nrCBV and nADC values of the FLAIR hyperintense tumor were derived using each of the 4 normalization techniques.

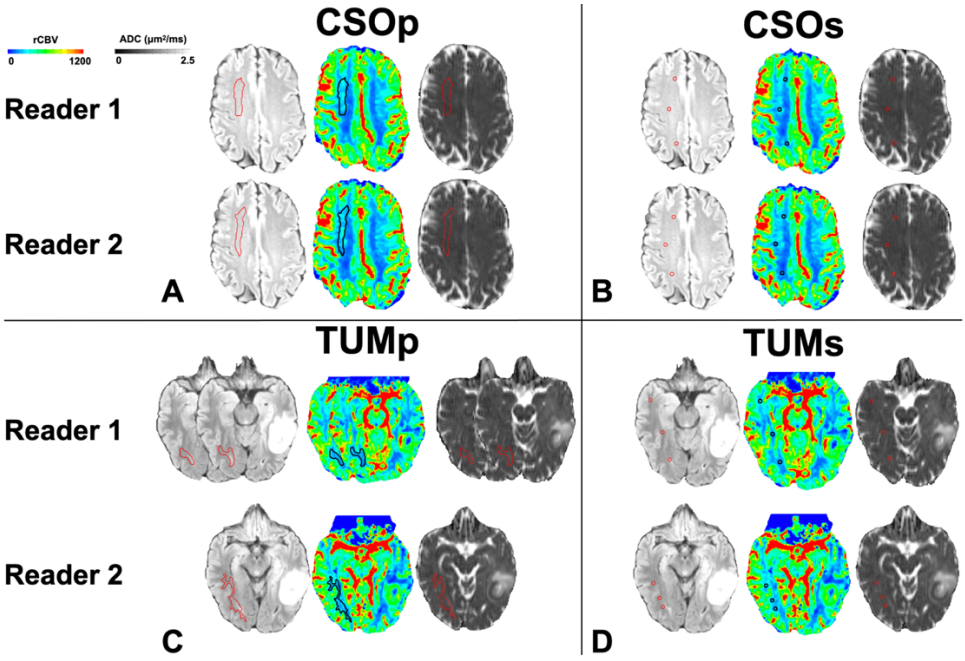

Figure 2.1. Example NAWM Segmentations from Both Readers. NAWM segmentations using **A**) the planar method in the centrum semiovale (CSOp); **B**) spherical method in the centrum semiovale (CSOs); **C**) planar method in the slice contralateral to the center of tumor (TUMp); and **D**) spherical method in the slice contralateral to the center of tumor (TUMs) on

T2/FLAIR images and rCBV and ADC maps. NAWM = normal appearing white matter; rCBV = relative cerebral blood volume; ADC = apparent diffusion coefficient

Statistical Analysis

All calculations and analyses were performed in MATLAB (Release 2020a, MathWorks, Natick, MA) or GraphPad Prism software (Version 8.4 GraphPad Software, San Diego, California). The D'Agostino & Pearson test was conducted to assess if data were normally distributed and to apply appropriate parametric or non-parametric statistical methods. To assess intrareader differences in nrCBV, nADC, and the time to create NAWM ROIs based on the normalization method, the Repeated-Measures ANOVA test with post-hoc Tukey's multiple comparisons tests and the Friedman test with post-hoc Dunn's multiple comparisons tests were performed for normally and non-normally distributed data, respectively. The intraclass correlation coefficient (ICC) (2,1) model was used to assess inter-reader reproducibility of nrCBV and nADC from each normalization method at each trial, and the ICC (3,1) model was used to assess intra-reader repeatability of nrCBV and nADC of each normalization method between trials.[77] Because ICC analyses requires normally distributed data,[78] the Box-Cox transformation was first performed on non-normally distributed data, and the transformed, normally distributed data was used for ICC analyses. In order to validate the nrCBV and nADC values obtained from each normalization method, receiver-operating characteristic (ROC) curve analyses were performed to assess the IDH-mutational status predictive performance of the nrCBV and nADC values obtained from different normalization methods. Significance level was set to α=0.05.

Results

Differences in nrCBV and nADC Values

Normality tests demonstrated that nADC data were normally distributed while nrCBV and time to create NAWM ROI's data were non-normally distributed, so appropriate parametric and non-parametric statistical methods were chosen for each metric. For each trial, each reader obtained overall significantly different nrCBV ($P<.001$) and nADC ($P<.001$) values between the four normalization methods (**Figures 2.2 & 2.3**). In post-hoc analyses, there were significant differences in nrCBV and nADC between CSO and TUM normalization methods (**Table 2.2; Figures 2.2 & 2.3**). For example, when comparing CSO and TUM methods in Trial 1, the median difference in nrCBV and mean difference in nADC ranged in magnitude between 0.10–0.27 and 0.07–0.09, respectively (**Table 2.2**). However, there were no significant differences in nrCBV or nADC between planar and spherical methods within the same normalization region (CSOp vs. CSOs or TUMp vs. TUMs). For these comparisons, the median difference in nrCBV and mean difference in nADC in Trial 1 was greatly reduced to magnitudes ranging between 0.02–0.05 and 0.002–0.001, respectively (**Table 2.2**).

ICC analyses indicated that each normalization method had excellent reproducibility ($r>0.90$ as stated by Koo et al.[77]) between-readers (**Table 2.3; Figure 2.4**) and within-readers when they repeated NAWM segmentations after 1 month (**Table 2.3; Figure 2.5**).

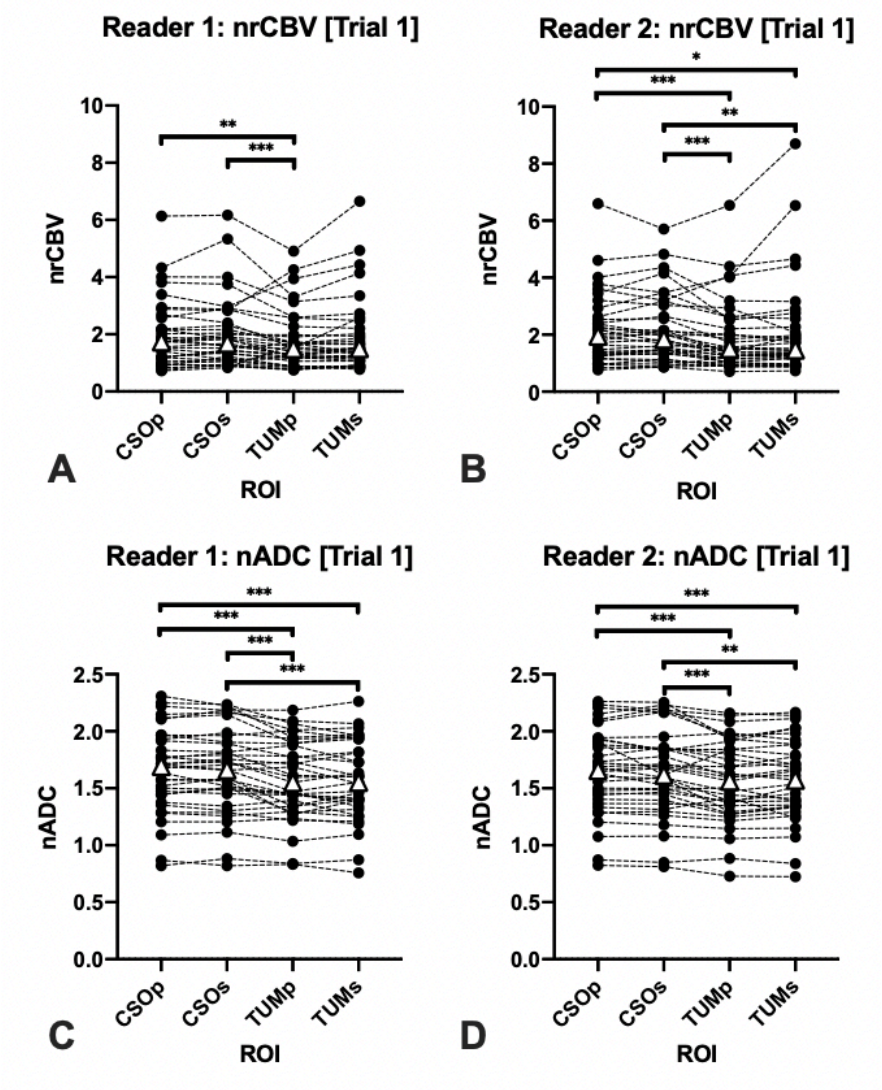

Figure 2.2. Differences in nrCBV and nADC Based on Normalization Method (Trial 1). Post-hoc analyses revealed significant differences for A/B) nrCBV and C/D) nADC between centrum semiovale (CSO) and tumor slice (TUM) methods for both readers in Trial 1, but not between planar (p) and spherical (s) methods within the same normalization region. ∆ indicates median; * indicates $P < .05$; ** indicates $P < .01$; *** indicates $P < .001$ nrCBV = normalized relative cerebral blood volume; nADC = normalized apparent diffusion coefficient

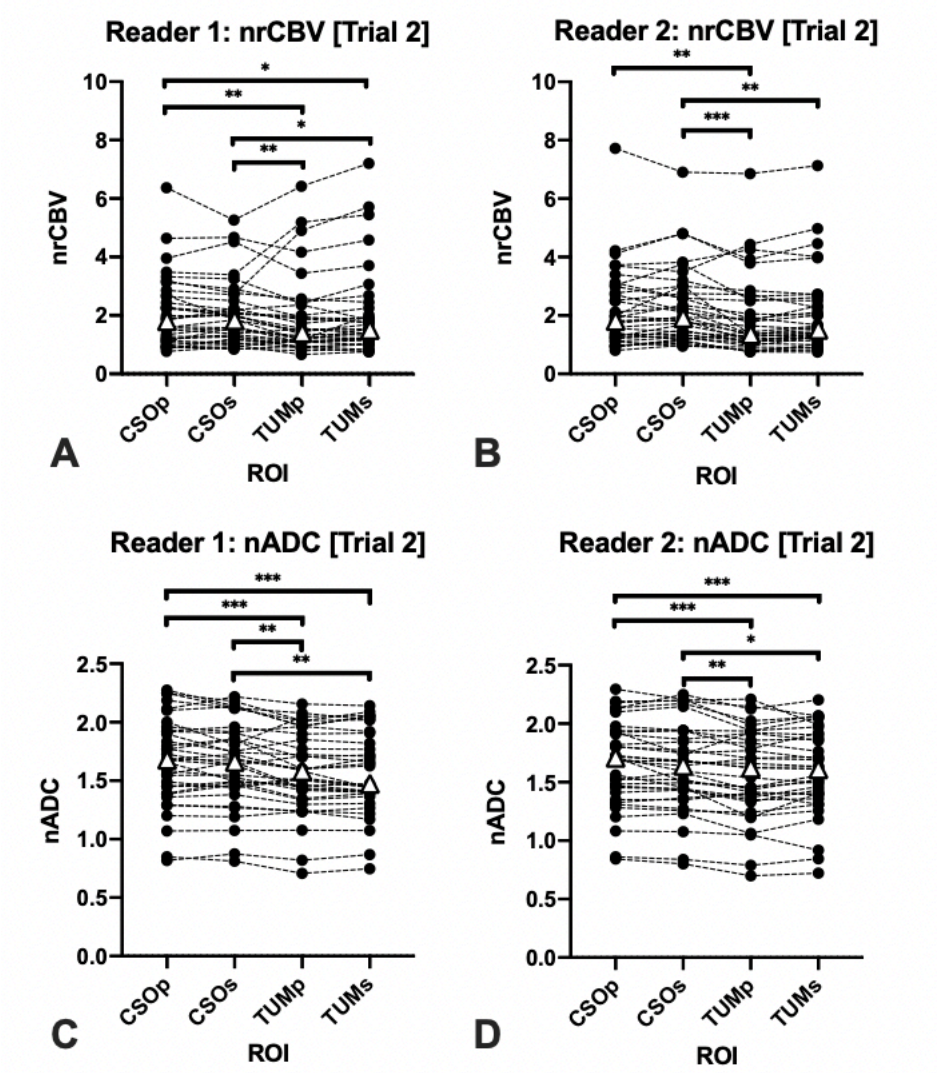

Figure 2.3. Differences in nrCBV and nADC Based on Normalization Method (Trial 2). Post-hoc analyses revealed significant differences for A/B) nrCBV and C/D) nADC between centrum semiovale (CSO) and tumor slice (TUM) methods for both readers in Trial 2, but not between planar (p) and spherical (s) methods within the same normalization region, similar to results from Trial 1. ∆ indicates median; * indicates $P < .05$; ** indicates $P < .01$; *** indicates $P < .001$

nrCBV (Non-parametric; Dunn's test)			nADC (Parametric; Tukey's test)		
Post-hoc Test Based on NAWM Method	**Reader 1: Rank Sum Difference (Median Difference) for Trials 1 / 2**	**Reader 2: Rank Sum Difference (Median Difference) for Trials 1 / 2**	**Post-hoc Test Based on NAWM Method**	**Reader 1: Mean Difference (95% CI) for Trials 1 / 2**	**Reader 2: Mean Difference (95% CI) for Trials 1 / 2**
CSOp vs. CSOs	-9 (-0.03) / 1 (0.04)	-6 (-0.03) / -16 (-0.13)	**CSOp vs. CSOs**	0.002 (-0.02–0.02) / 0.02 (-0.02–0.06)	0.01 (-0.02–0.04) / 0.02 (-0.01–0.05)
CSOp vs. TUMp	36 (0.17)** / 39 (0.23)**	41 (0.21)*** / 35 (0.22)**	**CSOp vs. TUMp**	0.08 (0.03–0.13)*** / 0.08 (0.04–0.13)***	0.09 (0.05–0.13)*** / 0.08 (0.04–0.13)***
CSOp vs. TUMs	19 (0.10) / 30 (0.11)*	31 (0.21)* / 19 (0.14)	**CSOp vs. TUMs**	0.09 (0.04–0.14)*** / 0.09 (0.04–0.13)***	0.08 (0.04–0.12)*** / 0.07 (0.03–0.10)***
CSOs vs. TUMp	45 (0.21)*** / 38 (0.22)**	47 (0.27)*** / 51 (0.29)***	**CSOs vs. TUMp**	0.08 (0.03–0.13)*** / 0.06 (0.02–0.11)**	0.08 (0.03–0.13)*** / 0.06 (0.02–0.10)**
CSOs vs. TUMs	28 (0.16) / 29 (0.20)*	37 (0.22)** / 35 (0.24)**	**CSOs vs. TUMs**	0.09 (0.04–0.13)*** / 0.07 (0.02–0.11)**	0.07 (0.02–0.11)** / 0.04 (0.01–0.08)*
TUMp vs. TUMs	-17 (-0.05) / -9 (-0.09)	-10 (-0.02) / -16 (-0.08)	**TUMp vs. TUMs**	0.006 (-0.03–0.04) / 0.002 (-0.02–0.03)	-0.01 (-0.04–0.02) / -0.02 (-0.06–0.02)

Table 2.2. Detailed Post-hoc Statistical Results of nrCBV and nADC Differences. * indicates $P < .05$; ** indicates $P < .01$; *** indicates $P < .001$

MRI Metric (NAWM)	Inter-reader Reproducibility ICC (95% CI) for Trials 1 / 2	Intra-reader Repeatability ICC (95% CI) for Readers 1 / 2
nrCBV (CSOp)	0.97 (0.79–0.99) / 0.95 (0.90–0.97)	0.99 (0.98–1) / 0.99 (0.98–0.99)
nrCBV (CSOs)	0.96 (0.86–0.99) / 0.94 (0.80–0.98)	0.98 (0.96–0.99) / 0.98 (0.96–0.99)
nrCBV (TUMp)	0.94 (0.87–0.97) / 0.97 (0.95–0.99)	0.98 (0.96–0.99) / 0.99 (0.98–0.99)
nrCBV (TUMs)	0.95 (0.90–0.97) / 0.92 (0.85–0.96)	0.98 (0.95–0.99) / 0.99 (0.98–0.99)
nADC (CSOp)	0.99 (0.99–1) / 1 (0.99–1)	1 (0.99–1) / 1 (1–1)
nADC (CSOs)	0.99 (0.98–0.99) / 0.98 (0.95–0.99)	0.99 (0.99–1) / 0.99 (0.98–1)
nADC (TUMp)	0.97 (0.94–0.99) / 0.97 (0.93–0.98)	0.99 (0.98–0.99) / 0.99 (0.97–0.99)
nADC (TUMs)	0.97 (0.95–0.99) / 0.98 (0.96–0.99)	0.99 (0.98–0.99) / 0.99 (0.97–0.99)

Table 2.3. Inter-reader Reproducibility Between Readers and Intra-reader Repeatability Between Trials for nrCBV and nADC.

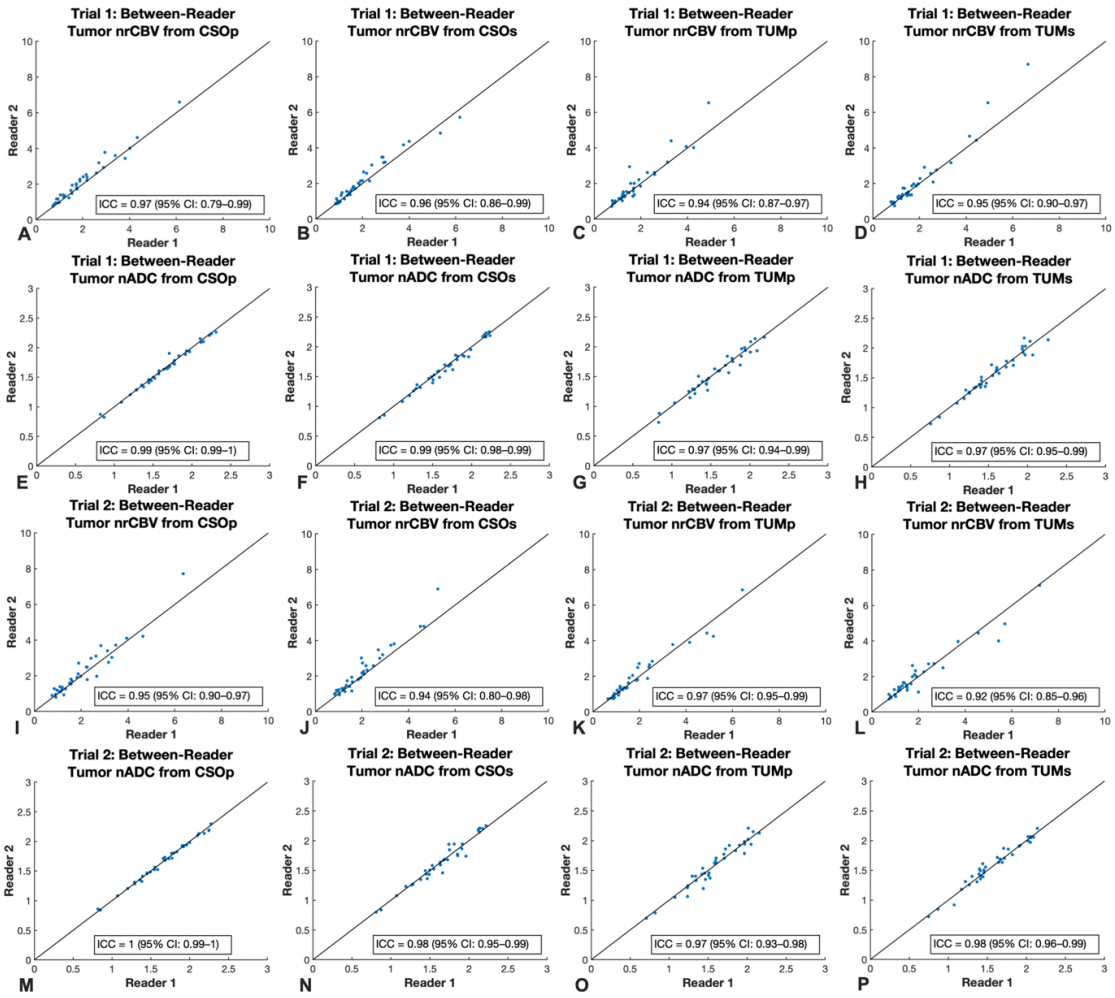

Figure 2.4. ICC Analyses Between Readers (Trials 1 & 2). nrCBV and nADC from A/E/I/M) CSOp, B/F/J/N) CSOs, C/G/K/O) TUMp, and D/H/L/P) TUMs displayed excellent (r>0.9) reproducibility between readers in both Trials 1 and 2. Because nrCBV data were non-normally distributed, all plots of ICC analyses display the non-transformed data points with the appropriate ICC statistical results from the normally distributed data following Box-Cox transformation.

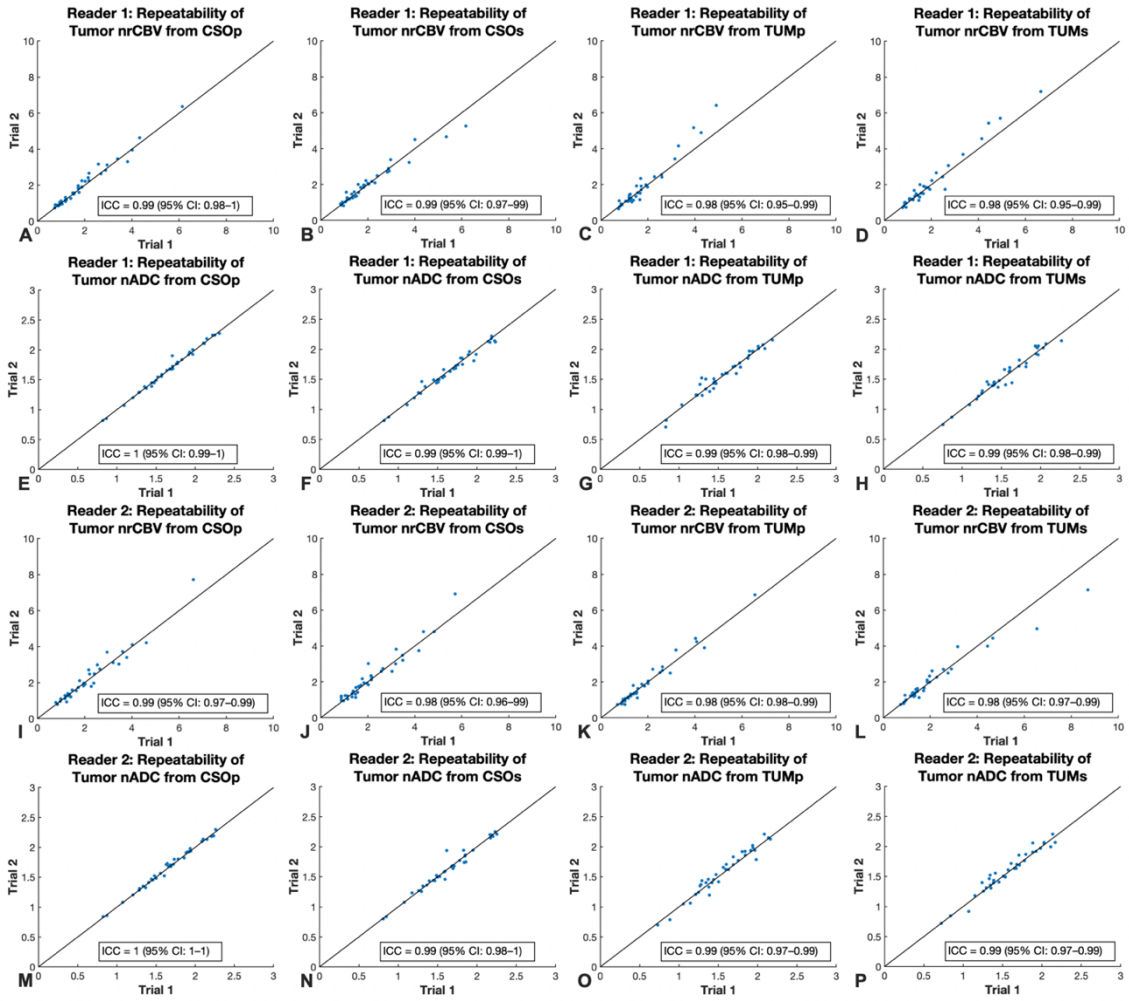

Figure 2.5. ICC Analyses Within Readers (Trials 1 & 2). Across both trials, nrCBV and nADC from **A/E/I/M**) CSOp, **B/F/J/N**) CSOs, **C/G/K/O**) TUMp, and **D/H/L/P**) TUMs displayed excellent (r>0.9) intra-reader repeatability for both readers. Because nrCBV data were non-normally distributed, all plots of ICC analyses display the non-transformed data points with the appropriate ICC statistical results from the normally distributed data following Box-Cox transformation.

IDH-Mutation Status Classification and Time Duration

As a validation step, ROC curve analyses for IDH-mutation status prediction revealed that the nrCBV and nADC values yielded similar area under the curve values regardless of normalization method (**Figures 2.6 & 2.7**; Trial 1 AUC for nrCBV=0.73–0.80; AUC for nADC=0.88–0.91). There were significant differences in the times to create each ROI (*P<.001*; **Table 2.4; Figure 2.8**). In general, CSO methods were quicker than TUM methods, particularly for the planar method (Median time savings of CSOp vs. TUMp = 11 seconds, *P<.001* for Reader 1; 16 seconds, *P<.01* for Reader 2) and the spherical method was quicker than the planar method, particularly for the TUM region (Median time savings of TUMs vs. TUMp = 11 seconds, *P<.01* for Reader 1; 23 seconds, *P<.001* for Reader 2).

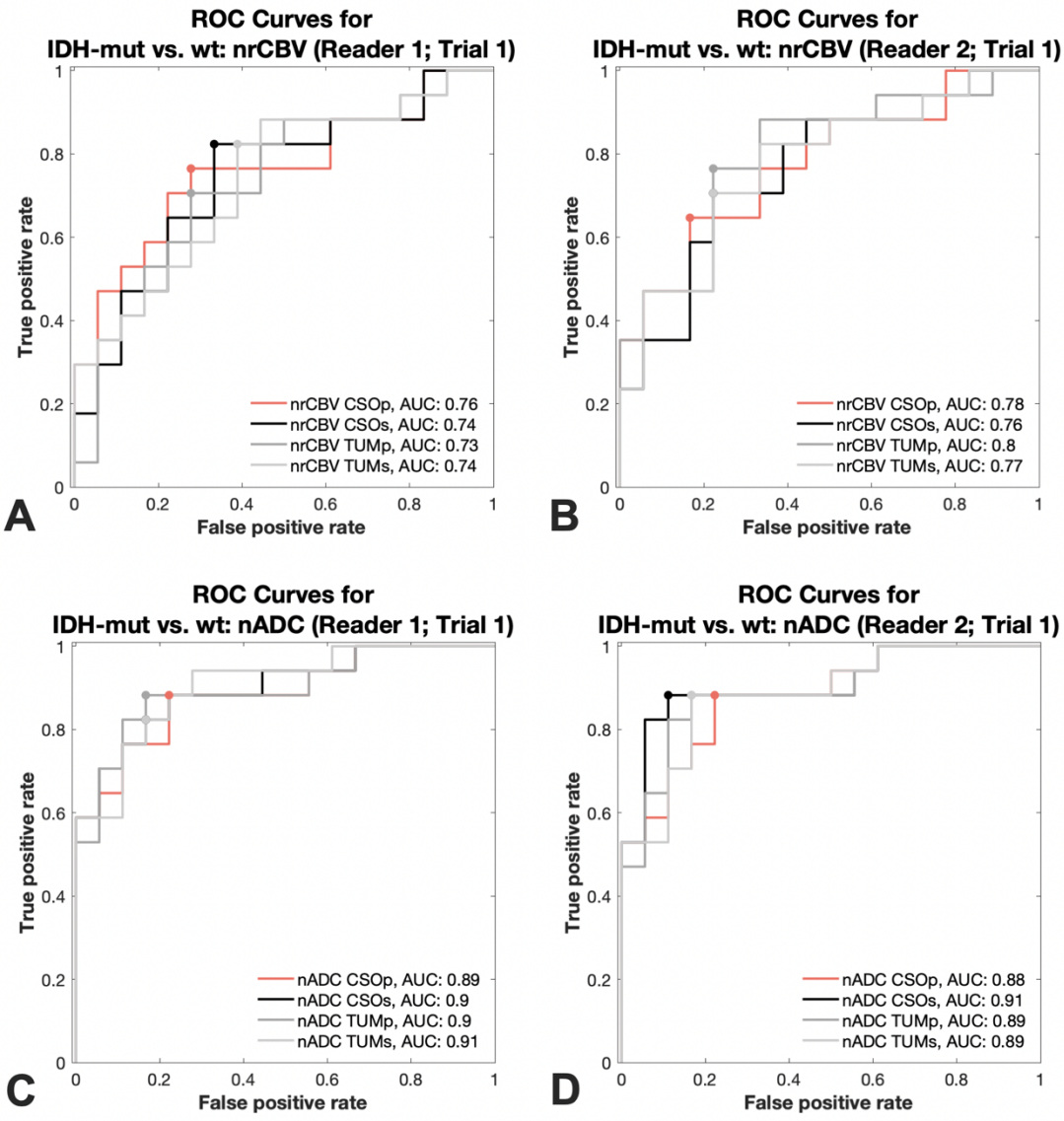

Figure 2.6. Receiver-Operating Characteristic (ROC) Curves for Predicting IDH Mutation Status (Trial 1). Different normalization methods resulted in similar area under the curve values for IDH-mutation status prediction using A/B) nrCBV and C/D) nADC. nrCBV = normalized relative cerebral blood volume; nADC = normalized apparent diffusion coefficient

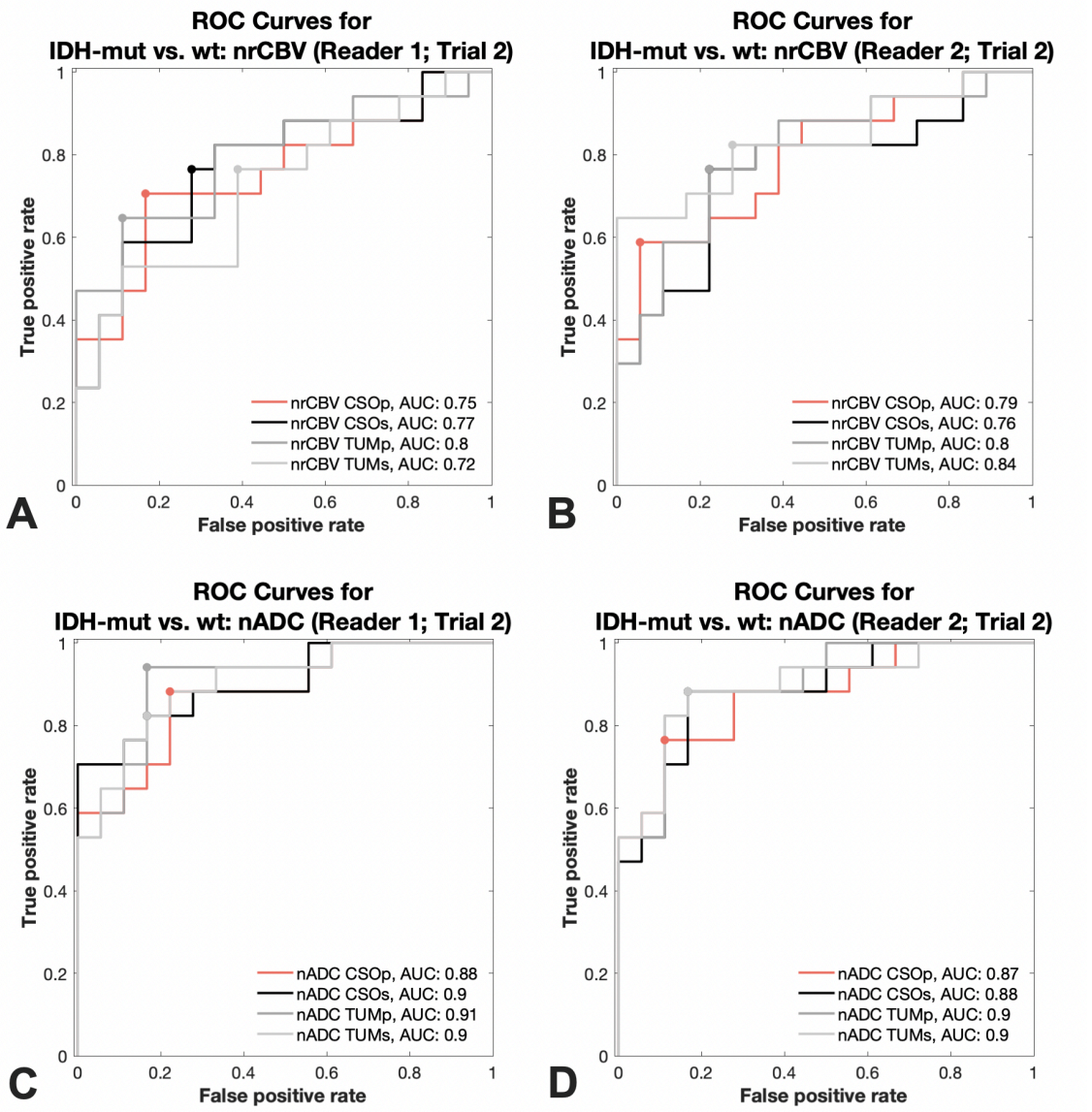

Figure 2.7. Receiver-Operating Characteristic (ROC) Curves for Predicting IDH Mutation Status (Trial 2). Different normalization methods resulted in similar area under the curve values for IDH-mutation status prediction using **A**/**B**) nrCBV and **C**/**D**) nADC in Trial 2, similar to results from Trial 1.

Time to Create ROIs (Non-Parametric; Dunn's test)		
Post-hoc Test Based on NAWM Method	**Reader 1: Rank Sum Difference (Median Difference in Seconds) for Trial 2**	**Reader 2: Rank Sum Difference (Median Difference in Seconds) for Trial 2**
CSOp vs. CSOs	-7 (-1)	43.5 (11)***
CSOp vs. TUMp	-51 (-11)***	-38.5 (-16)**
CSOp vs. TUMs	-16 (-2)	15 (5)
CSOs vs. TUMp	-44 (-11)***	-82 (-28)***
CSOs vs. TUMs	-9 (-2)	-28.5 (-4)*
TUMp vs. TUMs	35 (11)**	53.5 (23)***

Table 2.4. Detailed Post-hoc Statistical Results of Differences in Times to Create ROIs.

* indicates $P < .05$; ** indicates $P < .01$; *** indicates $P < .001$

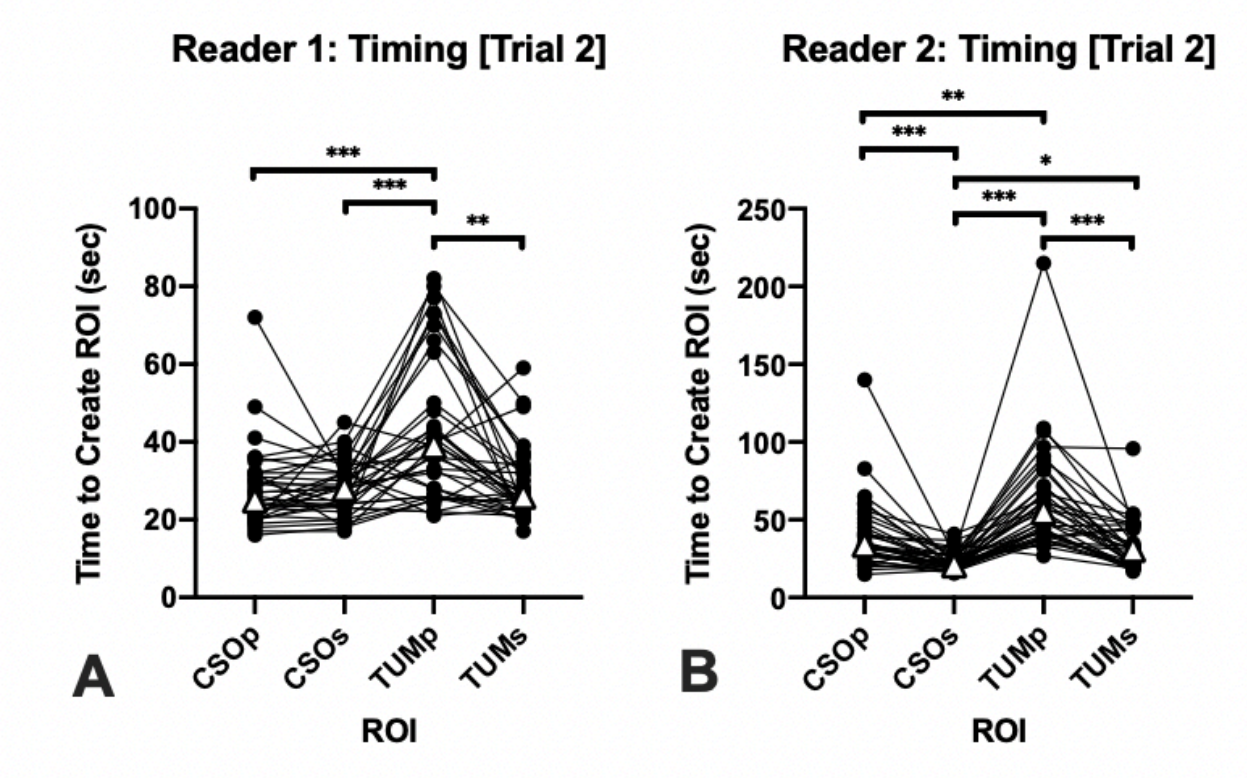

Figure 2.8. Time to Create NAWM ROIs. Significant differences in the time to create each ROI were observed. Broadly, CSO methods were quicker than TUM methods, and spherical methods were quicker than planar methods. ∆ indicates median; * indicates $P < .05$; ** indicates $P < .01$; *** indicates $P < .001$ NAWM = normal appearing white matter; ROI = region of interest; CSO = centrum semiovale; TUM = tumor

Discussion

The primary finding of the present study was that nrCBV and nADC values were significantly different based on the NAWM region, but not based on planar or spherical methods within the same NAWM region. As a result, the present findings support that it is imperative to be consistent in ROI-based normalization methods for both nrCBV and nADC. This study adds to previous literature by showing that nrCBV is significantly different based on NAWM normalization methods,[44, 45] and, to our knowledge, being the first to demonstrate differences in nADC in glioma patients based on NAWM normalization method, which are in line with previous findings that ADC is significantly different across contralateral NAWM regions in glioma patients.[68] In order to increase reproducibility and to better guide threshold-based interpretations of nrCBV and nADC across institutions, it is critical for research studies to describe the anatomical location and size of the NAWM ROI for rCBV and ADC normalization as done in some studies.[43, 52, 53, 55, 60, 61] For example, the excellent inter-reader reproducibility for nADC observed in the present study is in line with the high ICC values for nADC by two readers in a study by Thust et al., where the authors explicitly stated that each rater segmented NAWM ROIs in the CSO with similar volume to the tumor.[61] Furthermore, providing additional detail on the selection of a specific slice of the target NAWM region (e.g. CSO ~3 mm above the lateral ventricles in the present study) as done by Smits et al. and Cho et al. for nrCBV[43, 53] and Hagiwara et al. for nADC[60] may reduce variability and subjectivity in the normalization process.

All four normalization methods in the present study had similar intra-reader repeatability and inter-reader reproducibility as well as IDH-mutation status predictive performance, but there were significant reductions in time when performing the CSO methods compared to the TUM methods. One likely explanation for the increased time to create NAWM ROIs in TUM regions

was for cases where the tumor was located in regions with minimal contralateral white matter, such as near subcortical structures or in the temporal lobes (**Figure 2.1C&D**), so delineating a NAWM ROI that avoids gray matter, normal vessels, and ventricles was particularly challenging. Moreover, selecting a NAWM ROI in the tumor slice of those regions would be even more challenging if there was bilateral tumor infiltration. As a result, the present findings may support the usage of the centrum semiovale[43, 51-53, 60] as a target NAWM region instead of the white matter directly opposite the tumor[46, 47, 59] because the centrum semiovale is reliably a large region of white matter that is easily identifiable to neuroradiologists and research lab members alike, as also similarly stated by Thust et al.[61]

Of note, the current guidelines provided by QIBA's Stage 2 Consensus Profile for nrCBV propose a >2x2 cm TUMp NAWM ROI.[46] The present results of a similar 400-450 mm^2 TUMp ROI—which the study authors proposed given the difficulty of creating a 2 cm ROI in certain tumor regions described above—suggest that although tumor-slice ROIs provide similar diagnostic performance, intra-reader repeatability, and inter-reader reproducibility compared to CSO ROIs, CSO NAWM methods may be better options in terms of time-efficiency and ease.

Additionally, both readers had significantly reduced times creating TUMs ROIs compared to TUMp ROIs, and one reader had significantly reduced times creating CSOs ROIs compared to CSOp ROIs. The time reduction for the spherical methods compared to the planar methods may also be explained by similar reasons of ease. A significant advantage of the separable, spherical method is that it could be easier to avoid gray matter, vessels, and ventricles compared to a contiguous, planar method, especially in research settings in which lab members who are not radiologists may be involved. Furthermore, if the tumor is bilateral, spherical methods may be easier to avoid the lesion compared to planar methods. However, 3D ROIs may not be able to be

created in clinical software, so the CSOp method may be preferred in clinical settings when assessing quantitative maps generated from the scanner or from clinical software products. An alternative to the 3D CSOs method in the present study could also be placing 2D circular ROIs in the CSO as done by Smits et al.[53] to allow for use in clinical settings. One key difference between the study by Smits et al. and the present study was that the former placed their 2D planar ROIs on the original rCBV maps with a large 5 mm slice thickness, while in the present study, all ROIs were placed on rCBV and ADC maps registered to the post-contrast T1-weighted image with 1 mm slice thickness. Future studies may want to investigate differences in nrCBV and nADC normalization based 2D and 3D ROIs along with consideration of slice thickness.

Although NAWM normalization techniques are popular for nrCBV, it is worth mentioning other normalization approaches applied in some other studies. For example, there has also been interest in the automatic normalization, or "standardization", of rCBV parametric maps by transforming rCBV values to a standardized scale, precluding the need for manual NAWM ROIs.[44, 56-58] Standardization of rCBV has been shown to reduce variability compared to manual NAWM methods,[44, 56, 57] though standardized rCBV metrics had similar performance with NAWM-based nrCBV metrics for assessing post-treatment tumor burden in stereotactic biopsy samples of recurrent high-grade glioma.[58] Additionally, standardization requires the use of a training data set for each anatomical region and MRI protocol, which may explain why NAWM methods remain popular in research studies involving rCBV analyses. Intra-scan, non-manual rCBV normalization techniques—such as min-max normalization,[79] normalizing by the standard deviation across the whole brain,[44] and normalizing by the mean values outside the tumor[80]—have also been reported in limited cases. Some studies have also utilized normalization ROIs that include solely gray matter or a combination of gray and white matter,[66, 81-83] likely on the basis that gliomas can infiltrate into

gray matter. However, gray matter normalization has been demonstrated to cause systematic differences in tumor nrCBV compared to previously reported nrCBV thresholds obtained by the more conventional NAWM methods.[66] As a result, the present study did not explore automated or gray matter normalization methods given their limited use and instead, the present study aimed to assess variability within readers based on previously reported NAWM techniques in the literature.

It is also important to note that the usage of nADC remains controversial. Absolute ADC values are measured in units [e.g. mm^2/s], so normalization may not be justified. Additionally, there have been mixed findings on the potential benefit of nADC over ADC in glioma patients.[59-63] Nevertheless, ADC values of NAWM and cerebrospinal fluid have been reported to vary across patients in a multi-center trial,[67] which may support the increased implementation of nADC in the future. As a result, the characterization of various NAWM methods for nADC in the present study remains valuable as the potential clinical utility of nADC continues to be investigated.

This study has several limitations. Although the present study's sample size of IDH-mutant and IDH-wild-type gliomas was chosen based on power analysis using previously reported[63] nADC and nrCBV differences between IDH-status, there still remains the possibility that the sample size was limited. Nevertheless, significant differences in nrCBV and nADC were observed between CSO and TUM normalization methods, and ROC analyses of nrCBV and nADC remained highly predictive of IDH-status within our study cohort, so we believe that the study size is justified. Increasing the sample size, though, may potentially allow for better capturing the heterogeneity of brain tumors, such as tumor location and presence of bilateral infiltration, that can lead to potential challenges during NAWM normalization. Additionally, one patient was scanned at 1.5T. However, CBV and ADC are theoretically independent of field strength.[84] Further, we believe including this patient is acceptable given that we assessed intra-patient, paired

differences based on NAWM techniques, and that ADC and rCBV NAWM normalization should compensate for field strength differences,[64] if any. This study was also limited to datasets acquired from a single institution. A multi-center study may be valuable to better assess intra-reader repeatability and inter-reader reproducibility of the ROI-based normalization methods used in this study. Finally, automated normalization methods were not compared to the multiple ROI-based normalization methods in this study, but these approaches may provide for faster and more reproducible results.

Conclusions

There can be significant differences in nrCBV and nADC values depending on the selected NAWM region. CSOs normalization may be useful in research settings while CSOp normalization may be useful in clinical settings. Studies involving normalized MRI metrics based on ROI methods should clearly state the anatomical region, size, and approximate slice location of the normalization ROI to improve reproducibility and data interpretation for outside institutions.

Chapter 3. Digital Subtraction Maps of T2-Weighted and T2-Weighted FLAIR MRI to Quantify T2-FLAIR Mismatch in Non-enhancing Diffuse Gliomas

Preface

This chapter is adapted from the following publication:

Cho NS, Sanvito F, Le VL, Oshima S, Teraishi A, Yao J, Telesca D, Raymond C, Pope WB, Nghiemphu PL, Lai A, Cloughesy TF, Salamon N, Ellingson BM. Quantification of T2-FLAIR Mismatch in Nonenhancing Diffuse Gliomas Using Digital Subtraction. *AJNR Am J Neuroradiol.* 2024 Feb 7;45(2):188-197. doi: 10.3174/ajnr.A8094. PMID: 38238098.

a. Selected for *AJNR* cover image (Vol. 45, Issue 2) and "Editor's Choice" designation
b. Nominated for the 2024 *AJNR* (1) Lucien Levy Best Research Article Award and (2) Early Career Award

Introduction

The presence of "T2-FLAIR mismatch sign" (T2FM-sign) on MRI, first described by Patel *et al.*,[38] has become a well-known and validated[85-91] non-invasive imaging biomarker with ~100% specificity albeit low sensitivity for diagnosing IDHm astrocytomas (1p/19q-intact; IDHm-A) and ruling out IDH-mutant oligodendrogliomas (1p/19q-codeleted; IDHm-O) and IDHwt gliomas. Patel *et al.* originally described this imaging biomarker as "presence or absence of complete/near-complete hyperintense signal on T2WI, and relatively hypointense signal on FLAIR except for a hyperintense peripheral rim",[38] and the authors reported a specificity of 100% in the two cohorts they tested and sensitivities of 22.0% and 45.5%.[38]

Other subsequent studies have also noted 100% specificity[85, 86] along with some instances of false positives resulting in specificities ranging 76.5–98%.[87-90] There is also potential for less conservative definitions of T2FM-sign, such as Lasocki *et al.* proposing that a reader-estimated ≥25% T2FM-volume was sufficient to assign as T2FM-sign positivity, which still yielded 100% specificity with 63% sensitivity;[86] Li *et al.* proposing simply a T2-weighted FLAIR hyperintense rim with hypointense core regardless of appearance on T2-weighted MRI, which also yielded 100% specificity with 71.3% sensitivity;[92] and Lee *et al.* proposing partial T2FM-sign in grade 4 IDHm gliomas when assessing only grade 4 gliomas, which yielded 99.6% specificity with 26.4% sensitivity.[93] Less conservative definitions have also been proposed to explain Juratli *et al.*'s finding of 76% specificity with 73% sensitivity.[88, 91]

However, despite the inherently quantitative nature of the T2FM-sign based on the relative extent of T2FM-volume within a tumor, to our knowledge, studies on T2FM-sign have mostly remained *qualitative* based on reader studies. A prior study by Mohammed *et al.* has previously used a geographically weighted regression-based classification model that resulted in classification

of IDHm-A with very high sensitivity and specificity.[94] Another study by Lee *et al.* utilized a "hot-spot" assessment of T2FM-areas by assessing relative T2-weighted and T2-weighted FLAIR hyperintensity in the T2FM-core region for glioma classification,[95] but the study did not assess whole tumor quantification of T2FM-volume. Quantifying T2FM-volume could be valuable to assess if there exists a quantitative percentage T2FM-volume that is analogous to T2FM-sign positivity for achieving 100% specificity for IDHm-A, such as Lasocki *et al*.'s reader-estimated ≥25% T2FM-volume[86] or other volumetric thresholds.

As a result, there remains continued need of methods for visualization and volumetric quantification of T2FM to specifically study IDHm-A exhibiting T2FM-sign. For example, IDHm-A with T2FM-sign are known for intratumoral heterogeneity as the T2FM-core subregion is known for the presence of microcysts or enlarged intercellular space on histology.[90, 96] These findings may also demonstrate the need for a reliable method to study IDHm-A with T2FM-sign specifically in the context of characterizing T2FM- and T2FNM-subregion differences. One such method could be subtraction maps of co-registered MRI scans, which have already shown utility for T1 post-/pre-contrast MRI for assessing contrast-enhancing tumor volume in glioblastoma.[32] While similar mathematics of relative T2-weighted and T2-weighted FLAIR hyperintensity signal have been used to study T2FM-sign only in the mismatched core region,[95] to our knowledge, whole-brain subtraction maps have not yet been applied for T2-weighted and T2-weighted FLAIR images to quantify the extent of T2FM from a whole tumor, volumetric perspective.

The present study explored usage of T2-weighted and T2-weighted FLAIR subtraction maps to study T2FM in non-enhancing gliomas. We hypothesized that (1) there exists a tumor % T2FM-volume threshold based on subtraction map values that can classify IDHm-A with 100% specificity; (2) % T2FM-volume may be associated with tumor volume and tumor grade; and (3)

the visual evaluation of T2-FLAIR subtraction maps would improve the sensitivity, specificity, and inter-reader agreement of T2FM-sign in a reader study.

Methods

Patient Selection

Two cohorts of patients with gliomas who underwent preoperative MRI from two different institutions were screened for analysis: (1) a test cohort from The Cancer Imaging Archive (TCIA) University of California San Francisco Preoperative Diffuse Glioma MRI (UCSF-PDGM) (n=495 total)[97-99] and (2) a validation cohort consisting of patients at our institution enrolled in prospective trials (IRB #14-001261, #21-000514, #21-002112) and/or assessed in a prior study[41] (n=150 total). All patients in the institutional cohort provided written informed consent. Patients with the following inclusion criteria were included in the study: (1) non-enhancing, adult-type diffuse glioma according to the World Health Organization 2021 classification,[3] (2) no prior pharmacological or radiation treatment, (3) no prior surgery except for biopsy, (4) known IDH-mutational status, (5) if IDH-mutant, known 1p/19q status, and (6) supratentorial location (**Figure 3.1**) All patients in the TCIA UCSF-PDGM were treatment-naïve except for biopsy. Tumor molecular diagnosis ground truth was based on histopathological analysis. IDH status was determined by targeted next-generation DNA sequencing for the TCIA cohort[100] and by polymerase chain reaction sequencing and/or immunohistochemistry for the institutional cohort.[70] 1p/19q codeletion status was determined using fluorescence in situ hybridization for both cohorts. A total of 70 patients from the TCIA UCSF-PDGM and 34 patients from the institutional cohort were included for study (**Figure 3.1**). Two distinct lesions in the left and right hemispheres of one patient in the TCIA cohort were assessed separately. Patient data are summarized in **Table 3.1**.

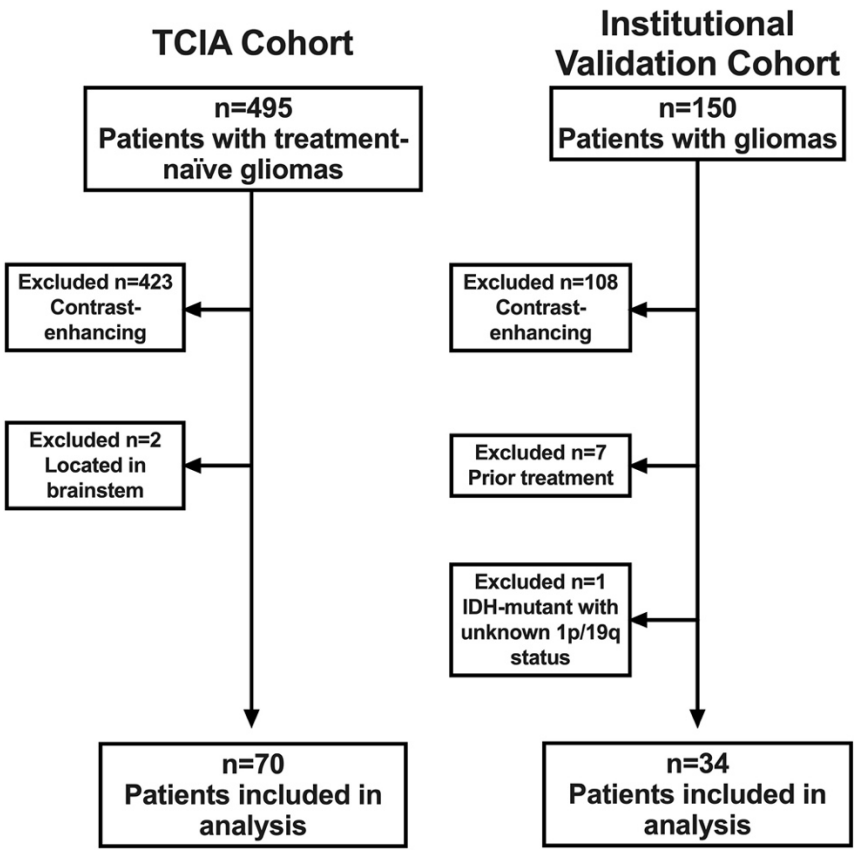

Figure 3.1. Patient Selection Flowchart. TCIA = The Cancer Imaging Archive; IDH = isocitrate dehydrogenase

Characteristic	TCIA Cohort (n=70 patients with n=71 lesions)	Institutional Cohort (n=34 patients/lesions)
Age: Mean (Range)	43 (22–78)	42 (22–79)
Sex: M/F	41/29	18/16
Diagnosis: n (%)		
IDHm Astrocytoma	46 (64.8%)	19 (55.9%)
Grade 2	33	11
Grade 3	13	7
Grade 4	0	1
IDHm Oligodendroglioma	9 (12.7%)	9 (26.5%)
Grade 2	9	8
Grade 3	0	1
IDHwt Glioma	16 (22.5%)	6 (17.6%)

Table 3.1. Clinical Data of Patients. TCIA = The Cancer Imaging Archive; IDHm = isocitrate dehydrogenase mutant; IDHwt = isocitrate dehydrogenase wild type

Image Acquisition and Pre-Processing

Both cohorts were scanned using 3.0T scanners (TCIA: GE Healthcare; Discovery 750; Institutional: Siemens; Prisma, Skyra, Trio, Vida) and underwent standardized protocols for T2-weighted and T2-weighted FLAIR MRI: TCIA[97] 3D T2-weighted Sagittal FSE: TR/TE=2200/100ms; slice thickness=1.2mm; in-plane resolution=1x1mm; TCIA 3D T2-weighted FLAIR Coronal FSE: TR/TE/TI=5700/115/1650ms; slice thickness=1.2mm; in-plane

resolution=1x1mm; Institutional 2D T2-weighted Axial FSE: TR ranging 4381–8450ms; TE ranging 86–116ms; slice thickness=3mm; in-plane resolution ranging 0.31–0.94 x 0.31–0.94mm; Institutional 3D T2-weighted Sagittal FSE (n=1 patient): TR/TE=3200/412ms; slice thickness=1 mm; in-plane resolution=0.98x0.98mm; Institutional T2-weighted FLAIR 2D Axial: TR ranging 7080–9980ms; TE ranging 81–89ms; TI=2500ms; slice thickness=3mm; in-plane resolution ranging 0.47–0.94 x 0.47–0.94mm.

The provided TCIA data were already pre-processed as follows:[97, 98] scans were registered to the 3D T2-weighted FLAIR image (Advanced Normalization Tools) and then skull-stripped using the open-source, deep-learning algorithm brain_mask (https://www.github.com/ecalabr/brain_mask/). The institutional data were pre-processed similarly: scans were registered to the 3D T1-post-contrast image (*tkregister2*; Freesurfer[101] | *flirt*: Functional Magnetic Resonance Imaging of the Brain Software Library[102]) and then skull-stripped using the open-source, deep-learning algorithm HD-BET[103] (https://github.com/MIC-DKFZ/HD-BET).

T2-FLAIR Subtraction Maps & Tumor Imaging Analysis

T2-FLAIR subtraction maps were generated as follows: (1) skull-stripped T2-weighted MRI were further precisely registered to skull-stripped T2-weighted FLAIR MRI using *flirt*; (2) T2-weighted MRI and T2-weighted FLAIR MRI were normalized using z-score normalization and then by performing voxel-wise subtraction by the mean T2-weighted and T2-weighted FLAIR signal intensity, respectively, of the NAWM using 3 spherical VOI's within the contralesional superior centrum semiovale avoiding T2/FLAIR hyperintensities as described previously[41, 60] so that the resulting signal intensity in NAWM would be ~0; and then (3) performing voxel-wise

subtraction of the normalized T2-weighted MRI and the normalized T2-weighted FLAIR MRI (normalized T2-weighted minus normalized T2-weighted FLAIR). Tumor VOIs of the T2-weighted hyperintensity of the institutional cohort were created by a lab member with 2 years of experience in tumor segmentation analysis (NSC) using a semi-automated thresholding method involving Analysis of Functional NeuroImages (AFNI) software[104] (NIMH Scientific and Statistical Computing Core; Bethesda, MD, USA; https://afni.nimh.nih.gov) as previously described.[32, 105] The provided TCIA segmentations were also refined using this thresholding technique for consistency. Voxels corresponding to cerebrospinal fluid and macroscopic cysts (characterized as having round shape, well-defined borders, CSF-like signal intensity, and lacking wall enhancement) were excluded from the tumor VOIs. All final tumor VOIs were inspected by a radiologist (SO) with 11 years of experience in neuroimaging analysis who was blinded to the tumor molecular diagnosis.

The whole tumor VOIs were then split using the T2-FLAIR subtraction maps into "T2-FLAIR mismatch" (*positive* values in T2-FLAIR subtraction map) and "T2-FLAIR non-mismatch" (*negative* values in T2-FLAIR subtraction map) subregion VOIs (T2FM-subregion and T2FNM-subregion, respectively) using a consistent threshold of 0. By doing so, tumor T2FM subregions would be defined as regions where the normalized T2-weighted MRI signal intensity is greater than the normalized T2-weighted FLAIR signal intensity, while the remaining voxels in the tumor mask would be assigned to the T2FNM subregion. T2FM- and T2FNM-subregion volumes were obtained. Tumor percentage T2FM volume (% T2FM-volume) was calculated as T2FM-subregion volume divided by total tumor volume. To assess the potential impacts of slight image misregistration on % T2FM-volume calculation, two deliberately misregistered T2-FLAIR subtraction maps were generated using the AFNI Nudge Dataset plugin—one from 2-voxel

posterior shift of the co-registered T2-weighted MRI and one from 2-degree counter-clockwise shift of the co-registered T2-weighted MRI—and tumor VOI's were split again into T2FM- and T2FNM-subregions. The median thickness of the peripheral T2FNM-subregion for tumors exhibiting T2FM-subregions was calculated using AFNI software by creating a 1-voxel-wide border segmentation of the T2FNM-subregion VOI (*3DDepthMap -rimify*) followed by manually removing non-peripheral voxels, and then creating a 3D depth map from the T2FM-subregion voxels after cluster filtering T2FM-subregion voxels at a threshold of >30 voxels. The external border segmentation was then encoded with distance from the T2FM-subregion via voxel-wise multiplication of the depth map (**Figure 3.2**), and the median value was taken to be the T2FNM-subregion thickness.

Reader Study: T2-FLAIR Mismatch Sign Using T2-FLAIR Subtraction Maps

Two radiologists with 7 years (FS; reader 1) and 11 years (SO; reader 2) of neuroimaging experience who were blinded to the molecular diagnosis performed a reader study. For this analysis, the two cohorts were pooled. The readers were first given only the co-registered T2-weighted and T2-weighted FLAIR MRI scans and asked (1) to assess the presence of T2FM-sign as first described by Patel *et al.*[38] ("presence or absence of complete/near-complete hyperintense signal on T2WI, and relatively hypointense signal on FLAIR except for a hyperintense peripheral rim") and (2) to estimate the % T2FM-volume, similar to Lasocki *et al.*'s proposed semi-quantitative definition of ≥25% T2FM-volume as sufficient for T2FM-sign.[86] The readers were then provided the T2-FLAIR subtraction maps in the same session and asked to repeat their assessments before assessing the next patient. T2-FLAIR subtraction maps were visualized using a standardized color bar with values ranging from -3 to +3, where red to yellow shades represented

mismatched voxels with positive values, teal to blue shades represented non-mismatched voxels with negative values, and gray represented voxels with values close to zero (**Figure 3.2**).

Statistical Analysis

Statistical analysis was performed using GraphPad Prism Software (Version 8.4 GraphPad Software, San Diego, California). Receiver operating characteristic (ROC) curves were first generated on the TCIA cohort to assess performance of empiric % T2FM-volume thresholds for classifying IDHm-A vs. IDHm-O/IDHwt gliomas. ROC curves were also computed in the institutional cohort, and the same % T2FM-volume thresholds were applied to validate their diagnostic performance. For group comparisons, datasets were tested for normality using the Shapiro-Wilk test to determine whether to apply non-/parametric statistical methods. Contingency tables for IDHm-A distribution based on cohort, tumor grade, and % T2FM-volume were assessed using Fisher's exact tests. Tumor characterization analyses comparing T2FM- and T2FNM-subregions were conducted only in IDHm-A that demonstrated both subregions at an empiric threshold of ≥15% T2FM-volume. Differences in % T2FM-volume and tumor volume were assessed using either t-tests or Mann-Whitney tests. Correlations in T2FNM-subregion thickness and % T2FM-volume were assessed using either Pearson or Spearman correlations, and relationships of T2FNM-subregion thickness based on % T2FM-volume categorizations were assessed using Kruskal-Wallis test with post-hoc Dunn's multiple comparisons tests. For the reader study, inter-reader agreement Cohen's Kappa scores were calculated, and the Wald test was performed to assess overall changes in reader sensitivity & specificity for IDHm-A. Significance was set to $P < 0.05$. All bar graphs with error bars display the mean and SD.

Results

Representative Cases

Eight representative cases across both cohorts are shown in **Figures 3.2 and 3.3**. **Figure 3.2** displays "typical" true positive and true negative cases in the reader study. Patients 3.2A & 3.2B are diagnosed with IDHm-A, and T2-FLAIR subtraction maps clearly visualize T2FM-subregions within these tumors and demonstrate 59.6% and 48.0% T2FM-volume, respectively. (**Figures 3.2A/B**, true positive results). Patients 3.2C & 3.2D are diagnosed with IDHm-O and IDHwt glioblastoma, respectively, that demonstrate heterogeneous T2-weighted FLAIR hyperintensity, but T2-FLAIR subtraction maps demonstrate no corresponding T2FM-subregions (**Figures 3.2C/D**, true negative results). **Figure 3.3** demonstrates typical false negative and atypical false positive cases. Patients 3.3A & 3.3B are diagnosed with IDHm-A but T2-FLAIR subtraction maps do not show T2FM-subregions (**Figures 3.3A/B,** false negative results). Patients 3.3C & 3.3D are diagnosed with IDHm-O and IDHwt glioblastoma, respectively. These patients were interpreted as having T2-FLAIR mismatch sign when using T2-FLAIR subtraction maps by at least one of the readers and demonstrated 35.0% and 12.5% T2FM-volume, respectively **(Fig 3.3C/D**, false positive results).

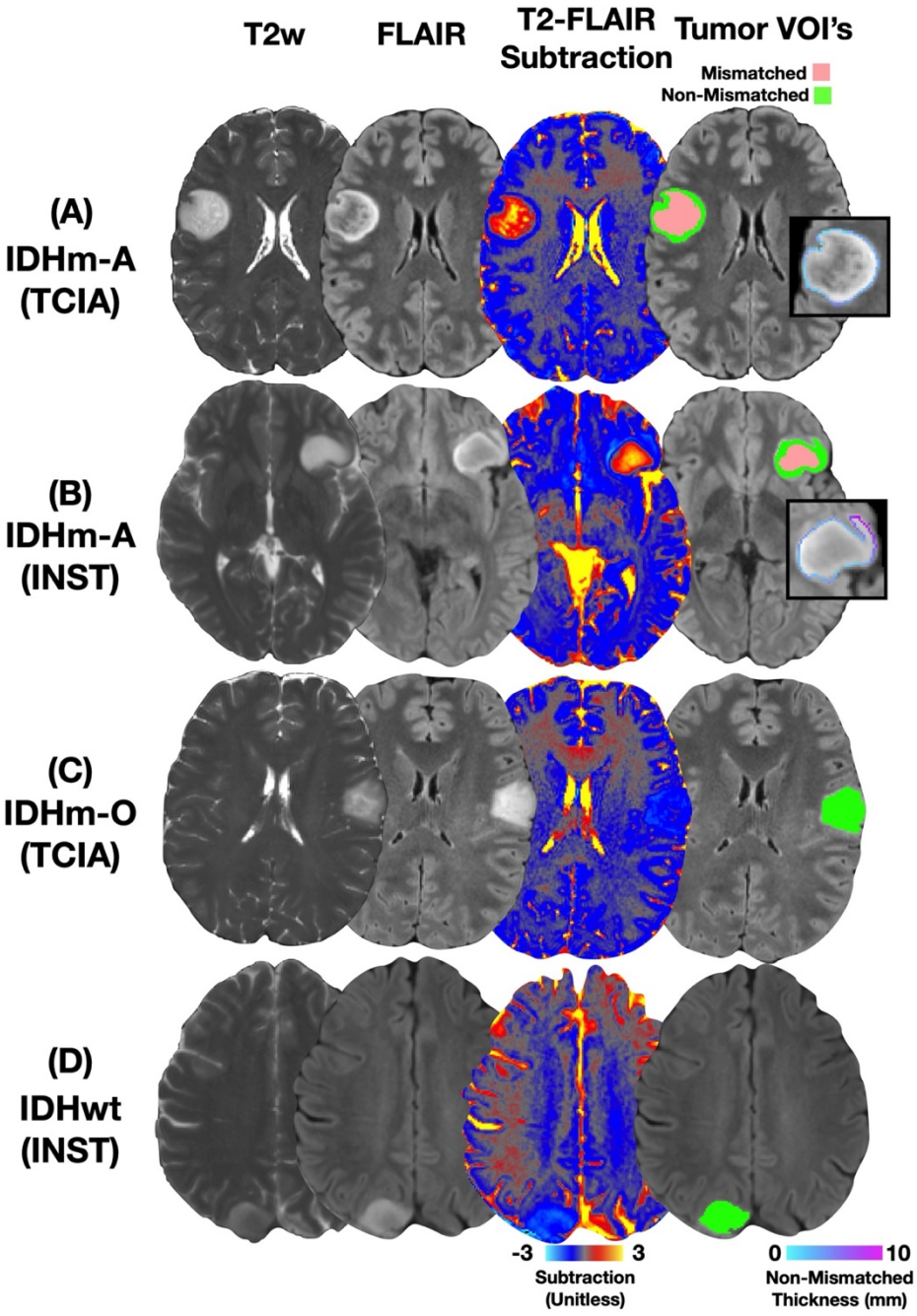

Figure 3.2. Representative True Positive and True Negative "Typical" Cases with T2-FLAIR Subtraction Maps and Tumor Segmentations. (**A**) Patient A is a 38 year old female from the TCIA cohort diagnosed with grade 2 IDH-mutant astrocytoma demonstrating 59.6% T2-FLAIR mismatch volume (true positive result). (**B**) Patient B is a 23 year old male from the

institutional cohort diagnosed with grade 2 IDH-mutant astrocytoma demonstrating 48.0% T2-FLAIR mismatch volume (true positive result). (**C**) Patient C is a 35 year old female from the TCIA cohort diagnosed with grade 2 IDH-mutant oligodendroglioma demonstrating heterogeneous T2-weighted and T2-weighted FLAIR hyperintensity and no T2-FLAIR mismatch on the subtraction map (true negative result). (**D**) Patient D is a 59 year old male from the institutional cohort diagnosed with grade 4 IDH-wild-type glioblastoma. The relative hypointense central T2-weighted FLAIR signal with a peripheral hyperintense rim may mimic a T2-FLAIR mismatch sign at first glance, but the corresponding absence of T2-FLAIR mismatch on the subtraction map from the heterogeneous T2-weighted hyperintensity clearly show the lack of T2-FLAIR mismatch (true negative result). Corresponding tumor segmentation volumes of interest of "T2-FLAIR mismatch" (pink) and "T2-FLAIR non-mismatch" (green) subregions (**A-D**) as well as the "T2-FLAIR non-mismatch" subregion external borders encoded with thickness (**A/C**) are shown. TCIA = The Cancer Imaging Archive; INST = Institutional; T2FM = T2-FLAIR mismatch; VOI = Volume of interest; IDHm-A = Isocitrate dehydrogenase mutant astrocytoma; IDHm-O = Isocitrate dehydrogenase mutant oligodendroglioma; IDHwt = IDH-wild type glioma

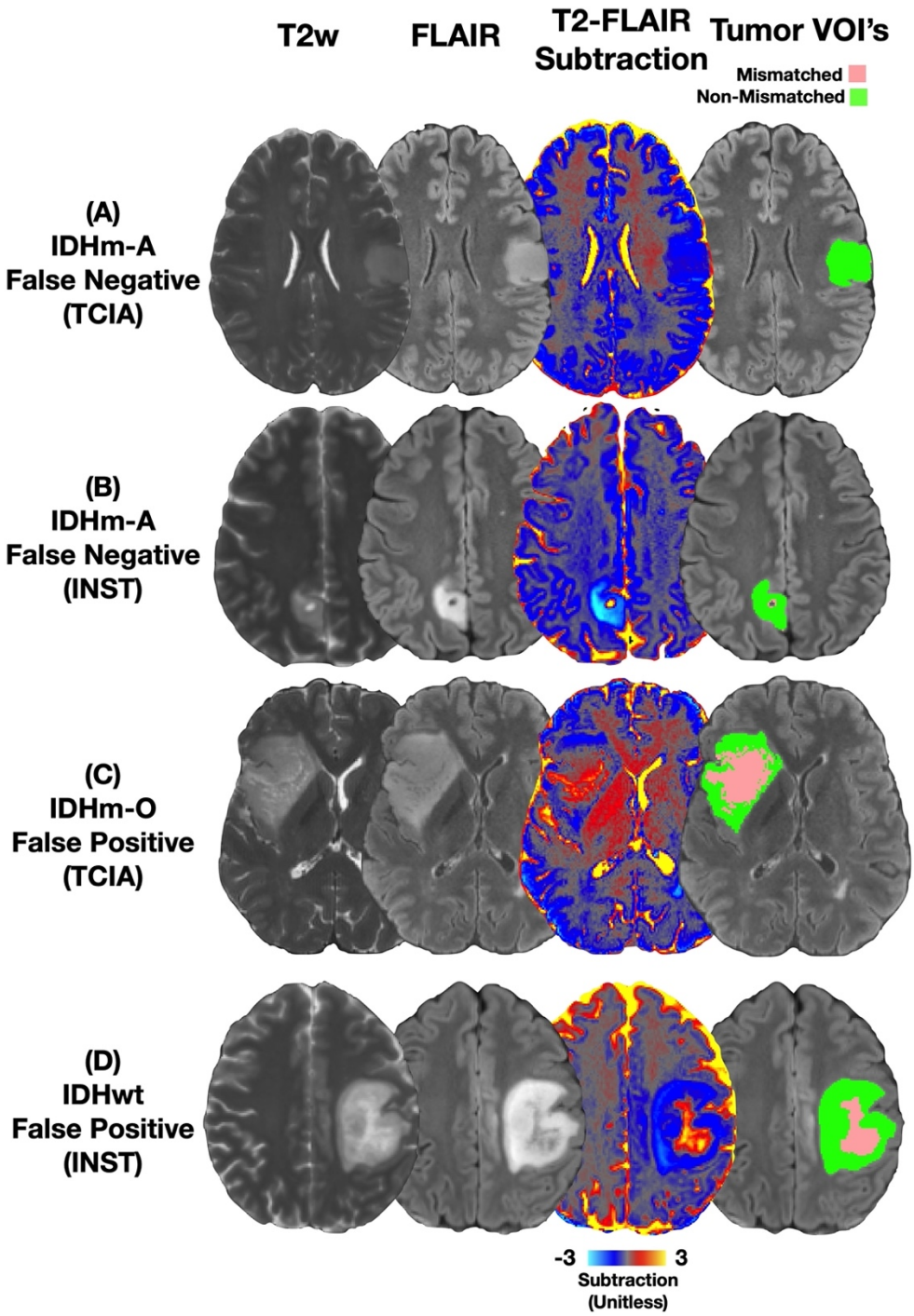

Figure 3.3. Representative False Negative and False Positive Cases with T2-FLAIR Subtraction Maps and Tumor Segmentations. (**A**) Patient A is a 38 year old male from the

TCIA cohort diagnosed with grade 2 IDH-mutant astrocytoma with no T2-FLAIR mismatch on the subtraction map (false negative result). (**B**) Patient B is a 36 year old female from the institutional cohort diagnosed with grade 2 IDH-mutant astrocytoma with no T2-FLAIR mismatch on the subtraction map excluding the cystic portion (false negative result). (**C**) Patient C is a 45 year old male from the TCIA cohort diagnosed with grade 2 IDH-mutant oligodendroglioma demonstrating 35.0% T2-FLAIR mismatch volume that was assessed as a false positive for T2-FLAIR mismatch sign by one reader using subtraction maps (false positive result). (**D**) Patient D is a 35 year old female diagnosed with IDH-wild type glioblastoma demonstrating 12.5% T2-FLAIR mismatch volume that was assessed as a false positive for T2-FLAIR mismatch sign by both readers using subtraction maps. Corresponding tumor segmentation volumes of interest of "T2-FLAIR mismatch" (pink) and "T2-FLAIR non-mismatch" (green) subregions are shown (**A-D**) (false positive result). TCIA = The Cancer Imaging Archive; INST = Institutional; T2FM = T2-FLAIR mismatch; VOI = Volume of interest; IDHm-A = Isocitrate dehydrogenase mutant astrocytoma; IDHm-O = Isocitrate dehydrogenase mutant oligodendroglioma; IDHwt = IDH-wild type glioma

Diagnostic Performance of Quantitative Percentage T2FM-Volume

In the TCIA cohort, % T2FM-volume was significantly higher in IDHm-A (mean (95% Confidence Interval): 18.0% (11.4–24.6%)) compared to IDHm-O/IDH-wt gliomas (5.38% (0.94–9.81%); *P*=0.03; **Figure 3.4A**). ROC curves for using % T2FM-volume to classify IDHm-A versus IDHm-O/IDHwt gliomas demonstrated an area under curve (AUC) of 0.657 (*P*=0.03) (**Figure 3.4B)**. A threshold of ≥42% T2FM-volume was sufficient to achieve 100% specificity while also having 19.6% sensitivity; a threshold of ≥25% T2FM-volume showed 92.0% specificity and 32.6% sensitivity; and a threshold of ≥15% T2FM-volume showed 88.0% specificity and 39.1% sensitivity for IDHm-A **(Figure 3.4B)**. An optimal threshold maximizing the likelihood ratio at 5.44 was ≥38% T2FM-volume, which showed 96.0% specificity and 21.7% sensitivity.

Similar results were shown in the institutional validation cohort. % T2FM-volume was significantly higher in IDHm-A compared to IDHm-O/IDHwt (IDHm-A = 32.1% T2FM-volume (21.9–42.2%) vs. IDHm-O/IDHwt = 4.14% T2FM-volume (1.32–6.97%); *P*<0.0001; **Figure 3.4C**). ROC curve analyses showed an AUC=0.919 (*P*<0.0001, **Figure 3.4D**), and using the same thresholds as the TCIA cohort, a threshold of ≥42% T2FM-volume showed 100% specificity and 31.6% sensitivity; a threshold of ≥25% T2FM-volume showed 100% specificity and 63.2% sensitivity; and a threshold of ≥15% T2FM-volume showed 93.3% specificity and 79.0% sensitivity for IDHm-A. The TCIA optimal threshold of ≥38% T2FM-volume showed 100% specificity and 36.8% sensitivity. There was a significant higher proportion of IDHm-A with ≥25% T2FM-volume in the institutional cohort compared to the validation cohort (*P*=0.03; **Table 3.2**).

The diagnostic results when pooling both cohorts showed significant higher % T2FM-volume in IDHm-A (22.1% (16.5–27.8%)) compared to IDHm-O/IDHwt gliomas (4.91% (2.04-7.79%); *P*=0.0002; **Figure 3.4E**), and the ROC curve AUC was 0.715 (*P*=0.0002; (%T2FM-

volume threshold: Specificity/Sensitivity) ≥42% T2FM-volume: 100%/23.1%; ≥38% T2FM-volume: 97.5/26.2%; ≥25% T2FM-volume: 95%/41.5%; ≥15% T2FM-volume: 90%/50.8%; **Figure 3.4F**).

When assessing the potential impact of slight image misregistration on % T2FM-volume, the mean magnitude difference in % T2FM-volume across both cohorts was 1.04% (0.88%–1.20%) (**Figure 3.5**). Considering empiric thresholds of 1.0% and 5.0% T2FM-volume as potential "noise floors" when utilizing T2-FLAIR subtraction maps, the sensitivity values for IDHm-A at a threshold ≥1.0% T2FM-volume were 73.9%, 100%, and 81.5% for the TCIA, institutional, and pooled cohorts, respectively, and that for ≥5.0% T2FM-volume were 45.7%, 84.2%, and 56.9% for the TCIA, institutional, and pooled cohorts, respectively (**Figure 3.5**).

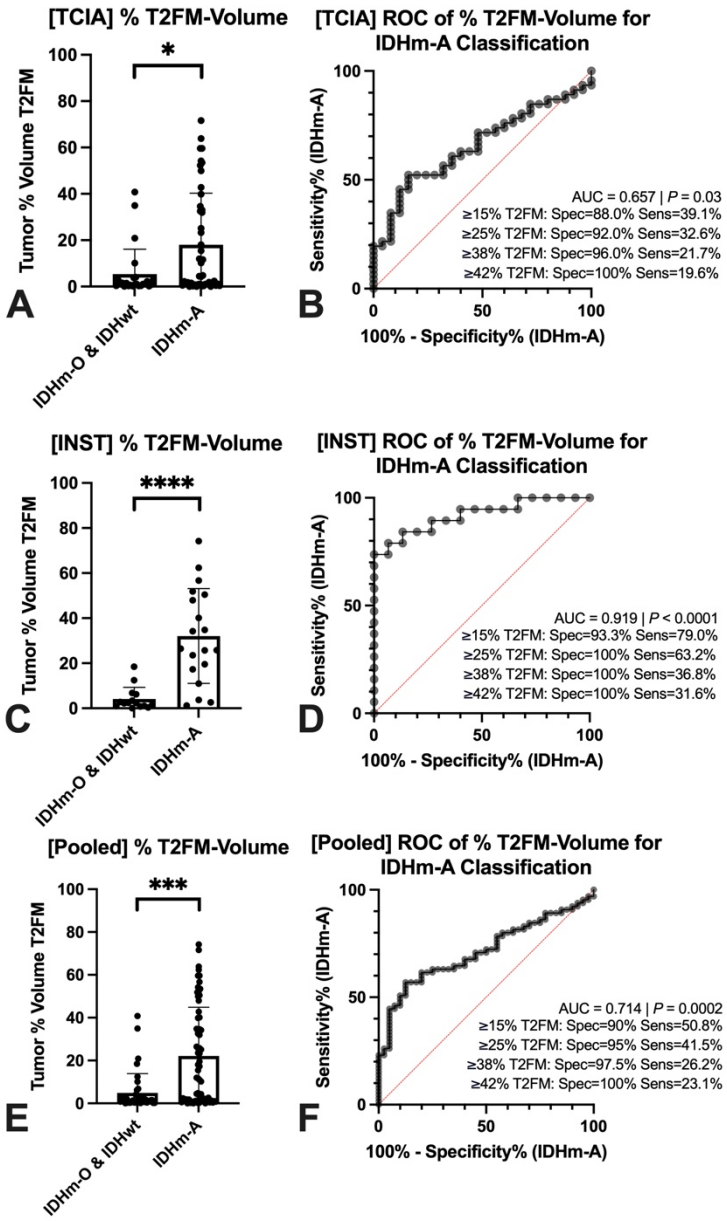

Figure 3.4. Tumor Percentage of T2-FLAIR Mismatch Volume and Diagnostic Performance for IDH-Mutant Astrocytoma Classification. Results are shown for both the TCIA cohort (**A, B**) and the institutional cohort (**C, D**). IDH-mutant astrocytomas (IDHm-A) had higher percentages of % T2-FLAIR mismatch volume (% T2FM-volume) compared to the other molecular signatures (**A, C**). ROC curves show that a specificity of 100% for IDHm-A diagnosis could be achieved with a threshold of ≥42% T2FM-volume in both cohorts (**B, D**), although in

the validation cohort a threshold of ≥25% T2FM-volume sufficed (**D**). The summary results when pooling the two cohorts are also shown (**E, F**). TCIA = The Cancer Imaging Archive; INST = Institutional; ROC = Receiver-operating characteristic; AUC = Area under curve; T2FM = T2-FLAIR mismatch; IDHm-O = Isocitrate dehydrogenase mutant oligodendroglioma; IDHwt = Isocitrate dehydrogenase wild-type glioma; IDHm-A = Isocitrate dehydrogenase mutant astrocytoma; * indicates $P < 0.05$, *** indicates $P < 0.001$; **** indicates $P < 0.0001$

≥25% T2FM-Volume IDHm-A Distribution Across Cohorts			
	<25% T2FM-Volume IDHm-A	**≥25% T2FM-Volume IDHm-A**	**Fisher's Exact p-value**
TCIA	31	15	*P*=0.03
INST	7	12	
Tumor Grade Distribution Across Cohorts			
	IDHm-A Grade 2	**IDHm-A Grade 3-4**	**Fisher's Exact p-value**
TCIA	33	13	*P*=0.38
INST	11	8	
TCIA: Tumor Grade Distribution Based on 25% T2FM-Volume			
	IDHm-A Grade 2	**IDHm-A Grade 3-4**	**Fisher's Exact p-value**
<25% T2FM-Volume	24	7	*P*=0.30
≥25% T2FM-Volume	9	6	
INST: Tumor Grade Distribution Based on 25% T2FM-Volume			
	IDHm-A Grade 2	**IDHm-A Grade 3-4**	**Fisher's Exact p-value**
<25% T2FM-Volume	6	1	*P*=0.15
≥25% T2FM-Volume	5	7	

Table 3.2. Contingency Tables of Percentage T2-FLAIR Mismatch Volume and Tumor Grade in IDH-Mutant Astrocytomas. IDHm-A = isocitrate dehydrogenase mutant astrocytoma; TCIA = The Cancer Imaging Archive cohort; INST = institutional cohort

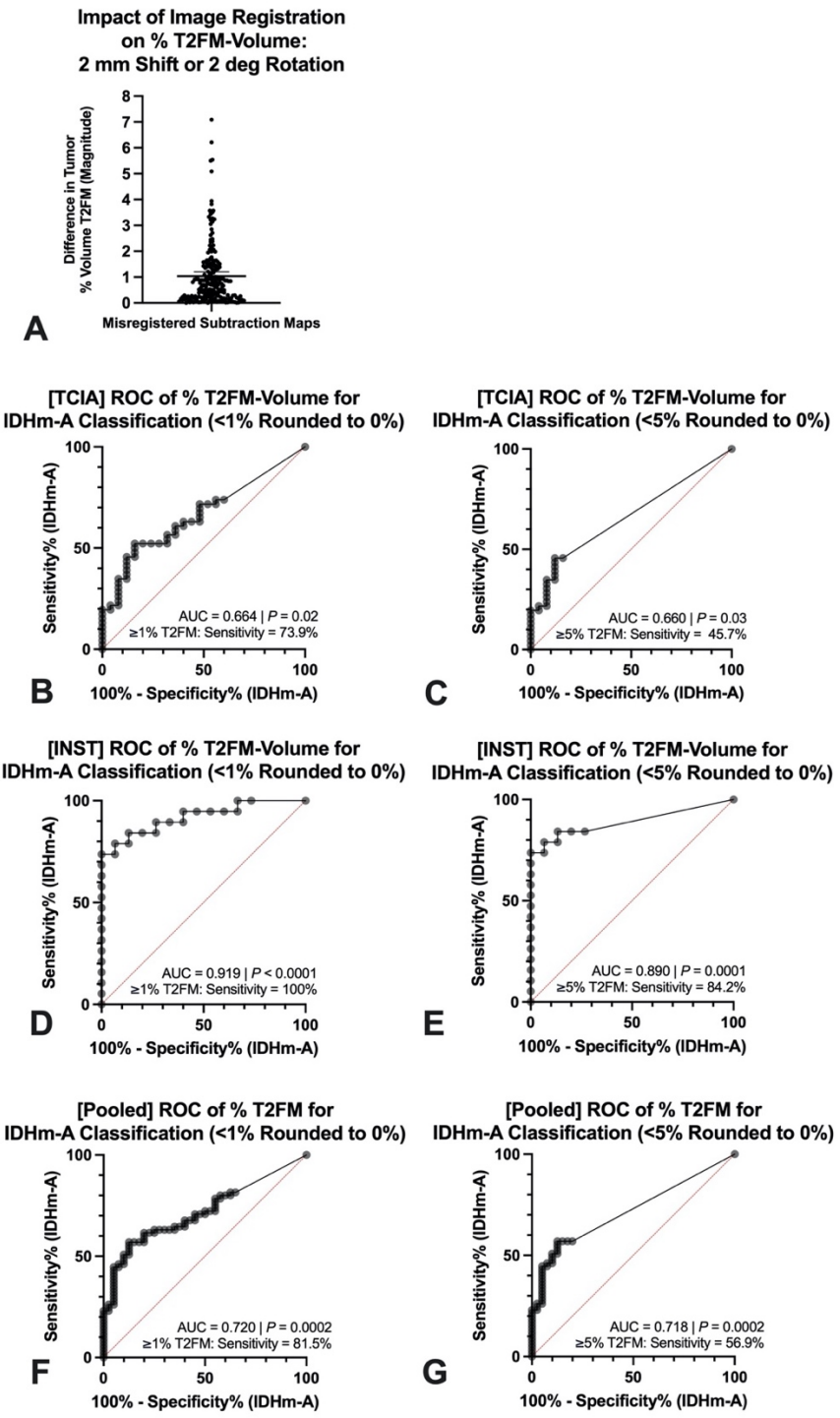

Figure 3.5 Assessment of Finite Image Misregistration and Empiric "Noise Floors" of % T2-FLAIR Mismatch Volume on T2-FLAIR Subtraction Maps. (A) Finite 2 mm posterior translation or 2 degree counter-clockwise rotation misregistration resulted in an average

magnitude difference of 1.04% T2-FLAIR mismatch (T2FM)-volume. In subsequent ROC curve analyses, **(B)** AUC in the TCIA cohort was 0.664 and **(C)** 0.660 for classifying IDH mutant astrocytoma when considering a <1% = 0% T2FM-volume and a <5% = 0% T2FM-volume noise floor, respectively. In the institutional cohort, **(D)** AUC was 0.919 and **(E)** 0.890 for classifying IDH mutant astrocytoma when considering a <1% = 0% T2FM-volume and a <5% = 0% T2FM-volume noise floor, respectively. In the pooled cohort, **(F)** AUC was 0.720 and **(G)** 0.718 for classifying IDH mutant astrocytoma when considering a <1% = 0% T2FM-volume and a <5% = 0% T2FM-volume noise floor, respectively. TCIA = The Cancer Imaging Archive; INST = Institutional; ROC = Receiver-operating characteristic; AUC = Area under curve; T2FM = T2-FLAIR mismatch

Relationships Between Tumor Subregions, Volumes, and Histopathological Grade

In both cohorts, there was a significant negative correlation between T2FNM-subregion thickness and % T2FM-volume (TCIA: R=-0.86, *P*<0.0001 | Institutional: R=-0.88, *P*<0.0001; **Figure 3.6A/D**). When also categorizing IDHm-A as 15–25% T2FM-volume, 25-42% T2FM-volume, and ≥42% T2FM-volume, there was an overall significant difference in T2FNM-subregion thickness within each cohort with similar results (TCIA: *P*=0.001; 15–25% T2FM: 7.08 mm (5.62–8.54 mm); 25–42% T2FM: 5.55 mm (3.84–7.26 mm); ≥42% T2FM: 3.14 mm (2.53–3.76 mm) | Institutional: *P*=0.001; 15–25% T2FM: 7.06 mm (3.88–10.3 mm); 25–42% T2FM: 5.07 mm (3.54–6.60 mm); ≥42% T2FM: 3.04 mm (2.29–3.79 mm); **Figure 3.7**).

% T2FM-volume was significantly lower in grade 2 IDHm-A compared to grade 3–4 IDHm-A in both cohorts (TCIA: *P*=0.008; 13.4% T2FM (6.56–20.3%) vs. 29.6% T2FM (14.1–

45.2%) | Institutional: *P*=0.03; 23.2% T2FM (11.4–34.9%) vs. 44.4% T2FM (27.5–61.2%); **Figure 3.6B/E**). There were no significant differences in the frequencies of grade 2 vs. grade 3–4 IDHm-A between the TCIA and INST cohorts nor within each cohort based on a threshold of ≥25% T2FM-volume (*P*>0.05; **Table 3.2**). There were also no significant relationships between % T2FM-volume with patient age or sex in either cohort (*P*>0.05; **Figure 3.8**). Tumor volumes were also significantly higher in IDHm-A with ≥15% T2FM-volume compared to IDHm-A with <15% T2FM-volume in both cohorts (TCIA: *P*=0.01; 35.5mL (23.3–47.7mL) vs. 70.7mL (41.7–99.7mL) | Institutional: *P*=0.04; 22.5mL (-4.85–49.8mL) vs. 60.8 mL (33.4–88.2mL); **Figure 3.6C/F**).

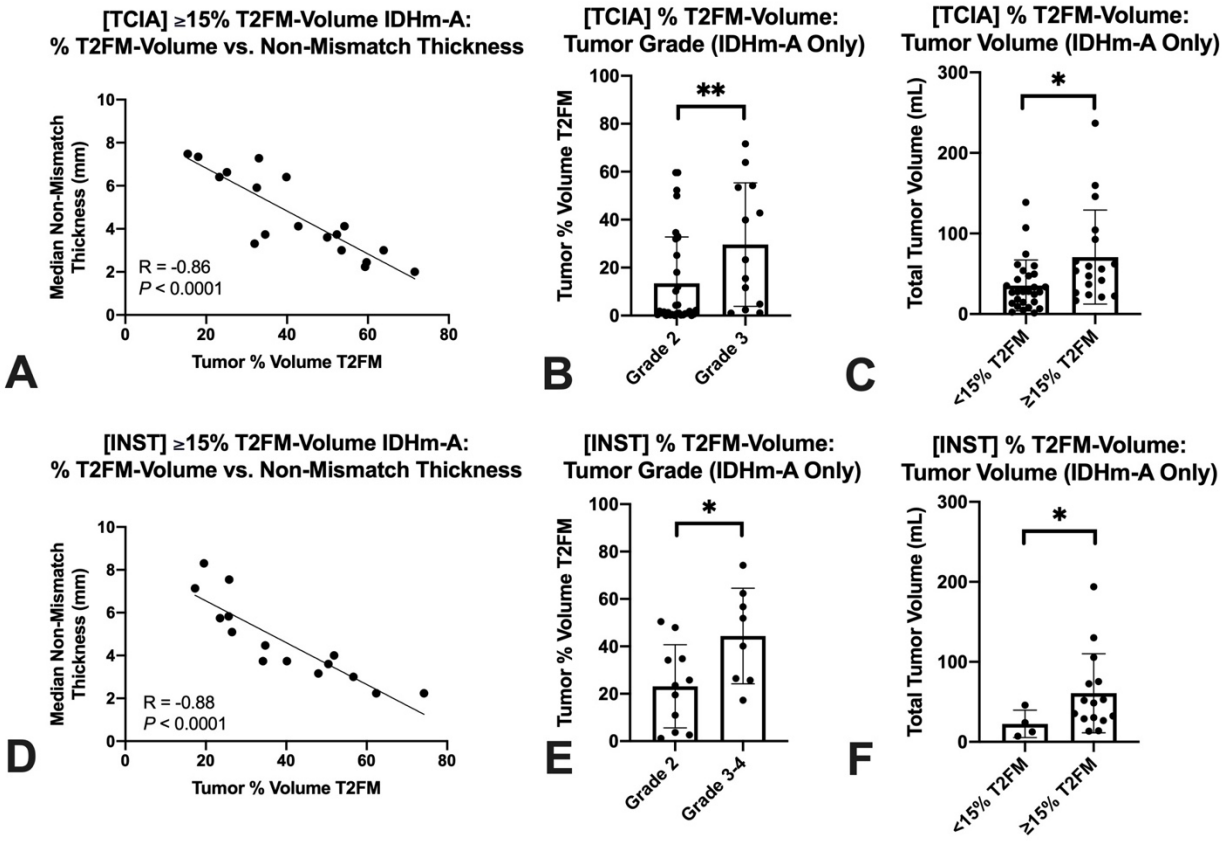

Figure 3.6. T2-FLAIR Non-Mismatch Thickness, Tumor Grade, and Tumor Volume Relationships Based on Tumor Percentage T2-FLAIR Mismatch Volume. In both cohorts, tumor % T2-FLAIR mismatch volume (% T2FM-volume) was significantly negatively correlated with T2-FLAIR non-mismatch-subregion thickness (**A, C:** $P < 0.0001$). Grade 3–4 IDHm-A had significantly higher % T2FM-volume compared to grade 2 IDHm-A (**B:** TCIA, $P=0.008$ | **E**: Institutional, $P=0.03$), and tumor volumes were significantly greater in ≥15% T2FM-volume IDHm-A compared to <15% T2FM-volume IDHm-A (**C:** TCIA, $P=0.01$ | **F:** Institutional, $P=0.04$).

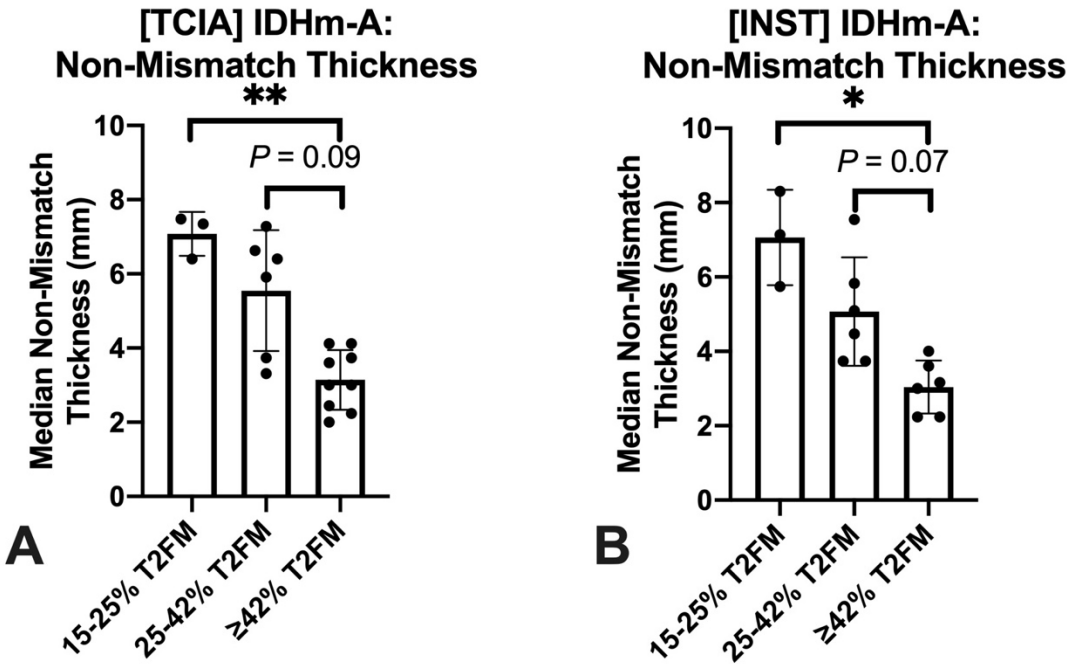

Figure 3.7. Differences in T2-FLAIR Non-Mismatch Thickness in IDH-Mutant Astrocytomas Grouped by % T2-FLAIR Mismatch Volume. T2-FLAIR non-mismatch (T2FNM)-subregion thickness was significantly different across 15–25% T2-FLAIR mismatch (T2FM)-volume, 25–42% T2FM-volume, and ≥42% T2FM-volume IDH mutant astrocytoma (IDHm-A) in the TCIA (**A:** P=0.001) and institutional cohorts (**B:** P=0.001). Post-hoc tests showed that ≥42% T2FM-volume IDHm-A had significantly thinner T2FNM subregions compared to 15–25% T2FM-volume IDHm-A in the TCIA (**A**: P=0.007) and institutional cohorts (**B**: P=0.01).

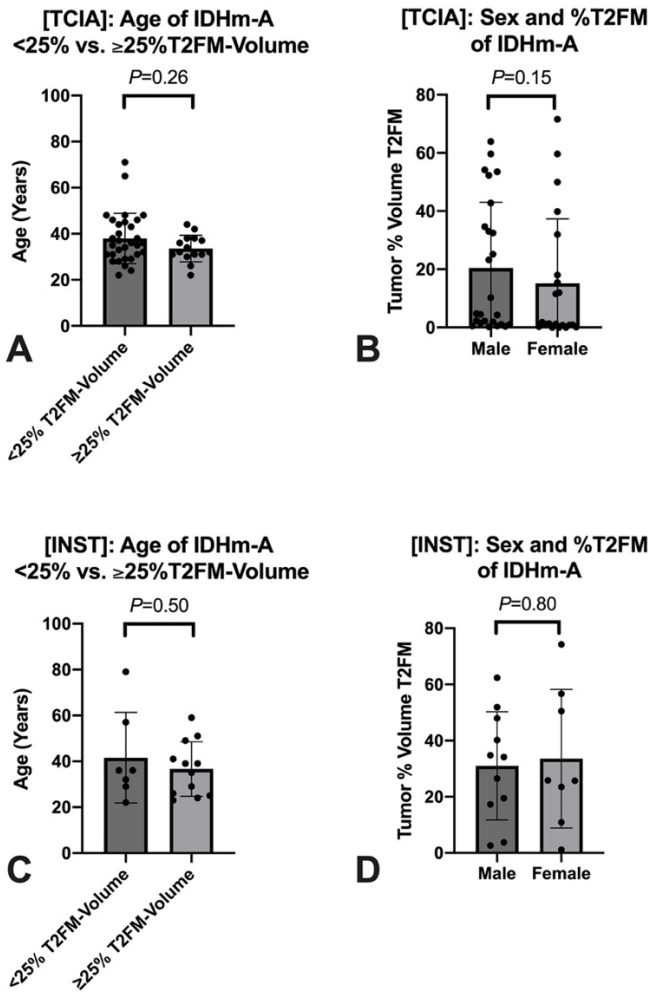

Figure 3.8. Assessment of Patient Age and Sex with Percentage T2-FLAIR Mismatch Volume. There were no significant relationships in age (**A/C**) or sex (**B/D**) with %T2FM-volume in either cohort. IDHm-A = Isocitrate dehydrogenase mutant astrocytoma; TCIA = The Cancer Imaging Archive; INST = Institutional; T2FM = T2-FLAIR Mismatch;

Reader Study Results

The reader study results across all patients are summarized in **Table 3.3.** When assessing T2FM-sign definitions by Patel *et al.*[38] and Lasocki *et al.*[86] without subtraction maps, there were significant differences in sensitivity & specificity for reader 1 (P=0.001) and a trend towards significance for reader 2 (P=0.052). Using the Patel *et al.*[38] and Lasocki *et al.*[86] definitions without subtraction maps, Reader 1 interpreted 24 (1 false positive) and 37 cases (4 false positives) of T2FM-sign, respectively, and Reader 2 interpreted 23 (3 false positives) and 30 cases (3 false positives) of T2FM-sign, respectively. Specificity was unchanged for reader 2 (92.5%) between definitions while slightly decreased for reader 1 using the Lasocki *et al.*[86] definition (90.0%) compared to the Patel *et al.*[38] definition (97.5%). The Lasocki *et al.*[86] definition had slightly improved sensitivity compared to the Patel *et al.*[38] definition for both readers (35.4% (Patel *et al.*[38]) vs. 50.8% (Lasocki *et al.*[86]) | 30.8% vs. 41.5%). The pooled sensitivity and specificity from the two cohorts using quantitative % T2FM-volume and by visual assessment are summarized in **Table 3.4**.

For both readers, there was no significant changes in sensitivity and specificity after the inclusion of T2-FLAIR subtraction maps (P>0.05). Specificity was unchanged for reader 2, and there was a slight decrease in specificity for reader 1 with T2-FLAIR subtraction maps with the Patel *et al.*[38] (97.5% vs. 92.5% | unchanged at 92.5%) and Lasocki *et al.*[86] definitions (90.0% vs. 85.0% | unchanged at 92.5%). There was slightly improved sensitivity using either the Patel *et al.*[38] (Reader 1: 35.4% (*without* subtraction map) vs. 36.9% (*with* subtraction map) | Reader 2: 30.8% vs. 38.5%) or Lasocki *et al.*[86] definitions (50.8% vs. 55.4% | 41.5% vs. 49.2%).

Inter-reader agreement for T2FM-sign was substantial[106] for both definitions and with/without subtraction maps (Cohen's Kappa: 0.70–0.78; **Table 3.3**). There were also slight,

non-significant (P>0.05) improvements in inter-reader agreement using T2-FLAIR subtraction maps with either the Patel *et al.*[38] (Cohen's Kappa 0.70 vs. 0.78) or Lasocki *et al.*[86] definitions (0.76 vs. 0.78).

T2-FLAIR Mismatch Sign: Sensitivity and Specificity Estimates				
Classification Definition	**Reader**	**With Subtraction Map**	**Sensitivity (95% CI)**	**Specificity (95% CI)**
Patel *et al.*[38]	Reader 1	No	35.4 (23.9–48.2)	97.5 (86.8–99.9)
		Yes	36.9 (25.3–49.8)	92.5 (79.6–98.4)
	Reader 2	No	30.8 (19.9–43.5)	92.5 (79.6–98.4)
		Yes	38.5 (26.7–51.4)	92.5 (79.6–98.4)
Lasocki *et al.*[86]	Reader 1	No	50.8 (38.1–63.4)	90.0 (76.3–97.2)
		Yes	55.4 (42.5–67.7)	85.0 (70.2–94.3)
	Reader 2	No	41.5 (29.4–54.4)	92.5 (79.6–98.4)
		Yes	49.2 (36.6–61.9)	92.5 (79.6–98.4)
T2-FLAIR Mismatch Sign: Inter-Reader Agreement				
Classification Definition	**With Subtraction Map**		**Cohen's Kappa (95% CI)**	
Patel *et al.*[38]	No		0.70 (0.53–0.87)	
	Yes		0.78 (0.64–0.92)	
Lasocki *et al.*[86]	No		0.76 (0.63–0.89)	
	Yes		0.78 (0.65–0.9)	

Table 3.3. Reader Study Results of T2-FLAIR Mismatch Sign Using T2-FLAIR Subtraction Maps.

Classification Definition	Sensitivity	Specificity
≥42% T2FM-volume	23.1%	100%
≥25% T2FM-volume	41.5%	95%
≥15% T2FM-volume	50.8%	90%
Patel *et al.*[38] (Reader min–max)	30.8–38.5%	92.5–97.5%
Lasocki *et al.*[86] (Reader min–max)	41.5–55.4%	85.0–92.5%

Table 3.4. Pooled Diagnostic Performance of Quantitative Percentage T2-FLAIR Mismatch Volume and Reader Assessment of T2-FLAIR Mismatch Sign for Classifying IDH-Mutant Astrocytoma. T2FM = T2-FLAIR mismatch

Discussion

The present study's primary objective was to add to the current literature by quantifying T2FM- and T2FNM-subregion volumes in non-enhancing gliomas using T2-FLAIR subtraction maps, with the main aim of diagnosing IDHm-A with near-100% specificity. The collective findings demonstrate that % T2FM-volume thresholds may serve as a quantitative threshold for classifying IDHm-A with 100% specificity as demonstrated in two independent cohorts; percentage T2FM-volume is influenced by tumor volume and grade in IDHm-A; and T2-FLAIR subtraction maps may be more useful as an objective tool for quantitative tumor imaging analysis than for visual assessment of T2FM-sign by experienced radiologists. The present study adds to the current literature by providing a method for the automated quantification of % T2FM-volume and performing subregion segmentations in IDHm-A using T2-FLAIR subtraction maps. The present study also expands upon a previous study assessing the relative signal intensity of T2FM in a "hot-spot" region within the T2FM-core[95] by creating a subtraction map for whole tumor visualization and assessment.

Quantitative T2-FLAIR subtraction maps may serve as a useful, *complementary* tool for studying T2FM-sign in IDHm-A. The finding that ≥42% T2FM-volume can classify IDHm-A with 100% specificity suggest that % T2FM-volume calculated from quantitative subtraction maps may help radiologists avoid false positives as shown in **Figure 3.3** and serve as a potential imaging biomarker of IDHm-A in combination with the radiographic T2FM-sign.[38, 85-91] It is worth noting that in the present study, we purposely do not describe the subtraction map-defined T2FM- and T2FNM-subregions synonymously as the "core" and "rim" subregions in IDHm-A, respectively, as in previous radiographic studies on T2FM sign.[38] While T2-FLAIR subtraction maps allow for determining presence of T2FM-subregions, the present utilization of T2-FLAIR subtraction maps

may be limited in determining presence of the corresponding hyperintense T2-weighted FLAIR rim specifically distinct from more broadly-defined T2FNM-subregions that are also present in gliomas not exhibiting T2FM sign.

The present findings of a threshold of ≥42% T2FM-volume demonstrating 100% specificity for IDHm-A and lower thresholds of ≥15% and ≥25% T2FM-volume demonstrating 88.0–100% specificity may also be perceived similarly to other studies proposing a less conservative definition of T2FM-sign[86, 92, 93] and as demonstrated in our representative false positive cases, particularly when considering T2FM subtraction maps do not explicitly account for the hyperintense T2-weighted FLAIR "rim". Nevertheless, % T2FM-volume was also found to be inversely related to T2FNM-subregion thickness in IDHm-A, which may demonstrate that T2FNM-subregions are potentially synonymous with a T2-weighted FLAIR hyperintense rim as T2FM-sign IDHm-A grows.

As for sensitivity, the present study demonstrates that high sensitivity cannot be achieved by lowering the % T2FM-volume threshold, which is in line with previous studies reporting low sensitivity of T2FM-sign.[38, 85, 86] Indeed, even when dramatically lowering to a ≥5.0% T2FM-volume threshold, which can be considered close to a noise floor, the sensitivity was 45.7–84.2% in the two cohorts. We believe the low sensitivity may be related to the biology of IDHm-A, which seemingly can lack any extent of mismatch in a non-negligible percentage of cases. For example, the differing AUC performance may be explained by the higher proportion of non-mismatched IDHm-A in the TCIA cohort compared to the institutional validation cohort although both cohorts demonstrated 100% specificity for IDHm-A using a high % T2FM-volume threshold. These findings potentially demonstrate a limitation of % T2FM-volume as a continuous measure for AUC-based classification compared to a categorical measure for 100% specificity-based

classification through a % T2FM-volume threshold (i.e. ≥42% T2FM-volume) at the cost of sensitivity. Additionally, even though there was no significant difference in tumor grade distribution of IDHm-A with or without ≥25% T2FM-volume threshold, which is in line with the literature showing no IDHm-A tumor grade differences based on T2FM-sign,[85, 87, 90] the % T2FM-volume was significantly higher in grade 3-4 IDHm-A compared to grade 2 and in tumors with larger volumes compared to smaller volumes in both cohorts. We speculate that % T2FM-volume development may be associated with tumor growth, however, a longitudinal assessment is warranted to verify this claim.

The present study demonstrates that T2-FLAIR subtraction maps may be useful to obtain partitioned segmentations of T2FM-/T2FNM-subregion in IDHm-A for quantitative studies of T2FM-sign in gliomas. Previous studies showed that mismatched areas show either microcystic changes or enlarged intercellular space on histology.[38, 96] Future studies could use T2-FLAIR subtraction maps to objectively partition subregion segmentations to assess intratumoral heterogeneity, for there have been studies using quantitative MRI to assess the tumor microenvironment of IDHm-A with T2FM-sign[95, 107] and utilization of the radiographic sign is now expanding and even being explored in pediatric populations.[108] In addition, the generation of T2-FLAIR subtraction maps utilizes readily available, open-source software and involves relatively routine pre-processing steps that are conducted for many quantitative imaging studies, including NIFTI conversion, image co-registration, skull-stripping, normalization, and voxel-wise arithmetic (i.e. subtraction), that could be performed by non-clinicians. Although off-line processing was required for this first demonstration study, it is conceivable that usage of these maps could eventually be used beyond research settings and expanded for clinical practice since the processing steps are not computationally demanding.

In the reader study portion of the present study, the inter-reader agreements without (0.70–0.76) and with subtraction maps (0.78) were in line with values previously reported in the literature.[38, 85] Additionally, the specificity of the Patel *et al.*[38] definition applied by the readers (specificity ranging 92.5–97.5%) was similar to that of the ≥25% T2FM-volume threshold (95%). The specificity for the Lasocki *et al.*[86] definition (specificity ranging 85–92.5%) was similar to that of the ≥15% T2FM-volume threshold (90%). The sensitivity values were also comparable between the Patel *et al.*[38] definition and the ≥25% T2FM-volume threshold (30.8–38.5% vs 41.5%) and between the Lasocki *et al.*[86] definition and the ≥15% T2FM-volume threshold (50.8% vs 41.5–55.4%), respectively.

Interestingly, there were no significant differences in sensitivity, specificity, nor inter-reader agreement of T2FM-sign when adding T2-FLAIR subtraction maps for either the Patel *et al.*[38] or Lasocki *et al.*[86] definitions, although there was a significant difference comparing the Patel *et al.*[38] and Lasocki *et al.*[86] definitions for one reader and a significant trend in the other. There are possible reasons to explain these results. First, these findings may further support that the radiographic definitions of T2FM-sign are very robust in definition and that additional tools such as T2-FLAIR subtraction maps may not provide additional diagnostic benefit for estimating % T2FM-volume for T2FM-sign positivity, especially for experienced radiologists. Second, the reader study design involved using a standardized T2-FLAIR subtraction map windowing and color scale with gray voxels depicting voxels around 0 (either positive or negative), so the reader's interpretation of the gray voxels may have impacted their assessments. In the future, reader studies involving radiologists with less experience and a more binarized color bar without an intermediate color zone may be useful to better understand the potential diagnostic utility of T2-FLAIR subtraction maps. Although subtraction maps did not show a striking benefit as a tool for

qualitative evaluations, it should be noted that their potential quantitative usages to compute % T2FM-volume and T2FM-/T2FNM-subregions are to be considered a valuable complementary tool that does not suffer from inter-reader variability. The inter-reader agreement for T2FM-sign in both ours and previous studies was substantial, but not perfect, and speculatively may also be worse in less experienced readers, which further supports this notion.

There are several limitations to this study that should be addressed. First, the sample size was limited, so further studies assessing the potential usefulness of T2-FLAIR subtraction maps in other, expanded cohorts are warranted. Second, given that T2FM sign is known to be impacted by pulse sequence parameters,[89] it is conceivable that there may be institutional- or patient-specific thresholds to better distinguish T2FM- from T2FNM-subregions compared to the positive- and negative-value thresholds, respectively, used in the current study. For example, lower FLAIR inversion times have been shown to increase the visibility of T2FM sign,[89] which may analogously lead to larger %T2FM-volume, and other sequence parameter variations may have similar effects. However, we believe the usage of straightforward positive- and negative-value thresholds with intensity-normalized anatomical images to minimize the impact of sequence parameter differences and additional NAWM normalization to further minimize patient-specific differences is valid as a first demonstration of the potential utility of T2-FLAIR subtraction maps for consistent analyses across and within our multi-institutional cohorts. Nevertheless, a more thorough investigation of the impact of acquisition parameters on T2FM sign, T2-FLAIR subtraction maps, and % T2FM-volume calculation may be warranted. A potential approach to overcome the inherent low sensitivity of T2FM could be represented by a combination of T2-FLAIR subtraction maps with advanced imaging such as diffusion,[95, 107] perfusion,[95, 107] and chemical exchange saturation transfer MRI[109] as did some prior studies on visual T2FM-sign. Lastly, while the reader study

results did not show marked improvement in T2FM-sign assessment using T2-FLAIR subtraction maps in experienced radiologists, future reader studies assessing the potential usefulness of T2-FLAIR subtraction maps, including perhaps for radiology trainees, may be warranted.

Conclusions

T2-FLAIR subtraction maps may be a useful tool to quantitatively assess T2FM-sign in non-enhancing gliomas and to obtain objective segmentations of T2FM- and T2FNM-subregions based on specific thresholds. Whole tumor quantification of % T2FM-volume may complement T2FM-sign for classifying IDHm-A with 100% specificity. Conversely, there appeared to be no significant benefit in using T2-FLAIR subtraction maps for visual assessment of T2FM-sign by experienced radiologists.

Chapter 4. Diffusion and Quantitative T2-FLAIR Mismatch Imaging Phenotyping of Human Non-Enhancing Gliomas Using Digital Subtraction Maps of T2-Weighted and T2-Weighted FLAIR MRI

Preface

This chapter is adapted from the following manuscript under review:

Cho NS, Sanvito F, Le VL, Oshima S, Teraishi A, Yao J, Telesca D, Raymond C, Pope WB, Nghiemphu PL, Lai A, Salamon N, Cloughesy TF, Ellingson BM. Diffusion MRI is superior to quantitative T2-FLAIR mismatch in predicting molecular subtypes of human non-enhancing gliomas. *Under Review.*.

Introduction

As discussed in **Chapter 3**, the "T2-FLAIR mismatch sign" (T2FM-sign) on T2-weighted MRI and T2-weighted FLAIR MRI is an established qualitative imaging feature with near 100% specificity for classifying isocitrate dehydrogenase-mutant 1p/19q-intact astrocytomas (IDHm-A) from IDH-mutant 1p/19-codeleted oligodendrogliomas (IDHm-O) and IDH-wild-type (IDHwt) gliomas but low sensitivity.[38, 42, 85, 87-91, 110]

There have been several approaches to potentially increase the sensitivity of the T2FM-sign. One approach has been to utilize looser definitions of the T2FM-sign, such as a visually-estimated tumor ≥25% T2FM-volume threshold proposed by Lasocki *et al.*[86] or assessing only for T2-weighted FLAIR hyperintense rim & hypointense core and not using the T2-weighted MRI scan proposed by Li *et al.*,[92] which achieved 100% specificity for IDHm-A with 63% and 71.3% sensitivity in their cohorts, respectively. Another approach has been to combine the T2FM-sign with quantitative MRI measures that have been previously well-described to classify IDHm-A from other molecular subgroups, such as combining T2FM-sign with apparent diffusion coefficient (ADC) from diffusion MRI[95] or normalized relative cerebral blood volume (nrCBV) from dynamic susceptibility contrast perfusion MRI.[95] However, one factor to consider about these prior approaches is that they were confined to the field's *qualitative,* binarized (yes/no) assessment of T2FM-sign.

As demonstrated in **Chapter 3**, we have now developed a method for *quantitative*, continuous assessment of T2FM volumetry using voxel-wise digital subtraction maps of T2-weighted and T2-weighed FLAIR MRI.[42] Cho *et al.* observed that quantitative ≥42% T2FM-volume achieved 100% specificity and 23.1% sensitivity for IDHm-A while ≥25% T2FM-volume still achieved high specificity of 95% with 41.5% sensitivity for IDHm-A,[42] which quantitatively

validated prior qualitative results by Lasocki *et al.*[86] who proposed a threshold of ≥25% T2FM-volume on visual evaluation for classifying IDHm-A.

Thus, there remains a present need for comparing and incorporating quantitative tumor %T2FM-volume with other well-known, quantitative imaging biomarkers for IDHm-A. For example, ADC values from diffusion MRI are known to be higher in IDHm-A compared to IDHm-O and IDHwt.[61, 69] ADC values are inversely related to cellular density,[111] and a prior study using *qualitatively*-defined T2FM and T2-FLAIR non-mismatch (T2FNM) subregions observed that the T2FM-core subregion has higher ADC values than the T2FNM-rim subregion.[107] Given this finding, there remains a contemporary need of re-assessing previously established ADC group differences between IDHm-A and other molecular subtypes in the context of "mismatched" and "non-mismatched" IDHm-A as well as exploring subregional differences in "mismatched" IDHm-A.

The purpose of the present study was to utilize T2-FLAIR subtraction and normalized ADC (nADC) maps to characterize IDHm-A and IDHm-A subregions and to compare the classification performance of %T2FM-volume and nADC for differentiating between IDHm-A and other molecular subtypes. We hypothesized that: (**i**) T2-FLAIR subtraction map-defined T2FM subregions would have higher nADC compared to T2FNM subregions in IDHm-A with ≥25% T2FM-volume ("mismatched" according to Cho *et al.*[42] and Lasocki *et al.*[86]), (**ii**) IDHm-A with ≥25% T2FM-volume ("mismatched") would have higher nADC compared to IDHm-A with <25% T2FM-volume ("non-mismatched"), and (**iii**) nADC would outperform %T2FM-volume in classifying IDHm-A from IDHm-O and IDHwt gliomas due to the inherently low sensitivity of T2FM-sign. In exploratory analyses, we also theorized that (**iv**) %T2FM-volume would not be associated with survival, as was demonstrated in prior studies using the visual T2FM-sign.[38, 87, 110]

Methods

Patient Cohort

A total of 104 patients with 105 lesions with biopsy-proven gliomas across The Cancer Imaging Archive University of California San Francisco (TCIA UCSF) and our institution with the following inclusion criteria were studied: (1) non-enhancing, adult-type diffuse glioma as classified by the World Health Organization 2021 criteria,[3] (2) supratentorial, (3) treatment-naïve except for biopsy, and (4) molecular status available (IDH status for all lesions and 1p/19q status if IDH-mutant). This patient cohort was assessed in a prior study and in **Chapter 3**.[42] IDH and 1p/19q molecular status were determined by targeted next-generation sequencing, polymerase chain reaction sequencing, or immunohistochemistry and fluorescence in situ hybridization, respectively.[70, 100] Patient clinical data are summarized in **Table 4.1**.

Image Acquisition and Pre-Processing

All patients underwent T2-weighted, T2-weighted FLAIR, and diffusion MRI on 3T scanners. T2-weighted and T2-weighted FLAIR were obtained using previously described protocols.[42] ADC maps were generated from diffusion MRI datasets acquired with b-values of 0 and 1000 s/mm^2. The TCIA data were already pre-processed and registered to the 3D T2-weighted FLAIR MRI (Advanced Normalization Tools) and skull-stripped using "brain_mask" (https://www.github.com/ecalabr/brain_mask/), and the institutional data were pre-processed using an analogous pipeline of registering to the 3D T1-post-contrast MRI (*tkregister2*; Freesurfer [101] | *flirt*: Functional Magnetic Resonance Imaging of the Brain Software Library[102]) and skull-stripped using "HD-BET" (https://github.com/MIC-DKFZ/HD-BET).[103] Normalized ADC

(nADC) maps were created by voxel-wise dividing ADC by the mean ADC value of 3 spherical VOIs in the normal appearing white matter (NAWM) of the contralateral centrum semiovale.[41]

T2-FLAIR Subtraction Maps

Voxel-wise T2-FLAIR digital subtraction maps were generated for each patient as previously described.[42] In brief, an additional, refined co-registration of the skull-stripped T2-weighted and T2-weighted FLAIR MRI was performed using FLIRT. Then, images were z-score- and NAWM-normalized to the contralateral centrum semiovale so that the NAWM signal intensity would be ~0. Lastly, the normalized T2-weighted and T2-weighted FLAIR MRI were voxel-wise subtracted to create T2-FLAIR subtraction maps. A consistent threshold of 0 on the T2-FLAIR subtraction maps was used for all analyses, where positive values corresponded to T2FM-subregions and negative values corresponded to T2FNM-subregions.

Brain Tumor Imaging Analysis

All initial tumor VOI segmentations for the institutional data were performed by a lab member with 2 years of experience in tumor segmentation analysis (N.S.C.). The institutional and provided TCIA tumor segmentations were further refined via a semi-automated thresholding method using Analysis of Functional NeuroImages (AFNI) software (https://afni.nimh.nih.gov)[76] for consistency. Macroscopic cysts and CSF were excluded from the tumor segmentations. Lastly, a radiologist with 11 years of experience in neuroimaging analysis (S.O.) inspected all final tumor VOI segmentations while being blinded to the clinical data. T2FM and T2FNM subregion VOIs were then created from the tumor VOIs using the T2-FLAIR subtraction maps, and T2FM and T2FNM volumes were calculated to quantify percentage T2FM-volume (%T2FM-volume).

IDHm-A were stratified based on ≥25% T2FM-volume ("mismatched" IDHm-A) or <25% T2FM-volume ("non-mismatched" IDHm-A) using previously-defined thresholds.[42, 86] Median nADC values from the tumor, T2FM subregion, and T2FNM subregion were also obtained.

Statistical Analysis

GraphPad Prism software was used for statistical analyses. Paired t-tests were performed to assess differences in nADC between T2FM and T2FNM subregions IDHm-A with ≥25% T2FM-volume. Repeated-measures ANOVA tests with post-hoc Holm-Sidak corrections were performed to assess group differences in nADC between different molecular types. Unpaired t-tests were performed to assess differences in nADC across IDHm-A tumor grades. Paired ROC curve analyses of %T2FM-volume and nADC to classify IDHm-A from IDHm-O/IDHwt, IDHm-A from IDHm-O, and IDHm-A from IDHwt were performed, and the DeLong test was performed to compare the paired area under curve (AUC) values of nADC versus %T2FM-volume for each classification pairing. Multiple logistic regression was performed to assess the classification performance of the combination of nADC and %T2FM-volume and the combination of nADC, %T2FM-volume, and age for classifying IDHm-A. Survival analysis was restricted to the TCIA cohort-only because all data from the institutional data were censored in terms of overall survival, and one patient with 2 lesions was excluded from survival analysis. Log-rank tests were performed assessing any relationships of nADC, %T2FM-volume, tumor volume, and molecular status as categorical variables with overall survival. Univariate and multivariate Cox survival analysis were performed on the same variables to assess any relationships with overall survival as continuous measures while controlling for factors such as age, extent of resection, and grade. Significance was set at α=0.05 for all analyses.

Characteristic	Patient Cohort (n=104 patients with n=105 lesions)
Age: Mean (Range)	42 (22–79)
Sex: M/F	59/45
Diagnosis: n (%)	
IDHm Astrocytoma	65 (61.9%)
Grade 2	44
Grade 3	20
Grade 4	1
IDHm Oligodendroglioma	18 (17.1%)
Grade 2	17
Grade 3	1
IDHwt Glioma	22 (21.0%)

Table 4.1 Clinical Data of Patients.

Results

Quantitative T2-FLAIR Mismatch and nADC Phenotyping of Gliomas

Four representative cases are shown in **Figure 4.1. Figure 4.1A** shows a 36-year-old male patient who was diagnosed with an IDHm-A exhibiting a high median nADC of 3.02 and 53.5% T2FM-volume ("mismatched" IDHm-A). **Figure 4.1B** shows a 36-year-old female patient who was diagnosed with an IDHm-A exhibiting a moderately high median nADC of 2.15 nADC with only 10.9% T2FM-volume ("non-mismatched" IDHm-A). **Figure 4.1C** shows a 27-year-old female patient who was diagnosed with an IDHm-O exhibiting a lower median nADC of 1.78 and 6.8% T2FM-volume. **Figure 4.1D** shows a 75-year-old female patient who was diagnosed with an IDHwt glioma exhibiting a low median nADC of 1.62 and <1% T2FM-volume.

Within IDHm-A exhibiting ≥25% T2FM-volume ("mismatched"), there was significantly higher nADC in T2FM-subregions compared to T2FNM subregions (P<0.0001, mean difference=0.58, **Figure 4.2A**). When assessing all IDHm-A, IDHm-A with ≥25% T2FM-volume ("mismatched") had significantly higher whole tumor nADC compared to IDHm-A with <25% T2FM-volume ("non-mismatched") (P<0.0001, **Figure 4.2B**). Across glioma molecular subtypes while considering IDHm-A with ≥25% T2FM-volume and IDHm-A with <25% T2FM-volume as separate entities, both IDHm-A subgroups demonstrated significantly higher nADC compared to IDHm-O (P<0.0001 for ≥25% T2FM-volume IDHm-A, P=0.03 for <25% T2FM-volume IDHm-A, **Figure 4.2B**) and IDHwt (P<0.0001 for both ≥25% and <25% T2FM-volume IDHm-A, **Figure 4.2B**). There was also a trend towards significance for increased nADC in IDHm-O compared to IDHwt after multiple comparisons p-value correction (P=0.09, **Figure 4.2B**). The T2FNM-subregion of IDHm-A with ≥25% T2FM-volume demonstrated no significant difference in nADC with the whole tumor nADC of IDHm-A with <25% T2FM-volume (P=0.39, **Figure 4.2C**).

T2FNM-subregions of IDHm-A with ≥25% T2FM-volume still demonstrated significantly higher nADC compared to IDHm-O (P=0.0063, **Figure 4.2C**) and compared to IDHwt (P<0.0001, **Figure 4.2C**). There were no significant differences in nADC between grade 2 and grade 3 IDHm-A, whether across all IDHm-A (P=0.56), only IDHm-A ≥25% T2FM-volume (P=0.38), or only IDHm-A <25% T2FM-volume (P=0.22).

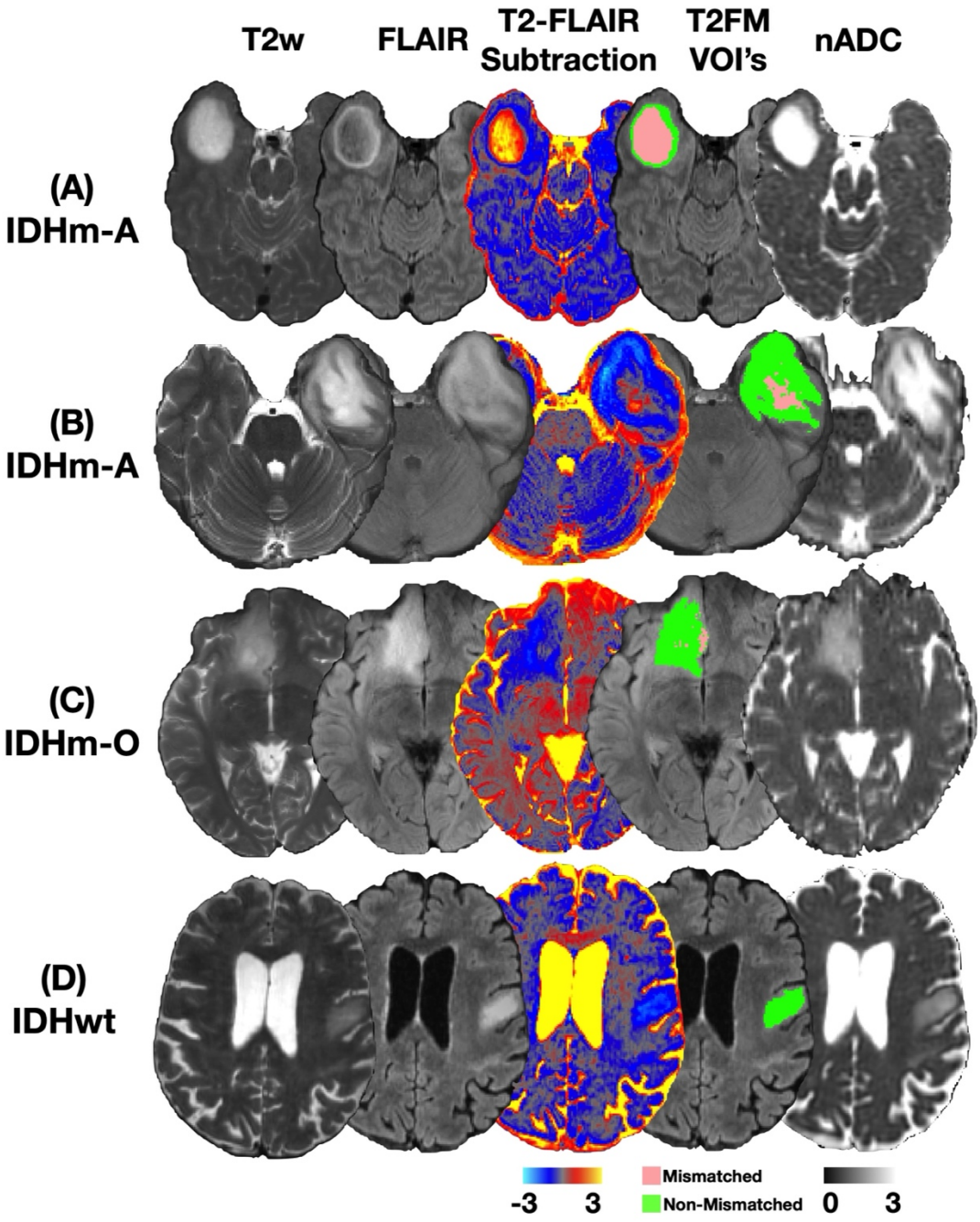

Figure 4.1. Four Representative Cases with Quantitative T2-FLAIR Subtraction and nADC Maps. (**A**) Patient A is a 36-year-old male diagnosed with IDH-mutant astrocytoma (IDHm-A) with 3.02 nADC and 53.5% T2-FLAIR mismatch volume (T2FM-volume) ("mismatched"). (**B**) Patient B is a 36-year-old female diagnosed with IDHm-A with 2.15 nADC and 10.9% T2FM-

volume (“non-mismatched”). (**C**) Patient C is a 27-year-old female diagnosed with IDH-mutant oligodendroglioma (IDHm-O) with 1.78 nADC and 6.8% T2FM-volume. (**D**) Patient D is a 75-year-old female diagnosed with IDH-wild type (IDHwt) glioma with 1.62 nADC and <1% T2FM-volume. Tumor segmentation volumes of interests (VOIs) denoting T2FM subregions (pink) and T2-FLAIR non-mismatch (T2FNM) subregions (green) are shown. IDHm-A = isocitrate dehydrogenase mutant astrocytoma; IDHm-O = isocitrate dehydrogenase mutant oligodendroglioma; IDHwt = isocitrate dehydrogenase wild type glioma; T2FM = T2-FLAIR mismatch; nADC = normalized apparent diffusion coefficient

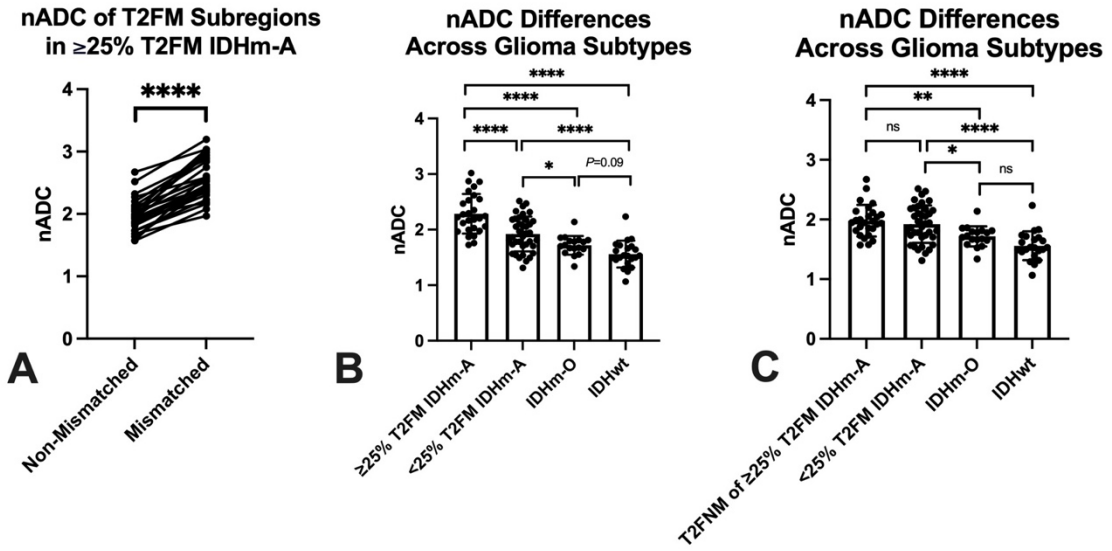

Figure 4.2. Intra-tumoral and Group nADC Differences Based on Quantitative T2-FLAIR Mismatch and Glioma Molecular Subtypes. T2-FLAIR mismatch (T2FM) subregions of IDH-mutant astrocytomas (IDHm-A) with ≥25% T2FM-volume had significantly higher nADC compared to T2-FLAIR non-mismatch (T2FNM) subregions (P<0.0001, **A**). IDHm-A with ≥25% T2FM-volume had significantly higher nADC compared to IDHm-A with <25% T2FM-volume (P<0.0001, **B**) and both IDHm-A subgroups had significantly higher nADC compared to IDH-mutant oligodendroglioma (IDHm-O) (≥25% T2FM-volume IDHm-A: P<0.0001, <25% T2FM-volume IDHm-A: P=0.03, **B**) and IDH-wild type (IDHwt) (both P<0.0001, **B**). T2FNM subregions of IDHm-A with ≥25% T2FM-volume also had significantly higher nADC compared to IDHm-O (P=0.0063, **C**) and IDHwt (P<0.0001, **C**), but no difference with IDHm-A with <25% T2FM-volume (P=0.39, **C**). IDHm-A = isocitrate dehydrogenase mutant astrocytoma; IDHm-O = isocitrate dehydrogenase mutant oligodendroglioma; IDHwt = isocitrate dehydrogenase wild type glioma; T2FM = T2-FLAIR mismatch; nADC = normalized apparent

diffusion coefficient; ns = not significant; * denotes $P < .05$; ** denotes $P < .01$; *** denotes $P < .001$; **** denotes $P < .0001$

Diagnostic Performance of nADC and Percentage T2-FLAIR Mismatch Volume

Paired ROC analyses were performed to compare the diagnostic performance of nADC vs. %T2FM-volume in differentiating IDHm-A from other molecular types. Both nADC and %T2FM-volume classified IDHm-A vs. IDHm-O/IDHwt individually ($P<0.0001$ and $P=0.0002$, respectively), but the AUC of nADC was significantly greater than the AUC of %T2FM-volume (nADC AUC=0.848, %T2FM-volume AUC=0.714[42], $P=0.01$ comparing AUC's, **Figure 4.3A**). In post-hoc analyses, the AUC of nADC remained greater than the AUC of %T2FM-volume for classifying IDHm-A just from IDHm-O (**Figure 4.3B**) and IDHm-A just from IDHwt (**Figure 4.3C**), although the AUC difference was significant only for classification from IDHwt (*IDHm-A vs. IDHm-O*: nADC AUC=0.805, %T2FM-volume AUC=0.703, $P=0.14$ comparing AUC's | *IDHm-A vs. IDHwt*: nADC AUC=0.883, %T2FM-volume AUC=0.722, $P=0.005$ comparing AUC's). **Table 4.2** summarizes empiric thresholds of nADC and %T2FM-volume for achieving 100% and ~95% specificity for the ROC analyses in **Figure 4.3,** and the results show that nADC has greater sensitivity for IDHm-A compared to %T2FM-volume at these high-specificity thresholds (e.g. *IDHm-A vs. IDHm-O/IDHwt* with 95% specificity: nADC=70.8% sensitivity, %T2FM-volume=41.5% sensitivity). Multiple logistic regression results combining (**i**) nADC and %T2FM-volume and (**ii**) nADC, %T2FM-volume, and age demonstrated only *marginal* increases in AUC for classifying IDHm-A compared to using nADC-alone (*IDHm-A vs. IDHm-O/wt:* AUC 0.848 to 0.880, *IDHm-A vs. IDHm-O:* AUC 0.805 to 0.816, *IDHm-A vs. IDHwt:* AUC 0.883 to 0.938) (**Table 4.3**).

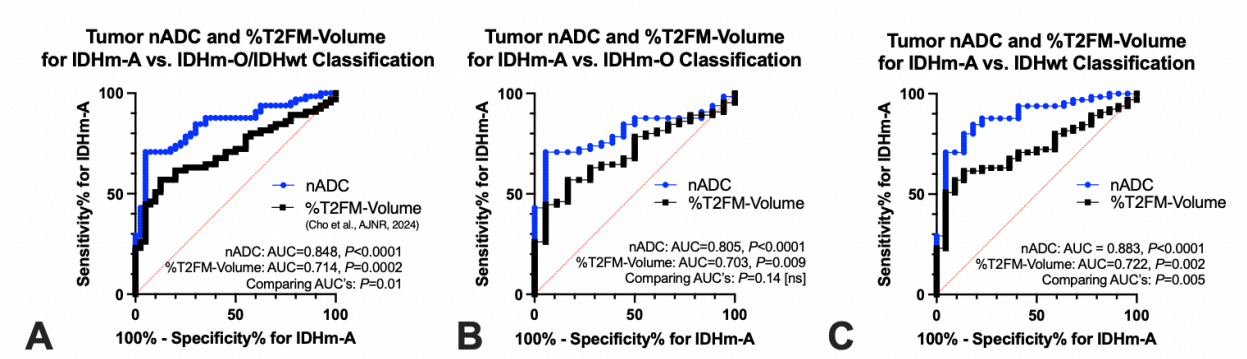

Figure 4.3. Comparing Diagnostic Performance of Tumor nADC and Percentage T2-FLAIR Mismatch Volume for IDH-mutant Astrocytoma Classification. The area under curve (AUC) of nADC was significantly higher than the AUC of percentage T2-FLAIR mismatch volume (%T2FM-volume) for classifying IDH-mutant astrocytoma (IDHm-A) from IDH-mutant oligodendroglioma (IDHm-O) and IDH-wild type (IDHwt) (*P*=0.01 comparing AUC's, **A**). The AUC of nADC was higher, but not significantly, than the AUC of %T2FM-volume for classifying IDHm-A from IDHm-O (*P*=0.14 comparing AUC's, **B**) and significantly higher for classifying IDHm-A from IDHwt (*P*=0.005 comparing AUC's, **C**). Refer to **Table 4.2** for summary cutoffs of %T2FM-volume and nADC for molecular classification.

Classification: IDHm-A vs. IDHm-O/IDHwt		
Threshold	**Sensitivity (IDHm-A)**	**Specificity (IDHm-A)**
nADC > 2.240	29.2%	100%
%T2FM-Volume > 42.00%$^{+}$	23.1%	100%
nADC > 1.864	70.8%	95.0%
%T2FM-Volume > 25.00%$^{+}$	41.5%	95.0%
Classification: IDHm-A vs. IDHm-O		
Threshold	**Sensitivity (IDHm-A)**	**Specificity (IDHm-A)**
nADC > 2.145	43.1%	100%
%T2FM-Volume > 37.42%	26.2%	100%
nADC > 1.864	70.8%	94.4%
%T2FM-Volume > 22.05%	44.6%	94.4%
Classification: IDHm-A vs. IDHwt		
Threshold	**Sensitivity (IDHm-A)**	**Specificity (IDHm-A)**
nADC > 2.240	29.2%	100%
%T2FM-Volume > 41.77%	23.1%	100%
nADC > 1.849	70.8%	95.5%
%T2FM-Volume > 13.94%	50.8%	95.5%

Table 4.2. Summary of nADC and %T2-FLAIR Mismatch Volume Thresholds for Classifying IDH-mutant Astrocytomas with 100% Specificity and ~95% Specificity. $^{+}$

Previously reported in Cho et al., AJNR, 2024; IDHm-A = isocitrate dehydrogenase mutant

astrocytoma; IDHm-O = isocitrate dehydrogenase mutant oligodendroglioma; IDHwt = isocitrate dehydrogenase wild type glioma; %T2FM-volume = percentage T2-FLAIR mismatch volume; nADC = normalized apparent diffusion coefficient

Classification: IDHm-A vs. IDHm-O/IDHwt		
Model Variables	**Area Under Curve**	**P-value**
nADC-alone (ROC in Fig 4.3A)	0.848	<0.0001
nADC and %T2FM-Volume	0.851	<0.0001
nADC, %T2FM-Volume, and Age	0.880	<0.0001
Classification: IDHm-A vs. IDHm-O		
Model Variables	**Area Under Curve**	**P-value**
nADC-alone (ROC in Fig 4.3B)	0.805	<0.0001
nADC and %T2FM-Volume	0.810	<0.0001
nADC, %T2FM-Volume, and Age	0.816	<0.0001
Classification: IDHm-A vs. IDHwt		
Model Variables	**Area Under Curve**	**P-value**
nADC-alone (ROC in Fig 4.3C)	0.883	<0.0001
nADC and %T2FM-Volume	0.886	<0.0001
nADC, %T2FM-Volume, and Age	0.938	<0.0001

Table 4.3. Summary of Multiple Logistic Regression Results of nADC, %T2FM-Volume, and Age for Classifying IDH-mutant Astrocytomas. IDHm-A = isocitrate dehydrogenase mutant astrocytoma; IDHm-O = isocitrate dehydrogenase mutant oligodendroglioma; IDHwt = isocitrate dehydrogenase wild type glioma; %T2FM-volume = percentage T2-FLAIR mismatch volume; nADC = normalized apparent diffusion coefficient; ROC = receiver-operating characteristic

For exploratory survival analysis, only 4 out of 44 patients with IDHm-A (9%) reached overall survival endpoint. Log-rank tests showed no significant association between %T2FM-volume and overall survival in IDHm-A (P=0.20, ≥2% T2FM-volume median survival=2191 days, <2% T2FM-volume median survival undefined, Mantel Haenszel hazard ratio=4.76 (95% CI: 0.43–52.79), **Figure 4.4A**), but there were trends towards significance for nADC (P=0.07 with nADC≥2.07 associated with longer OS, Mantel Haenszel hazard ratio=0.12 (95% CI: 0.01–1.20), **Figure 4.4B**) and tumor volume (P=0.051 with volume ≥60mL associated with shorter OS, Mantel Haenszel hazard ratio=16.14 (95% CI: 0.98–264.9), **Figure 4.4C**) despite the large proportion of censored patients. Log-rank tests showed significant differences in overall survival between IDHwt, IDHm-O, and IDHm-A with $OS_{IDHwt} < OS_{IDHm\text{-}A} < OS_{IDHm\text{-}O}$ (P<0.0001, **Figure 4.4D**). Cox survival analysis assessing overall survival in IDHm-A with %T2FM-volume, nADC, and tumor volume as continuous measures demonstrated no significant results in univariate analyses (P>0.05) or multivariate analyses controlling for age, extent of resection, and grade (P>0.05).

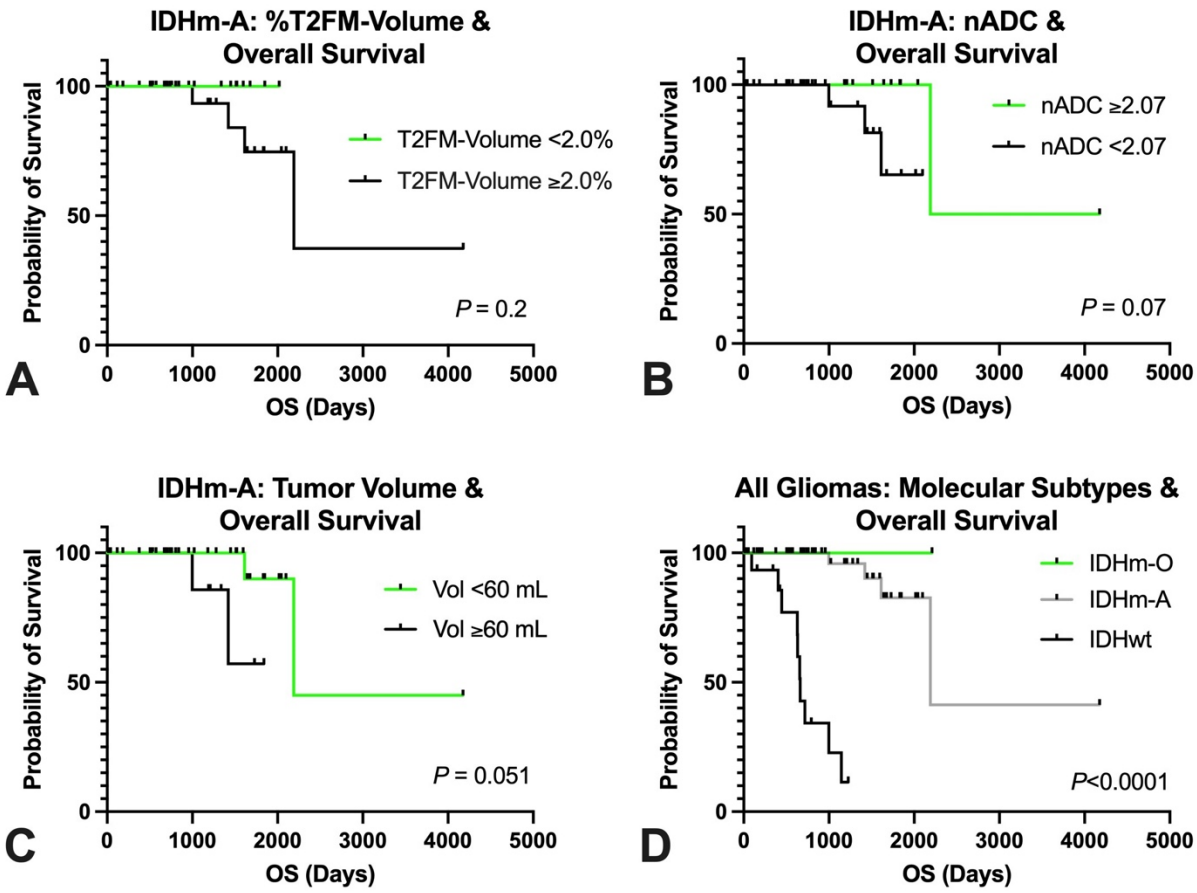

Figure 4.4. Summary of Log-Rank Survival Analysis. There was no significant association of %T2FM-volume with overall survival within IDH-mutant astrocytomas (*P*=0.2, **A**), but there were trends towards significance for normalized ADC (nADC) (*P*=0.07, **B**) and tumor volume (*P*=0.051, **C**). There were significant differences in overall survival across molecular subtypes. IDHm-A = isocitrate dehydrogenase mutant astrocytoma; IDHm-O = isocitrate dehydrogenase mutant oligodendroglioma; IDHwt = isocitrate dehydrogenase wild type glioma; %T2FM-volume = percentage T2-FLAIR mismatch volume; nADC = normalized apparent diffusion coefficient; OS = overall survival

Discussion

Results from the current study suggest that diffusivity alterations may be a better discriminator for IDHm-A compared with the presence of T2FM. Our results suggest the previously-described low sensitivity of T2FM-sign for IDHm-A may not have necessarily been limited due to its previously qualitative and binarized assessment,[38] but instead T2FM may be a feature with an inherently low-sensitivity for IDHm-A.[42] Consistent with the previous work from Lee *et al.*[95] who found that the combination of ADC characteristics and *visual* T2FM-sign improved the classification performance of IDHm-A from IDHwt gliomas, the present study observed increased performance when using the combination of nADC and *quantitative* %T2FM-volume; however, the present results also suggest that diffusion MRI alone may be sufficient to identify non-enhancing IDHm-A.

In corroboration of the findings reported by Foltyn *et al.*,[107] the current study documented a significantly higher ADC in the T2-FLAIR subtraction map-defined T2FM-core subregions in IDHm-A compared to T2FNM-rim subregions. This finding may be explained by both the higher expression of mTOR-related genes in IDHm-A exhibiting T2FM[38, 96] resulting in higher proliferation[112, 113] and correspondingly lower ADC[114] in the rim as well as the presence of increased water mobility due to microcystic changes or enlarged intercellular space within the T2FM core region.[38, 90, 96, 110] Interestingly, the higher ADC in T2FM-areas raises a possibility that prior studies that established ADC differences across gliomas—namely, highest ADC in IDHm-A, then IDHm-O, then IDHwt[61, 69]—were potentially biased by the proportion of IDHm-A exhibiting T2FM. As a result, the present study adds to the literature by re-assessing nADC glioma differences using ≥25% T2FM-volume IDHm-A ("mismatched) and <25% T2FM-volume IDHm-A ("non-mismatched") as separate tumor entities. Nevertheless, even IDHm-A with <25% T2FM-volume

still had higher nADC compared to IDHm-O and IDHwt, which suggests that there are diffusivity changes in IDHm-A inherent to their tumor biology that are not necessarily solely explained by the development of microcystic changes in T2FM-regions. Furthermore, these analyses demonstrate the value of T2-FLAIR subtraction maps for characterizing "mismatched" IDHm-A and their tumor subregions.

Exploratory analysis found no significant association between quantitative %T2FM-volume within IDHm-A and survival, which appears in line with previous studies.[38, 87, 110] Similarly, lower nADC and larger tumor volume trended towards lower overall survival in IDHm-A, which is also consistent with prior studies.[115-117] However, it should be noted that our findings warrant cautious interpretation given that only 9% of the analyzed IDHm-A patients died during the observation period. While the median overall survival of the analyzed IDHm-A was still a considerable ~3 years including censored data, the median overall survival of low-grade IDHm-A is ~9 years,[118] which presents a limitation of this study. Future studies with more mature survival data are necessary to confirm this observation.

Conclusions

Diffusion MRI is better than %T2FM-volume for classifying IDHm-A amongst non-enhancing gliomas, and quantitative %T2FM-volume may not be prognostic in terms of predicting overall survival in non-enhancing human gliomas.

Chapter 5. Pseudo-Resting-State Functional MRI Derived from Dynamic Susceptibility Contrast Perfusion MRI: Comparison with Resting-State Functional MRI and Cognitive Impairment Prediction

Preface

This chapter is adapted from the following accepted manuscript:

Cho NS*, Wang C*, Van Dyk K, Sanvito F, Oshima S, Yao J, Lai A, Salamon N, Cloughesy TF, Nghiemphu PL, Ellingson BM. Pseudo-resting-state functional MRI derived from dynamic susceptibility contrast perfusion MRI can predict cognitive impairment in glioma. *In Press. American Journal of Neuroradiology.* *Contributed equally.

The invention in this chapter has been filed for a provisional patent:

Ellingson BM, **Cho NS**, Wang C. Resting-state functional magnetic resonance imaging (MRI) derived from dynamic susceptibility contrast (DSC) perfusion MRI. Provisional U.S. Patent #63/570,544. Filed March 27, 2024.

Introduction

Although management of brain tumor patients typically involves assessing changes in tumor size on anatomic MRI techniques (e.g. T2-weighted FLAIR and contrast-enhanced T1-weighted images), the utilization of advanced MRI techniques is becoming more common and may provide valuable new insights into tumor biology and other important information that may improve clinical management.

For example, blood oxygenation level dependent (BOLD) functional MRI (fMRI) has an important role in neuro-oncological care for the pre-surgical mapping of eloquent cortex adjacent to brain tumors,[119] particularly the language and motor networks, as it has been shown to reduce post-surgical morbidity in a recent meta-analysis.[120] Pre-surgical fMRI mapping is typically performed using task-based functional MRI (tb-fMRI) during which the patient carries out multiple paradigms in the scanner to generate activation maps of eloquent cortex (e.g. finger-tapping, sentence completion).[120] However, tb-fMRI in the clinical setting may be challenging because image quality is reliant on optimal patient performance—which can be especially challenging for patients diagnosed with neurological conditions—as well as the availability of highly-trained personnel or advanced equipment to administer the paradigms.[121]

Evidence suggests blood oxygenation level dependent (BOLD) resting-state functional MRI (rs-fMRI)[119, 122] may have clinical utility for pre-surgical mapping (e.g., motor and language networks),[123-127] precluding the need for potentially challenging task paradigms for patients as in tb-fMRI.[119, 121] Additionally, rs-fMRI measures of functional connectivity (FC)—particularly within the default mode network (DMN)[128, 129]—may be useful for studying neurocognition in patient populations, including patients with brain tumors.[130-134] Neurocognitive assessment in patients with brain tumors is particularly important for therapeutic response evaluation[135] and is

gaining considerable attention because reduced neurocognition has a profound impact on post-treatment morbidity and cancer survivorship.[136]

Unfortunately, neither rs-fMRI nor neuropsychological test batteries are routinely performed clinically, mostly due to limitations in exam time and cost. As a result, there is a present need to be able to conduct rs-fMRI analyses and to identify cognitive decline in patients within current clinical workflows. Of note, during an rs-fMRI scan, patients are scanned using a T2*-sensitive sequence while at "rest." Based on MR physics principles, it may be conceivable to acquire "pseudo-rs-fMRI" data from a dynamic susceptibility contrast (DSC) perfusion MRI scan. DSC perfusion MRI is also dynamically-acquired with a T2*-sensitive gradient echo-EPI sequence with strong BOLD-weighting like BOLD rs-fMRI, except DSC is performed during the injection of a contrast agent bolus. DSC perfusion MRI is also used much more extensively in clinical settings than BOLD rs-fMRI for brain tumors to assess tumor vascularity.[21, 69, 137, 138]

We theorized a "pseudo-rs-fMRI" signal could be derived from DSC perfusion to quantify FC and that these metrics can be used to estimate cognitive impairment in patients with brain tumors. We hypothesized that: (1) pseudo-rs-fMRI derived from DSC perfusion MRI would yield similar qualitative network mapping results as rs-fMRI by investigating three commonly studied resting-state networks given their relevance to clinical care and neuroscience research: the default mode, motor, and language networks;[128, 129, 139] and (2) there would be observable FC differences between cognitively impaired versus non-impaired patients, particularly of the default mode network, using rs-fMRI and pseudo-rs-fMRI.

Methods

Patient Cohort

This study was performed in compliance with the Health Insurance Portability and Accountability Act (HIPAA) and was approved by our institutional review board. All patients provided informed consent. Consecutive patients seen at our neuro-oncology clinic that were previously diagnosed with diffuse glioma and had completed all therapies/surgeries and off-therapy for at least 6 months prior to enrollment in a prospective trial (IRB #17-001500) assessing cognitive assessment using a neuropsychological test battery were eligible for study.[134] The inclusion criteria for the present study were: (1) right-handed, (2) received rs-fMRI scanning, and (3) received DSC perfusion MRI with near whole-brain coverage within the same session. A total of 24 consecutive patients with the above inclusion criteria were recruited. Clinical data are summarized in **Table 5.1** with further detailed diagnosis provided in **Table 5.2**. A portion of patients were assessed in a prior study.[134]

Characteristic	Patient Cohort (n=24)
Age (Mean Years (Range))	45 (22–70)
Sex (M/F)	16/8
Cognitive Impairment Status (Impaired/Non-impaired)	13/11
Handedness (Right/Left)	24/0
IDH Status (Mutant/Wild-type/Unknown)	19/2/3

Table 5.1. Clinical Data of Patients.

Diagnosis	Number (n=19 total)
Grade 2 IDH-Mutant 1p/19q-Intact Astrocytoma	3
Grade 3 IDH-Mutant 1p/19q-Intact Astrocytoma	6
Grade 4 IDH-Mutant 1p/19q-Intact Astrocytoma	1
Grade 2 IDH-Mutant 1p/19q-Codeleted Oligodendroglioma	2
Grade 3 IDH-Mutant 1p/19q-Codeleted Oligodendroglioma	2
IDH-Mutant Glioma with Unknown 1p/19q Status	5

Table 5.2. Detailed Diagnosis of IDH-Mutant Glioma Patients.

Cognitive Impairment Assessment

Cognitive function was assessed using a previously described neuropsychological test battery[134] informed by International Cognition and Cancer Task Force recommendations,[140] expert recommendations,[141] and the authors' prior clinical experience. The test battery included learning, memory, attention, processing speed, working memory, language, and visuospatial measures (see **Table 5.3** for detailed assessment list).[134] Each score was normalized to Z-scores using published normative data as reference. Patients were categorized as "cognitively impaired" if 2 or more of their test scores were $Z \leq -2$ and as "cognitively non-impaired" if otherwise, criteria based off

International Cognition and Cancer Task Force recommendations and accounting for the number of tests to limit the likelihood of falsely identifying chance impairment.[140, 142]

Domain	Test
Estimate of pre-morbid verbal intellectual function	Test of Premorbid Functioning
Verbal learning and memory	The Hopkins Verbal Learning Test – Revised
Visuospatial learning and memory	Brief Visuospatial Memory Test – Revised
Processing speed, attention, executive functions	Wechsler Adult Intelligence Scale-IV Coding and Digit Span subtests; The Trail-Making; The Golden Stroop
Language	Verbal fluency – FAS and animal naming; The Boston Naming Test
Visuospatial	The Rey-Osterrieth Complex Figure

Table 5.3. Neuropsychological Test Battery Assessments.

Image Acquisition

MPRAGE T1 pre-/post-contrast MRI, T2-weighted FLAIR MRI, DSC perfusion MRI, and rs-fMRI scans were acquired at 3T using Siemens Prisma, Skyra, or Vida scanners (Siemens, Erlangen, Germany). Rs-fMRI was acquired during the same session as the anatomical & DSC perfusion MRI and prior to the DSC perfusion MRI as per recommended guidelines.[139] Anatomical MPRAGE T1 pre-/post-contrast MRI and T2-weighted FLAIR MRI were acquired in compliance with the standardized brain tumor imaging protocol.[71] All DSC perfusion MRI was acquired after administration of a 0.1 mmol/kg bolus of Gd-DTPA. Rs-fMRI and DSC perfusion MRI scans parameters are summarized in **Table 5.4**.

	Patient Cohort (n=24)	
Sequence	Full Rs-fMRI	DSC Perfusion
Number of Patients	24	24
Scanner Model	Prisma, Skyra, Vida	
Field Strength	3 Tesla	3 Tesla
Echo Time (TE)	28ms	17ms
Repetition Time (TR)	2s	1.35-1.72s
Flip Angle	77^{o}	35^{o}
Number of Volumes	300 (265 for n=1)	120
Number of Slices	38	24-30
Slice Thickness	4mm	5mm
Acquisition Matrix	64 x 64	128 x 128
Field of View (FOV)	220mm	240mm

Table 5.4. DSC Perfusion MRI and Full Resting-State Functional MRI Scanning Parameters.

Image Pre-Processing: Full and Truncated Resting-State Functional MRI

Full rs-fMRI data were pre-processed in accordance to recently published pre-processing recommendations[139] using the CONN toolbox (https://web.conn-toolbox.org/).[143] In brief, the standard CONN pre-processing pipeline steps of functional realignment/unwarping and slice-timing correction were performed. Next, outlier identification, image registration to MNI space, and segmentation of gray matter, white matter, and cerebrospinal fluid were performed. Then, the full rs-fMRI data were smoothed using an 8 mm full width at half maximum Gaussian kernel and denoised by regressing motion correction parameters along with white matter and cerebrospinal fluid signal and applying a bandpass filter of 0.01–0.1 Hz. Because DSC perfusion MRI is of shorter duration than typical rs-fMRI acquisitions, a truncated rs-fMRI was created by taking the first 100 volumes and pre-processed as described above to serve as a comparison.

Image Pre-Processing: Pseudo-Resting-State Functional MRI from DSC Perfusion MRI

DSC perfusion MRI was pre-processed by first performing motion-correction using FSL's *mcflirt* function (https://fsl.fmrib.ox.ac.uk/fsl/fslwiki/MCFLIRT)[144] and then applying a bi-directional leakage-correction algorithm to obtain a leakage-corrected signal[145].[146, 147] Pseudo-rs-fMRI data was then extracted by performing voxel-wise, Gamma-variate modeling of the contrast agent bolus and then performing voxel-wise subtraction of the modelled contrast agent bolus from the leakage-corrected signal to create a residual "pseudo-rs-fMRI" signal (**Figure 5.1**). Pseudo-rs-fMRI data were then loaded into the CONN toolbox[143] for further standard rs-fMRI-related pre-processing as performed for the rs-fMRI data in this study except for volume censoring.

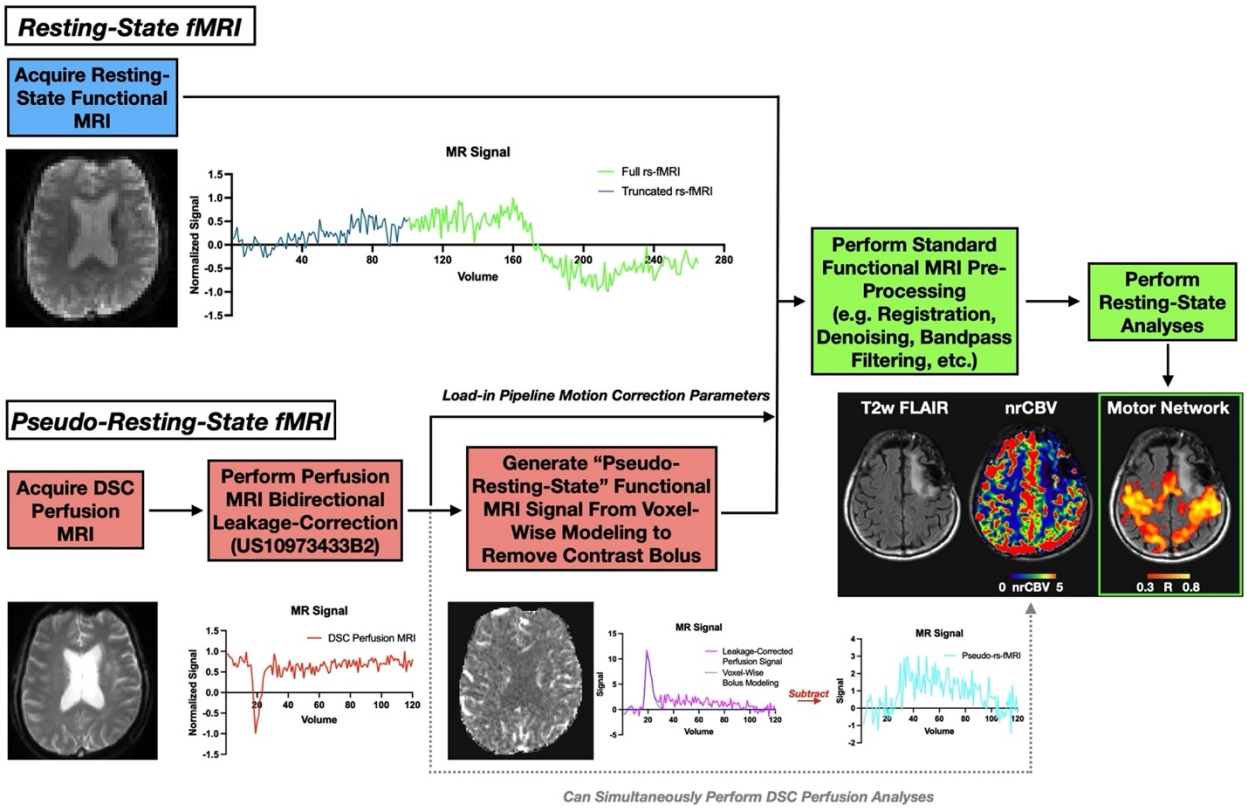

Figure 5.1. Schematic of Pseudo- and Resting-State Functional MRI Processing Pipeline. Pseudo-resting-state functional MRI is derived from dynamic-susceptibility contrast (DSC) perfusion MRI through bidirectional leakage-correction and voxel-wise modeling of the contrast bolus and then incorporated into typical resting-state functional MRI pre-processing pipelines while still being able to simultaneously perform DSC perfusion MRI analyses. DSC = dynamic-susceptibility contrast; rs-fMRI = resting-state functional MRI; nrCBV = normalized relative cerebral blood volume

Image Post-Processing: Generating Pseudo-/Resting-State Seed-to-Voxel Network Maps

Default mode network, motor network, and language network seed-to-voxel maps were generated for each patient in pseudo-rs-fMRI, full rs-fMRI, and truncated rs-fMRI using consistent seed ROI's selected from CONN's built-in network ROI parcellations in MNI atlas space.[143] Specifically, the default mode network was generated by seeding the medial prefrontal cortex ROI, the motor network was generated by seeding the left lateral sensorimotor cortex ROI, and the language network was generated by seeding the left inferior frontal gyrus ROI. Group-level average network maps were then created through AFNI (Analysis of Functional NeuroImages, https://afni.nimh.nih.gov/)[76] *3dttest++* command. Dice scores were used to evaluate the similarity between rs-fMRI and pseudo-rs-fMRI. Dice scores range from 0 to 1, where a Dice score of 0 is no overlap and a Dice score of 1 is perfect overlap. Dice scores were computed for each patient and the group-average seed-to-voxel maps between the resting-state network maps generated by (1) pseudo-rs-fMRI & full rs-fMRI as well as (2) truncated rs-fMRI & full rs-fMRI using MATLAB. Network map Dice scores for each image pairing were calculated within the overlap of perfusion slice coverage & regions of full rs-fMRI activation with $r > 0.3$ for pseudo-rs-fMRI vs. full rs-fMRI and truncated rs-fMRI vs. full rs-fMRI assessments.

Functional Connectivity Differences Based on Cognitive Impairment Status

When performing quantitative analyses assessing connectivity differences between cognitively impaired and non-impaired patients, voxels within any resection cavities were excluded from the analyses. Resection cavity masks were segmented using AFNI software[76] and the MNI-registered T1-weighted pre-contrast or T2-weighted FLAIR MRI scans by a lab member with 2 years of tumor segmentation experience (N.S.C.) and inspected by a radiologist with 11 years of neuroimaging experience (S.O.) who were blinded to the cognitive impairment status.

Both seed-to-voxel and ROI-to-ROI approaches were performed to identify functional connectivity differences based on cognitive impairment status using pseudo-rs-fMRI and full rs-fMRI. For the seed-to-voxel approach, difference maps were generated using the AFNI *3dttest++* command. For the ROI-to-ROI approach, connectivity matrices were extracted for each individual patient using the CONN toolbox. To further account for prior surgical resection and larger rs-fMRI slice coverage compared to DSC perfusion in some brain regions, the network ROI's were refined at the patient-level to exclude voxels outside the perfusion slice coverage and voxels within any prior resection cavities from quantitative FC analyses. ROIs in the cerebellum, supplementary motor area, and frontal eye fields were excluded from group analyses *a priori* due to limited perfusion slice coverage. Then, patient-specific ROIs were fed into CONN for signal extraction and further group difference analyses.

Statistical Analysis

Paired t-tests or Wilcoxon signed-rank tests were performed at a threshold of $P<0.05$ to compare Dice scores between pseudo-rs-fMRI & full rs-fMRI and truncated rs-fMRI & full rs-fMRI network maps depending on the normality of the data. The potential relationship between tumor hemispheric lateralization and cognitive impairment status was assessed using the Fisher's exact test. A multivariable general linear model (GLM) was implemented to identify functional differences between cognitively impaired and non-impaired patients for seed-to-voxel and ROI-to-ROI analyses using pseudo-rs-fMRI and full rs-fMRI with age and TR as covariates.

For seed-to-voxel analyses, the general linear model (GLM) was implemented using the AFNI *3dttest++* command. Cluster-level, family-wise error (FWE) correction was implemented through the *3dClustSim* command in AFNI with a threshold of $P<0.05$ (uncorrected) to estimate

the proper cluster threshold. For graphical presentation of seed-to-voxel results at the patient-level, average correlation values from the significant clusters using a mask of the intersection of the cluster and corresponding anatomical atlas ROI were assessed between cognitively impaired and non-impaired patients with t-tests. For ROI-to-ROI connectome analyses, the GLM was implemented using an in-house pipeline in MATLAB with age and TR included as covariates.

The level of significance for seed-to-voxel and ROI-to-ROI analyses for group differences was set at $P<0.05$ with a false discovery rate (FDR) of 0.05. Multiple logistic regression was performed using ROI-to-ROI FC to predict cognitive impairment status using pseudo-rs-fMRI and full rs-fMRI, and paired analyses comparing the area under curve (AUC) of the resulting receiver-operating characteristic (ROC) curves was performed using the Hanley & McNeil's paired statistical method.[148]

Results

Individual and Group-Level Functional Connectivity

Three representative patients and their default mode, motor, and language network map results using full rs-fMRI and pseudo-rs-fMRI are shown in **Figure 5.2**. Patient 1 is a 38-year-old male patient who is cognitively impaired and was diagnosed with IDH-mutant astrocytoma, and the Dice scores for the default mode, motor, and language networks were 0.873, 0.701, and 0.429, respectively (**Figure 5.2A**). Patient 2 is a 38-year-old male patient who is not cognitively impaired and was diagnosed with IDH-mutant astrocytoma, and the Dice scores for the default mode, motor, and language networks were 0.612, 0.740, and 0.819, respectively (**Figure 5.2B**). Patient 3 is a 41-year-old male patient who is not cognitively impaired and was diagnosed with IDH-mutant astrocytoma, and the Dice scores for the default mode, motor, and language networks were 0.472, 0.663, and 0.594, respectively (**Figure 5.2C**). **Figure 5.3** shows the network maps from pseudo-rs-fMRI and truncated rs-fMRI for comparison, the latter of which are visually noisier than those from the full rs-fMRI.

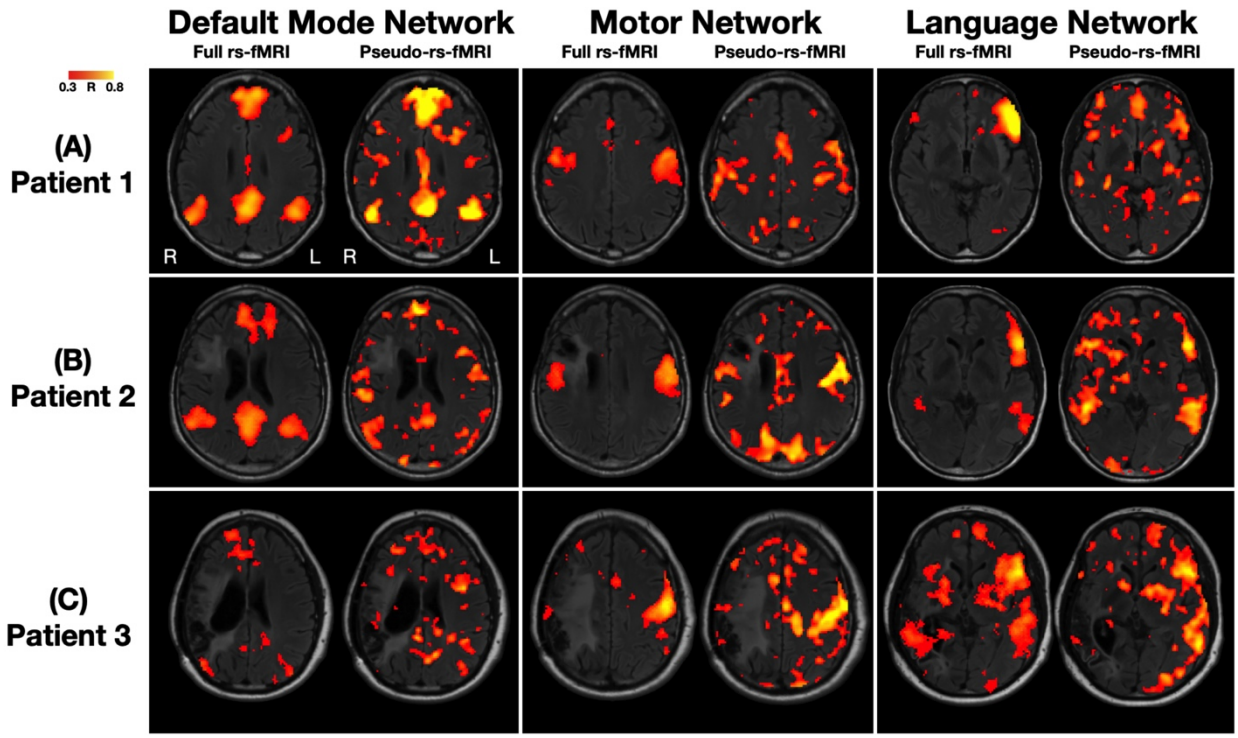

Figure 5.2. Three Representative Cases of Default Mode, Motor, and Language Network Maps using Full rs-fMRI and Pseudo-rs-fMRI. Patient 1 (**A**) is a 38-year-old male patient who is cognitively impaired and was diagnosed with IDH-mutant astrocytoma. Patient 2 (**B**) is a 38-year-old male patient who is not cognitively impaired and was diagnosed with IDH-mutant astrocytoma. Patient 3 (**C**) is a 41-year-old male patient who is not cognitively impaired and was diagnosed with IDH-mutant astrocytoma. See **Figure 5.3** for network maps using truncated rs-fMRI.

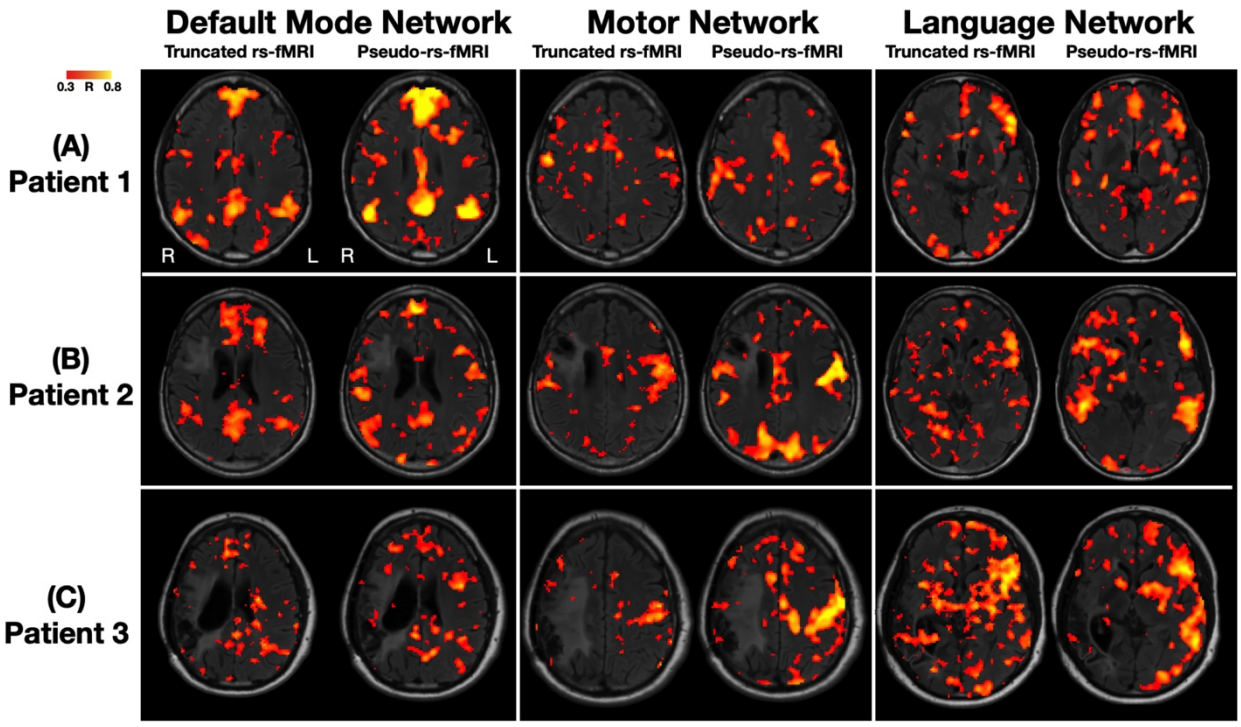

Figure 5.3. Three Representative Cases of Default Mode, Motor, and Language Network Maps using Truncated rs-fMRI and Pseudo-rs-fMRI. Patients 1–3 (**A–C**) are the same patients as in **Figure 5.2.** Here in this figure, the resting-state network maps using truncated resting-state functional MRI (rs-fMRI) are shown instead of the networks maps using full resting-state functional MRI.

The mean and standard deviation Dice scores between (1) pseudo-rs-fMRI & full rs-fMRI and (2) truncated rs-fMRI & full rs-fMRI are shown in **Figure 5.4** and **Table 5.5**. The mean and standard deviation Dice scores between pseudo-rs-fMRI & full rs-fMRI for the default mode, motor, and language networks were 0.689 (0.118), 0.730 (0.124), and 0.665 (0.142), respectively. There was no significant difference in Dice scores between pseudo-rs-fMRI & full rs-fMRI and truncated rs-fMRI & full rs-fMRI for the default mode network (P = 0.97, mean difference of

pseudo-rs-fMRI minus truncated rs-fMRI Dice scores = 0.002, **Figure 5.4A**) or language network (*P* = 0.30, mean difference = 0.036 **Figure 5.4C**), but there was a significant increase in Dice scores for pseudo-rs-fMRI & full rs-fMRI compared to truncated rs-fMRI & full rs-fMRI for the motor network (*P* = 0.02, mean difference = 0.085, **Figure 5.4B**).

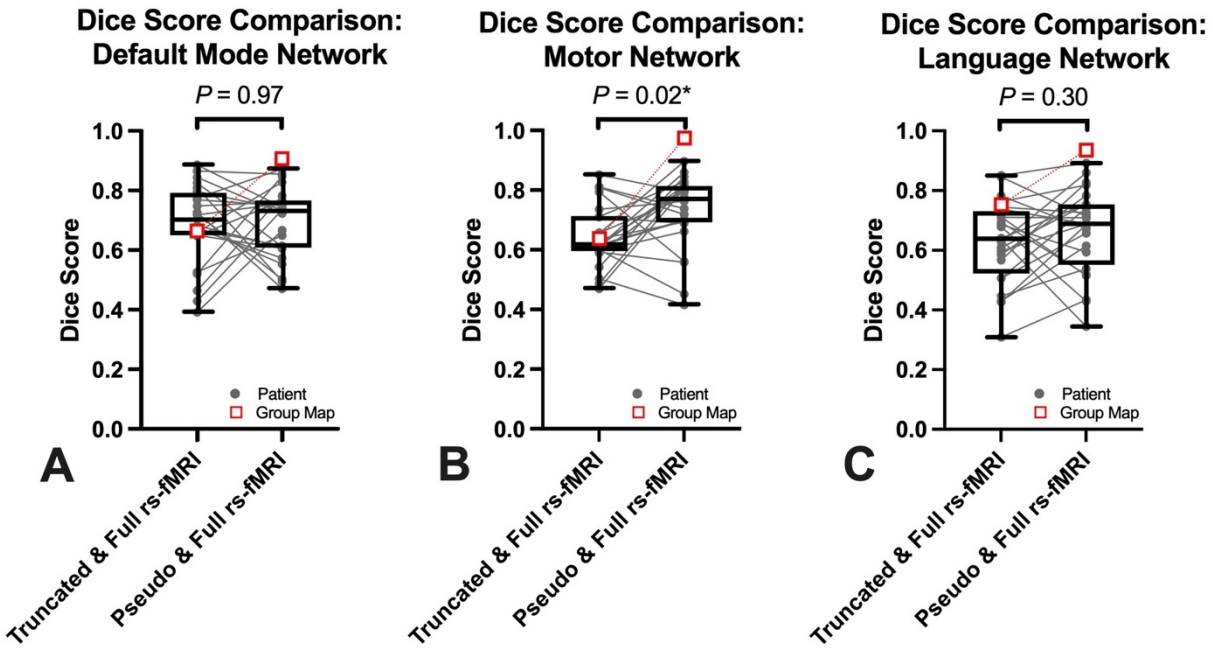

Figure 5.4. Comparison of Dice Scores of Network Maps from Pseudo-rs-fMRI and Truncated rs-fMRI with Full rs-fMRI. At the patient-level, no significant differences in Dice scores were observed for the default mode network (**A**) or language network (**C**), but there was a significant increase in Dice scores for pseudo-rs-fMRI compared to truncated rs-fMRI for the motor network (**B**). Box plots of the patient-level data and singular Dice score values of the group-average maps (red squares) are also overlaid for visualization.

Resting-State Network	Comparison	Average Dice Score of Individual Maps (SD)	Dice Score of Group-Average Maps
Default Mode Network	Pseudo-rs-fMRI & Full rs-fMRI	0.689 (0.118)	0.905
	Truncated-fMRI & Full rs-fMRI	0.688 (0.136)	0.663
Motor Network	Pseudo-rs-fMRI & Full rs-fMRI	0.730 (0.124)	0.973
	Truncated-fMRI & Full rs-fMRI	0.645 (0.102)	0.636
Language Network	Pseudo-rs-fMRI & Full rs-fMRI	0.665 (0.142)	0.935
	Truncated-fMRI & Full rs-fMRI	0.629 (0.138)	0.753

Table 5.5. Dice Scores of Resting-State Networks Between Pseudo-rs-fMRI, Full rs-fMRI, and a Truncated version of the Full rs-fMRI Signal.

The averaged group maps of the default mode, motor, and language networks from full rs-fMRI and pseudo-rs-fMRI at thresholds of $r > 0.2$ and $r > 0.3$, respectively for visualization, are shown in **Figure 5.5**. The default mode network in pseudo-rs-fMRI and full rs-fMRI show FC in the medial prefrontal cortex, left/right inferior parietal lobule, and posterior cingulate cortex. The motor network in pseudo-rs-fMRI and full rs-fMRI show FC in the left and right sensorimotor cortex and the anterior cingulate cortex, although the anterior cingulate cortex is not visualized in the full rs-fMRI-derived motor network map at a higher, matched threshold of $r > 0.3$ (**Figure 5.6**). Similarly, the language network in pseudo-rs-fMRI and full rs-fMRI show FC in the left and right inferior frontal gyrus and left Wernicke's area, although the left Wernicke's is not visualized in the full rs-fMRI-derived language network map at a higher, matched threshold of $r > 0.3$ (**Figure 5.6**). The Dice scores for the group maps for are also presented in **Figure 5.4** and **Table 5.5,** which ranged between 0.905–0.973 for pseudo-rs-fMRI & full rs-fMRI network maps.

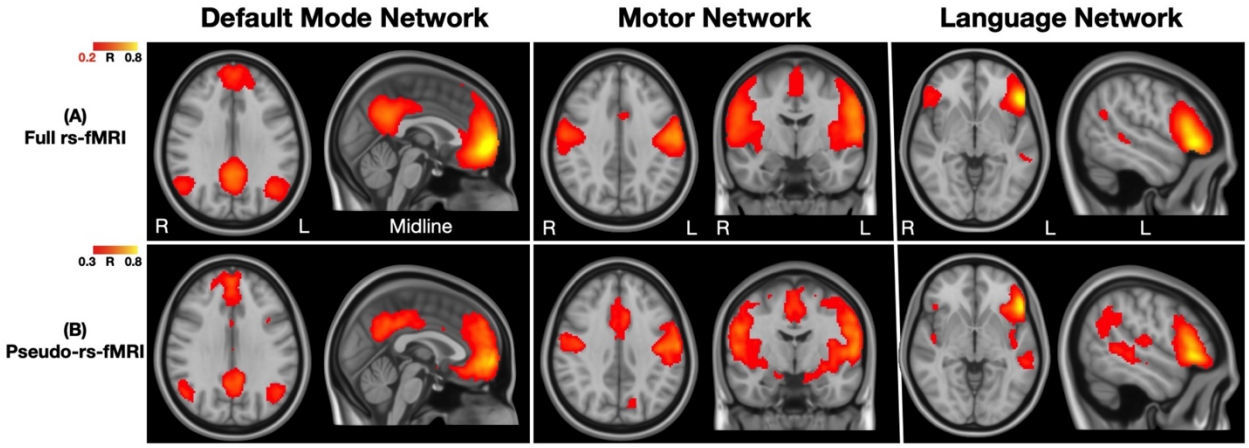

Figure 5.5. Group-average Maps of Default Mode, Motor, and Language Network Maps using Full rs-fMRI and Pseudo-rs-fMRI. Network maps are presented using full rs-fMRI (**A**) and pseudo-rs-fMRI (**B**). See **Figure 5.6** for the network maps of full rs-fMRI at a matched $r > 0.3$ threshold.

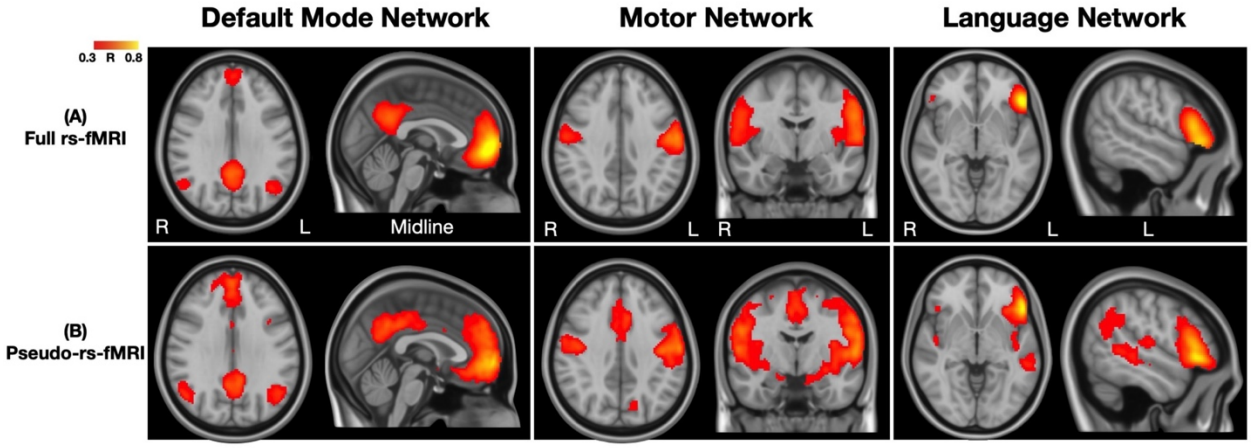

Figure 5.6. Group-average Maps of Default Mode, Motor, and Language Network Maps using Full rs-fMRI and Pseudo-rs-fMRI at a Matched Threshold of r > 0.3. Network maps for full rs-fMRI (**A**) and pseudo-rs-fMRI (**B**) are both shown using a threshold of r > 0.3.

Relationship Between Functional Connectivity and Cognitive Impairment

Seed-to-voxel analyses did not show any significant cluster differences after FWE-correction between cognitively impaired and non-impaired patients when seeding the medial prefrontal cortex of the default mode network. Additionally, no significant differences were found in the results of seed-to-voxel analyses between full rs-fMRI and pseudo-rs-fMRI using an interaction model assessing for significant differences between the two techniques after FWE-correction. To further explore potential similarities between full rs-fMRI and pseudo-rs-fMRI results, the cluster threshold for full rs-fMRI was empirically chosen to select for the top ~5% largest clusters, which corresponded to a threshold of 300 mm^3. At this lowered threshold, full rs-fMRI cluster threshold to 300 mm^3, full rs-fMRI revealed some significant functional differences between cognitively impaired and non-impaired patients (voxels $P<0.05$) that were also observed using pseudo-rs-fMRI with the same cluster threshold (voxels $P<0.05$) (**Figure 5.7**). Upon seeding

the medial prefrontal cortex of the default mode network, both full rs-fMRI and pseudo-rs-fMRI identified weaker connectivity to clusters in the bilateral precuneus in cognitively non-impaired patients compared to the cognitively impaired patients (left precuneus: P=0.0050 for full rs-fMRI, P=0.0193 for pseudo-rs-fMRI, right precuneus: P=0.0064 for full rs-fMRI, P=0.0260 for pseudo-rs-fMRI, **Figure 5.7**) as well as stronger connectivity to clusters in the right rostral middle frontal cortex (P=0.0007 for full rs-fMRI, P=0.0068 for pseudo-rs-fMRI, **Figure 5.7**) and right superior frontal cortex (P=0.0002 for full rs-fMRI, P=0.0121 for pseudo-rs-fMRI, **Figure 5.7**).

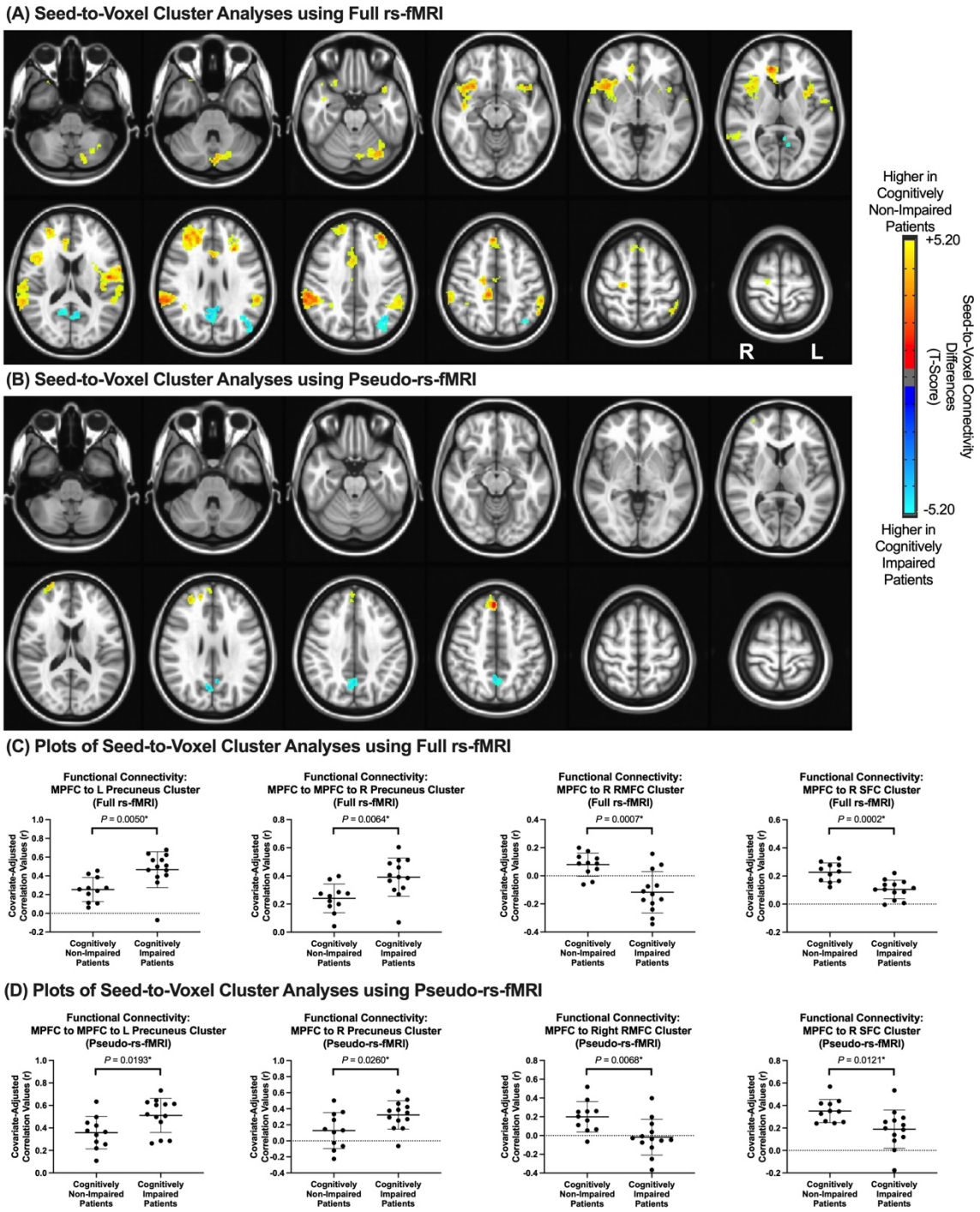

Figure 5.7. Seed-to-voxel Connectivity Alterations between Cognitively Non-impaired and Impaired Patients. The presented results do not include FWE-correction. Similar connectivity differences between cognitively non-impaired and cognitively impaired patients were observed

using full rs-fMRI and pseudo-rs-fMRI, namely stronger connectivity to the right rostral middle frontal cortex and right superior frontal cortex and weaker connectivity to the bilateral precuneus in cognitively non-impaired patients compared to the cognitively impaired patients (**A/B)**. Significant clusters were determined by thresholding voxels based on level of statistical significance (P<0.05) and cluster size of 300 mm^3. Representative clusters identified by (**C**) full rs-fMRI and (**D**) pseudo-rs-fMRI demonstrated significant seed-to-voxel connectivity differences between cognitively impaired and non-impaired patients. Note, whole brain results are presented for the rs-fMRI, but pseudo-rs-fMRI results were masked to exclude regions outside of inconsistent near-whole brain slice coverage, including regions in the cerebellum and upper-most superior brain, which explain the lack of clusters in those areas. MPFC = medial prefrontal cortex; RMFC = rostral middle frontal cortex; SFC = superior frontal córtex

Similarly, in ROI-to-ROI analyses, neither the full rs-fMRI nor pseudo-rs-fMRI yielded significant differences in FC after FDR-correction between cognitively impaired and non-impaired patients. Nevertheless, some reproducible ROI-to-ROI connectivity patterns were observed in the FDR-uncorrected results that were in line with the FWE-uncorrected seed-to-voxel results (**Figure 5.8A/B**). Specifically, there was stronger connectivity from the medial prefrontal cortex of the default mode network to the right rostral prefrontal cortex of the salience network in cognitively non-impaired patients compared to the cognitively impaired patients (P=0.0013 for full rs-fMRI, P=0.053 for pseudo-rs-fMRI, **Figure 5.8A/B**), analogous findings to the left rostral prefrontal cortex were only observed in full rs-fMRI (P=0.0004 for full rs-fMRI, P=0.58 for pseudo-rs-fMRI, **Figure 5.8A/B**) as in the seed-to-voxel analyses (**Figure 5.7**). Additionally, there were trends for weaker connectivity from the medial prefrontal cortex of the default mode network to the posterior

cingulate cortex of the default mode network in cognitively non-impaired patients compared to the cognitively impaired patients (P=0.18 for full rs-fMRI, P=0.10 for pseudo-rs-fMRI, **Figure 5.8A/B**).

When combining these three individual ROI-to-ROI FC results into a multiple logistic regression to predict cognitive impairment status, there were significant differences in predicted probability values for cognitive impairment using full rs-fMRI (P=0.0005) and pseudo-rs-fMRI (P=0.0143). Both full rs-fMRI and pseudo-rs-fMRI classified impairment status with significant AUC (full rs-fMRI: AUC=0.8881 (95% CI: 0.7445–1.000), P=0.0013 | pseudo-rs-fMRI: AUC=0.7762 (95% CI: 0.5892–0.9633), P=0.0221 | **Figure 5.8C**), and there was no statistically significant difference between the two AUC's for classification (P=0.29). There was also no significant relationship between tumor hemispheric lateralization and cognitive impairment status (P>0.99).

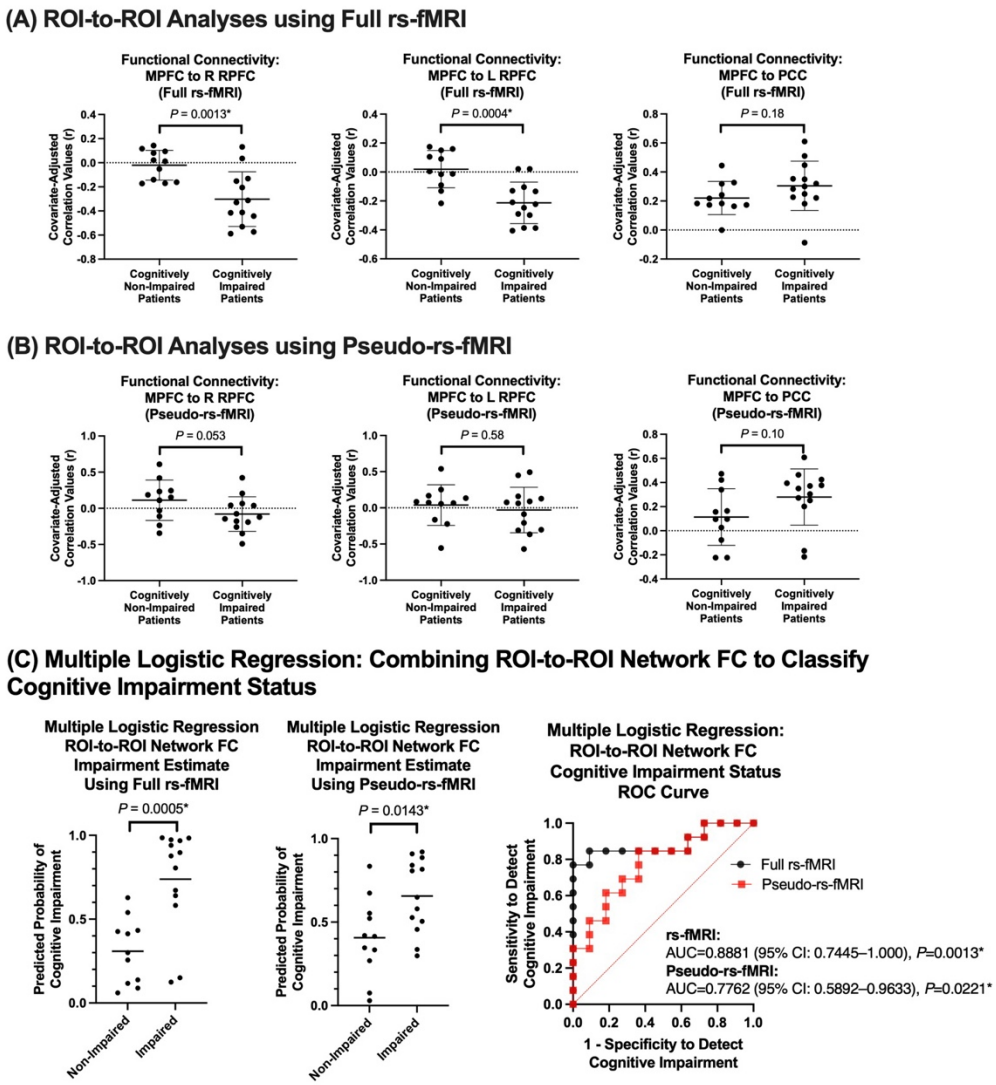

Figure 5.8. ROI-to-ROI Connectivity Alterations between Cognitively Non-impaired and Impaired Patients. For cognitively non-impaired patients compared to impaired patients, there was stronger connectivity from the medial prefrontal cortex to the right rostral prefrontal cortex using full rs-fMRI and pseudo-rs-fMRI (**A/B**), to the left rostral prefrontal cortex only observed in full rs-fMRI (**A/B**) as in the seed-to-voxel analyses, and trends for weaker connectivity to the posterior cingulate cortex in full rs-fMRI and pseudo-rs-fMRI (**A/B**). Multiple logistic regression combining these individual connectivity differences showed significant differences in predicted probability values for cognitive impairment using full rs-fMRI (*P*=0.0005) and pseudo-rs-fMRI

(*P*=0.0143) (**C**), and receiver operating characteristic (ROC) curve analyses demonstrated an area under curve (AUC) of 0.8881 (*P*=0.0013) using full rs-fMRI and 0.7762 (*P*=0.0221) using pseudo-rs-fMRI for cognitive impairment status classification (**C**). The difference in AUC for pseudo-rs-fMRI and rs-fMRI was not statistically significant (*P*=0.29). MPFC = medial prefrontal cortex; RPFC = rostral prefrontal cortex; PCC = posterior cingulate cortex; FC = functional connectivity; ROC = receiver operating characteristic; AUC = area under curve

Discussion

A major barrier for the widespread use of clinical rs-fMRI outside of select institutions for pre-surgical planning[123-127] and functional mapping of patients with brain tumors is the additional time and cost requirements. Results from the current study suggest that pseudo-rs-fMRI derived from DSC perfusion MRI may be useful for performing network mapping, seed-to-voxel, and ROI-to-ROI resting-state analyses similar to rs-fMRI in glioma patients with known cognitive status. The novelty and potential clinical utility of our method is that our pseudo-rs-fMRI approach using DSC perfusion MRI may theoretically preclude the need for an additional rs-fMRI scan because DSC perfusion MRI can provide combined advantages of assessing FC related to network mapping and cognition while simultaneously providing perfusion estimates of tumor vascularity. The observation that alterations in rs-fMRI correspond with functional impairment is consistent with traditional rs-fMRI studies in developmental disorders,[149] aging,[150] and other neurological diseases,[151, 152] but the ability to estimate these rs-fMRI metrics quickly and concurrently with DSC perfusion MRI metrics within clinical workflows using the proposed DSC post-processing technique opens up the possibility of estimating a wide range of rs-fMRI parameters in patients with brain tumors, including graph theory metrics,[130, 132] within-tumor connectivity,[153] and BOLD asynchrony,[154] as well as broad applicability to other neurologic disorders that require evaluation of DSC perfusion including stroke.

While our results suggested default mode, motor, and language network maps generated using pseudo-rs-fMRI derived from DSC perfusion were similar to maps using full rs-fMRI based on the Dice scores shown in **Table 5.5**, the pseudo-rs-fMRI-derived maps appeared noisier compared to rs-fMRI-derived maps at the patient-level while the group-average network maps appeared more similar as quantified by the higher Dice scores for the group maps. This observation

may be explained by the fact that DSC perfusion MRI is typically acquired for at least 2 minutes[72] (typically on the order of 2–3 minutes, ~3 minutes in the current study) while a traditional rs-fMRI is recommended to be acquired longer for at least 6 minutes (~10 minutes in the current study),[139, 155] directly leading to increased noise in the estimation of connectivity from decreased signal-to-noise ratio using pseudo-rs-fMRI. In support of this primary source of noise, truncating the full rs-fMRI to the first 100 timepoints (~3 minutes) resulted in similar Dice scores between pseudo-rs-fMRI and truncated rs-fMRI compared to the full rs-fMRI dataset. However, there was variation in the Dice scores and, for the motor network, the Dice scores for pseudo-rs-fMRI were significantly higher than that of truncated rs-fMRI perhaps due to variations in noise, so other factors beyond scan duration must be considered.

One additional source of this variation could be contributions to the DSC perfusion experiment itself, even after the contrast agent bolus is subtracted from the signal. It should be noted that even for rs-fMRI, even a slight variation in the patient's "rest" scanning condition such as simply whether one keeps their eyes open & fixated or keeps their eyes closed can impact the BOLD signal and the quality of rs-fMRI results.[155] Recent rs-fMRI guidelines for pre-surgical planning now even recommend eyes being kept open & fixated for the standardization of rs-fMRI.[139] However, in DSC perfusion MRI, patients are not instructed regarding eye fixation as it is not relevant for perfusion analyses, and there are additional sensory stimulations of the intravenous catheter and the delivery of contrast agent bolus during a DSC perfusion MRI scan that are not present during a typical rs-fMRI scan that may theoretically impact the resulting BOLD signal.

Another source of variation is likely related to differences in acquisition parameters between rs-fMRI and DSC perfusion MRI. Rs-fMRI scanning protocols are optimized to detect

the BOLD signal, while DSC perfusion MRI protocols are optimized to quantify cerebral blood volume and other perfusion metrics. Furthermore, the current study had variation in DSC perfusion MRI protocols, but some of these effects may have been mitigated through the use of leakage correction.[146, 147] However, the methodology and results presented demonstrate the ability to generate FC network maps and identify patients with cognitive impairment despite these potential sources of contamination.

Of note, our proposed pseudo-rs-fMRI method involves post-processing of DSC perfusion MRI that can be conducted retrospectively in institutional patient image databases, as done in the present study, as well as integrated into prospective image acquisition workflows optimized for DSC perfusion MRI and pseudo-rs-fMRI analyses. Ideally, a DSC perfusion MRI protocol that is dually-optimized for pseudo-rs-fMRI and perfusion analyses in brain tumors may involve (i) increasing the scan acquisition to 6 minutes to be compliant with rs-fMRI guidelines[139] but (ii) within the suggested maximal 8 minute delay between contrast agent injection and 3D post-contrast T1-weighted MRI in the standardized Brain Tumor Imaging Protocol[71] and then (iii) cropping the signal to shorter duration for perfusion analyses in order to be compliant with DSC perfusion MRI guidelines.[72] Increasing the slice coverage of DSC perfusion MRI to consistently cover the entire brain, such as with simultaneous multi-slice techniques,[156] could allow for further FC investigation of upper-most superior regions such as the supplementary motor area[157] and lower-most inferior regions such as the cerebellum,[158] both of which were unable to be explored in the present ROI-to-ROI analyses using pseudo-rs-fMRI. It is also conceivable that the proposed pseudo-rs-fMRI method can be utilized with multi-echo DSC perfusion MRI protocols for further flexibility in sequence parameters.[159]

It is important noting that the present study appeared to be underpowered, in that we consistently observed FWE-/FDR-uncorrected FC differences between cognitively impaired and non-impaired patients using full rs-fMRI and pseudo-rs-fMRI, and no differences after traditional FWE-/FDR-correction. For example, without FWE-/FDR-correction, there were consistent FC difference patterns in the default mode network, notably a finding of increased connectivity between the medial prefrontal cortex and the rostral prefrontal cortex of the salience network in non-impaired patients versus impaired patients as observed in a prior study[134] and increased connectivity between the medial prefrontal cortex and precuneus & posterior cingulate cortex of the default mode network in impaired versus non-impaired patients. The latter finding of increased default mode network connectivity in impaired patients may reflect a compensatory mechanism that has been previously observed in patients with brain tumors[160] and mild cognitive impairment compared to healthy controls.[161] The slight differences in seed-to-voxel and ROI-to-ROI results may be due to the lost spatial specificity of small clusters when performing ROI-to-ROI analyses. While the present results should be interpreted with caution because of the lack of FWE-/FDR-correction and limited sample size, these findings demonstrate the potential of pseudo-rs-fMRI for FC group analyses using seed-to-voxel and ROI-to-ROI approaches that should be validated in studies with larger sample sizes, which may also resolve the slight differences in seed-to-voxel and ROI-to-ROI results and usage of empiric cluster thresholds. Nevertheless, the multiple logistic regression results utilizing a *combination* of FC measures demonstrate that our DSC-perfusion MRI-derived pseudo-rs-fMRI approach may potentially have clinical utility in developing FC-based models for assessing a patient's cognitive status, and that these models would yield statistically similar results if rs-fMRI was acquired.

This study has some limitations that should be addressed. First, the sample size was limited. It should be recognized that the present study utilized a unique study cohort that had underwent DSC perfusion MRI, rs-fMRI, and cognitive assessment because this cohort would be valuable for a first demonstration of the proposed pseudo-rs-fMRI approach. Future studies with increased sample size and a fully-balanced impaired vs. non-impaired distribution would be beneficial to validate the present study's observations and to longitudinally explore any associations of cognitive impairment with treatment. Additionally, although there are efforts in the standardization of DSC perfusion MRI protocols,[72] there remains much heterogeneity in DSC perfusion MRI protocols across institutions, which may impact the generalizability of our findings. A multi-center assessment of our proposed pseudo-rs-fMRI technique with various DSC perfusion MRI protocols (e.g. sequence parameters, imaging systems, contrast agent amount, pre-load) would be very valuable. Resting-state analyses have also been previously explored utilizing arterial spin labeling (ASL) perfusion MRI,[162] which is an exogenous contrast agent-less perfusion MRI technique with T2*-weighting. However, some advantages of our proposed DSC-derived technique is that DSC perfusion MRI has higher spatial resolution and is more widely used in patients with gliomas than ASL perfusion MRI. Of course, DSC perfusion MRI involves a contrast agent bolus while ASL perfusion does not, similar to rs-fMRI, which is why we performed voxel-wise bolus modeling after leakage-correction to generate pseudo-rs-fMRI data from DSC perfusion MRI to minimize the impact of contrast agent. Nevertheless, future studies may consider exploring other strategies to remove the contrast agent effect on the DSC perfusion MRI signal as well as comparing ASL perfusion MRI-derived and DSC perfusion MRI-derived rs-fMRI FC analyses. Lastly, a future study utilizing both pseudo-rs-fMRI and task-based fMRI may be interesting, as done similarly in a prior study using rs-fMRI and task-based fMRI for assessing language dominance.[123]

Conclusions

Pseudo-rs-fMRI data derived from DSC perfusion MRI can be used to perform typical rs-fMRI FC analyses that may identify cognitive decline in patients with brain tumors while still simultaneously performing perfusion analyses.

Chapter 6. Assessment of Early Volumetric, Perfusion, and Diffusion MRI Changes in Human IDH1-Mutant Gliomas After IDH Inhibitor Therapy

Preface

This chapter is adapted from the following publication:

Cho NS, Hagiwara A, Eldred BSC, Raymond C, Wang C, Sanvito F, Lai A, Nghiemphu P, Salamon N, Steelman L, Hassan I, Cloughesy TF, Ellingson BM. Early volumetric, perfusion, and diffusion MRI changes after mutant isocitrate dehydrogenase (IDH) inhibitor treatment in IDH1-mutant gliomas. *Neurooncol Adv*. 2022 Aug 4;4(1):vdac124. doi: 10.1093/noajnl/vdac124. PMID: 36033919; PMCID: PMC9400453.

Introduction

Novel targeted therapies for IDH-mutant gliomas that circumvent the toxicities associated with chemoradiation may provide significant benefit for a younger patient population in terms of reduced morbidity. Magnetic resonance imaging (MRI) techniques, including dynamic susceptibility contrast (DSC) perfusion MRI and diffusion-weighted imaging (DWI), have been valuable in the management of patients with brain tumors.[163-166] However, early MRI biomarkers of treatment efficacy in IDH-mutant gliomas following IDH inhibition remain largely unknown. This retrospective longitudinal study explored early changes in anatomical, perfusion, and diffusion MRI in patients with IDH-mutant gliomas during treatment with IDH inhibitors as well as potential associations between MRI metrics and progression-free survival (PFS). We hypothesized that perfusion, diffusion, and volumetric MRI metrics can be early biomarkers of treatment response for IDH inhibitors in IDH-mutant gliomas.

Methods

Patient Selection

Patients diagnosed with IDH1-mutant gliomas who received ivosidenib (AG-120) or vorasidenib (AG-881), an inhibitor of the mutant IDH enzyme, daily off-label or as part of a clinical trial (clinicaltrials.gov NCT03343197; NCT02481154; NCT02073994) between September 2014 and May 2021 at our institution were reviewed. Patients with the following inclusion criteria were studied: 1) received treatment with IDH inhibitor; 2) obtained DSC-MRI, DWI, and anatomical MRI scans before treatment; 3) and at ~3–6 weeks and/or ~2–4 months after treatment initiation; 4) remained on treatment throughout scan interval. The most recent MRI study before the start of IDH inhibitor treatment was used as a baseline. Patients were excluded if there was disease progression before a scan date. Patients were excluded from survival analysis if they underwent surgical tumor resection within 6 months after IDH inhibitor start date (including patients in peri-operative trial NCT03343197). PFS was defined as the time between first dose of treatment to disease progression, death, or censor date. Disease progression was assessed by the treating neuro-oncologists according to the Response Assessment in Neuro-Oncology (RANO) and RANO-LGG criteria.[167, 168] *IDH1* mutation was confirmed in all patients by genomic sequencing analysis, immunohistochemistry, and/or polymerase chain reaction,[70] and 1p/19q codeletion status was determined using fluorescence in situ hybridization. Patient data are summarized in **Table 6.1** and **Table 6.2** summarizes treatment history. All patients provided informed consent approved by our institutional review board. All analyses were done in compliance with the Health Insurance Portability and Accountability Act (HIPAA).

Characteristics	All patients (n=29)	Patients Scanned at 3–6 Weeks of Treatment (n=23)	Patients Scanned at 3–6 Weeks of Treatment in Survival Analysis (n=12)	Patients Scanned at 2–4 Months of Treatment (n=14; All in Survival Analysis)
Average Age (Years) ± SD	42 ± 12	43 ± 11	40 ± 10	39 ± 13
Sex (Male/Female)	18/11	16/7	9/3	8/6
Tumor Location:				
Hemisphere (Left/Right)	17/12	13/10	6/6	7/7
Frontal Lobe	19	15	7	9
Temporal Lobe	7	5	4	5
Parietal Lobe	3	3	1	0
Tumor Grade (2/3/4)	19/7/3	14/6/3	4/6/2	9/4/1
Number of Recurrence (New/1st/2nd/3rd+)	2/12/7/8	1/9/5/8	0/2/4/6	1/4/6/3
1p/19q Codeletion Status (Codeleted/Non-Codeleted/N/A)	11/15/3	9/12/2	4/6/2	4/8/2
IDH Inhibitor Drug (AG-120/AG-881)	18/11	15/8	9/3	9/5
Median Progression-Free Survival in Days and Range (Days)	343 (23–1970)	302 (23–1449)	185 (23–580)	320.5 (79–1970)
Median Days Between Pre-Treatment Scan Date and Start	9 (0–49)	11 (0–33)	7 (0–33)	6.5 (0–49)

of IDH Inhibitor Treatment (Days)				
Median Days Between Post-Treatment Scan Date and Treatment Start Date and Range (Days)	N/A	27 (21–42)	31 (23–42)	113 (59–121)

Table 6.1. Clinical Data of Patients.

ID	Sex	Age	IDH Inhibitor	Dosing (Daily)
1	M	62	AG-120	600 mg
2	M	51	AG-120	250 mg for first 2 weeks, then 500 mg
3	F	48	AG-120	500 mg
4	F	65	AG-881	10 mg
5	F	51	AG-120	500 mg
6	M	38	AG-120	500 mg
7	M	47	AG-881	25 mg
8	M	33	AG-120	500 mg
9	F	34	AG-881	300 mg
10	M	48	AG-881	50 mg
11	F	63	AG-120	500 mg
12	M	59	AG-120	500 mg
13	M	43	AG-881	10 mg
14	F	40	AG-881	100 mg for first 3 months, then 200 mg
15	F	50	AG-881	100 mg
16	M	27	AG-120	500 mg
17	M	25	AG-120	500 mg
18	M	33	AG-120	500 mg
19	F	19	AG-881	10 mg
20	F	37	AG-120	500 mg

21	M	25	AG-120	500 mg
22	M	43	AG-881	200 mg
23	M	45	AG-120	500 mg
24	F	39	AG-120	500 mg
25	M	40	AG-881	50 mg
26	M	34	AG-120	500 mg
27	F	52	AG-881	50 mg
28	M	29	AG-120	500 mg
29	M	32	AG-120	500 mg

Table 6.2. Patient IDH Inhibitor Treatment Information.

Image Acquisition and Processing

Anatomical, DWI, and DSC perfusion MRI were obtained on 3T MRI scanners (Skyra or Prisma, Siemens Healthcare; Erlangen, Germany). Anatomical MRI, including 3D pre- and post-contrast (gadolinium-diethylenetriamine pentaacetic acid at a dose of 0.1 mmoL/kg body weight; Magnevist, Bayer Schering Pharma, Leverkusen, Germany) T1-weighted images, axial T2-weighted images, fluid-attenuated inversion recovery (FLAIR), and DWI images were collected according to the international standardized brain tumor imaging protocol (BTIP).[71] For DSC perfusion MRI, images were collected according to previously described imaging protocols.[72, 73] All DSC-MRI acquisitions covered the volume of contrast-enhancing and non-enhancing tumor.

DSC and Image Analysis

All parameter maps were registered to the post-contrast T1-weighted images using a six-degree-of-freedom rigid transformation and a mutual information cost function using FSL software (*flirt*; Functional Magnetic Resonance Imaging of the Brain Software Library; Oxford, England). A volume of interest (VOI) was segmented on the FLAIR hyperintense tumor with guidance from NS-HGlio artificial intelligence device (Neosoma Inc, Groton, MA, https://neosomainc.com) which automatically detects and segments the tumor compartments on MRIs in combination with an in-house, semi-automated thresholding method using the Analysis of Functional NeuroImages (AFNI) software (NIMH Scientific and Statistical Computing Core; Bethesda, MD, USA; https://afni.nimh.nih.gov).[76] DSC data were first motion-corrected using FSL (*mcflirt*, FMRIB library). Relative cerebral blood volume (rCBV) maps were calculated using a previously described bidirectional contrast agent leakage correction method.[74] Then, rCBV was normalized (nrCBV) by the mean of value of 3 spherical, intra-slice VOIs of 5-mm diameter placed in the contralateral normal appearing white matter (NAWM) in the centrum semiovale superior to the lateral ventricles as similarly described in a previous study[60] using ITK-SNAP software (https://www.itksnap.org/).[75] Median nrCBV, median ADC ($\mu m^2/ms$), median nrCBV/ADC ratio (median nrCBV/median ADC),[169] and tumor volume measurements were obtained and used for subsequent analyses.

Statistical Analysis

All calculations and analyses were performed in MATLAB (Release 2020a, MathWorks, Natick, MA) or GraphPad Prism software (Version 8.4 GraphPad Software, San Diego, California). To visualize population-based temporal trends in MRI metrics, local polynomial

regression fitting was performed on MRI metrics using all timepoints as cross-sectional analysis with a cubic function fixed at the origin using the *polyfix* MATLAB package as similarly performed in a previous study.[170] Patients were stratified based on median PFS, and all patients were used for this illustrative analysis regardless if patients were used for formal survival analysis in order to provide sufficient datapoints for curve-fitting. The Shapiro-Wilk test was conducted to assess if data were normally distributed and to apply appropriate parametric or non-parametric statistical methods. For normally distributed data, one-sample t-test analyses were conducted to assess percentage changes in MRI metrics compared to no change. For non-normally distributed data, Wilcoxon Signed-Rank analyses were conducted to assess percentage changes in MRI metrics.

Kaplan-Meier survival curves were generated to assess relationships between post-treatment nrCBV, ADC, median nrCBV/ADC ratio, or FLAIR volume, and changes in nrCBV, ADC, median nrCBV/ADC ratio, or FLAIR volume with PFS using the log-rank test. Optimal thresholds for Kaplan-Meier curves were determined by looping through quantitative values and then calculating the Mantel-Haenszel hazard ratio and corresponding *P* values for patient stratifications resulting in at least 4 patients in a group as described previously.[171] Cox proportional hazards regression analysis was performed on the significant MRI metrics from log-rank analyses to assess if relationships remained significant using continuous measures of MRI metrics and after controlling for clinical variables of age and tumor grade. Significance level was set at $\alpha = 0.05$, and all tests were two-tailed. Multiple comparisons corrections were not performed because of the limited sample size.

Results

Volumetric, Perfusion, and Diffusion Changes

Among 64 patients eligible for this study, a total of 29 patients met the inclusion and exclusion criteria (**Figure 6.1**). A total of 23 patients had data available at 3–6 weeks and 14 patients had data available at 2-4 months after starting treatment. Eight patients had data at both time points. Within the patients having imaging data available 3–6 weeks after starting therapy, 11 patients were excluded for PFS analysis because they underwent craniotomy within 6 months after the start of IDH inhibitor treatment.

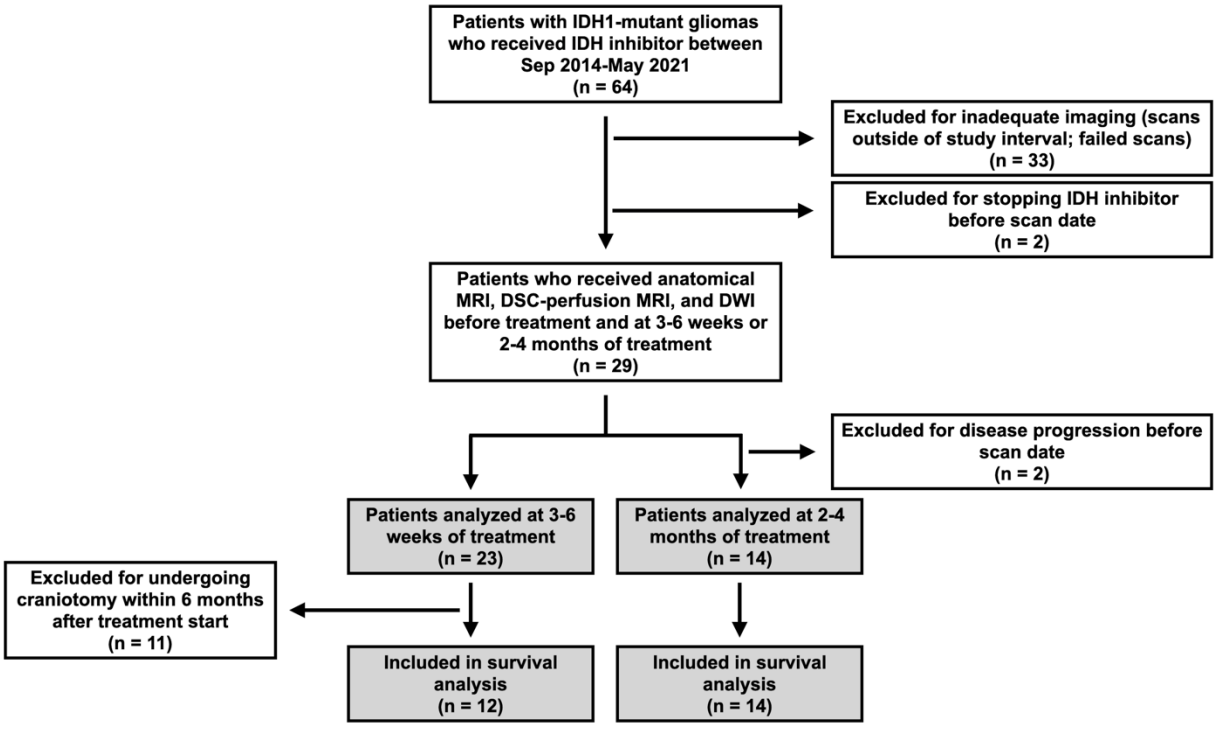

Figure 6.1. Flowchart of Patient Selection Process. IDH = isocitrate dehydrogenase; MRI = magnetic resonance imaging; DSC = dynamic susceptibility contrast; DWI = diffusion-weighted imaging

In order to assess how imaging measurements changed over time between patients exhibiting long vs. short PFS, we pooled cross-sectional nrCBV, ADC, and FLAIR volume measurements in all patients and time points and used polynomial regression to visualize possible trends (**Figure 6.2A-C**). While not significantly different, results show an intuitive early increase in FLAIR volume in the cohort of patients with a short PFS and a relatively flat trajectory in FLAIR volume within the cohort of patients exhibiting longer PFS. Results also suggest a transient increase in nrCBV may be observed shortly after starting treatment, but a sustained increase in nrCBV over time is observed in patients with a shorter PFS. Additionally, patients with a long PFS had relatively stable ADC, whereas a continuous decrease in ADC was seen in patients with shorter PFS. These trends are also illustrated in three representative cases of IDH1-mutant glioma patients with differential responses to IDH inhibition (**Figure 6.2D–H**). The first patient exhibited a large, early increase in nrCBV at the early 3–6 week timepoint after treatment and presented with a PFS of around 197 days (**Figure 6.2F**). Patient 2 demonstrated an increase in nrCBV and a decrease in ADC at the later 2–4 month timepoint and presented with a PFS of around 173 days (**Figure 6.2G**). Meanwhile, patient 3 exhibited a small decrease in nrCBV and a small increase in ADC at the later 2–4 month timepoint and presented with a PFS of around 1121 days (**Figure 6.2H**).

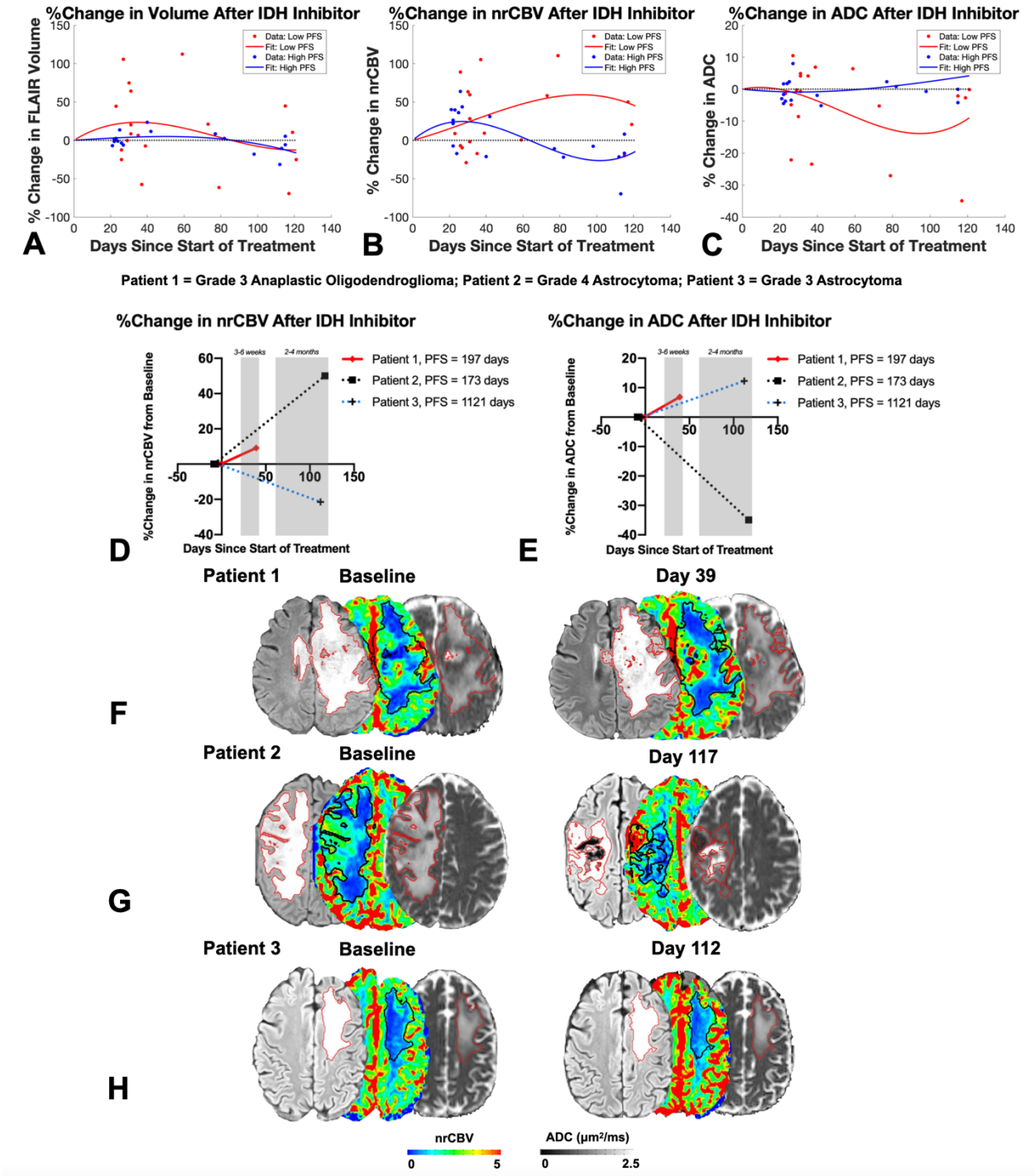

Figure 6.2. Temporal Trends of FLAIR Volume, nrCBV, and ADC Changes following IDH Inhibitor and Three Representative Cases. Local polynomial regression trend lines **(A-C)** depict an early rise in nrCBV following IDH inhibitor across patients followed by increased

nrCBV at later timepoints associated for the low PFS group. ADC differences appear at later timepoints with the low PFS group exhibiting decreased ADC. FLAIR volume also generally increases early in treatment. Patient 1 **(F)** is a grade 3 anaplastic oligodendroglioma with a large increase in nrCBV after day 39 of AG-120 treatment and presented with a PFS of around 197 days. For the 2–4 month timepoint cases, Patient 2 **(G)** is a grade 4 astrocytoma that demonstrated an increase in nrCBV and a decrease in ADC after day 117 of AG-120 treatment and presented with a PFS of around 173 days. Patient 3 **(H)** is a grade 3 astrocytoma who exhibited a small decrease in nrCBV and small increase in ADC after day 112 of AG-120 treatment. Patient 3 had a longer PFS of 1,121 days. IDH = isocitrate dehydrogenase; nrCBV = normalized relative cerebral blood volume; PFS = progression-free survival

Consistent with these visual trends, there was an overall significant increase in nrCBV (**Figure 6.3A-B**; One Sample T-test; $P = 0.004$; mean %change = 24.15% (95% CI: 8.52–39.79%)) and in median nrCBV/ADC ratio (Wilcoxon Signed-Rank test; $P = 0.003$; mean %change = 28.51% (8.84–48.18%)) 3–6 weeks after start of treatment, while there was no change in FLAIR volume (**Figure 6.3C**; Wilcoxon Signed-Rank test; $P = 0.23$; mean %change = 11.05% (-3.70–25.80%)) or ADC (**Figure 6.3D**; Wilcoxon Signed-Rank test; $P = 0.52$; mean %change = -1.77% (-5.28–1.73%)).

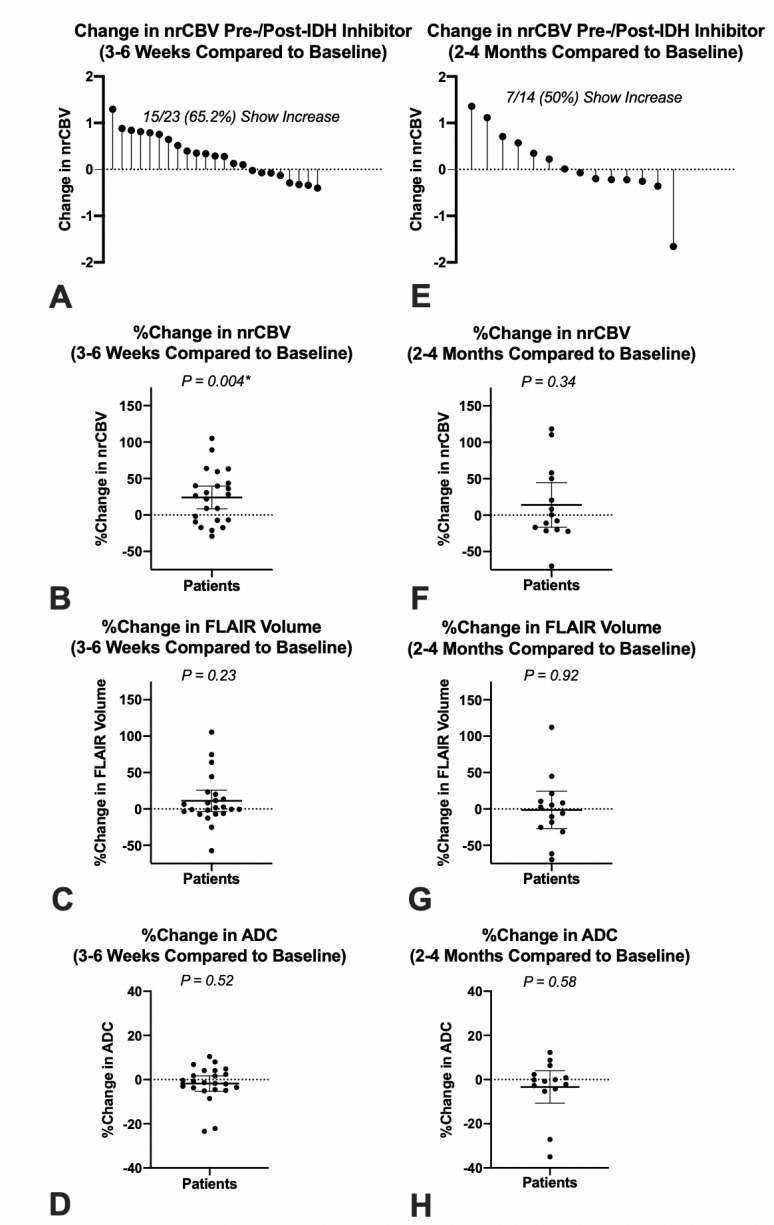

Figure 6.3. Quantitative Comparison of Changes in nrCBV, FLAIR Volume, and ADC after IDH Inhibitor Treatment. After 3–6 weeks of IDH inhibitor treatment, there was **(A, B)** a significant increase in nrCBV ($P = 0.004$) **(C)** and no change in FLAIR volume ($P = 0.23$) **(D)** or ADC ($P = 0.52$). After 2–4 months of IDH inhibitor treatment, **(E, F)** nrCBV, **(G)** FLAIR volume, and **(H)** ADC appeared to stabilize. Asterisks (*) indicate $P < 0.05$. IDH = isocitrate

dehydrogenase; nrCBV = normalized relative cerebral blood volume; ADC = apparent diffusion coefficient

Survival Analysis

A total of 15 of 23 patients (65.2%) exhibited an increase in nrCBV at the early 3–6 weeks time point. however, high post-treatment nrCBV >1.55 only *trended* toward shorter PFS by 3–6 weeks post-treatment (**Figure 6.4A;** Log-Rank test; $P = 0.05$; HR=5.35 (0.98–29.19); median PFS = 240 days vs. 55 days). High post-treatment median nrCBV/ADC ratio >1.20 yielded the same results as post-treatment nrCBV >1.55 with shorter PFS (**Figure 6.5A;** Log-Rank test; $P = 0.05$; HR=5.35 (0.98–29.19); median PFS = 240 days vs. 55 days). Additionally, increase in FLAIR volume >4 cm^3 at 3–6 weeks also trended towards shorter PFS (**Figure 6.4B;** Log-Rank test; $P = 0.06$; HR = 4.82 (0.92–25.30); median PFS = 227 days vs. 29 days), while the percentage change in FLAIR volume did not show a significant association with PFS. Post-treatment ADC, percentage change in ADC, and percentage change in nrCBV were not significantly associated with PFS.

At 2–4 months of treatment, there was no significant change in nrCBV (One Sample T-test; $P = 0.34$; mean %change = 14.08% (-16.49–44.65%)), ADC (Wilcoxon Signed-Rank test; $P = 0.58$; mean %change = -3.34 (-10.73–4.06%)), median nrCBV/ADC ratio (Wilcoxon Signed-Rank test; $P = 0.63$; mean %change = 25.42% (-17.05–67.88%)), or FLAIR volume (One-Sample T-test; $P = 0.92$; mean %change = 1.27% (-27.06–24.52%)) relative to baseline measurements (**Figure 6.3E–H**). At this timepoint, post-treatment nrCBV >1.80 (**Figure 6.4C;** Log-Rank test; $P = 0.01$; HR = 7.17 (1.60–32.14); median PFS = 1121 days vs. 270 days), increase in nrCBV >0% compared to baseline (**Figure 6.4D;** Log-Rank test; $P = 0.002$; HR = 9.91 (2.26–43.40); median PFS = 1121 days vs. 257 days), post-treatment ADC <1.15 $\mu m^2/ms$ (**Figure 6.4E;** Log-Rank test;

P = 0.02; HR = 9.23 (1.47-58.12); median PFS = 421 days vs. 215 days), change in ADC <-2% compared to baseline (**Figure 6.5B;** Log-Rank test; *P* = 0.01; HR = 7.32 (1.63–32.94); median PFS = 1121 days vs. 228 days), increased FLAIR volume >4cm^3 (**Figure 6.4F;** Log-Rank test; *P* = 0.03; HR = 7.62 (1.27–45.74); median PFS = 421 vs. 226.5 days), post-treatment median nrCBV/ADC ratio >1.50 (**Figure 6.4G;** Log-Rank test; *P* = 0.002; HR = 9.91 (2.26–43.40); median PFS = 1121 days vs. 257 days; same results as increase in nrCBV >0%), and increase in median nrCBV/ADC ratio >0% compared to baseline (**Figure 6.4H;** Log-Rank test; *P* = 0.02; HR = 6.22 (1.41–27.44); median PFS = 1121 vs. 270 days) were significantly associated with shorter PFS.

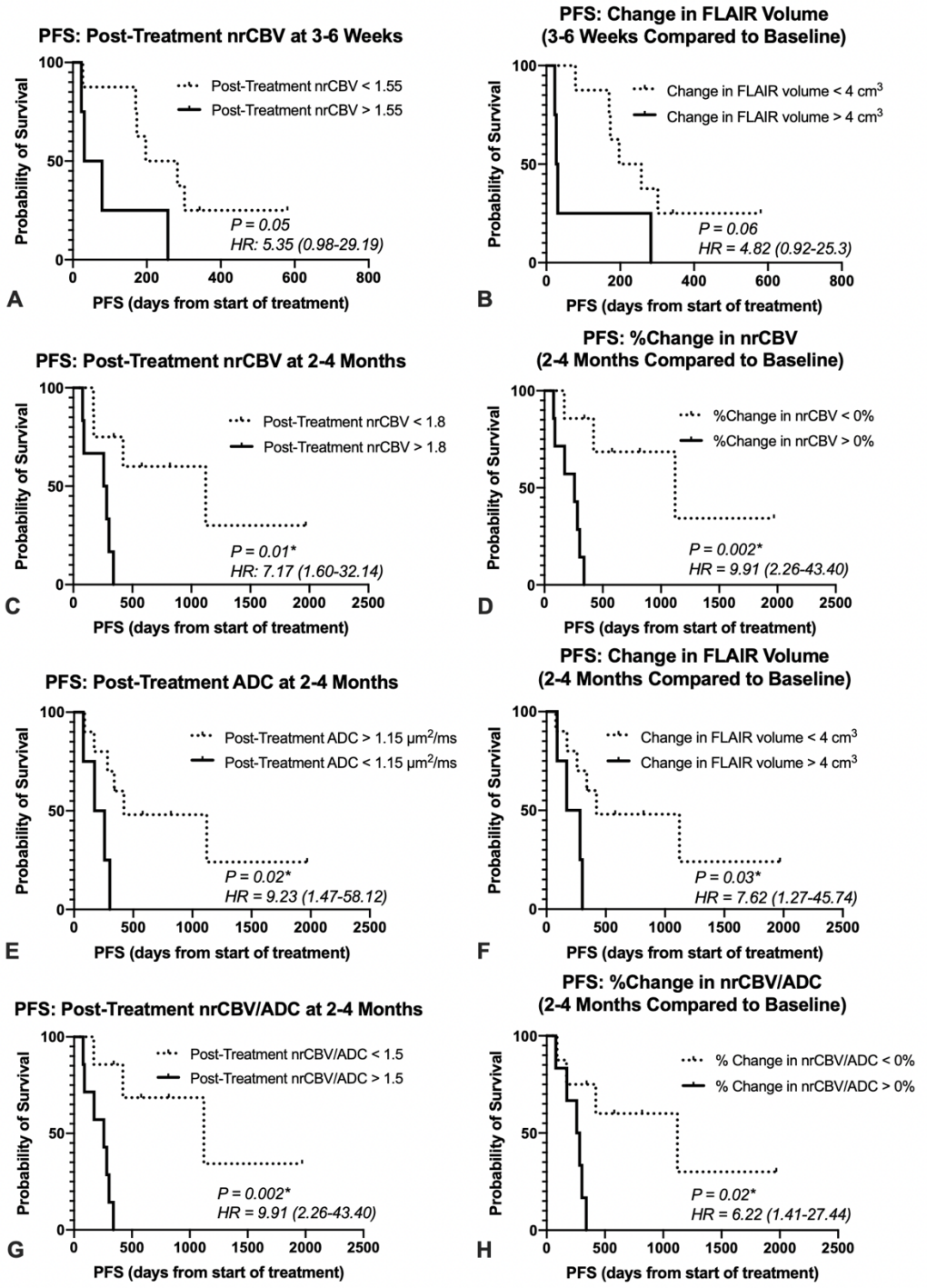

Figure 6.4. Survival Curves Displaying Relationships between nrCBV, ADC, FLAIR Volume, and PFS. (A) Relationship between PFS and nrCBV values at 3–6 weeks of treatment ($P = 0.05$). **(B)** Relationship between PFS and change in FLAIR volume at 3–6 weeks of

treatment compared to baseline ($P = 0.06$). **(C)** Relationship between PFS and nrCBV values at 2–4 months of treatment ($P = 0.01$). **(D)** Relationship between PFS and % change in nrCBV values at 2–4 months of treatment compared to baseline ($P = 0.002$). **(E)** Relationship between PFS and post-treatment ADC values at 2–4 months of treatment ($P = 0.02$). **(F)** Relationship between PFS and change in FLAIR volume at 2–4 months compared to baseline ($P = 0.03$). **(G)** Relationship between PFS and median nrCBV/ADC ratios at 2–4 months of treatment ($P = 0.002$). **(H)** Relationship between PFS and % change in median nrCBV/ADC ratios at 2–4 months of treatment compared to baseline ($P = 0.02$). Asterisks (*) indicate $P < 0.05$. PFS = progression-free survival; nrCBV = normalized relative cerebral blood volume; ADC = apparent diffusion coefficient

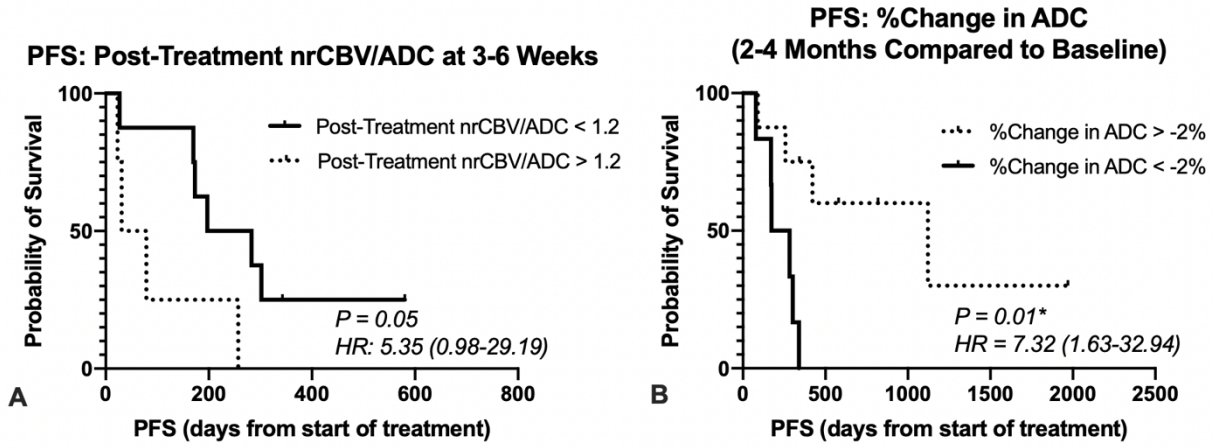

Figure 6.5. Additional Survival Curves Displaying Imaging Relationships with PFS. (A) Relationship between PFS and median nrCBV/ADC ratios at 3–6 weeks ($P = 0.05$). **(B)** Relationship between PFS and percentage change in ADC at 2–4 months ($P = 0.01$). Asterisks (*) indicate $P < 0.05$. PFS = progression-free survival; nrCBV = normalized relative cerebral blood volume; ADC = apparent diffusion coefficient

Univariate Cox regression analysis for PFS was significant when considering continuous measures of percentage change in nrCBV ($P = 0.02$), percentage change in ADC ($P = 0.04$), post-treatment median nrCBV/ADC ratio ($P = 0.04$), and percentage change in median nrCBV/ADC ratio ($P = 0.01$) at 2-4 months from initiation of IDH inhibitor treatment while post-treatment nrCBV ($P = 0.09$) and post-treatment ADC ($P = 0.06$) *trended* towards significance (**Table 6.3)**. After accounting for patient age and tumor grade, percentage change in nrCBV (**Table 6.3;** Multivariate Cox regression; $P = 0.03$), post-treatment median nrCBV/ADC ratio ($P = 0.03$), and percentage change in median nrCBV/ADC ratio ($P = 0.03$) remained significant.

MRI Metrics	PFS (Univariate)			PFS (Multivariate)		
2–4 Months:	**HR**	**Z-Value**	**P-Value**	**HR**	**Z-Value**	**P-Value**
Post-Treatment nrCBV	2.20 (0.89–5.45)	1.71	0.09	N/A		
%Change in nrCBV	1.02 (1.00–1.03)	2.34	0.02*	1.02 (1.00–1.04)	2.18	0.03*
Post-Treatment ADC	0.99 (0.99–1.00)	-1.89	0.06	N/A		
%Change in ADC	0.95 (0.90–0.998)	-2.04	0.04*	0.96 (0.91–1.01)	-1.64	0.10
Post-Treatment Median nrCBV/ADC Ratio	3.26 (1.05–21.95)	2.04	0.04*	3.77 (1.17–12.14)	2.22	0.03*
%Change in Median nrCBV/ADC Ratio	1.02 (1.00–1.03)	2.57	0.01*	1.02 (1.00–1.03)	2.17	0.03*
Change in FLAIR volume	0.99 (0.97–1.01)	-1.25	0.21	N/A		

Asterisks (*) indicate $P < 0.05$.

Table 6.3. Univariate and Multivariate Cox Regression Results for Progression-Free Survival.

Discussion

Results from the current study provide the first evidence that early, transient changes in tumor vascularity may occur following IDH inhibition in human IDH1-mutant gliomas. Results suggest a large proportion (~65%) of patients exhibit early increases in nrCBV within 3–6 weeks following treatment initiation, but by 2–4 months from treatment initiation far fewer and less substantial changes in nrCBV compared to baseline occur. While early, elevated post-treatment nrCBV *trended* toward shorter PFS by 3–6 weeks after the start of treatment, changes in nrCBV and median nrCBV/ADC ratio at 2–4 months after treatment were strong predictors of long-term PFS. Additionally, increases in FLAIR volume greater than 4 cm^3 at 3–6 weeks and 2–4 months from start of treatment were associated with shorter PFS. Finally, decreases in ADC and low ADC at 2–4 months from start of treatment were suggestive of lower PFS.

The biological mechanisms underpinning these transient and impactful changes in vascularity and tumor size are not well understood. It is possible that the initial increase in tumor volume and nrCBV at 3–6 weeks may reflect competing effects of continued tumor growth and therapeutic response early in the treatment course. To our knowledge, this study is the first to assess MRI changes following IDH inhibition as early as 3-6 weeks following initial treatment, so previous clinical studies describing tumor shrinkage in glioma patients[24, 25] may not have taken into consideration these early, transient changes. Nevertheless, patients on average exhibited at least a small increase in tumor volume at 3–6 weeks, which was associated with more favorable response compared with patients exhibiting more substantial increases over the same period, supporting the idea of a potential mixed response early after treatment.

Additionally, the early increase in nrCBV may reflect transiently increased vascularity or vascular volume. While it is possible that this early rise in nrCBV in the present study may also be

from continued tumor growth, we speculate that this observation may reflect downstream alterations caused by decreased D-2-HG levels, which could have led to elevated HIF-1α levels and promote increased hypoxic and subsequent proangiogenic signaling.[20, 21, 172] Importantly, this early rise in nrCBV and tumor volume were no longer observed after 2–4 months of treatment, and there was a PFS benefit in patients who exhibited less elevated nrCBV values or <0% change in nrCBV at this later timepoint. Although speculative, the apparent stabilization of nrCBV after 2–4 months of treatment in patients who had a longer PFS may reflect a useful timepoint to assess IDH inhibition using perfusion MRI.

It is also important to note that no significant changes in ADC were observed at either post-treatment timepoint compared to baseline but decreases in ADC at 2-4 months were associated with poorer PFS. As ADC is thought to be inversely proportional to tumor cell density,[173] this finding is consistent with the work presented by Molloy *et al*. where they observed no change in the cell density in genetically engineered IDH1-mutated cell lines after IDH inhibition, suggestive of no alteration in cell death or proliferation rate.[22] In patients with AML, IDH inhibitors act as cellular differentiation agents, not as cytotoxic agents.[174] Mutant IDH inhibition in glioma cells has also been demonstrated to promote differentiation.[23] The lack of observed changes in ADC in the current study appears to support the hypothesis that IDH inhibition may not have a strong cytotoxic effect in gliomas, and that the therapeutic effect of this treatment may be the result of glioma cell differentiation. Meanwhile, the decrease in ADC being associated with reduced PFS at the later 2–4 month timepoint is likely a reflection of continued tumor progression and treatment resistance. Furthermore, the ratio of median nrCBV/ADC was the only metric at 2–4 months of treatment where both post-treatment values and percentage change remained significant after accounting for tumor grade and age. Previous studies have concurrently examined perfusion and

diffusion characteristics of gliomas,[69] including median nrCBV/ADC ratios.[169] The present findings suggest that combined perfusion and diffusion metrics may be valuable in evaluating IDH inhibition given the individual associations of high nrCBV and low ADC with reduced PFS. While largely speculative, future studies aimed at more thoroughly documenting longitudinal changes in anatomic, physiologic, and metabolic MR imaging are warranted to better understand the temporal changes that occur after IDH inhibition in human IDH1-mutant gliomas.

There are several limitations in this study that should be addressed. First, the sample size in the current study was relatively small and derived from a single center consisting of a relatively heterogenous sample of patients. Because of the indolent nature of IDH-mutant gliomas, clinical trials of IDH inhibitors in patients with IDH-mutant gliomas have also included patients with recurrent gliomas who received prior therapies.[24, 25] Furthermore, the small study cohort involved patients with various tumor grades and 1p/19q codeletion status. While multivariate Cox regression analysis yielded significant results while controlling for tumor grade, 1p/19q codeletion status was unable to be included as a covariate because 1p/19q codeletion status was unavailable for some patients and dichotomization of our patient population based on 1p/19q status would have further reduced our limited sample size. It is possible that 1p/19q codeletion status may be a confound in the present findings that warrants further investigation. Increasing the sample size would also be valuable to perform multiple comparisons corrections on the present study's findings. Moreover, given the retrospective nature of this study and off-label use of IDH inhibitor in some patients, it was not possible to control for the time interval between scans and the usage of other concurrent treatments. Importantly, one patient received concurrent bevacizumab during IDH inhibitor treatment, but it is likely this did not confound our results because they exhibited a rise in nrCBV during the course of this study, even though anti-angiogenic therapy response should

cause a notable decrease in tumor volume and nrCBV.[165] Additionally, overall survival was unable to be tested given the relatively long overall survival of patients with IDH1-mutant gliomas and the only recent usage of IDH inhibitors in patients, which would result in a significant number of censored patients in the present study cohort. Finally, it is important to note that the associations of perfusion, diffusion, and volumetric MRI metrics with PFS in this limited patient cohort are not reflective of any potential benefit of IDH inhibitor therapy (see commentary on survival by tumor response by Anderson & Gelber[175]) in IDH1-mutant gliomas, but simply reflect patient stratifications based on radiographic assessment within patients treated with IDH inhibitors. As a result, future studies with a larger study cohort that can further assess the associations of age, tumor grade, 1p/19q co-deletion status, glioma recurrence status, contrast enhancement, prior treatments, and overall survival would be valuable to better understand the findings of this present study and, more broadly, add to the present study's findings on interpreting the radiographic response to IDH inhibitors in patients with IDH1-mutant gliomas.

Conclusions

The current pilot study demonstrated a transient increase in perfusion that appears to stabilize after 2–4 months, at which changes in perfusion and ADC relative to baseline were strongly associated with resulting PFS. Results suggest that FLAIR volume, nrCBV, and ADC measurements may be useful early imaging biomarkers for assessing IDH inhibitor treatment response in human IDH1-mutant gliomas.

Chapter 7. Structural, Diffusion, Perfusion, and Pseudo-Resting-State Functional MRI Biomarkers for Assessing Malignant Transformation in Molecular Subtypes of IDH-Mutant Gliomas

Introduction

Although isocitrate dehydrogenase (IDH)-mutant gliomas often initially present as relatively indolent, low-grade (WHO grade 2) gliomas, all grade 2 gliomas are expected to eventually undergo malignant transformation (MT) into higher-grade (grade 3-4) gliomas. After MT, these higher-grade gliomas are more aggressive, require urgent treatment, and have significantly worse prognosis.[176] Instead of resampling the tumor tissue to confirm the WHO grade, MT is often defined clinically and non-invasively by the emergence of contrast-enhancement in post-contrast T1-weighted MRI,[40] which typically reflects the most active tumor region. However, multiple studies have shown that contrast-enhancement can be present in low-grade gliomas and conversely, some higher-grade gliomas can be non-enhancing.[177, 178] As a result, there is a need for contemporary imaging biomarker studies on detecting MT using histologically-confirmed MT as ground truth and not just the emergence of contrast-enhancement.

Prior imaging studies have observed that apparent diffusion coefficient (ADC) values from diffusion MRI and normalized relative cerebral blood volume (nrCBV) from DSC perfusion MRI may be helpful in identifying MT.[179, 180] However, glioma classifications have changed in recent years; gliomas are currently precisely classified using molecularly-defined glioma subtypes based on IDH and 1p/19q-codeletion status.[3] Prior studies on imaging biomarkers of low-grade glioma

MT were performed when the field was based on histologically-defined glioma subtypes,[40, 180] which consequently grouped gliomas of different molecular characteristics with different prognoses and tumor biology (e.g. grouping together IDH-wild-type and IDH-mutant astrocytomas as "astrocytomas"). As a result, there is also an urgent need to study MT in IDH-mutant gliomas using molecularly-defined IDH-mutant 1p/19q-intact astrocytomas and IDH-mutant 1p/19q-codeleted oligodendrogliomas, and assessing MT in these tumor entities separately.

The present study explored volumetric, shape, diffusion, and perfusion MRI characteristics to study histologically-confirmed MT in IDH-mutant gliomas using contemporary molecular-based definitions of adult diffuse gliomas. As exploratory analyses, we also performed bimodal ADC histogram analyses, previously used mostly in the context of IDH-wild-type glioblastoma,[163, 171] as well as blood oxygenation level-dependent (BOLD) asynchrony analyses, a resting-state functional MRI-derived metric of tumor burden based altered vascular properties,[154] using our DSC perfusion MRI-derived pseudo-resting-state functional MRI (pseudo-rs-fMRI) approach described in **Chapter 5**. We hypothesized that contrast-enhancement would be present more often in gliomas with MT than non-MT. We also hypothesized that gliomas with MT would be associated with larger tumor volumes, lower sphericity, lower ADC, higher nrCBV, and higher BOLD asynchrony compared to gliomas with non-MT. We also hypothesized that different imaging biomarkers may be useful for identifying MT in IDHm-A and IDHm-O given their different tumor genetics.

Methods

Patient Cohort

This retrospective study was performed in compliance with the Health Insurance Portability and Accountability Act and was approved by the UCLA Institutional Review Board. All patients provided written informed consent. All tumors were grouped based on the molecular subtypes of the 2021 World Health Organization Classification of Central Nervous System Tumors,[3] and tumor grading was based on the criteria of the 2016 criteria. A total of n=64 patients were studied with the following inclusion criteria: (1) initial biopsy/surgery to confirm initial grade 2 IDH-mutant glioma presentation, (2) underwent another biopsy/surgery in the future with tumor grading, (3) 1p/19q codeletion status obtained, and (4) available T1-weighted pre-contrast, T1-weighted post-contrast, T2-weighted, and T2-weighted FLAIR MRI within 1 month prior of repeat biopsy/surgery (**Table 7.1**). Of these n=64 patients, n=37 patients were diagnosed with IDHm-A and n=27 patients were diagnosed with IDHm-O. Patients were categorized as having "malignant transformation" ("MT") if the tumor grade increased to grade 3 or 4 at the future surgery or "non-malignant transformation" ("non-MT") if the tumor grade diagnosis remained at grade 2.

	IDH-Mutant Astrocytoma (1p/19q-intact)	**IDH-Mutant Oligodendroglioma (1p/19q-codeleted)**
Characteristic	**Patients (n=37 total)**	**Patients (n=27 total)**
Average Age & Range (Years)	38 (24–63)	46 (25–72)
Sex (Male/Female)	23/14	16/11
Malignant Transformation / Non-Malignant Transformation	22/15	13/14

Table 7.1. Clinical Data of Patients.

Image Acquisition and Pre-Processing

The MRI scans were obtained from a variety of field strengths, vendors, scanners, and imaging protocols. DWI (n=61) and DSC perfusion MRI (n=53) was also available for most patients. ADC maps were generated using DWI. Normalized rCBV (nrCBV) maps were generated using the bi-directional, leakage-corrected perfusion MRI signal[74, 147] and then normalizing using an automated method of dividing by the median brain rCBV value as done in a prior study.[181] All

images were co-registered to the post-contrast T1-weighted MRI scan using linear registration (*tkregister2* (Freesurfer) and *flirt* (FSL), https://surfer.nmr.mgh.harvard.edu/fswiki/TkRegister, https://fsl.fmrib.ox.ac.uk/fsl/fslwiki/FLIRT). Pseudo-rs-fMRI data were obtained from DSC perfusion MRI with sufficient duration of 90–120 volumes using the method described in **Chapter 5.** In brief, voxel-wise Gamma-variate modeling was performed on the bi-directional leakage-corrected perfusion signal and then subtracted to generate pseudo-resting-state functional MRI data. Pseudo-rs-fMRI data were registered to Montreal Neurological Institute (MNI) standardized atlas space and pre-processed as described in **Chapter 5.** After visual inspection of usable processed pseudo-rs-fMRI data, the final cohort for pseudo-rs-fMRI analyses was n=23.

Tumor Imaging Analysis

Tumor segmentations of the total T2/FLAIR hyperintense tumor excluding necrotic regions were generated using the deep learning software, NS-HGlio artificial intelligence device (Neosoma Inc, Groton, MA, https://neosomainc.com). All tumor segmentations were inspected by a radiologist with 16 years of experience (M.N.), and any segmentation errors were corrected using a previously-described semi-automated method using Analysis of Functional NeuroImages (AFNI, https://afni.nimh.nih.gov/) software.[32] Tumors were considered "contrast-enhancing" if the contrast-enhancing tumor volume was >1000mm^3, analogous to the definition of measurable disease (10mm x 10mm x 10mm) in current Response Assessment in Neuro-Oncology 2.0 criteria[182] and "non-enhancing" if otherwise. Tumor volume, ADC, nrCBV, and morphologic sphericity values (*Pyradiomics,* https://www.radiomics.io/pyradiomics.html) were obtained for each patient. Histogram-derived ADC-L values were calculated by fitting a double-Gaussian curve within the tumor ADC values and obtaining the peak of the lower-end curve ("ADC-Low

Peak").[163, 171] Bimodality coefficients were also obtained for each ADC histogram (MATLAB, https://www.mathworks.com/matlabcentral/fileexchange/84933-bimodality-coefficient-calculation-with-matlab).

BOLD asynchrony maps were generated using the method described in Petridis *et al.*[154] for patients with usable pseudo-rs-fMRI data. In brief, tumor segmentations were registered to MNI analyses, and BOLD asynchrony maps were generated by seeding the tumor region of the pre-processed pseudo-rs-fMRI without bandpass filtering to create a "tumor connectivity" z-score connectivity map, and then subtracting the "tumor connectivity" map by the connectivity map when seeding the contralesional hemisphere to create the BOLD asynchrony map. Tumor median BOLD asynchrony values were obtained.

Statistical Analysis

All statistical analyses were performed using GraphPad Prism Software. All analyses were performed separately within IDHm-A and IDHm-O. Fisher's exact tests were performed to assess any relationships between the frequencies of contrast-enhancing and non-enhancing tumors between MT and non-MT categories. For group analyses, the D'Agostino & Pearson test was performed to assess the normality of the data, and parametric t-tests or non-parametric Mann-Whitney tests were performed to assess tumor volume, ADC, bimodality coefficient, rCBV, BOLD asynchrony, and sphericity differences between MT vs. non-MT gliomas. Two-way ANOVA testing was performed to assess any interactions between variables. Correlations were assessed using parametric Pearson's or non-parametric Spearman's correlations depending on the normality of the data. Significance level was set to $P<0.05$. All bar graphs display the mean and 95% confidence interval.

Results

Contrast-Enhancement and Whole Tumor Volume

Two representative cases that underwent histologically-confirmed MT despite being non-enhancing are shown in **Figure 7.1A/B.** Patient A is a 48-year-old male patient diagnosed with a grade 4 IDHm-A, and Patient B is a 39-year-old male patient diagnosed with a grade 3 IDHm-O. When enumerating the number of contrast-enhancing & non-enhancing tumors between MT and non-MT gliomas, there was a significantly higher proportion of contrast-enhancing cases in the MT group for both IDHm-A (P=0.04, **Figure 7.1C, Table 7.2**) and IDHm-O (P=0.02, **Figure 7.1D, Table 7.2**). When assessing only gliomas with MT, 41% of IDHm-A with MT and 62% of IDHm-O with MT were non-enhancing (**Table 7.2**). When assessing only gliomas with contrast-enhancement, 81% of the contrast-enhancing IDHm-A were MT and 100% of the contrast-enhancing IDHm-O were MT (**Table 7.2**). Tumor volumes were also significantly larger in the MT group vs. non-MT group for both IDHm-A (P=0.02, mean (95% CI) MT vs. Non-MT: 75,916 mm^3 (47,387–104,446 mm^3) vs. 35,031 mm^3 (12,498–57,564 mm^3), **Figure 7.1E**) and IDHm-O (P=0.04, mean (95% CI) MT vs. Non-MT: 68,728 mm^3 (37,677–99,779 mm^3) vs. 36,844 mm^3 (21,963–51,725 mm^3), **Figure 7.1F**).

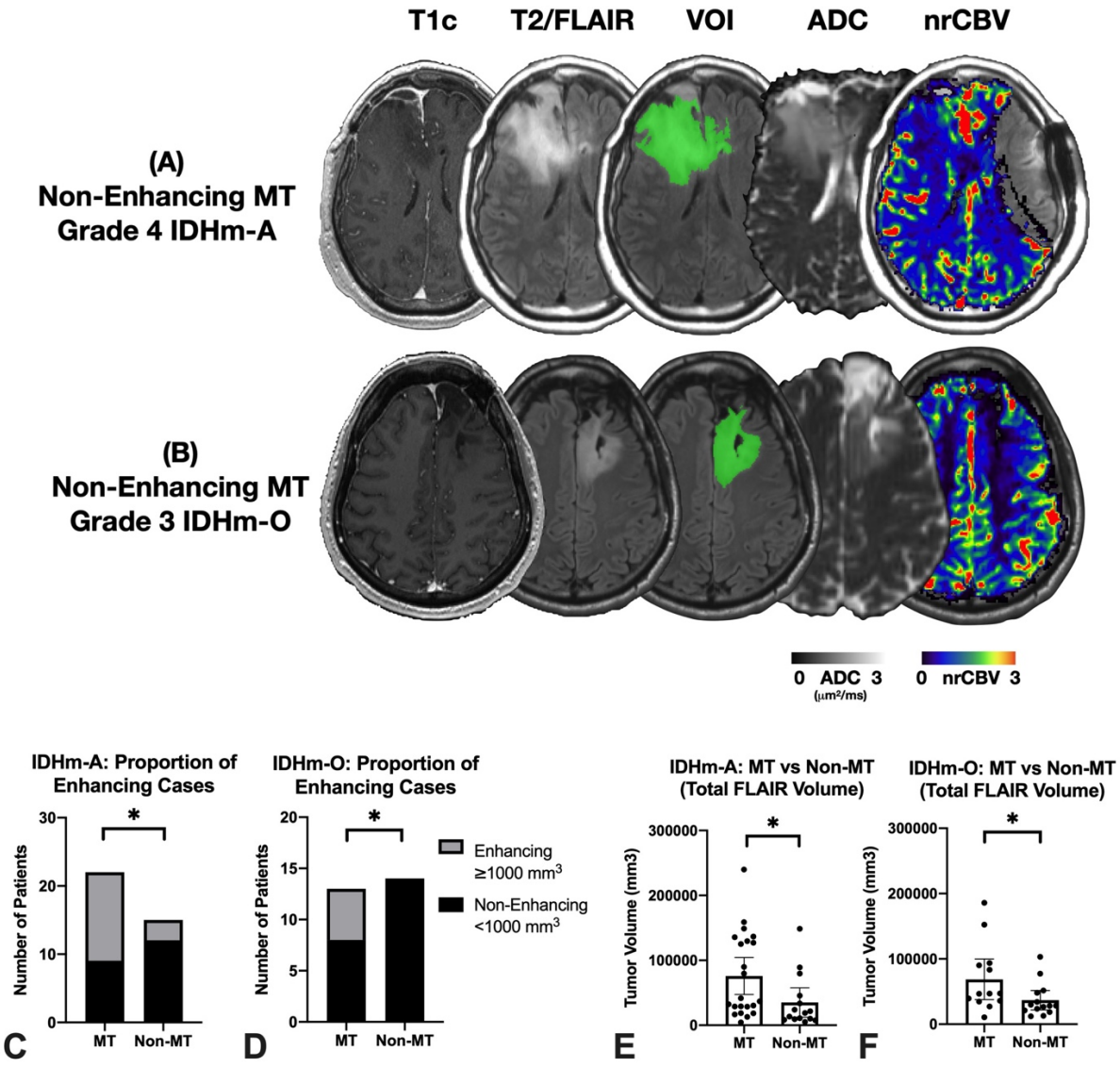

Figure 7.1. Representative Cases and Differences in Proportion of Enhancing Cases & Tumor Volume in Malignant Transformation. (**A**) Patient A is a 48-year-old male patient diagnosed with a non-enhancing grade 4 IDH-mutant astrocytoma (IDHm-A). (**B**) Patient B is a 39-year-old male patient diagnosed with a non-enhancing grade 3 IDH-mutant oligodendroglioma (IDHm-O). (**C/D**) There was a significant larger proportion of contrast-enhancing cases in the MT vs. non-MT group for both IDHm-A ($P<0.05$) and IDHm-O ($P<0.05$), but there was also a considerable number of non-enhancing cases in the MT groups. (**E/F**) Tumor

volumes were significantly larger in the MT vs. non-MT group for both IDHm-A (P<0.05) and IDHm-O (P<0.05).

IDH-Mutant Astrocytoma		
Characteristic	**Non-Enhancing** **(N, % row total, % column total)**	**Enhancing (>1000mm^3)** **(N, % row total, % column total)**
MT	9 (41%, 43%)	13 (59%, 81%)
Non-MT	12 (80%, 57%)	3 (20%, 19%)
IDH-Mutant Oligodendroglioma		
Characteristic	**Non-Enhancing** **(N, % row total, % column total)**	**Enhancing (>1000mm^3)** **(N, % row total, % column total)**
MT	8 (62%, 36%)	5 (38%, 100%)
Non-MT	14 (100%, 64%)	0 (0%, 0%)

Table 7.2 Proportion of Enhancing and Non-Enhancing Cases in Malignant Transformation. MT = malignant transformation

Diffusion, Perfusion, Shape, and BOLD Asynchrony Characteristics

Group differences using ADC, nrCBV, and sphericity were observed when assessing MT vs. non-MT *only* for IDHm-A but not IDHm-O. Specifically, while median ADC trended towards significance and lower in MT vs. non-MT IDHm-A (P=0.06, mean (95% CI) MT vs. non-MT: 1.267 (1.185–1.348) μm^2/ms vs. 1.363 (1.314–1.412) μm^2/ms, **Figure 7.2A**), 10^{th} percentile ADC was significantly lower in MT vs. non-MT IDHm-A (P=0.03, 0.9061 (0.8602–0.9519) μm^2/ms vs. 0.9708 (0.9400–1.002) μm^2/ms, **Figure 7.2B**). Median nrCBV was also higher in MT vs. non-MT IDHm-A (P=0.002, 0.7859 (0.6267–0.9451) vs. 0.5240 (0.4658–0.5822), **Figure 7.2C**). Lastly, while whole T2/FLAIR tumor sphericity was not significantly different between MT vs. non-MT IDHm-A (P>0.05), the sphericity of specifically non-enhancing tumor was significantly lower between MT vs. non-MT IDHm-A (P=0.03, 0.3708 (0.3411–0.4004) vs. 0.4336 (0.3742–0.4929), **Figure 7.2D**). Neither whole T2/FLAIR tumor median ADC, 10^{th} percentile ADC, median nrCBV, nor non-enhancing tumor sphericity were significantly different between MT vs. non-MT IDHm-O (P>0.05, **Figure 7.2E–H**).

In exploratory analyses, bimodal ADC histogram analyses using ADC-L or bimodality coefficients did not significantly differ between MT vs. non-MT for either IDHm-A or IDHm-O (P>0.05). However, correlations between ADC-L and bimodality coefficients were significantly negatively correlated only in MT IDHm-A (P=0.003, R=-0.64, **Figure 7.3A**) and MT IDHm-O (P=0.02, R=-0.63, **Figure 7.3B**), and there was no significant correlation for the non-MT groups (IDHm-A: P=0.72, R=0.11, **Figure 7.3C** | IDHm-O: P=0.69, R=0.12, **Figure 7.3D**).

Lastly, two representative cases of BOLD asynchrony maps are shown in **Figure 7.4A/B**. Patient **A** is a 48-year-old female patient diagnosed with IDHm-A that underwent MT into grade 4. Patient **B** is a 42-year-old male patient diagnosed with IDHm-O that underwent MT into grade

3. Both patients demonstrated BOLD asynchrony intratumoral heterogeneity with visual hotspots. When assessing group differences between MT vs. non-MT cohorts, there were non-significant visual trends of increased BOLD asynchrony in IDHm-A MT vs. non-MT (*P*=0.33, **C**) and decreased BOLD asynchrony in IDHm-O MT vs. non-MT patient groups (*P*=0.06, **D**). These differing trends in BOLD asynchrony were significant for an interaction term between tumor subtype and transformation status (*P*=0.04).

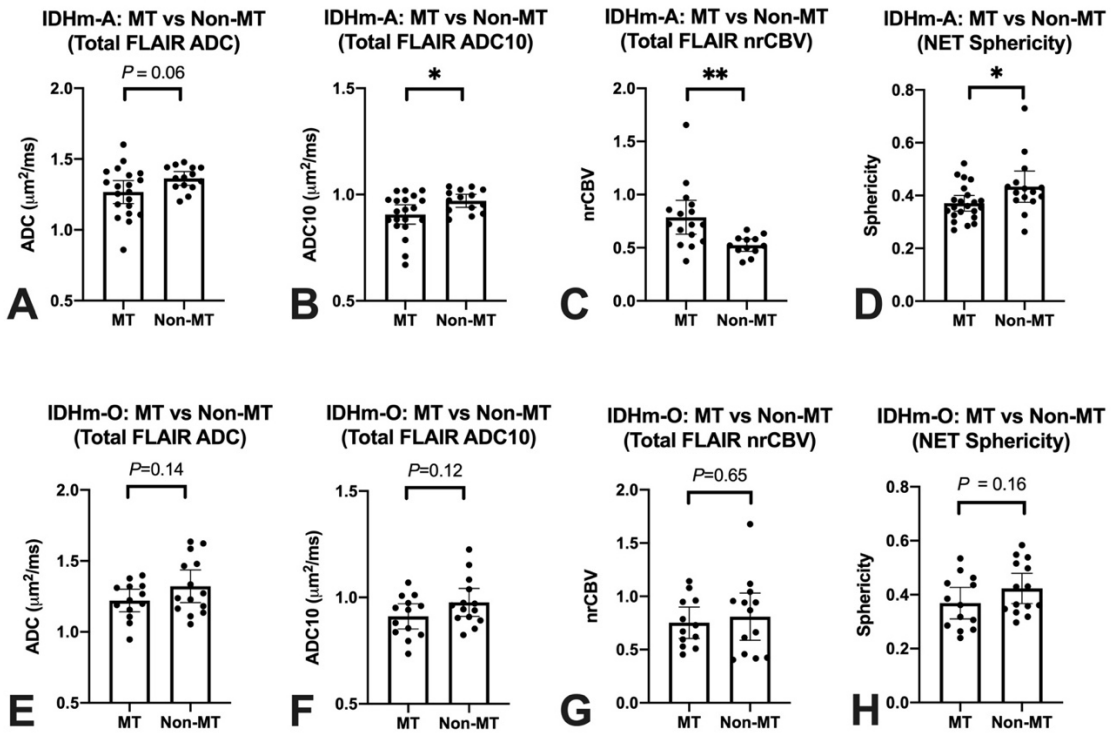

Figure 7.2. Diffusion, Perfusion, and Sphericity Differences in Malignant Transformation. Within IDHm-A only, there was trending lower median apparent diffusion coefficient (ADC), significantly lower 10th percentile ADC, and significantly higher normalized relative cerebral blood volume (nrCBV) of the whole T2/FLAIR hyperintense tumor as well as significantly lower non-enhancing tumor (NET) sphericity in the malignant transformation (MT) group compared to the non-MT group. None of these imaging biomarkers were significantly different between MT vs. non-MT IDHm-O.

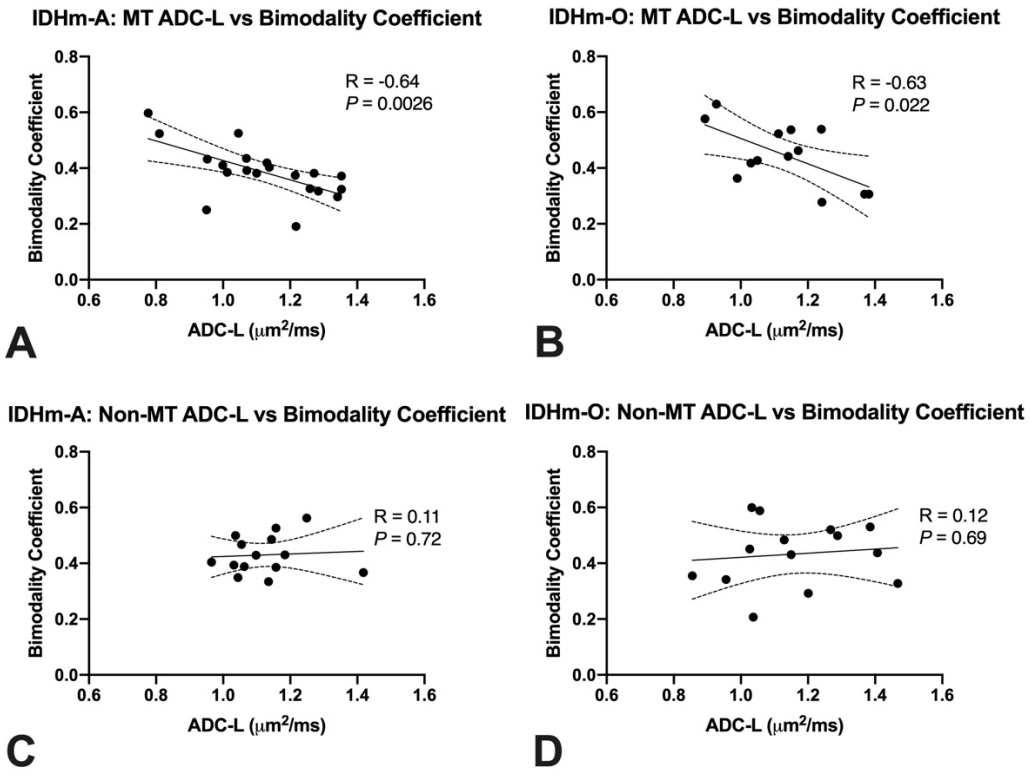

Figure 7.3. Diffusion Histogram-Based ADC-L and Bimodality Coefficient Correlations.

ADC-L and bimodality coefficients were significantly negatively correlated only within MT IDH-mutant astrocytomas (**A**, *P*=0.003) and IDH-mutant oligodendrogliomas (**B**, *P*=0.02). There was no significant correlation within their non-MT counterparts (**C**/**D**).

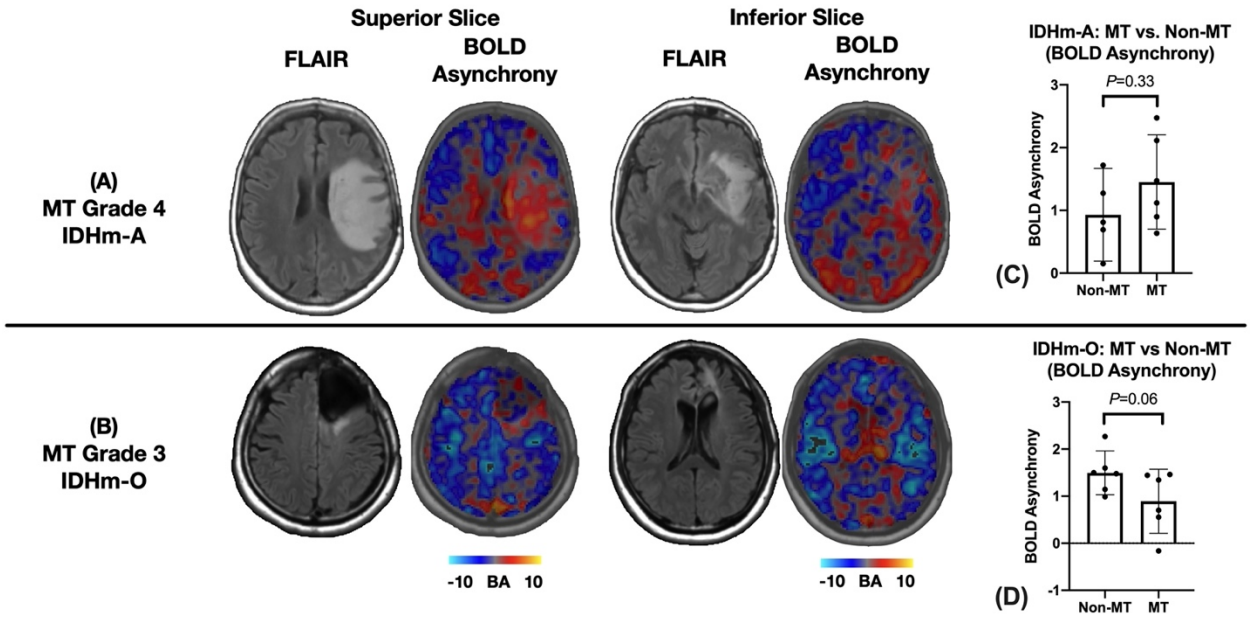

Figure 7.4. Representative Cases and Group Differences of BOLD Asynchrony. Patient **A** is a 48-year-old female patient diagnosed with grade 4 IDH-mutant astrocytoma (IDHm-A). Patient **B** is a 42-year-old male patient diagnosed with grade 3 IDH-mutant oligodendroglioma (IDHm-O). Both representative cases (**A/B**) demonstrated intratumor heterogeneity, including hotspots, of BOLD asynchrony maps derived from pseudo-resting-state functional MRI data. There were non-significant visual trends in BOLD asynchrony differences between malignant transformation (MT) and non-malignant transformation (Non-MT) groups for both IDHm-A (**C**) and IDHm-O (**D**) that were significant for an interaction term between molecular subtype and transformation status ($P<0.05$).

Discussion

The primary findings of this study are that: (1) large tumor volume is useful for identifying MT in both IDHm-A and IDHm-O but (2) shape, diffusion, and perfusion characteristics are useful for identifying MT only in IDHm-A, and not in IDHm-O. This study adds to the literature by utilizing contemporary definitions of human gliomas and assessing a unique cohort with histologically-confirmed MT from an initial grade 2 glioma presentation transforming to a grade 3/4 glioma in the future.

The present finding that contrast-enhancement is more likely, but not perfectly indicative of higher-grade glioma is in line with prior studies on brain tumors.[177, 178] In fact, nearly half of the IDHm-A and IDHm-O with MT were non-enhancing. Additionally, some IDHm-A with non-MT were contrast-enhancing, which emphasizes the need for studies on MT to use histologically-confirmed MT from a repeated biopsy as ground truth and not just the presence of contrast-enhancement. Moreover, using a volumetric threshold for determining the presence of contrast-enhancement adapted from the RANO 2.0 criteria of "measurable disease" for clinical trials[182] may be useful for assessing presence of contrast-enhancement in research studies, since some gliomas may be only minimally contrast-enhancing.

MT in IDHm-A was associated with lower ADC, which is in line with prior studies on gliomas assessing MT[179] and tumor grade differences.[183] This study also utilized the metric 10th-percentile ADC as did a prior study on glioma MT,[179] which may demonstrate the usefulness of percentile-based metrics for identifying subtle tumor changes. The lower ADC values in the IDHm-A MT cohort compared to non-MT likely reflect increased tumor proliferation and cell density[111] as the glioma progresses into a higher-grade glioma. Increased tumor cellular growth can also lead to tumor angiogenesis,[184] which also explains the finding of higher nrCBV in the

IDHm-A MT cohort compared to non-MT. This study adds to the growing literature on the usefulness of diffusion and perfusion MRI for assessing glioma group differences.[69, 179, 180]

The shape feature of sphericity is also beginning to be utilized to study gliomas, though mostly for studying IDH-wild-type glioblastoma[185, 186] and brain metastases.[181] The present study demonstrates that sphericity may also have utility for studying IDHm-A MT, for the lower sphericity in the MT cohort may reflect the combination of infiltrative tumor behavior and vasogenic edema associated with more aggressive tumors.[34] Bimodality coefficients and ADC-L were significantly negatively correlated only in MT IDHm-A and IDHm-O as well, which may reflect an interplay between ADC histogram characteristics and tumor biology in MT that is not present in non-MT IDH-mutant gliomas.

Notably, diffusion, perfusion, or shape features were not useful in identifying MT in IDHm-O. IDHm-Os are known for their intermediate diffusion and perfusion characteristics between less aggressive IDH-mutant and more aggressive IDH-wild-type astrocytomas,[69] so it is conceivable that these imaging modalities may not be sensitive to detect tumor changes associated with MT in IDHm-O. Nevertheless, tumor volume and contrast-enhancement were able to identify IDHm-O MT, which can serve as useful biomarkers for MT in IDHm-O. Future studies exploring other advanced imaging biomarkers for characterizing MT, particularly for IDHm-O, would be valuable.

For example, the present study's exploratory analyses utilizing BOLD asynchrony maps demonstrate the potential application of the DSC perfusion MRI-derived pseudo-rs-fMRI approach described in **Chapter 5** to perform advanced resting-state analyses in a cohort that obtained DSC perfusion MRI but not rs-fMRI. BOLD asynchrony results using pseudo-rs-fMRI demonstrated opposite, non-significant trends between IDHm-A and IDHm-O, perhaps due to very limited sample size. However, there was a significant interaction term between IDHm-A vs.

IDHm-O and transformation status for the BOLD asynchrony results. IDHm-A MT trended towards higher BOLD asynchrony compared to non-MT, which are in line with the present nrCBV findings and consistent with prior findings that BOLD asynchrony is positively associated with histologic markers of tumor burden in treatment-naïve IDH-mutant gliomas.[154] On the other hand, the opposite BOLD asynchrony trends in IDHm-O may reflect subtle tumor vascular BOLD changes upon MT that may be occurring without macroscopic tumor vascular density alterations as reflected by the concurrent lack of difference in nrCBV between IDHm-O MT vs. non-MT. However, these possible explanations are speculative based on non-significant visual trends, so larger studies with BOLD asynchrony should be performed to better understand these preliminary observations.

This study has a few limitations. Increasing the sample size would be beneficial to draw firmer conclusions on the present results. However, this study explored a unique cohort of patients with 2+ biopsies/surgeries with initial presentation as grade 2 IDH-mutant gliomas, so we believe the findings of the present study are valuable to the field. Additionally, longitudinal analyses were not performed but may be useful to study MT, particularly tumor growth rates.[40] Lastly, the availability of more advanced metabolic MR techniques, such as CEST MRI[187] or MR spectroscopy,[188] would also be useful to explore in the future for studying metabolic shifts associated with MT.[30]

Conclusions

Presence of measurable contrast-enhancement is not perfectly concordant with histologically-confirmed MT. Tumor volumetry is useful for identifying MT in IDH-mutant gliomas. Shape, diffusion, and perfusion characteristics were only useful for identifying MT in

IDHm-A but not in IDHm-O, reflecting the different tumor biology of these molecular subtypes and their need for separate imaging biomarkers. ADC histogram and pseudo-rs-fMRI BOLD asynchrony approaches may be useful for characterizing tumor biology alterations upon malignant transformation.

Chapter 8. "Digital Flipbooks" of Patient MRI Scans for Enhanced Visual Assessment of IDH-Mutant Gliomas

Preface

This chapter is adapted from the following manuscript under review:

Cho NS*, Lam VL*, Sanvito F*, Oshima S, Harper J, Chun S, Raymond C, Lai A, Nghiemphu PL, Yao J, Everson R, Salamon N, Cloughesy TF, Ellingson BM. Digital "flipbooks" for enhanced visual assessment of simple and complex brain tumors. *Neuro-Oncology.* In Press. *Contributed equally

Introduction

Serial evaluation of magnetic resonance imaging (MRI) before and after gadolinium-based contrast[189] is critically important in neuro-oncology in order to identify early changes in brain tumor size to (1) determine the urgency of treatment intervention if the tumor is being managed with a wait-and-watch approach, (2) monitor therapeutic benefit, and/or (3) judiciously change therapies if tumor progression is observed, either in routine clinical care or when discontinuing patients enrolled in a clinical trial.[182] During the evaluation of interval imaging, it is important to discriminate between clinically meaningful and non-meaningful changes. On one hand, acting on subtle non-meaningful changes too early may be detrimental, for instance in a case where the treatment is unnecessarily changed, or re-resection/-irradiation is performed. On the other hand, the time interval for follow-up MRI scans can vary from ~3 months early in the treatment course to up to 1 year for well-controlled disease,[190] so it is imperative to identify *actual* disease progression as early as possible as tumor growth can lead to permanent neurological disabilities. Ultimately, interval imaging may provide information about potential complications caused by the tumor or the treatment that could guide clinical management.

Conventional radiographic assessment of serial MRI scans takes the form of a side-by-side comparison of images acquired at different timepoints. However, the interpretation of subtle alterations on MRI for tumor response assessment can sometimes be difficult using the traditional side-by-side read methodology for multiple reasons. First, it is challenging for the human visual system to compare side-by-side images since it is difficult to assess the spatial correspondence between signal alterations with this approach. Additionally, technical aspects further limit the reliability of side-by-side reads, such as variations in head tilt, imprecise slice matching, and sequence protocol variation.[191-194] Furthermore, the number of timepoints that can be directly

compared is limited by screen size, which can add to the difficulty and reporting time for accurate clinical decision making, especially for cases with many follow-up MRI and/or a long disease course.

Despite the obvious value of standardized response assessment paradigms that include physical measurements, including Response Assessment in Neuro-Oncology (RANO) low-grade glioma (RANO LGG),[167] RANO brain metastases (RANO BM),[195] RANO meningioma,[196] RANO for leptomeningeal disease (RANO LMD),[197] pediatrics RANO (RAPNO),[198] immunotherapy RANO (iRANO),[199] the modified RANO (mRANO) criteria,[200] and the recently published RANO 2.0 for gliomas[182], the current routine for clinical care is the radiologic side-by-side read. Nevertheless, there exist limitations when utilizing quantitative standardized response criteria such as the difficulty in evaluating subtle changes in tumor growth dynamics in non-measurable, multifocal, complex, and/or highly infiltrative tumors. As a result, there remains a clear need for an improved tool to augment *qualitative* brain tumor clinical assessment that balances time-efficiency with enhanced tumor visualization for select, challenging cases.

Digital "Flipbooks" for Brain Tumor Assessment

Patient-specific digital "flipbooks"[201] can be constructed to *qualitatively* assess wholistic tumor growth dynamics and brain changes over time. These flipbooks display successive, co-registered MRI exams across multiple follow-up time points, with multiple imaging slices of a single timepoint shown as an array or "montage" on a PowerPoint slide, PDF, or video. By quickly moving through successive slides, changes in the size of tumor and normal brain structures appear to the user as *motion*, quickly catching the eye by exploiting motion-perceiving neurons in the middle temporal visual cortex[202-204].

Flipbooks give greater insight into changes within the totality of tumor burden that is lost when evaluating only a single image slice. By displaying the entire brain at each timepoint using a "mosaic" view of images after alignment and registration allows more precise temporal evolution of radiographic findings while preserving stereotactic, regional correspondence across timepoints. Flipbooks also allow visualization of non-tumor structures that provide additional insight into disease status or ongoing pathophysiological processes, including tissue loss linked to atrophic changes and/or Wallerian degeneration, or tissue gain due to tumor growth, mass effect, or midline shift that might indicate infiltrative or difficult to demarcate disease. Compared to conventional side-by-side visualization, even when a clinical PACS software can perform longitudinal image co-registration of multiple timepoints, flipbooks remove the distractions of shifting focus back-and-forth between a single image slice on side-by-side viewing panels, facilitate the co-localization of findings at different timepoints by means of superimposition, and correct issues that may arise by comparing different image orientations. Of note, we are introducing the concept of flipbooks as an additional, available tool that clinicians can utilize as needed for select patient cases to

enhance side-by-side clinical reads—*not* as a replacement for side-by-side reads nor as an alternate to standardized response criteria such as RANO 2.0.[182]

Flipbooks Methodology

Each flipbook contains a series of images, usually of a single image contrast (e.g. T1-weighted post-contrast or T2-weighted FLAIR images), displayed across consecutive timepoints for a single patient using separate "pages" or slides. The process begins by first retrieving the DICOM images of the highest-resolution scans for each timepoint of interest, then converting these DICOM images to the Neuroimaging Informatics Technology Initiative (NIFTI) standardized format using *dcm2niix* (https://github.com/rordenlab/dcm2niix) (**Figure 8.1A**). Next, images from multiple timepoints are registered to a single timepoint, often a clinically relevant "baseline" with highest-image resolution. While 3D images are optimal for flipbooks given their thin slice thickness, 2D images can still be employed and registered to a 3D image with resampling and interpolation. Image registration with resampling and interpolation can be performed using the *FLIRT* tool from FSL (FMRIB Software Library; http://www.fmrib.ox.ac.uk/fsl),[144] an open-source and freely available library of analysis tools for functional, structural, and diffusion brain MRI images. A 6 degree-of-freedom rigid body linear transformation is preferred so the tumor size is not altered during alignment, but a 12 degree-of-freedom affine transformation may also be appropriate in certain circumstances. Following registration, an optional step of skull-stripping can be performed using brain masks obtained from *BET2* (Brain Extraction Tool; https://fsl.fmrib.ox.ac.uk/fsl/fslwiki/BET/UserGuide)[205] or *HD-BET* (https://github.com/MIC-DKFZ/HD-BET)[206]. However, skull-stripping may not be warranted for cases where evaluation of extra-axial structures may be important, such as meningiomas and leptomeningeal disease. Brain-

extracted images can also be bias-field corrected using *FAST* (FMRIB's Automated Segmentation Tool; https://fsl.fmrib.ox.ac.uk/fsl/fslwiki/FAST) in order to reduce signal inhomogeneities (e.g. dark spots or gradients of light-to-dark dependent on head coil orientation and elements).

After registration, mosaic images can be created with image viewers such as *AFNI* (Analysis of Functional NeuroImages; http://afni.nimh.nih.gov/afni)[76] or "FSL eyes", using their montage or lightbox visualization modes, respectively, in order to display multiple slices simultaneously on one screen (**Figure 8.1B**). The user should select the number of total slices, extent of coverage, and interslice gap for an adequate overview of the tumor. Window level and width can be automatically or manually adjusted to produce images with the best visual clarity of the tumor and kept as consistently as possible for each timepoint. Once the images are sufficient, a screenshot or saved TIFF/JPEG image is captured for each timepoint and imported into PowerPoint (Microsoft Corporation, Redmond, WA), Keynote, PDF, or another document type with one timepoint per slide or page. It is important that the dimensions and positioning are consistent for each time point so it is possible to scroll through "pages" or slides like a physical flipbook (**Figure 8.1C-D**). Additional information such as the date of scan, relevant medical history, Karnofsky Performance Status score, and image annotations may be added to the slides to add more context to the patient. Also, different slide transition effects (e.g. fade) may be added for smoother viewing between timepoints.

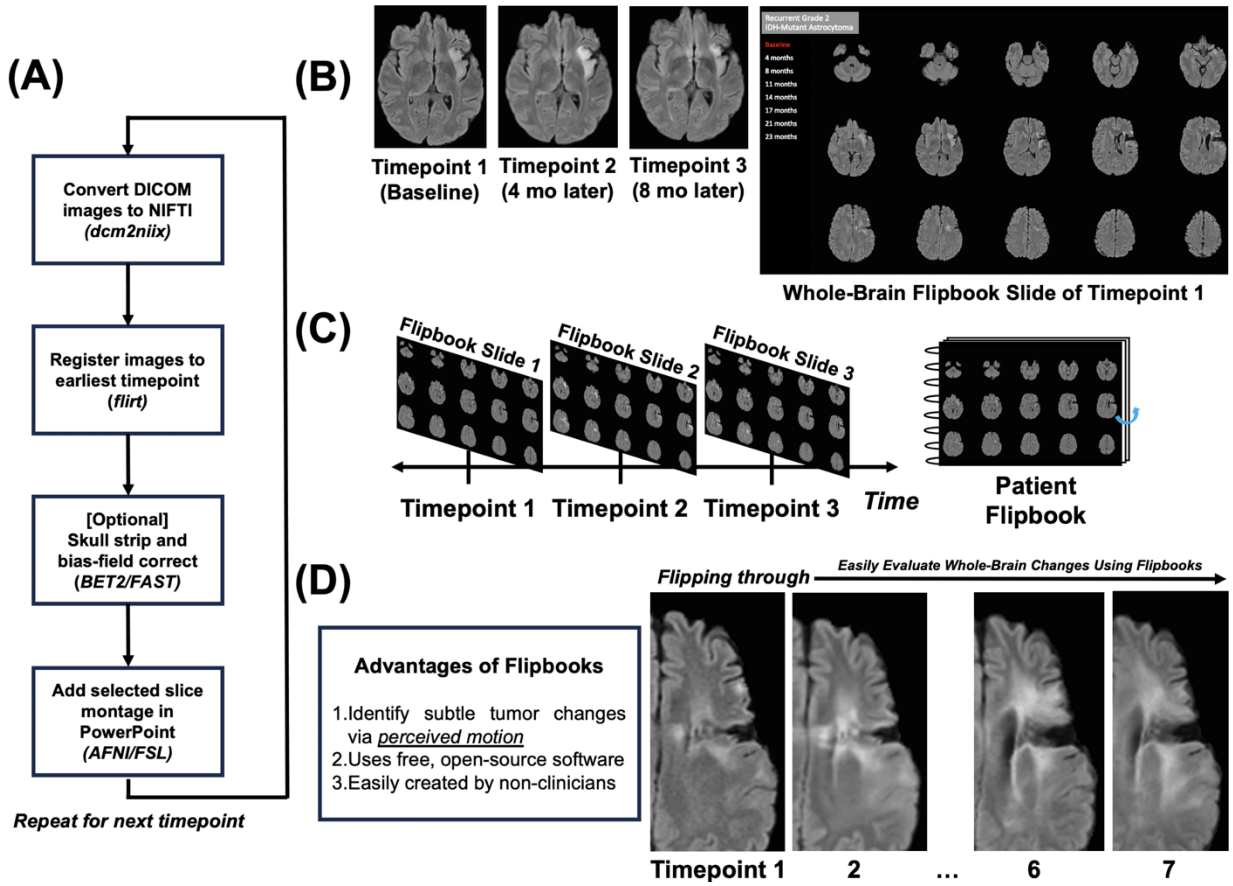

Figure 8.1. Overview of Creating Patient Scan Digital Flipbooks. (**A**) Step-by-step schematic for creating digital flipbooks. (**B**) Example consecutive, co-registered T2-weighted FLAIR images and an example baseline flipbook slide for a patient with grade 2 IDH-mutant astrocytoma. (**C**) Schematic demonstrating patient scan visualization using digital flipbooks. (**D**) Summary of the advantages of digital flipbooks by "flipping through" patient scans.

Clinical Use of Digital Flipbooks for IDH-Mutant Gliomas

While all flipbooks are useful for all patients, there are specific scenarios where flipbooks may be of particular benefit, including for IDH-mutant gliomas. Such scenarios include evaluation of slow tumor growth in low-grade IDH-mutant gliomas, assessment of infiltrative "non-measurable" components (e.g., gliomatosis cerebri pattern), differentiation between delayed post-surgical changes and residual disease, visualization and identification of pseudoprogression, evaluation of multifocal disease (e.g., multifocal gliomas), and/or identification of "mixed" response. Note, example flipbooks are presented in this thesis chapter with each slide presented on a single page. A figure legend is provided only for the first slide. Viewing of the flipbook on PDF format is achieved by setting viewer to "click-mode" instead of scroll.

Malignant Transformation of Low-Grade IDH-Mutant Glioma

Low-grade (grade 2) IDH-mutant tumors are particularly known for their slow growth—studies on low-grade gliomas before molecular classification demonstrated an average tumor diameter growth of only 4.1 mm/year[207] and average tumor percentage volume growth of 16%/year,[40] which makes their assessment using side-by-side reads particularly challenging. Additionally, it is important to identify malignant transformation to a higher-grade 3 or 4 tumor as soon as possible because prognosis is worsened upon malignant transformation.[176] One characteristic of malignant transformation is that transformed tumors rapidly accelerate in growth[40] compared to non-malignant transformation tumor progression.

In this context, digital flipbooks can aid the longitudinal evaluation of subtle T2/FLAIR changes over time such as by enhancing the visual perception of gradual or accelerated tissue expansion due to tumor infiltration as well as any gradual tissue shrinkage linked to treatment response. Additionally, the impacts of tumor growth or shrinkage on the surrounding anatomical structures can be more easily appreciated, including mass effect on surrounding brain tissue and/or ex vacuo enlargement of ventricles and sulci. Compared to side-by-side visualization, the regional correspondence across the superimposed, co-registered timepoints remarkably help when evaluating small changes during interval imaging. Additionally, flipbooks may also be used to guide semi-quantitative visual response assessments such as the Modified Levin Criteria.[201] In this criteria, assessment scores range from -3 to 3, where negative scores are associated with worsening tumor and positive scores are associated with improving tumor, and increased magnitude is associated with increased confidence.[201]

Figure 8.2 (T2-weighted FLAIR MRI flipbook) shows a representative case of a 23-year-old male patient initially diagnosed with a grade 2 IDH-mutant astrocytoma that later underwent malignant transformation. This glioma also demonstrated T2-FLAIR mismatch sign.[38] After continued tumor growth was observed after initial resection, the patient received 12 cycles of temozolomide (1 yr 5 mo — 2 yr 5 mo) which had some effect. Upon later recurrence, the patient received 6 cycles of CCNU (3 yr 9 mo — 4 yr 4 mo), but then the tumor rapid grew exponentially at the end of the flipbooks, including a large expansion of contrast-enhancement at the final timepoint. Tumor re-resection and biopsy 4 days after the conclusion of the flipbooks indicated that the glioma had transformed into a grade 4 IDH-mutant astrocytoma. The patient died 1 year later. This flipbook is particularly beneficial for identifying the accelerated tumor growth, mass effect, and midline shift due to the transforming tumor towards the conclusion of the flipbooks that

also aid the Modified Levin Score assessments. Furthermore, the longitudinal re-development of T2-FLAIR mismatch areas as the tumor recurs is better appreciated from the superimposed, co-registered images in the flipbook.

Conversely, **Figure 8.3** (T2-weighted FLAIR MRI flipbook) shows a representative case of a 32-year-old male patient initially diagnosed with a grade 2 IDH-mutant astrocytoma that underwent tumor progression *without* malignant transformation. Upon tumor resection, the tumor was untreated. Throughout the time interval of the flipbook, the tumor demonstrated very slow, subtle growth since the initial surgery without exponential growth observed in the prior representative case (**Figure 8.2**). The tumor was resected again 5 days after the conclusion of the flipbooks, and tissue biopsy confirmed the tumor remained as a grade 2. The flipbook is useful here to identify the small regions of tumor growth along the resection cavity border using the Modified Levin Criteria.

(Slide 1/21)

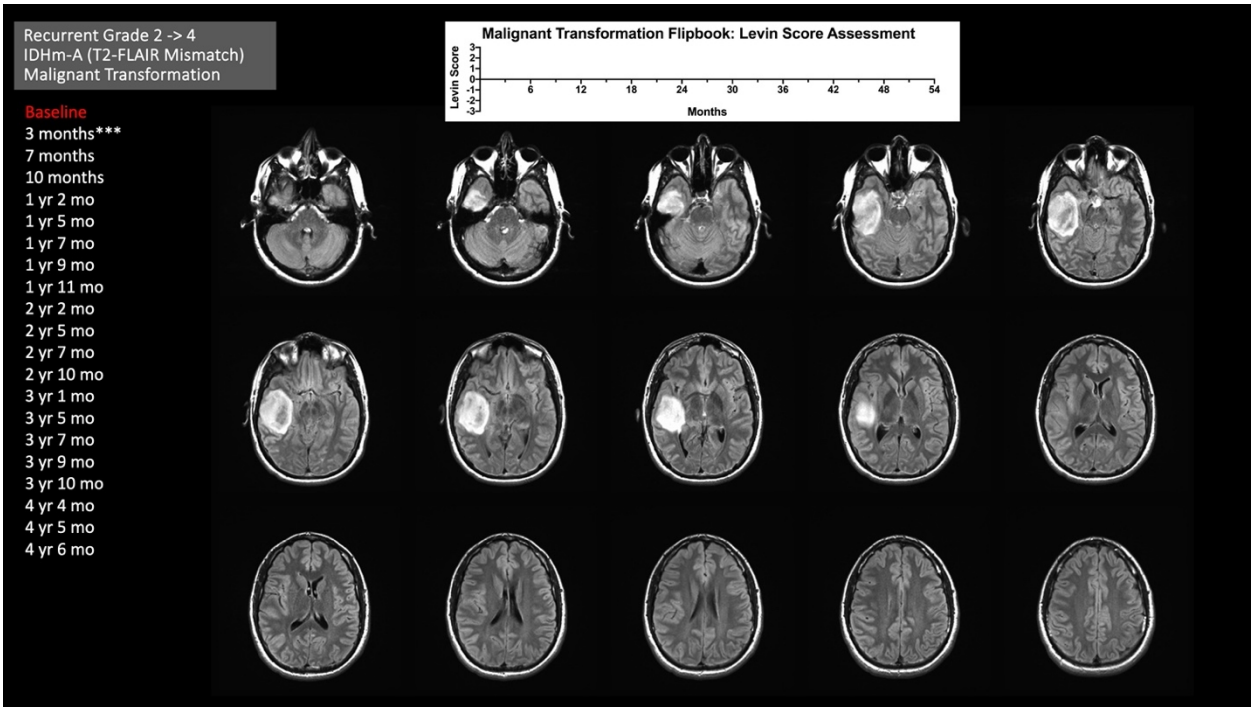

Figure 8.2 Representative Case of Using Flipbooks for Assessing Low-Grade IDH-Mutant Glioma Malignant Transformation (T2-Weighted FLAIR MRI). Serial T2-weighted FLAIR images of a 23-year-old male patient with recurrent grade 2 IDH-mutant astrocytoma that underwent histologically-confirmed malignant transformation to a grade 4 IDH-mutant astrocytoma upon the conclusion of the flipbooks. The flipbooks allow for visualization of the accelerated tumor growth towards the end of the flipbook as well as the longitudinal re-development of T2-FLAIR mismatch upon initial tumor resection. The post-contrast T1-weighted MRI scan is also shown for the final timepoint only, demonstrating large contrast-enhancement. **(Please view the flipbook in PDF format as "clickable" page view, not as "scroll" view.)**

(Slide 2/21)

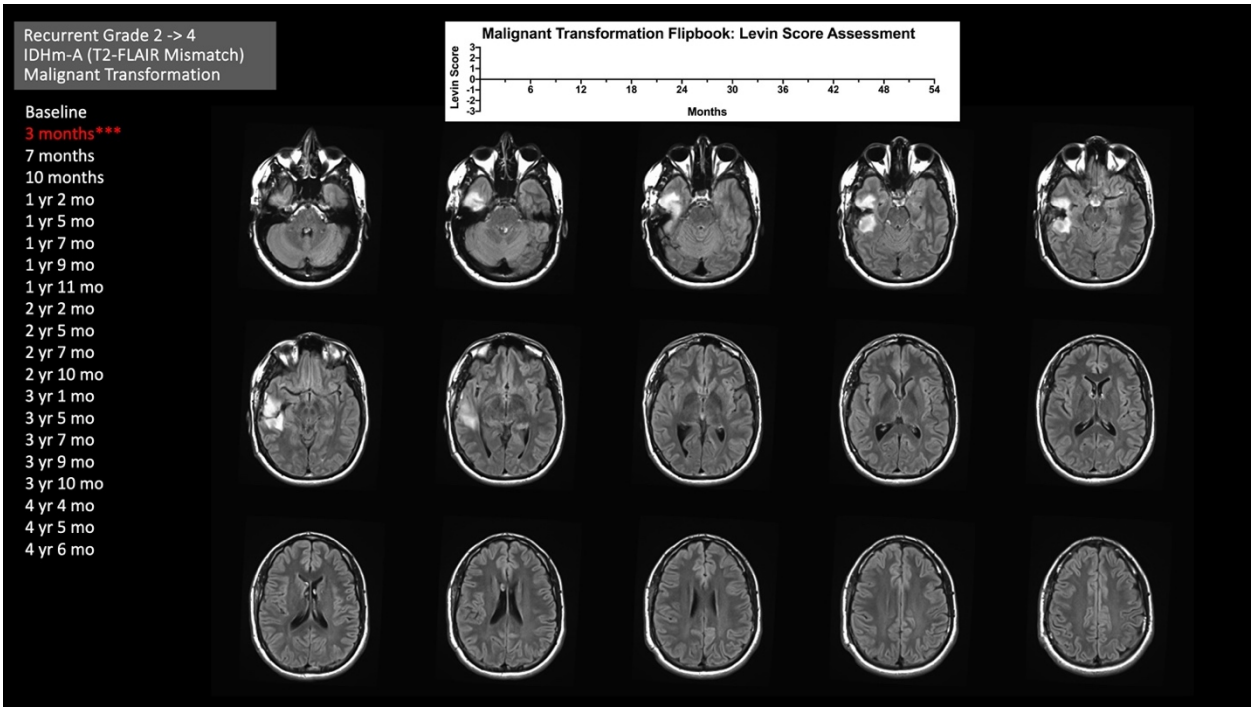
Recurrent Grade 2 -> 4
IDHm-A (T2-FLAIR Mismatch)
Malignant Transformation
Baseline
3 months***
7 months
10 months
1 yr 2 mo
1 yr 5 mo
1 yr 7 mo
1 yr 9 mo
1 yr 11 mo
2 yr 2 mo
2 yr 5 mo
2 yr 7 mo
2 yr 10 mo
3 yr 1 mo
3 yr 5 mo
3 yr 7 mo
3 yr 9 mo
3 yr 10 mo
4 yr 4 mo
4 yr 5 mo
4 yr 6 mo
Malignant Transformation Flipbook: Levin Score Assessment
Levin Score
3
2
1
0
-1
-2
-3
6
12
18
24
30
36
42
48
54
Months

(Slide 3/21)

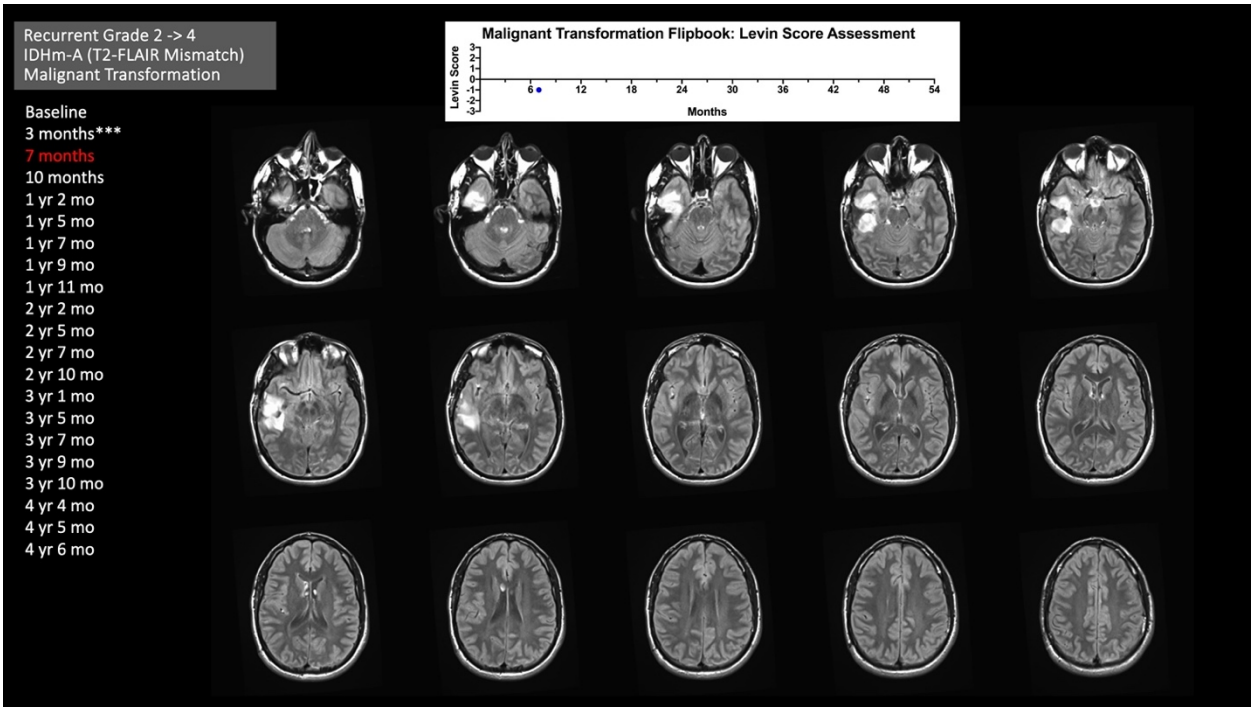
Recurrent Grade 2 -> 4
IDHm-A (T2-FLAIR Mismatch)
Malignant Transformation
Baseline
3 months***
7 months
10 months
1 yr 2 mo
1 yr 5 mo
1 yr 7 mo
1 yr 9 mo
1 yr 11 mo
2 yr 2 mo
2 yr 5 mo
2 yr 7 mo
2 yr 10 mo
3 yr 1 mo
3 yr 5 mo
3 yr 7 mo
3 yr 9 mo
3 yr 10 mo
4 yr 4 mo
4 yr 5 mo
4 yr 6 mo
Malignant Transformation Flipbook: Levin Score Assessment
Levin Score
3
2
1
0
-1
-2
-3
6
12
18
24
30
36
42
48
54
Months

(Slide 4/21)

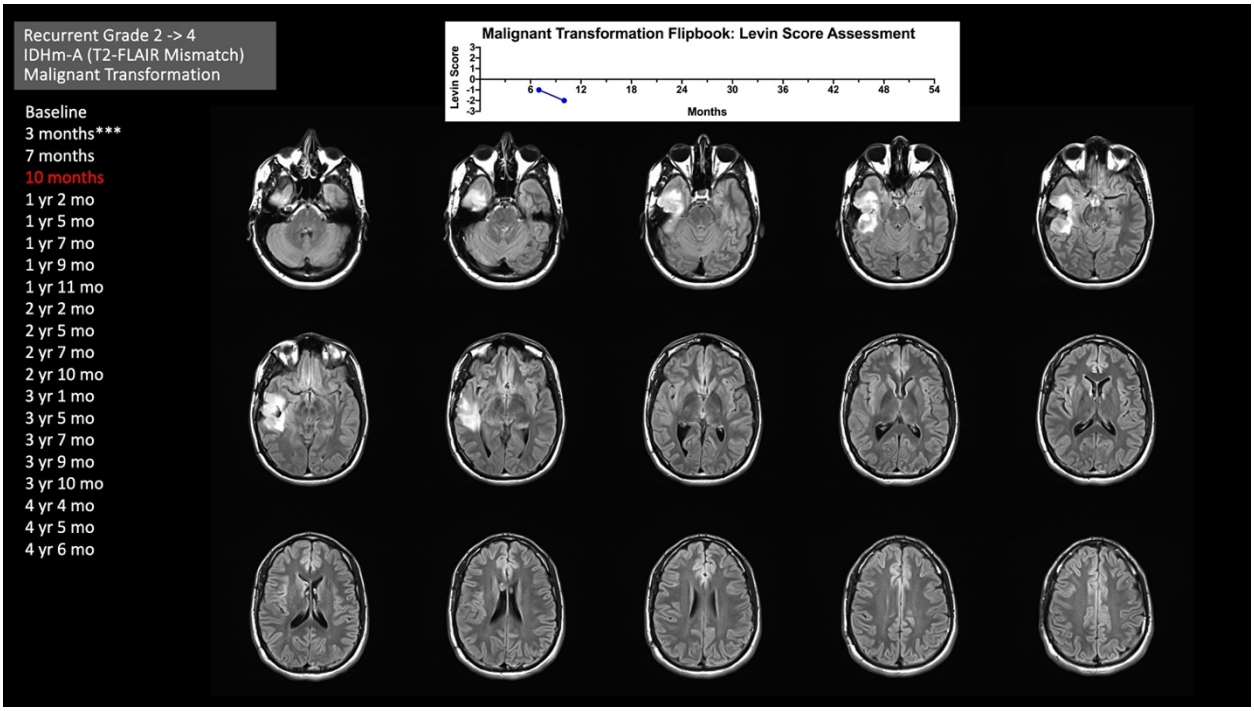
Recurrent Grade 2 -> 4
IDHm-A (T2-FLAIR Mismatch)
Malignant Transformation
Baseline
3 months***
7 months
10 months
1 yr 2 mo
1 yr 5 mo
1 yr 7 mo
1 yr 9 mo
1 yr 11 mo
2 yr 2 mo
2 yr 5 mo
2 yr 7 mo
2 yr 10 mo
3 yr 1 mo
3 yr 5 mo
3 yr 7 mo
3 yr 9 mo
3 yr 10 mo
4 yr 4 mo
4 yr 5 mo
4 yr 6 mo
Malignant Transformation Flipbook: Levin Score Assessment
Levin Score
3
2
1
0
-1
-2
-3
6
12
18
24
30
36
42
48
54
Months

(Slide 5/21)

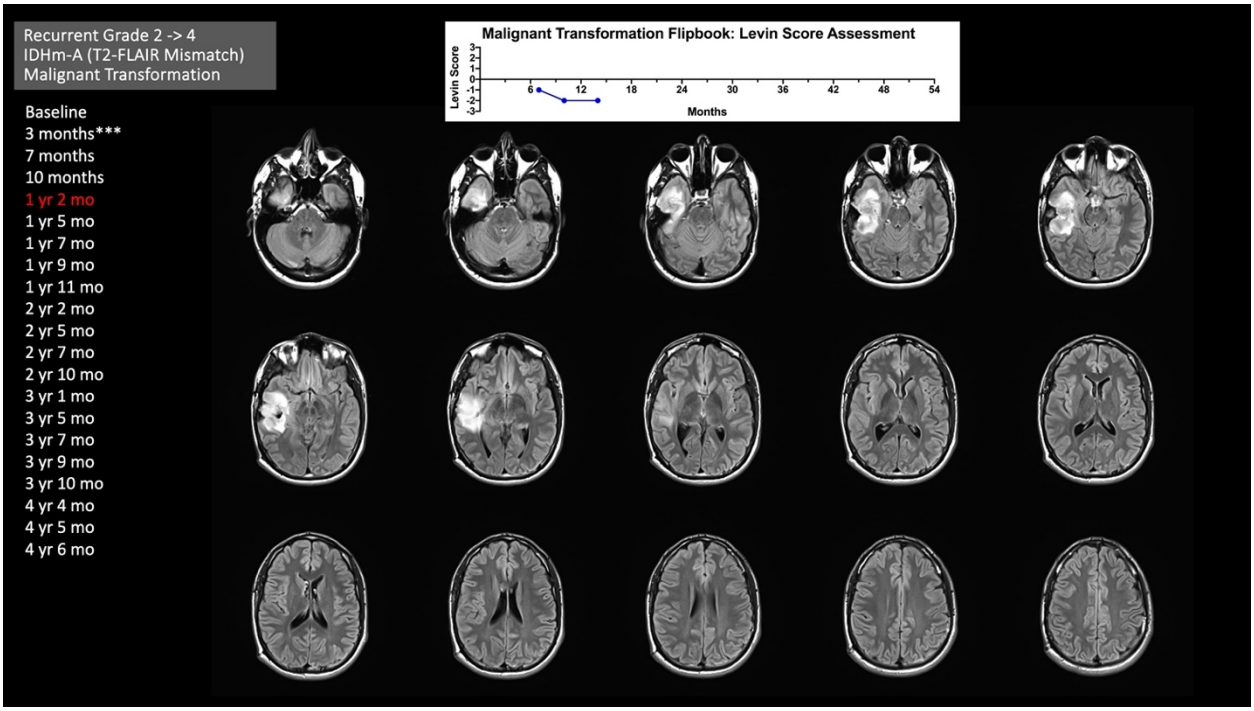
Recurrent Grade 2 -> 4
IDHm-A (T2-FLAIR Mismatch)
Malignant Transformation
Baseline
3 months***
7 months
10 months
1 yr 2 mo
1 yr 5 mo
1 yr 7 mo
1 yr 9 mo
1 yr 11 mo
2 yr 2 mo
2 yr 5 mo
2 yr 7 mo
2 yr 10 mo
3 yr 1 mo
3 yr 5 mo
3 yr 7 mo
3 yr 9 mo
3 yr 10 mo
4 yr 4 mo
4 yr 5 mo
4 yr 6 mo
Malignant Transformation Flipbook: Levin Score Assessment
Levin Score
Months

(Slide 6/21)

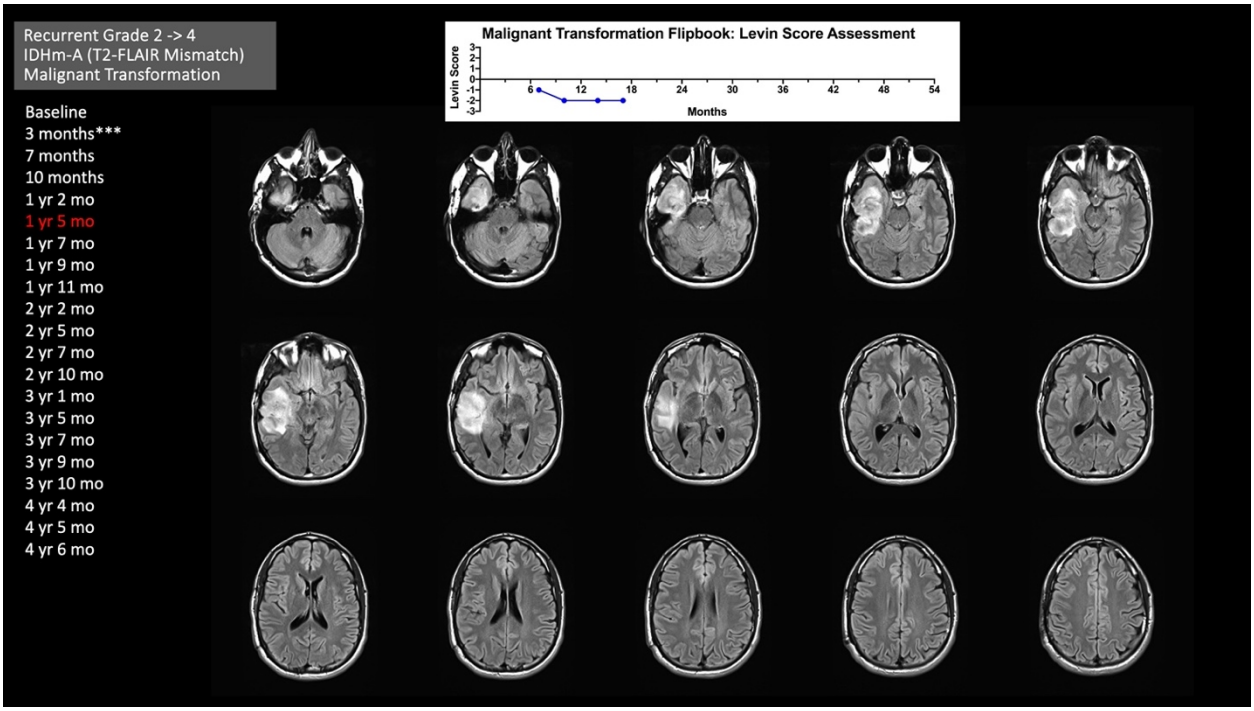
Recurrent Grade 2 -> 4
IDHm-A (T2-FLAIR Mismatch)
Malignant Transformation
Baseline
3 months***
7 months
10 months
1 yr 2 mo
1 yr 5 mo
1 yr 7 mo
1 yr 9 mo
1 yr 11 mo
2 yr 2 mo
2 yr 5 mo
2 yr 7 mo
2 yr 10 mo
3 yr 1 mo
3 yr 5 mo
3 yr 7 mo
3 yr 9 mo
3 yr 10 mo
4 yr 4 mo
4 yr 5 mo
4 yr 6 mo
Malignant Transformation Flipbook: Levin Score Assessment
Levin Score
Months

(Slide 7/21)

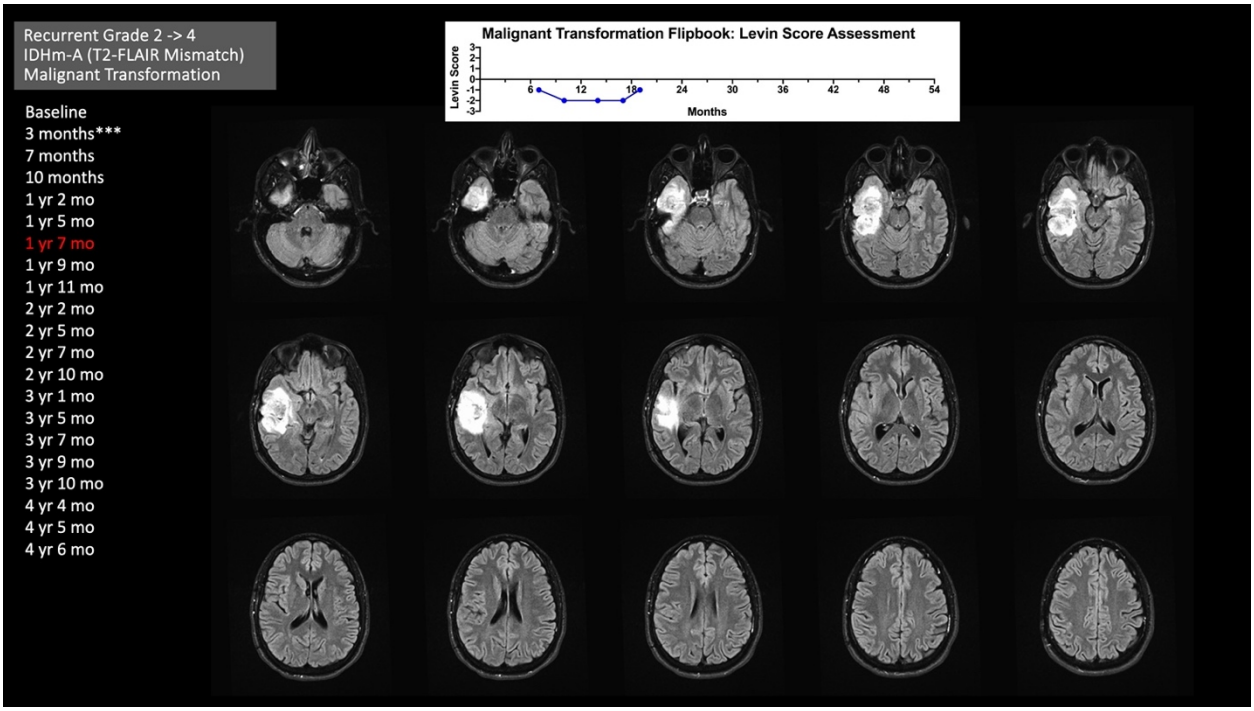
Recurrent Grade 2 -> 4
IDHm-A (T2-FLAIR Mismatch)
Malignant Transformation
Baseline
3 months***
7 months
10 months
1 yr 2 mo
1 yr 5 mo
1 yr 7 mo
1 yr 9 mo
1 yr 11 mo
2 yr 2 mo
2 yr 5 mo
2 yr 7 mo
2 yr 10 mo
3 yr 1 mo
3 yr 5 mo
3 yr 7 mo
3 yr 9 mo
3 yr 10 mo
4 yr 4 mo
4 yr 5 mo
4 yr 6 mo
Malignant Transformation Flipbook: Levin Score Assessment
Levin Score
Months

(Slide 8/21)

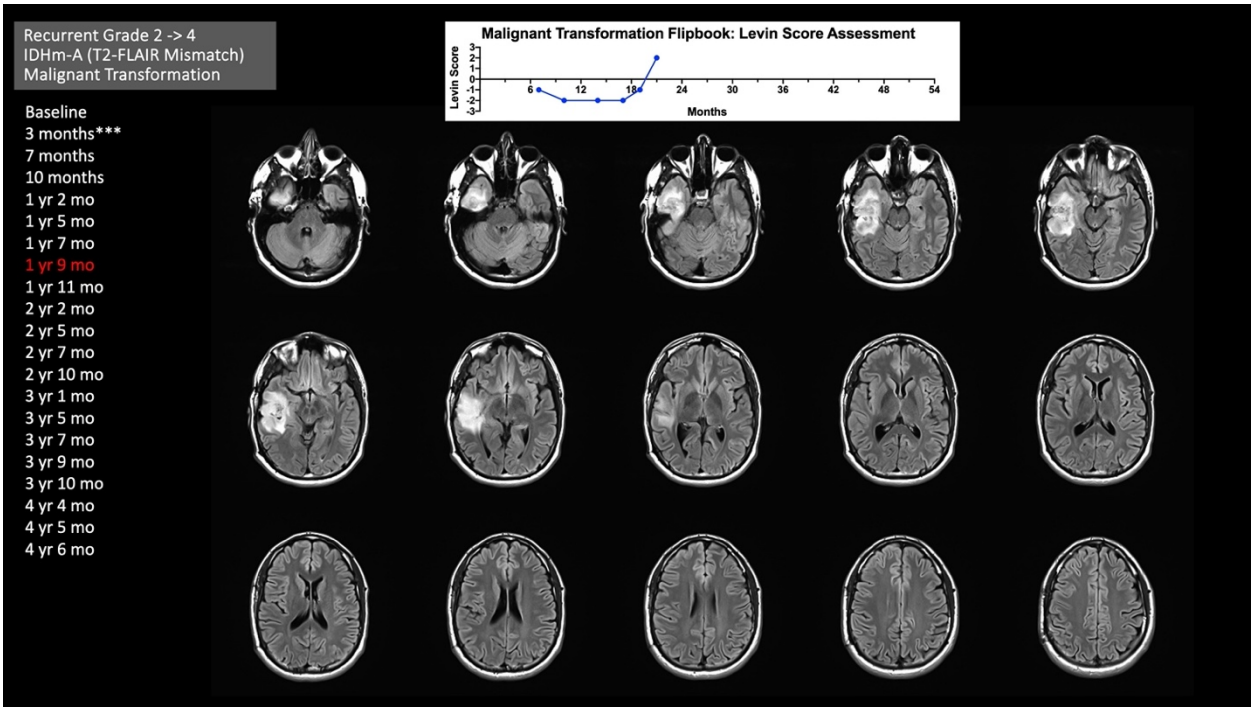
Recurrent Grade 2 -> 4
IDHm-A (T2-FLAIR Mismatch)
Malignant Transformation
Baseline
3 months***
7 months
10 months
1 yr 2 mo
1 yr 5 mo
1 yr 7 mo
1 yr 9 mo
1 yr 11 mo
2 yr 2 mo
2 yr 5 mo
2 yr 7 mo
2 yr 10 mo
3 yr 1 mo
3 yr 5 mo
3 yr 7 mo
3 yr 9 mo
3 yr 10 mo
4 yr 4 mo
4 yr 5 mo
4 yr 6 mo
Malignant Transformation Flipbook: Levin Score Assessment
Levin Score
Months

(Slide 9/21)

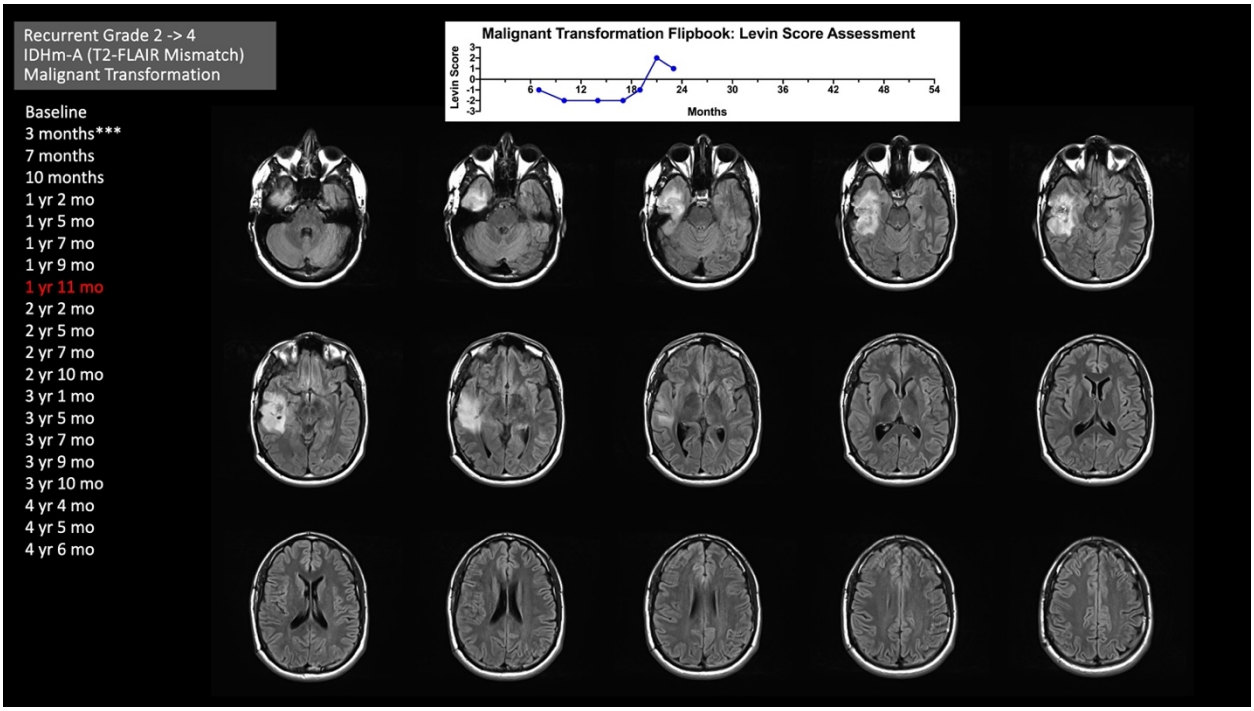
Recurrent Grade 2 -> 4
IDHm-A (T2-FLAIR Mismatch)
Malignant Transformation
Baseline
3 months***
7 months
10 months
1 yr 2 mo
1 yr 5 mo
1 yr 7 mo
1 yr 9 mo
1 yr 11 mo
2 yr 2 mo
2 yr 5 mo
2 yr 7 mo
2 yr 10 mo
3 yr 1 mo
3 yr 5 mo
3 yr 7 mo
3 yr 9 mo
3 yr 10 mo
4 yr 4 mo
4 yr 5 mo
4 yr 6 mo
Malignant Transformation Flipbook: Levin Score Assessment
Levin Score
Months

(Slide 10/21)

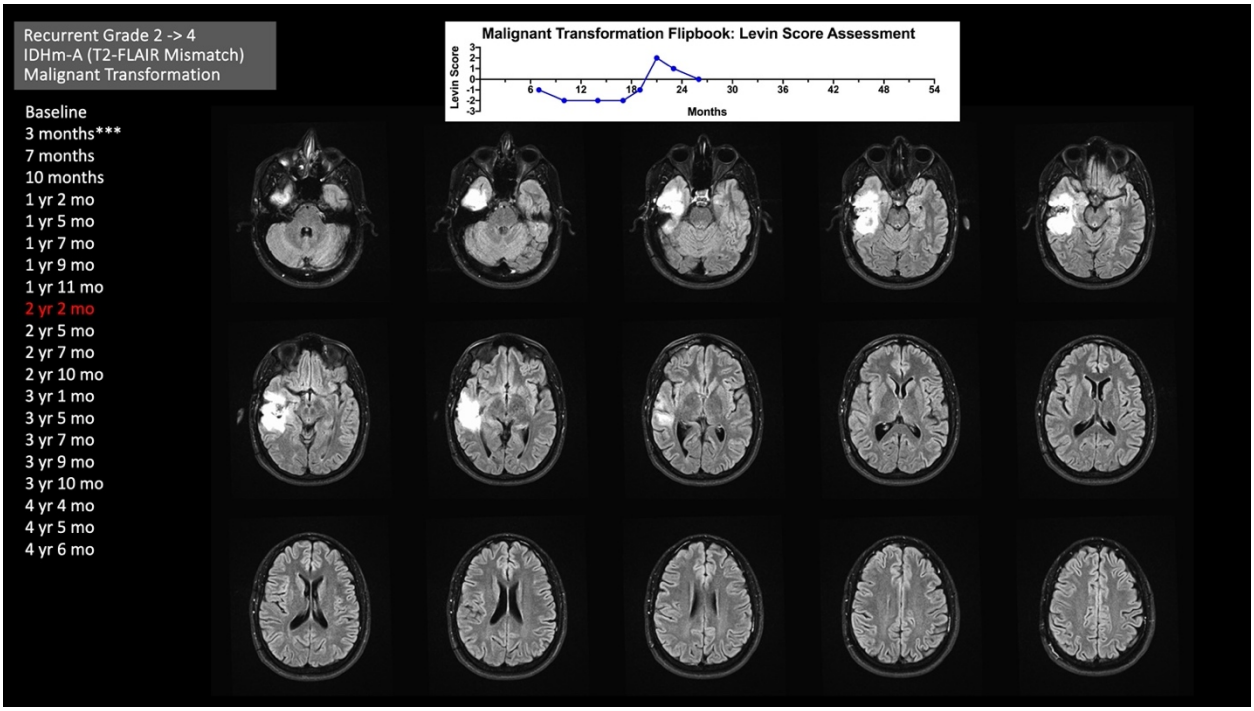
Recurrent Grade 2 -> 4
IDHm-A (T2-FLAIR Mismatch)
Malignant Transformation
Baseline
3 months***
7 months
10 months
1 yr 2 mo
1 yr 5 mo
1 yr 7 mo
1 yr 9 mo
1 yr 11 mo
2 yr 2 mo
2 yr 5 mo
2 yr 7 mo
2 yr 10 mo
3 yr 1 mo
3 yr 5 mo
3 yr 7 mo
3 yr 9 mo
3 yr 10 mo
4 yr 4 mo
4 yr 5 mo
4 yr 6 mo
Malignant Transformation Flipbook: Levin Score Assessment
Levin Score
Months

(Slide 11/21)

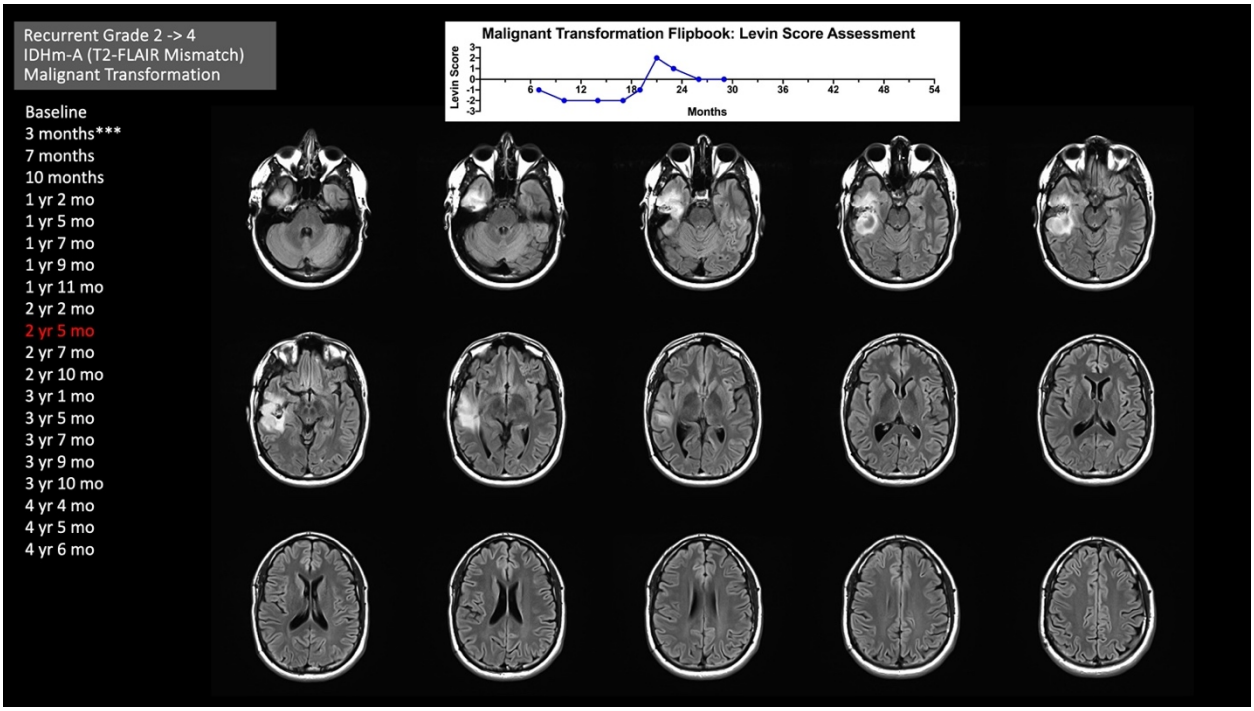
Recurrent Grade 2 -> 4
IDHm-A (T2-FLAIR Mismatch)
Malignant Transformation
Baseline
3 months***
7 months
10 months
1 yr 2 mo
1 yr 5 mo
1 yr 7 mo
1 yr 9 mo
1 yr 11 mo
2 yr 2 mo
2 yr 5 mo
2 yr 7 mo
2 yr 10 mo
3 yr 1 mo
3 yr 5 mo
3 yr 7 mo
3 yr 9 mo
3 yr 10 mo
4 yr 4 mo
4 yr 5 mo
4 yr 6 mo
Malignant Transformation Flipbook: Levin Score Assessment
Levin Score
Months

(Slide 12/21)

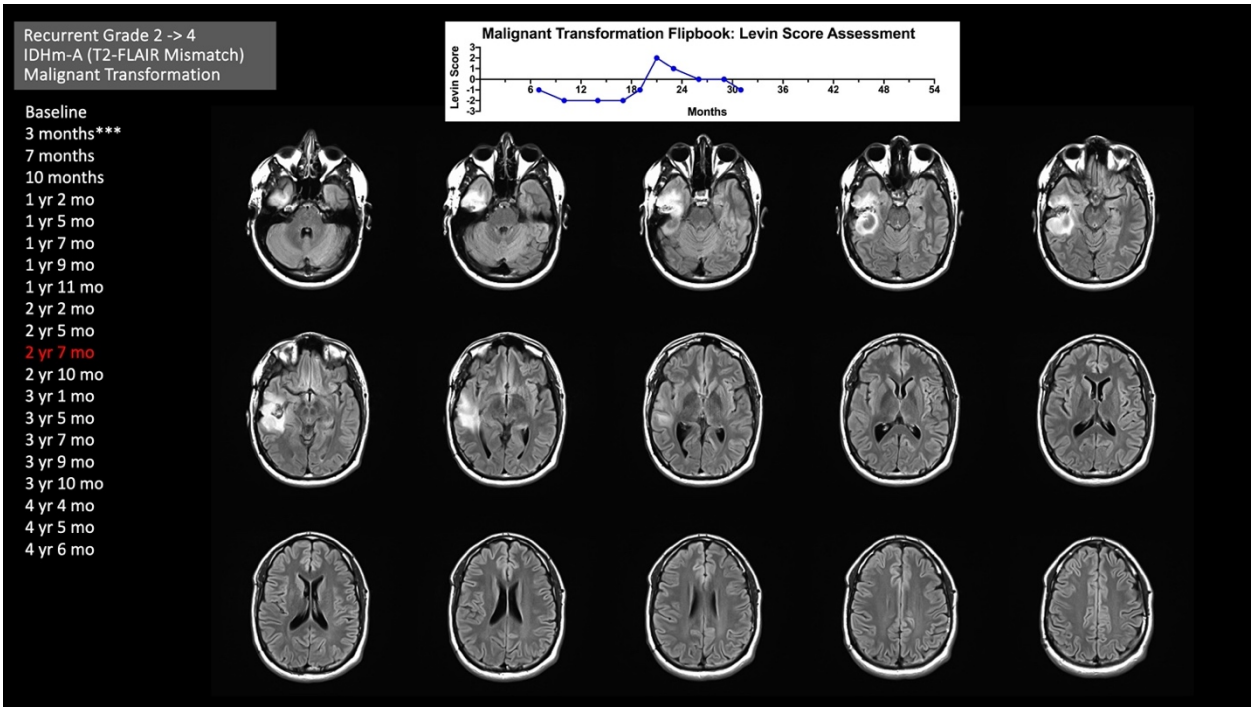
Recurrent Grade 2 -> 4
IDHm-A (T2-FLAIR Mismatch)
Malignant Transformation
Baseline
3 months***
7 months
10 months
1 yr 2 mo
1 yr 5 mo
1 yr 7 mo
1 yr 9 mo
1 yr 11 mo
2 yr 2 mo
2 yr 5 mo
2 yr 7 mo
2 yr 10 mo
3 yr 1 mo
3 yr 5 mo
3 yr 7 mo
3 yr 9 mo
3 yr 10 mo
4 yr 4 mo
4 yr 5 mo
4 yr 6 mo
Malignant Transformation Flipbook: Levin Score Assessment
Levin Score
Months

(Slide 13/21)

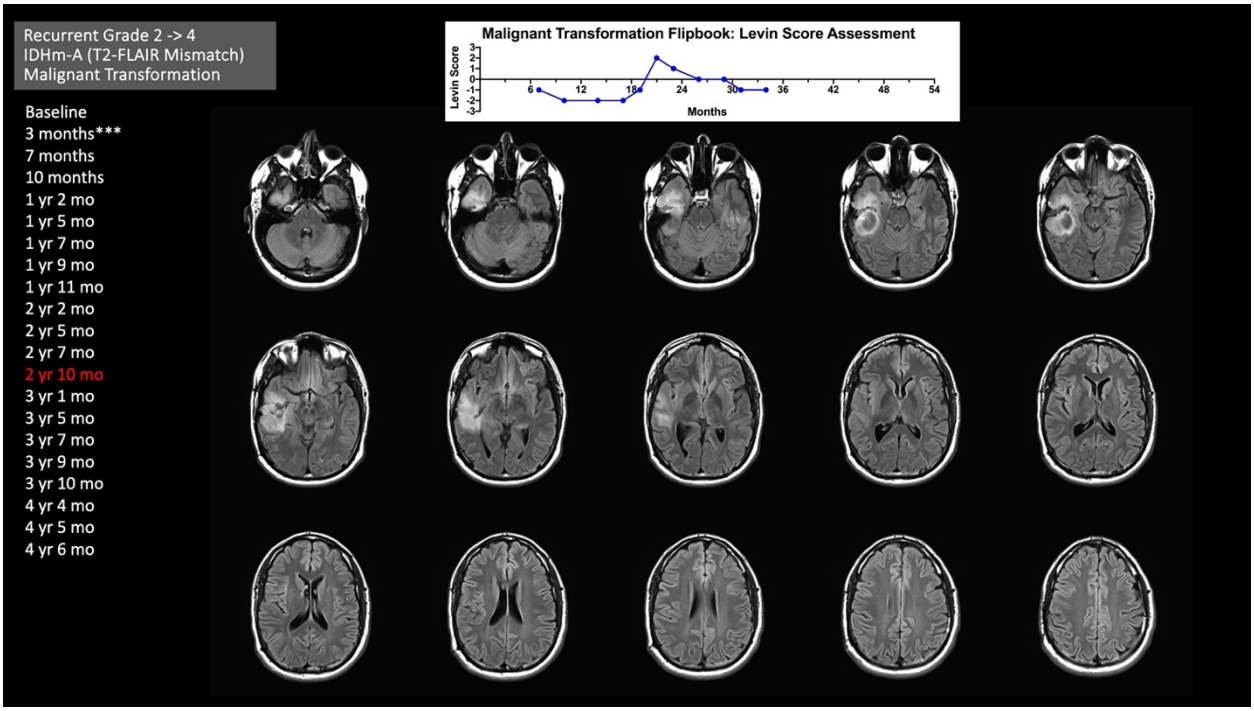
Recurrent Grade 2 -> 4
IDHm-A (T2-FLAIR Mismatch)
Malignant Transformation
Baseline
3 months***
7 months
10 months
1 yr 2 mo
1 yr 5 mo
1 yr 7 mo
1 yr 9 mo
1 yr 11 mo
2 yr 2 mo
2 yr 5 mo
2 yr 7 mo
2 yr 10 mo
3 yr 1 mo
3 yr 5 mo
3 yr 7 mo
3 yr 9 mo
3 yr 10 mo
4 yr 4 mo
4 yr 5 mo
4 yr 6 mo
Malignant Transformation Flipbook: Levin Score Assessment
Levin Score
Months

(Slide 14/21)

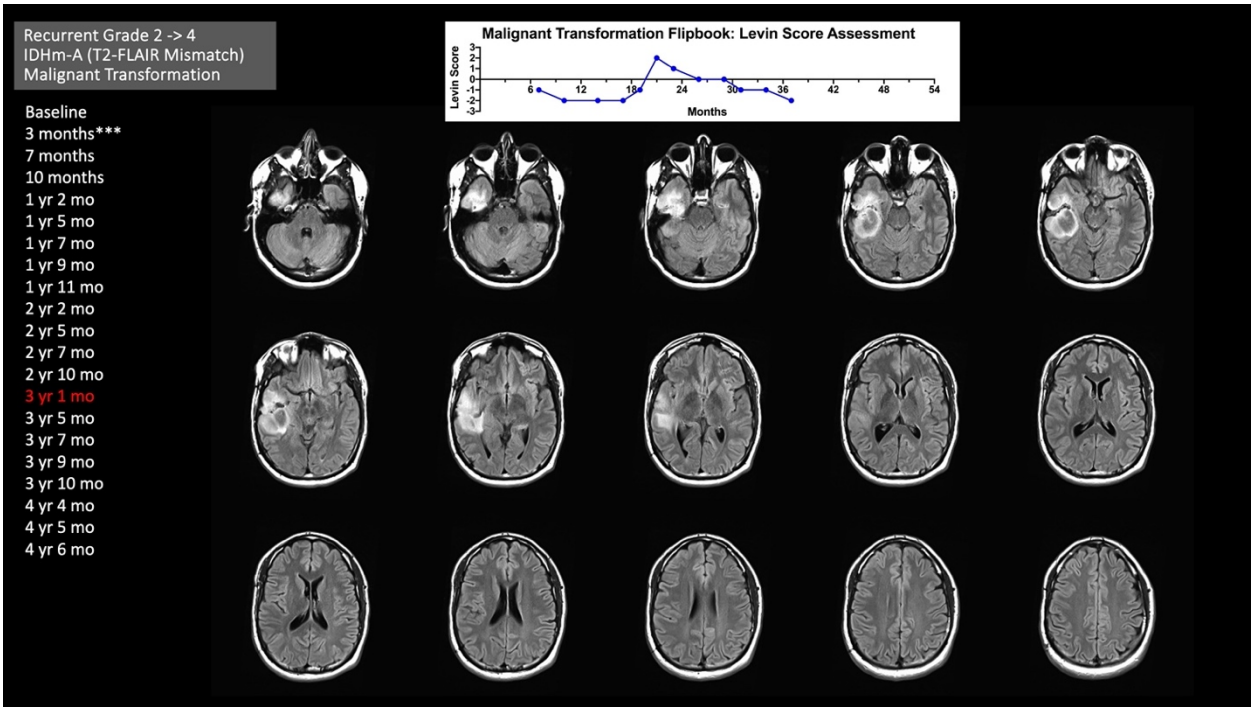
Recurrent Grade 2 -> 4
IDHm-A (T2-FLAIR Mismatch)
Malignant Transformation
Baseline
3 months***
7 months
10 months
1 yr 2 mo
1 yr 5 mo
1 yr 7 mo
1 yr 9 mo
1 yr 11 mo
2 yr 2 mo
2 yr 5 mo
2 yr 7 mo
2 yr 10 mo
3 yr 1 mo
3 yr 5 mo
3 yr 7 mo
3 yr 9 mo
3 yr 10 mo
4 yr 4 mo
4 yr 5 mo
4 yr 6 mo
Malignant Transformation Flipbook: Levin Score Assessment
Levin Score
Months

(Slide 15/21)

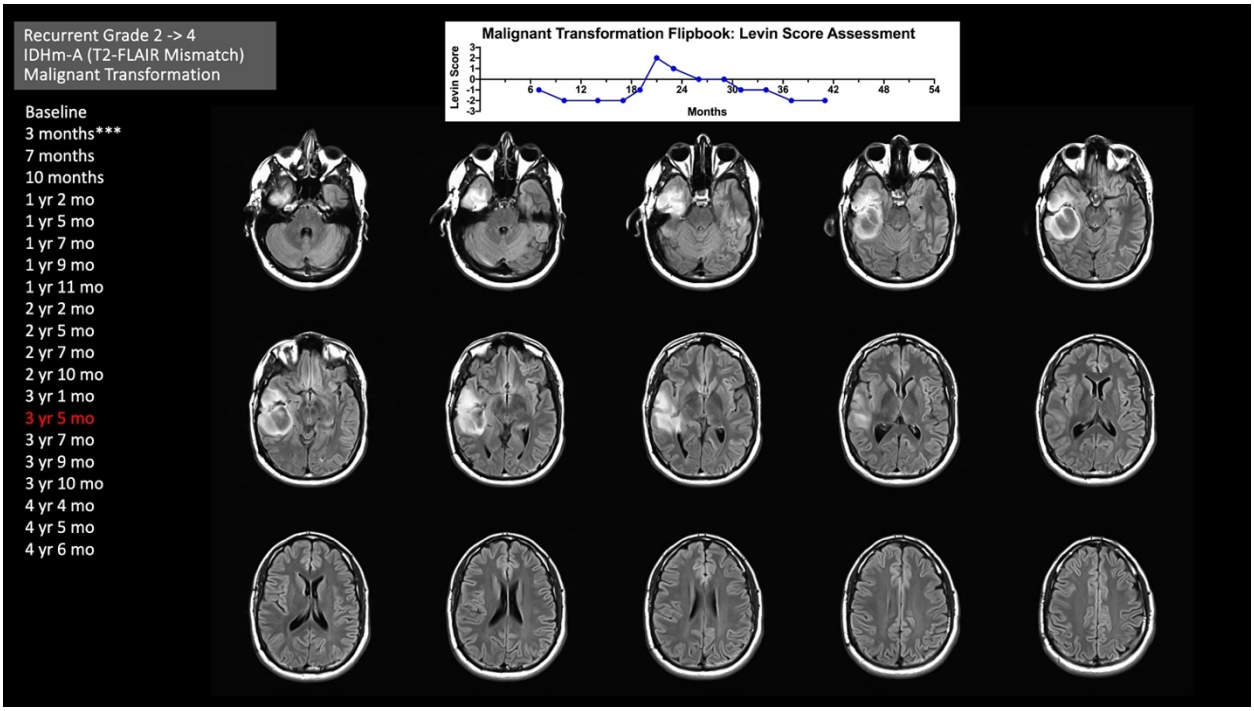
Recurrent Grade 2 -> 4
IDHm-A (T2-FLAIR Mismatch)
Malignant Transformation
Baseline
3 months***
7 months
10 months
1 yr 2 mo
1 yr 5 mo
1 yr 7 mo
1 yr 9 mo
1 yr 11 mo
2 yr 2 mo
2 yr 5 mo
2 yr 7 mo
2 yr 10 mo
3 yr 1 mo
3 yr 5 mo
3 yr 7 mo
3 yr 9 mo
3 yr 10 mo
4 yr 4 mo
4 yr 5 mo
4 yr 6 mo
Malignant Transformation Flipbook: Levin Score Assessment
Levin Score
Months

(Slide 16/21)

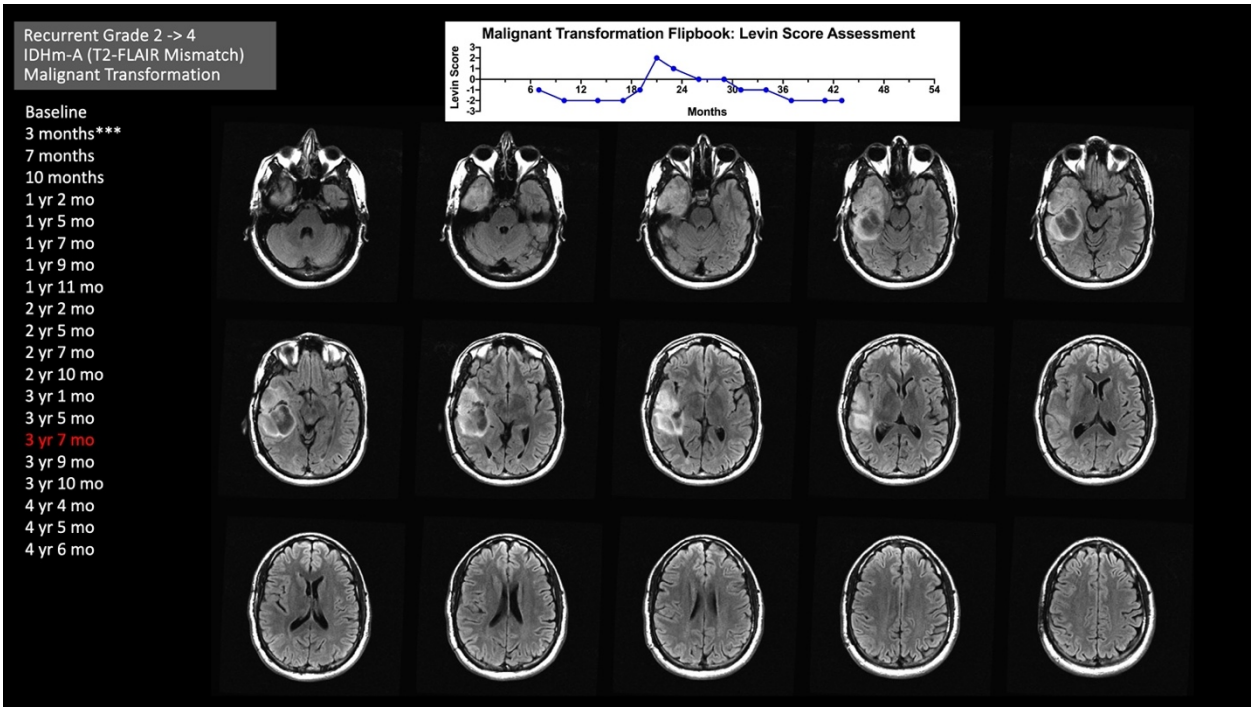
Recurrent Grade 2 -> 4
IDHm-A (T2-FLAIR Mismatch)
Malignant Transformation
Baseline
3 months***
7 months
10 months
1 yr 2 mo
1 yr 5 mo
1 yr 7 mo
1 yr 9 mo
1 yr 11 mo
2 yr 2 mo
2 yr 5 mo
2 yr 7 mo
2 yr 10 mo
3 yr 1 mo
3 yr 5 mo
3 yr 7 mo
3 yr 9 mo
3 yr 10 mo
4 yr 4 mo
4 yr 5 mo
4 yr 6 mo
Malignant Transformation Flipbook: Levin Score Assessment
Levin Score
Months

(Slide 17/21)

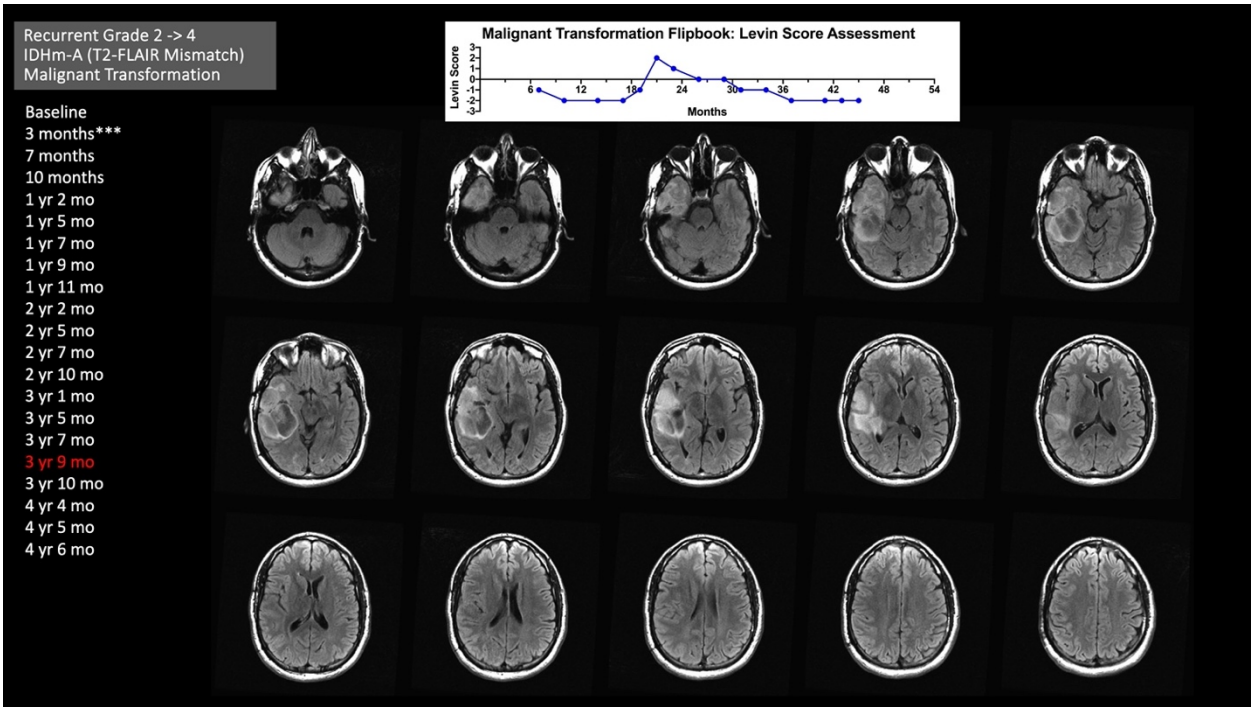
Recurrent Grade 2 -> 4
IDHm-A (T2-FLAIR Mismatch)
Malignant Transformation
Baseline
3 months***
7 months
10 months
1 yr 2 mo
1 yr 5 mo
1 yr 7 mo
1 yr 9 mo
1 yr 11 mo
2 yr 2 mo
2 yr 5 mo
2 yr 7 mo
2 yr 10 mo
3 yr 1 mo
3 yr 5 mo
3 yr 7 mo
3 yr 9 mo
3 yr 10 mo
4 yr 4 mo
4 yr 5 mo
4 yr 6 mo
Malignant Transformation Flipbook: Levin Score Assessment
Levin Score
Months

(Slide 18/21)

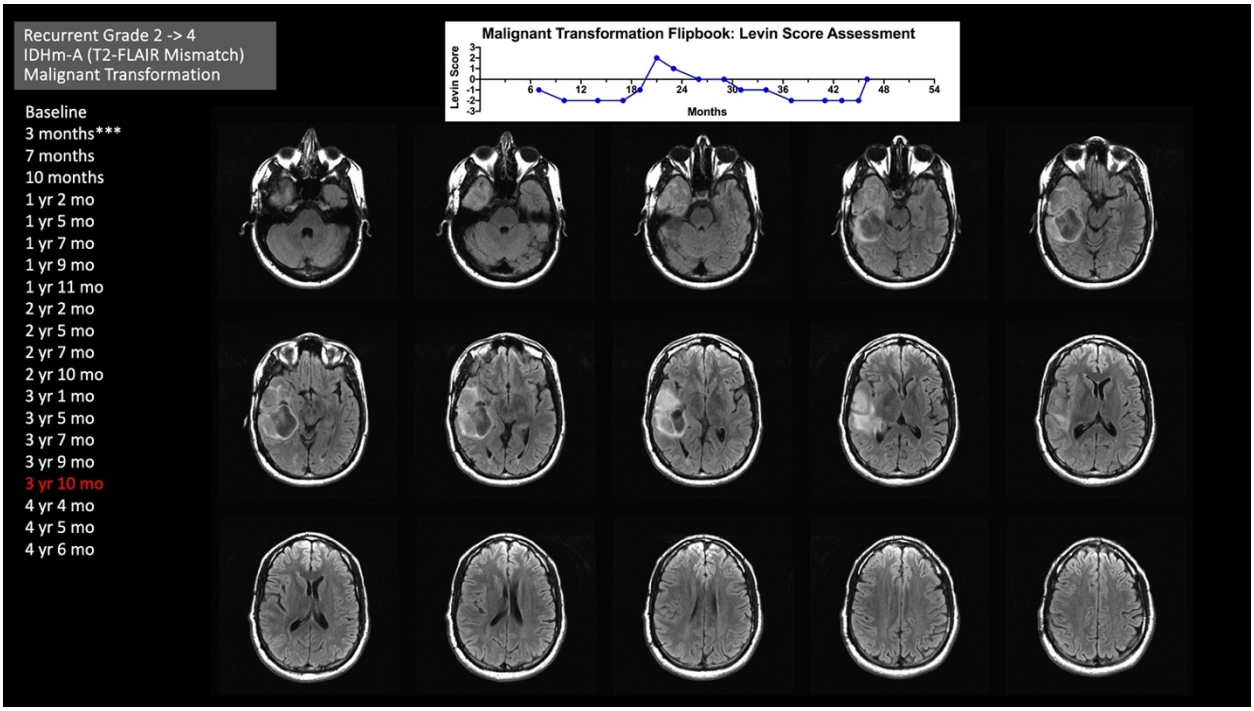
Recurrent Grade 2 -> 4
IDHm-A (T2-FLAIR Mismatch)
Malignant Transformation
Baseline
3 months***
7 months
10 months
1 yr 2 mo
1 yr 5 mo
1 yr 7 mo
1 yr 9 mo
1 yr 11 mo
2 yr 2 mo
2 yr 5 mo
2 yr 7 mo
2 yr 10 mo
3 yr 1 mo
3 yr 5 mo
3 yr 7 mo
3 yr 9 mo
3 yr 10 mo
4 yr 4 mo
4 yr 5 mo
4 yr 6 mo
Malignant Transformation Flipbook: Levin Score Assessment
Levin Score
Months

(Slide 19/21)

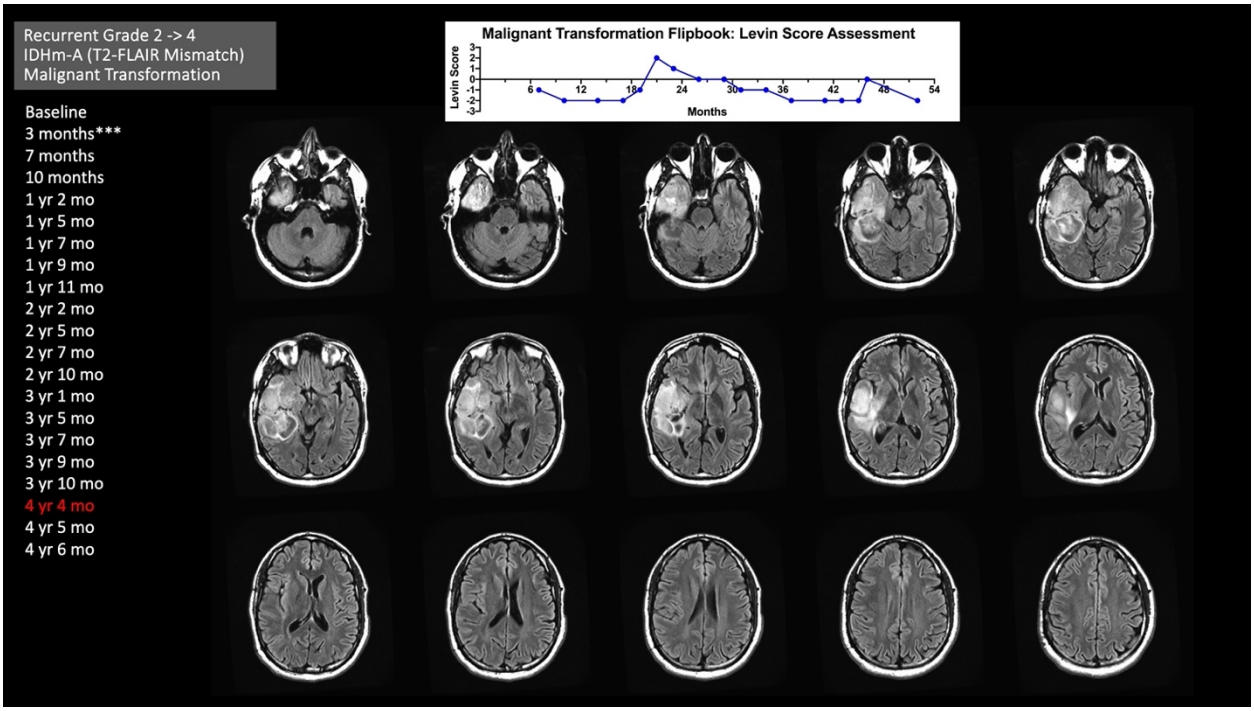
Recurrent Grade 2 -> 4
IDHm-A (T2-FLAIR Mismatch)
Malignant Transformation
Baseline
3 months***
7 months
10 months
1 yr 2 mo
1 yr 5 mo
1 yr 7 mo
1 yr 9 mo
1 yr 11 mo
2 yr 2 mo
2 yr 5 mo
2 yr 7 mo
2 yr 10 mo
3 yr 1 mo
3 yr 5 mo
3 yr 7 mo
3 yr 9 mo
3 yr 10 mo
4 yr 4 mo
4 yr 5 mo
4 yr 6 mo
Malignant Transformation Flipbook: Levin Score Assessment
Levin Score
Months

(Slide 20/21)

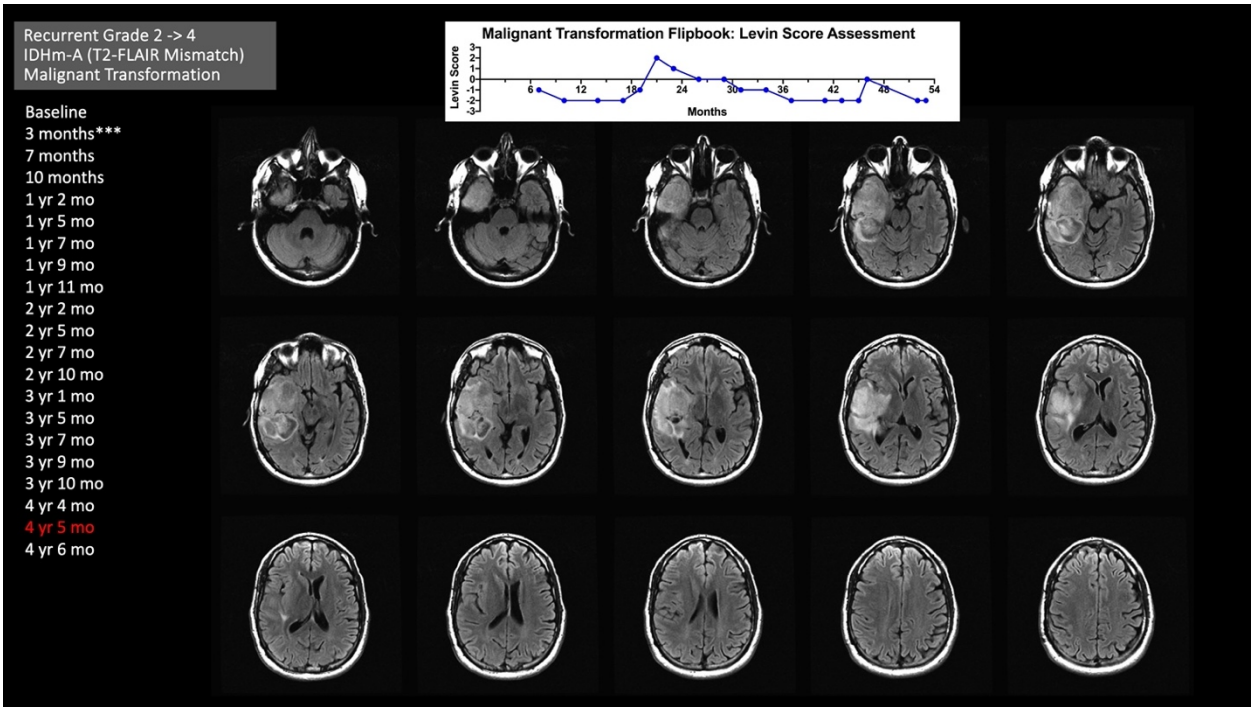
Recurrent Grade 2 -> 4
IDHm-A (T2-FLAIR Mismatch)
Malignant Transformation
Baseline
3 months***
7 months
10 months
1 yr 2 mo
1 yr 5 mo
1 yr 7 mo
1 yr 9 mo
1 yr 11 mo
2 yr 2 mo
2 yr 5 mo
2 yr 7 mo
2 yr 10 mo
3 yr 1 mo
3 yr 5 mo
3 yr 7 mo
3 yr 9 mo
3 yr 10 mo
4 yr 4 mo
4 yr 5 mo
4 yr 6 mo
Malignant Transformation Flipbook: Levin Score Assessment
Levin Score
Months

(Slide 21/21)

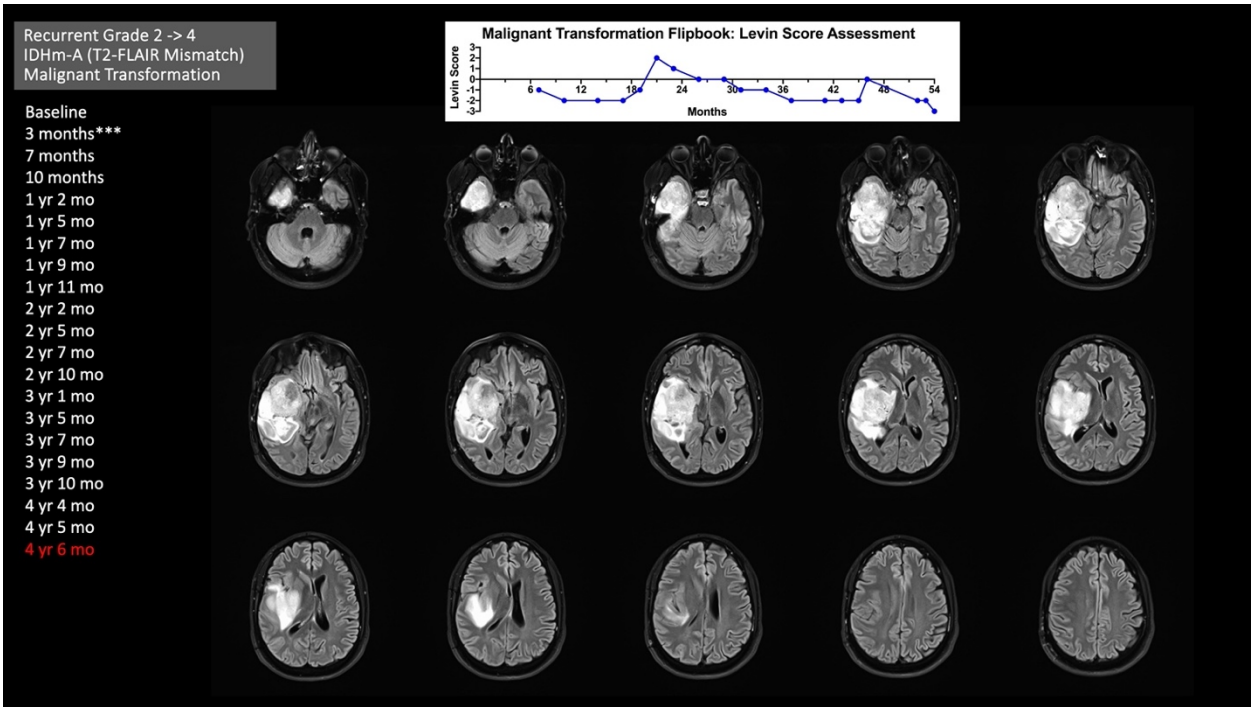
Recurrent Grade 2 -> 4
IDHm-A (T2-FLAIR Mismatch)
Malignant Transformation
Baseline
3 months***
7 months
10 months
1 yr 2 mo
1 yr 5 mo
1 yr 7 mo
1 yr 9 mo
1 yr 11 mo
2 yr 2 mo
2 yr 5 mo
2 yr 7 mo
2 yr 10 mo
3 yr 1 mo
3 yr 5 mo
3 yr 7 mo
3 yr 9 mo
3 yr 10 mo
4 yr 4 mo
4 yr 5 mo
4 yr 6 mo
Malignant Transformation Flipbook: Levin Score Assessment
Levin Score
Months

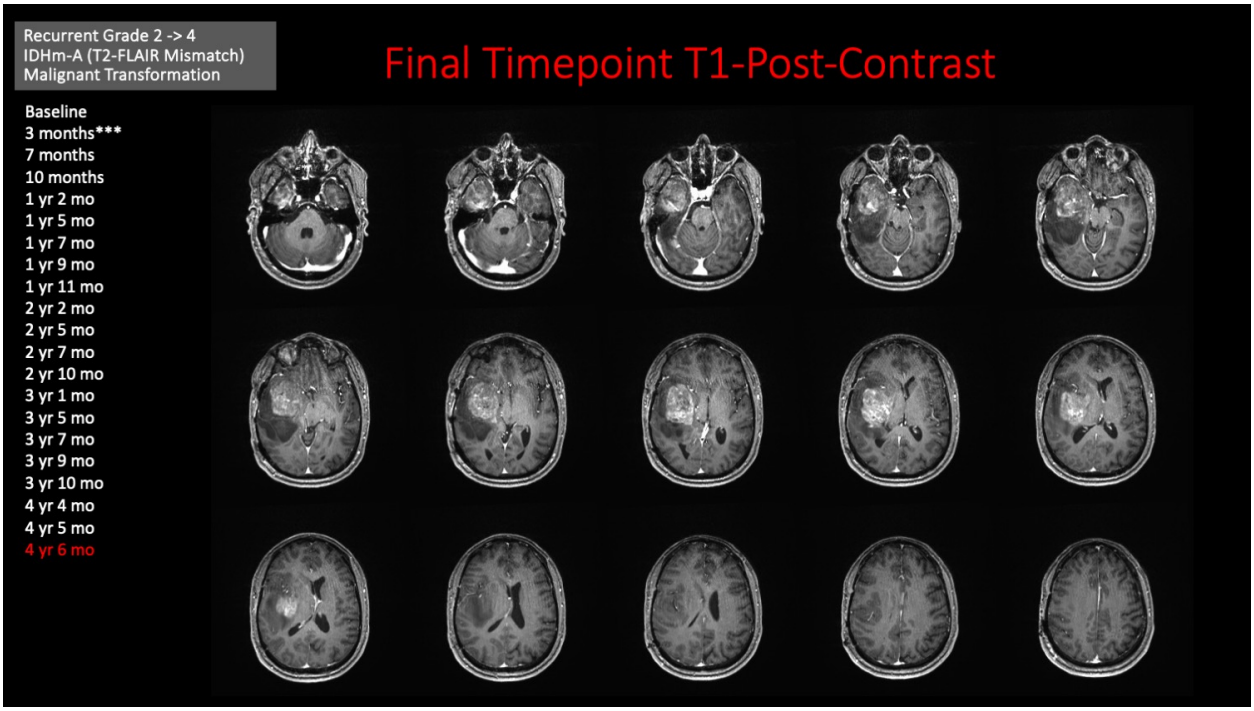
Recurrent Grade 2 -> 4
IDHm-A (T2-FLAIR Mismatch)
Malignant Transformation
Final Timepoint T1-Post-Contrast
Baseline
3 months***
7 months
10 months
1 yr 2 mo
1 yr 5 mo
1 yr 7 mo
1 yr 9 mo
1 yr 11 mo
2 yr 2 mo
2 yr 5 mo
2 yr 7 mo
2 yr 10 mo
3 yr 1 mo
3 yr 5 mo
3 yr 7 mo
3 yr 9 mo
3 yr 10 mo
4 yr 4 mo
4 yr 5 mo
4 yr 6 mo

(Slide 1/14)

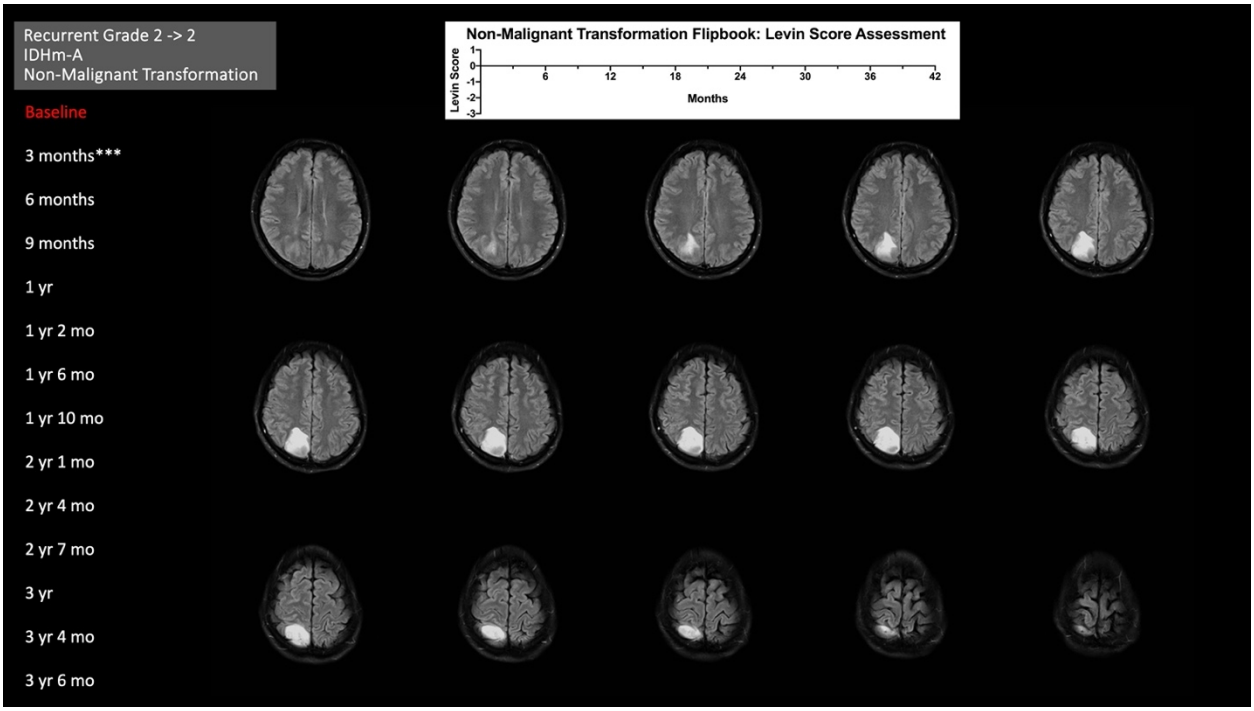

Figure 8.3 Representative Case of Using Flipbooks for Assessing Low-Grade IDH-Mutant Glioma Progression Without Malignant Transformation (T2-Weighted FLAIR MRI). Serial T2-weighted FLAIR images of a 32-year-old male patient with recurrent grade 2 IDH-mutant astrocytoma that remained as grade 2 upon re-resection soon after the conclusion of the flipbooks. The tumor was not treated during the interval of the flipbooks. Subtle tumor growth throughout the 3.5 years along the resection cavity border can be visualized using the flipbooks. **(Please view the flipbook in PDF format as "clickable" page view, not as "scroll" view.)**

(Slide 2/14)

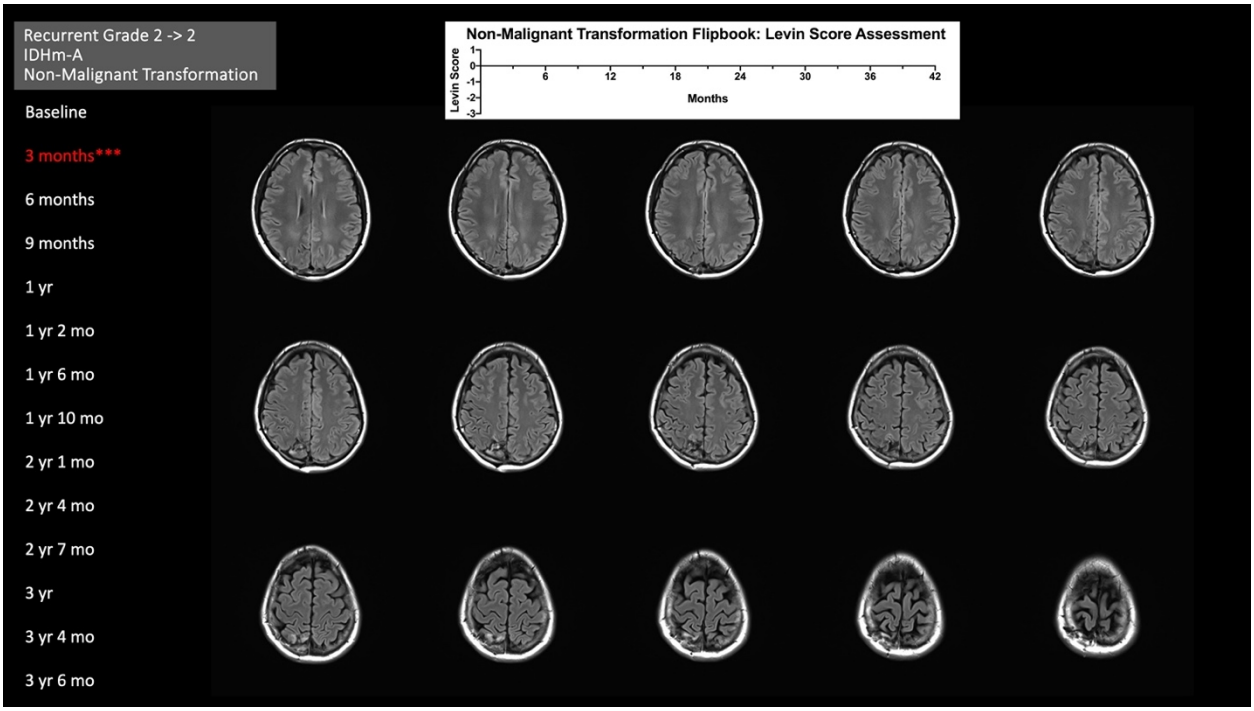
Recurrent Grade 2 -> 2
IDHm-A
Non-Malignant Transformation
Baseline
3 months***
6 months
9 months
1 yr
1 yr 2 mo
1 yr 6 mo
1 yr 10 mo
2 yr 1 mo
2 yr 4 mo
2 yr 7 mo
3 yr
3 yr 4 mo
3 yr 6 mo
Non-Malignant Transformation Flipbook: Levin Score Assessment
Levin Score
1
0
-1
-2
-3
6
12
18
24
30
36
42
Months

(Slide 3/14)

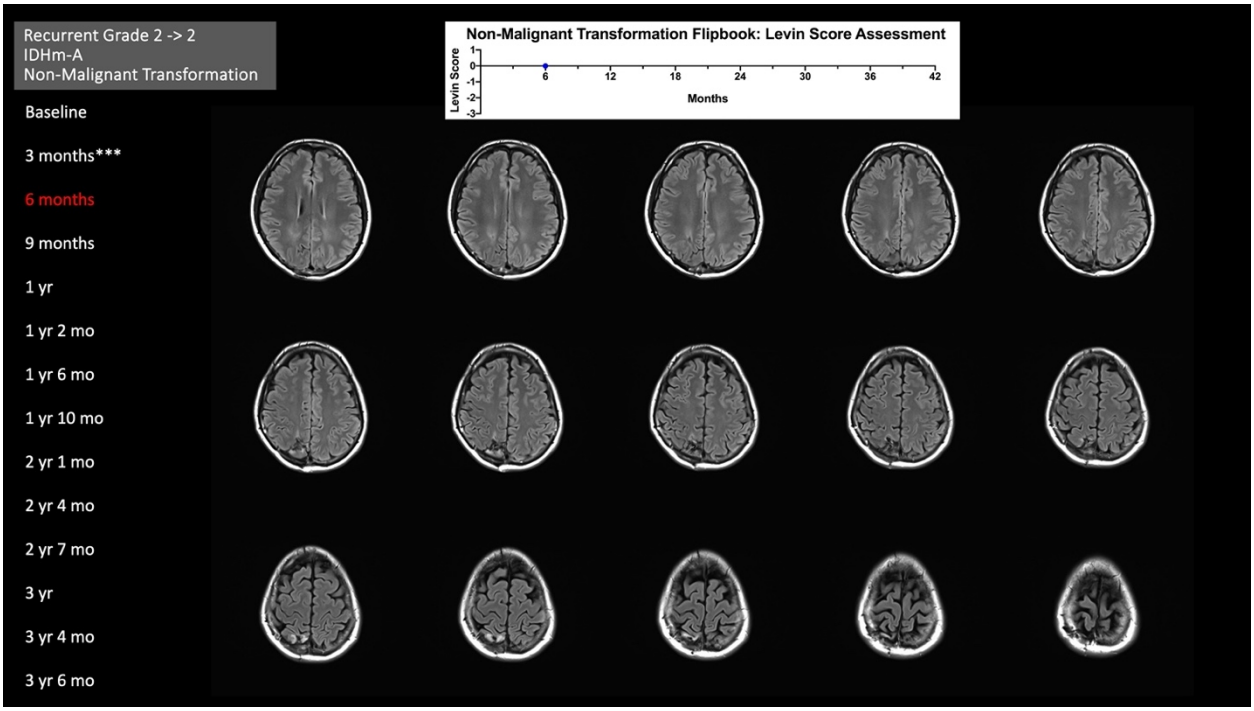
Recurrent Grade 2 -> 2
IDHm-A
Non-Malignant Transformation
Baseline
3 months***
6 months
9 months
1 yr
1 yr 2 mo
1 yr 6 mo
1 yr 10 mo
2 yr 1 mo
2 yr 4 mo
2 yr 7 mo
3 yr
3 yr 4 mo
3 yr 6 mo
Non-Malignant Transformation Flipbook: Levin Score Assessment
Levin Score
1
0
-1
-2
-3
6
12
18
24
30
36
42
Months

(Slide 4/14)

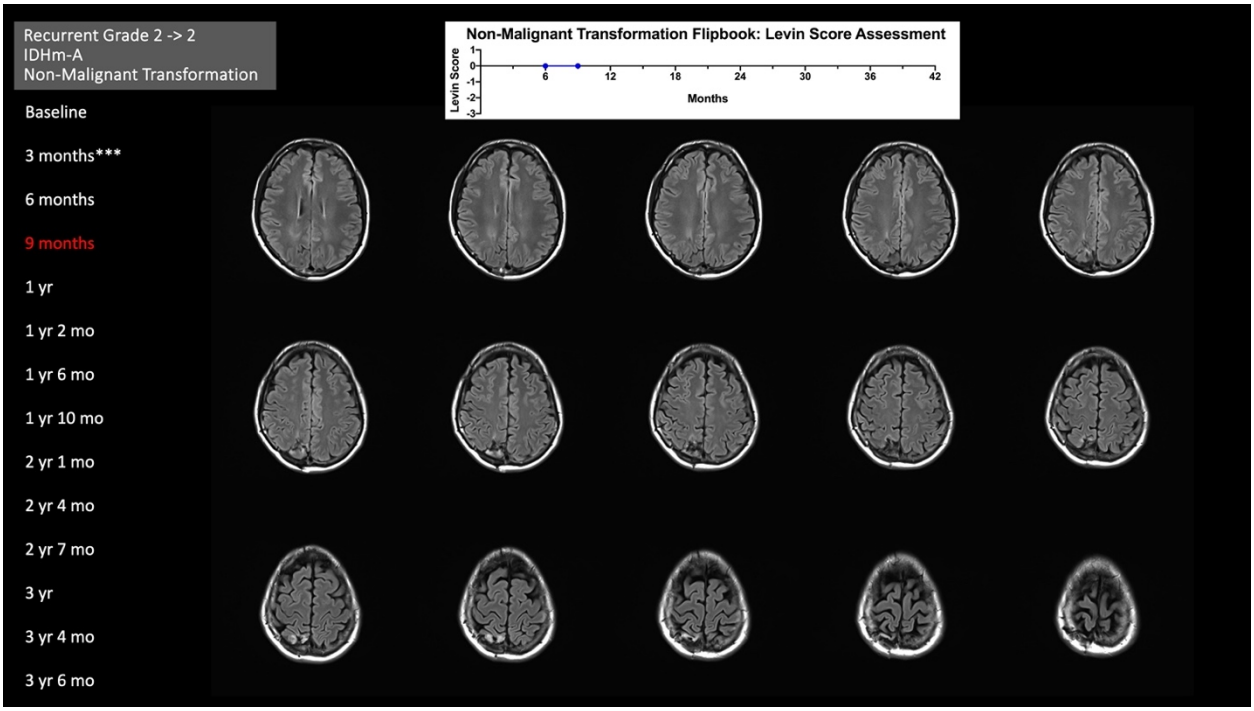
Recurrent Grade 2 -> 2
IDHm-A
Non-Malignant Transformation
Baseline
3 months***
6 months
9 months
1 yr
1 yr 2 mo
1 yr 6 mo
1 yr 10 mo
2 yr 1 mo
2 yr 4 mo
2 yr 7 mo
3 yr
3 yr 4 mo
3 yr 6 mo
Non-Malignant Transformation Flipbook: Levin Score Assessment
Levin Score
1
0
-1
-2
-3
6
12
18
24
30
36
42
Months

(Slide 5/14)

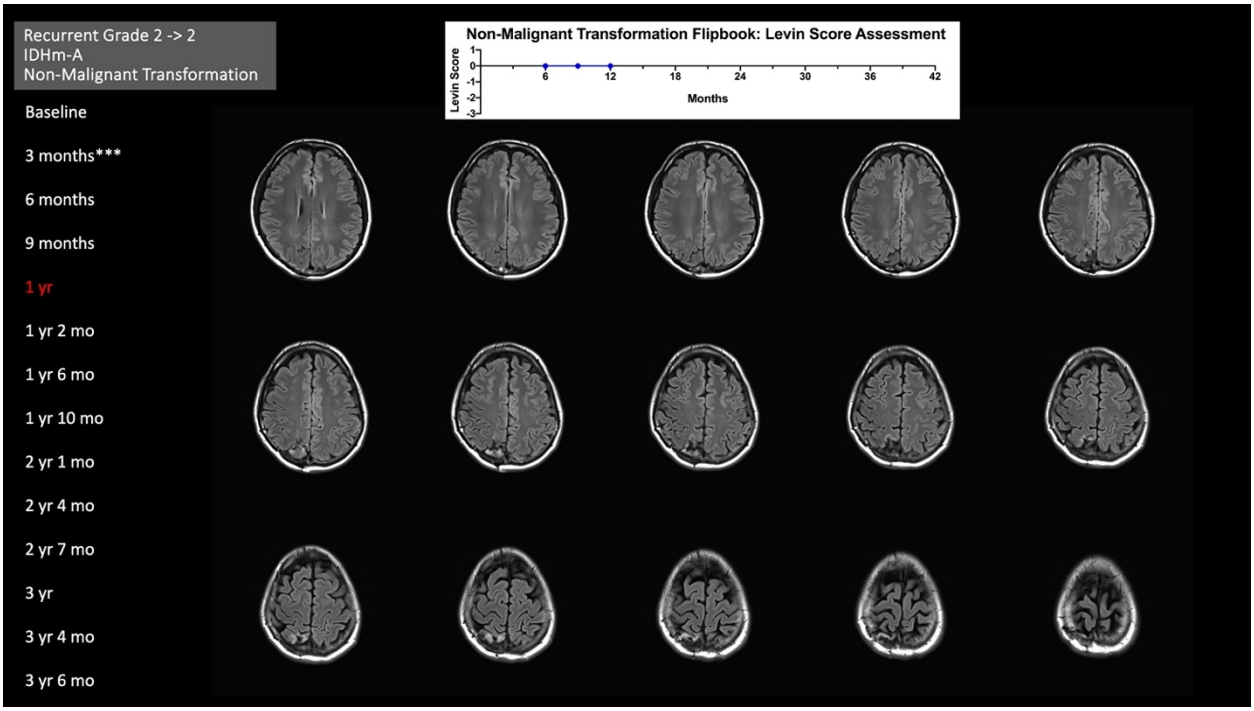
Recurrent Grade 2 -> 2
IDHm-A
Non-Malignant Transformation
Baseline
3 months***
6 months
9 months
1 yr
1 yr 2 mo
1 yr 6 mo
1 yr 10 mo
2 yr 1 mo
2 yr 4 mo
2 yr 7 mo
3 yr
3 yr 4 mo
3 yr 6 mo
Non-Malignant Transformation Flipbook: Levin Score Assessment
Levin Score
1
0
-1
-2
-3
6
12
18
24
30
36
42
Months

(Slide 6/14)

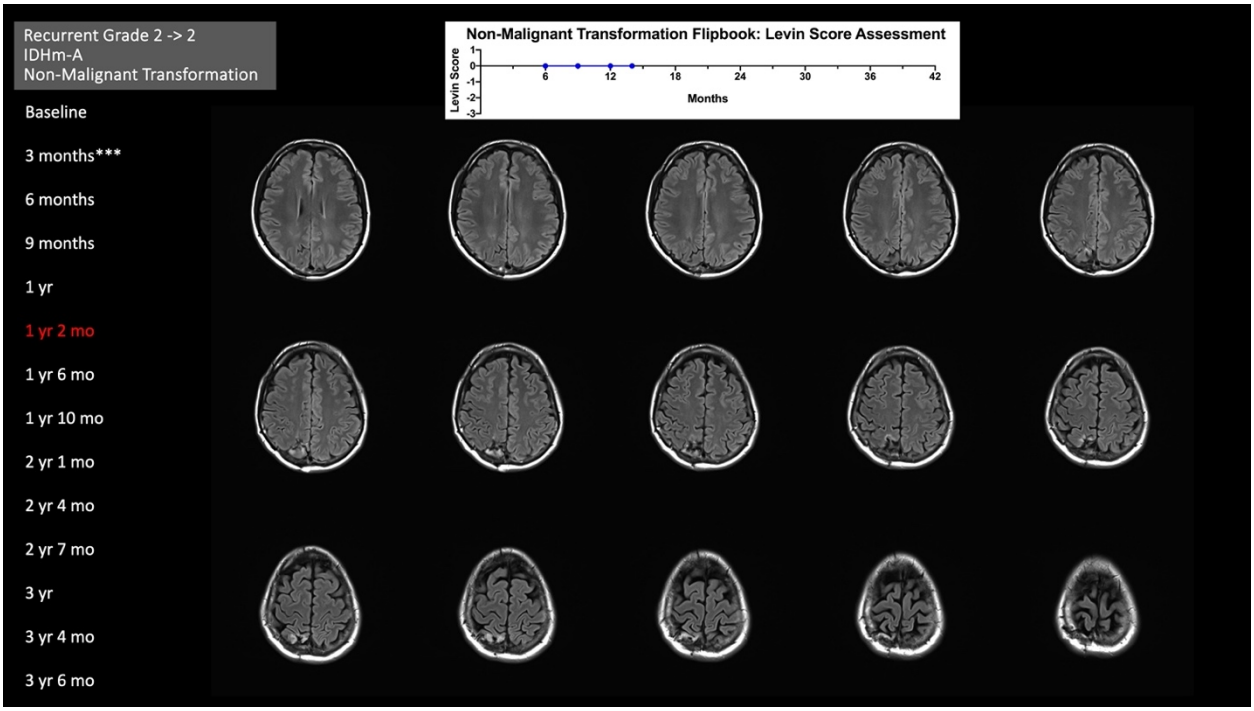
Recurrent Grade 2 -> 2
IDHm-A
Non-Malignant Transformation
Baseline
3 months***
6 months
9 months
1 yr
1 yr 2 mo
1 yr 6 mo
1 yr 10 mo
2 yr 1 mo
2 yr 4 mo
2 yr 7 mo
3 yr
3 yr 4 mo
3 yr 6 mo
Non-Malignant Transformation Flipbook: Levin Score Assessment
Levin Score
1
0
-1
-2
-3
6
12
18
24
30
36
42
Months

(Slide 7/14)

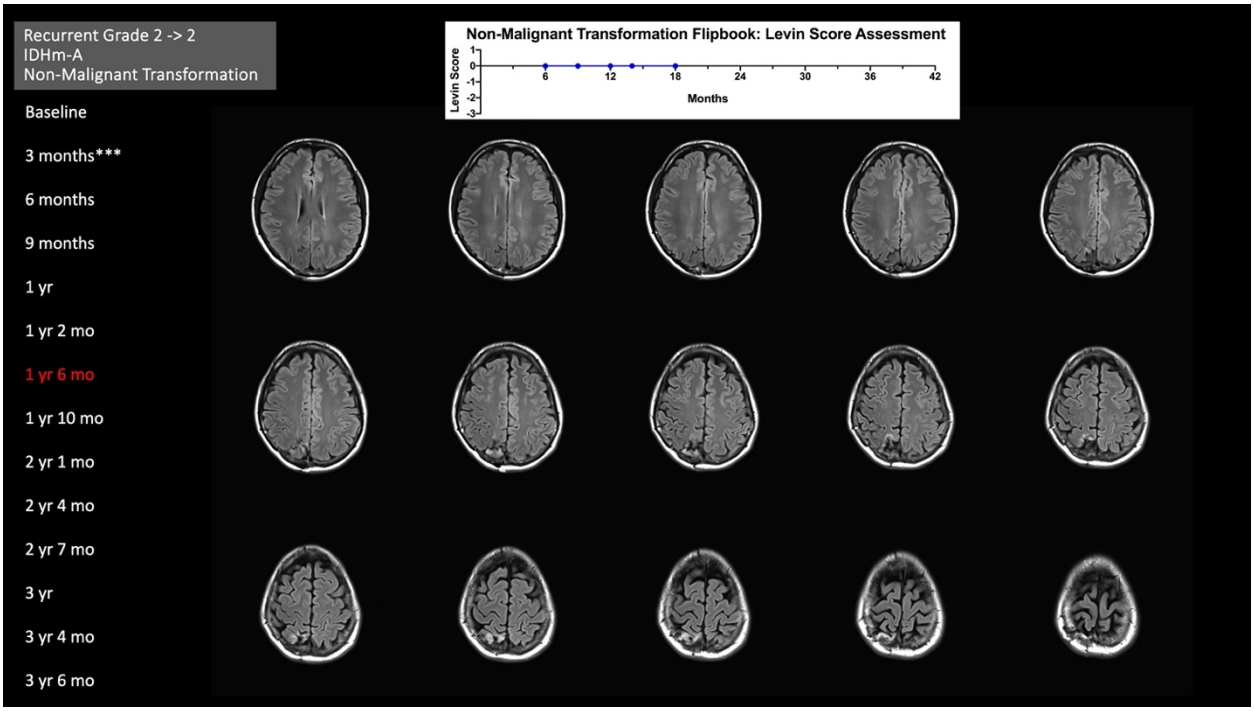
Recurrent Grade 2 -> 2
IDHm-A
Non-Malignant Transformation
Baseline
3 months***
6 months
9 months
1 yr
1 yr 2 mo
1 yr 6 mo
1 yr 10 mo
2 yr 1 mo
2 yr 4 mo
2 yr 7 mo
3 yr
3 yr 4 mo
3 yr 6 mo
Non-Malignant Transformation Flipbook: Levin Score Assessment
Levin Score
1
0
-1
-2
-3
6
12
18
24
30
36
42
Months

(Slide 8/14)

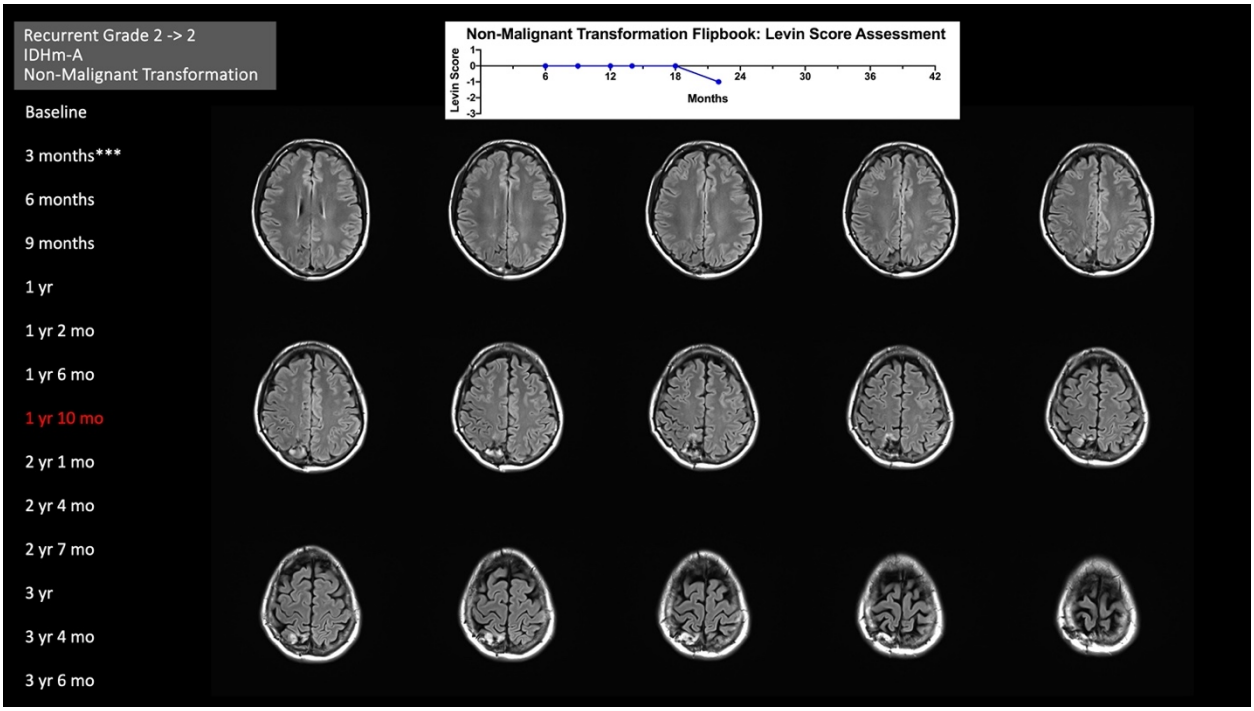
Recurrent Grade 2 -> 2
IDHm-A
Non-Malignant Transformation
Baseline
3 months***
6 months
9 months
1 yr
1 yr 2 mo
1 yr 6 mo
1 yr 10 mo
2 yr 1 mo
2 yr 4 mo
2 yr 7 mo
3 yr
3 yr 4 mo
3 yr 6 mo
Non-Malignant Transformation Flipbook: Levin Score Assessment
Levin Score
1
0
-1
-2
-3
6
12
18
24
30
36
42
Months

(Slide 9/14)

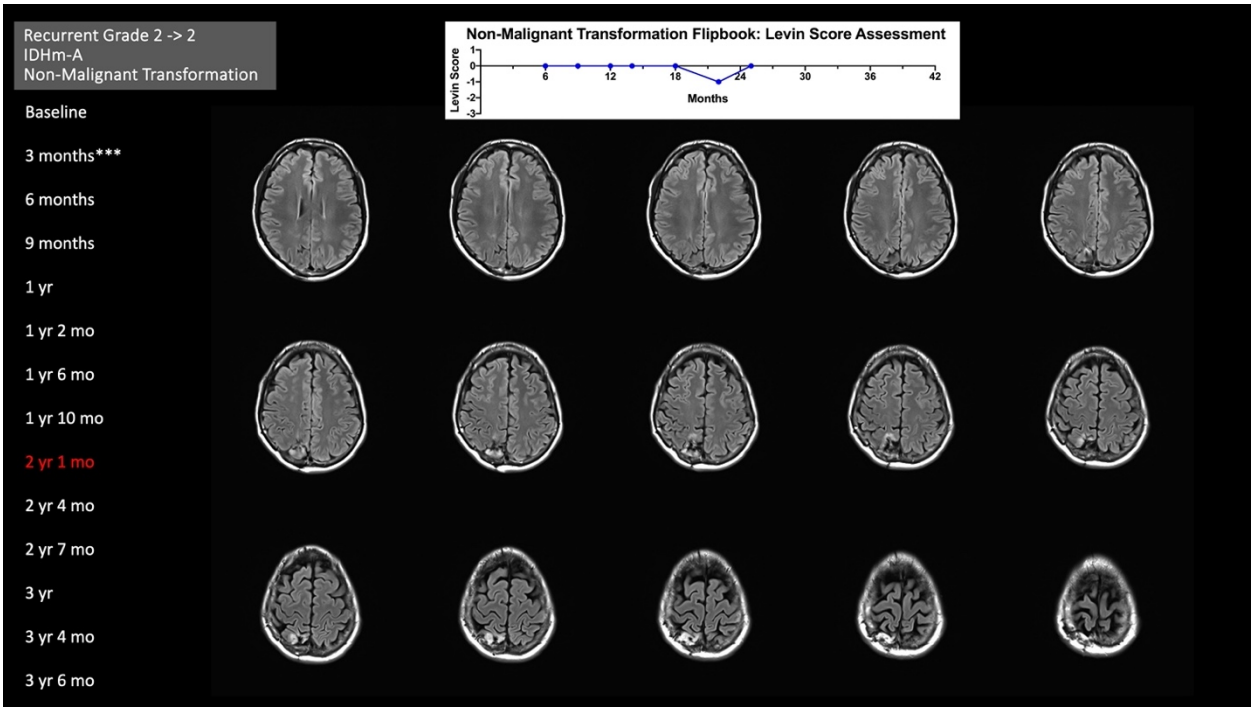
Recurrent Grade 2 -> 2
IDHm-A
Non-Malignant Transformation
Baseline
3 months***
6 months
9 months
1 yr
1 yr 2 mo
1 yr 6 mo
1 yr 10 mo
2 yr 1 mo
2 yr 4 mo
2 yr 7 mo
3 yr
3 yr 4 mo
3 yr 6 mo
Non-Malignant Transformation Flipbook: Levin Score Assessment
Levin Score
1
0
-1
-2
-3
6
12
18
24
30
36
42
Months

(Slide 10/14)

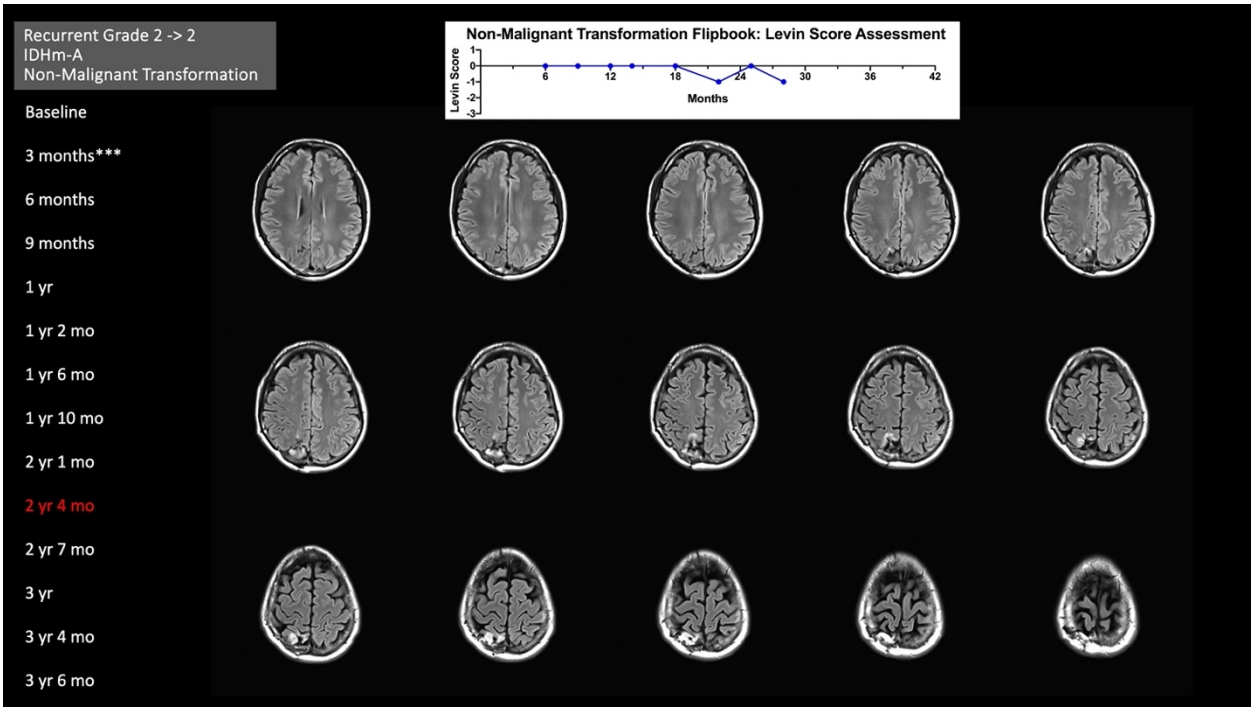
Recurrent Grade 2 -> 2
IDHm-A
Non-Malignant Transformation
Baseline
3 months***
6 months
9 months
1 yr
1 yr 2 mo
1 yr 6 mo
1 yr 10 mo
2 yr 1 mo
2 yr 4 mo
2 yr 7 mo
3 yr
3 yr 4 mo
3 yr 6 mo
Non-Malignant Transformation Flipbook: Levin Score Assessment
Levin Score
1
0
-1
-2
-3
6
12
18
24
30
36
42
Months

(Slide 11/14)

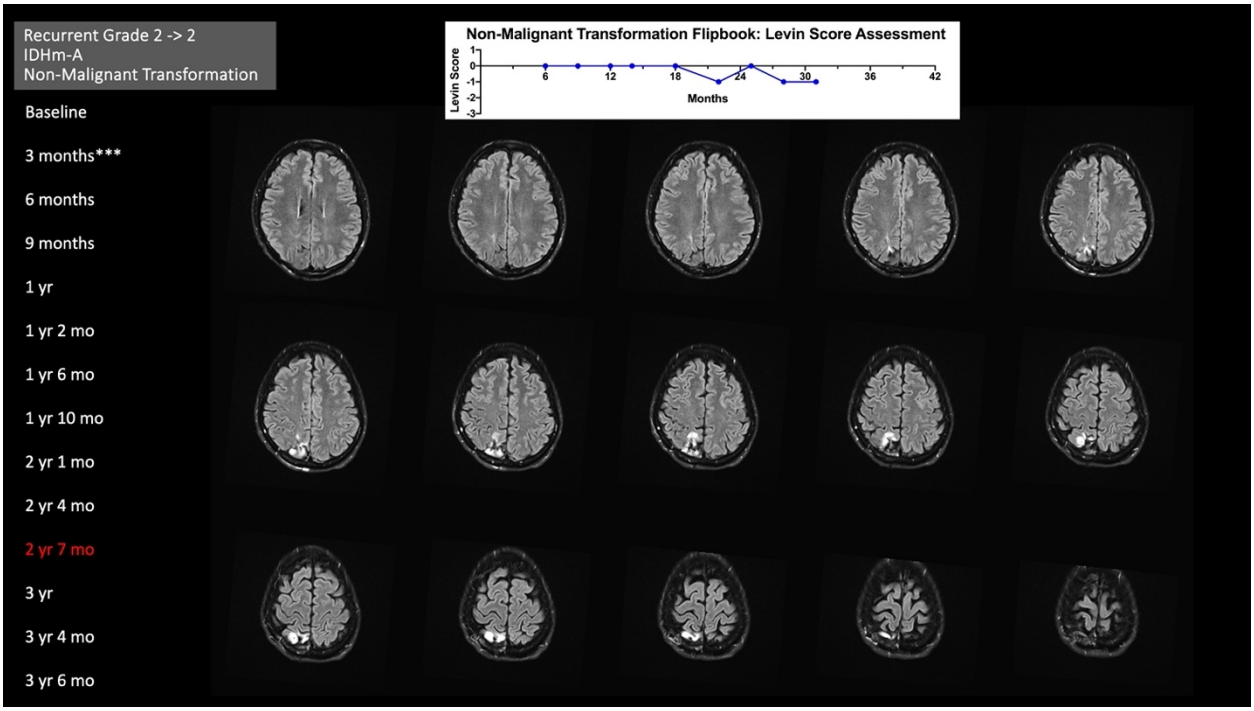
Recurrent Grade 2 -> 2
IDHm-A
Non-Malignant Transformation
Baseline
3 months***
6 months
9 months
1 yr
1 yr 2 mo
1 yr 6 mo
1 yr 10 mo
2 yr 1 mo
2 yr 4 mo
2 yr 7 mo
3 yr
3 yr 4 mo
3 yr 6 mo
Non-Malignant Transformation Flipbook: Levin Score Assessment
Levin Score
1
0
-1
-2
-3
6
12
18
24
30
36
42
Months

(Slide 12/14)

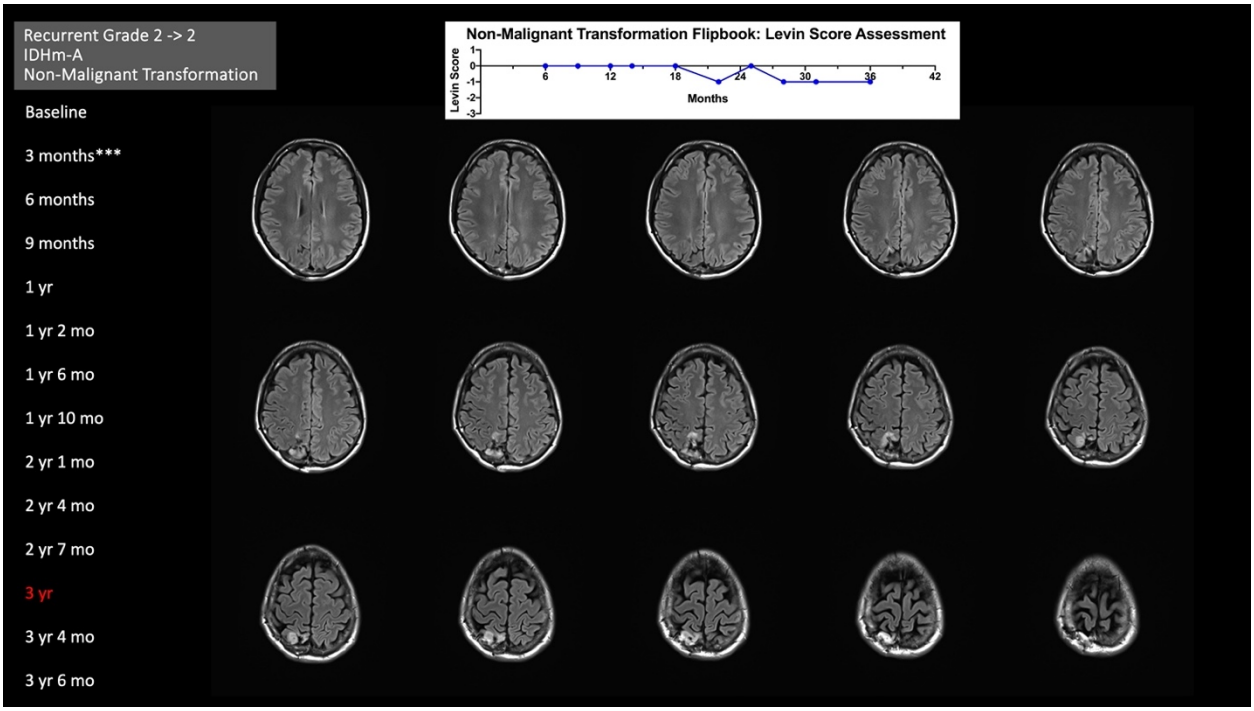
Recurrent Grade 2 -> 2
IDHm-A
Non-Malignant Transformation
Baseline
3 months***
6 months
9 months
1 yr
1 yr 2 mo
1 yr 6 mo
1 yr 10 mo
2 yr 1 mo
2 yr 4 mo
2 yr 7 mo
3 yr
3 yr 4 mo
3 yr 6 mo
Non-Malignant Transformation Flipbook: Levin Score Assessment
Levin Score
1
0
-1
-2
-3
6
12
18
24
30
36
42
Months

(Slide 13/14)

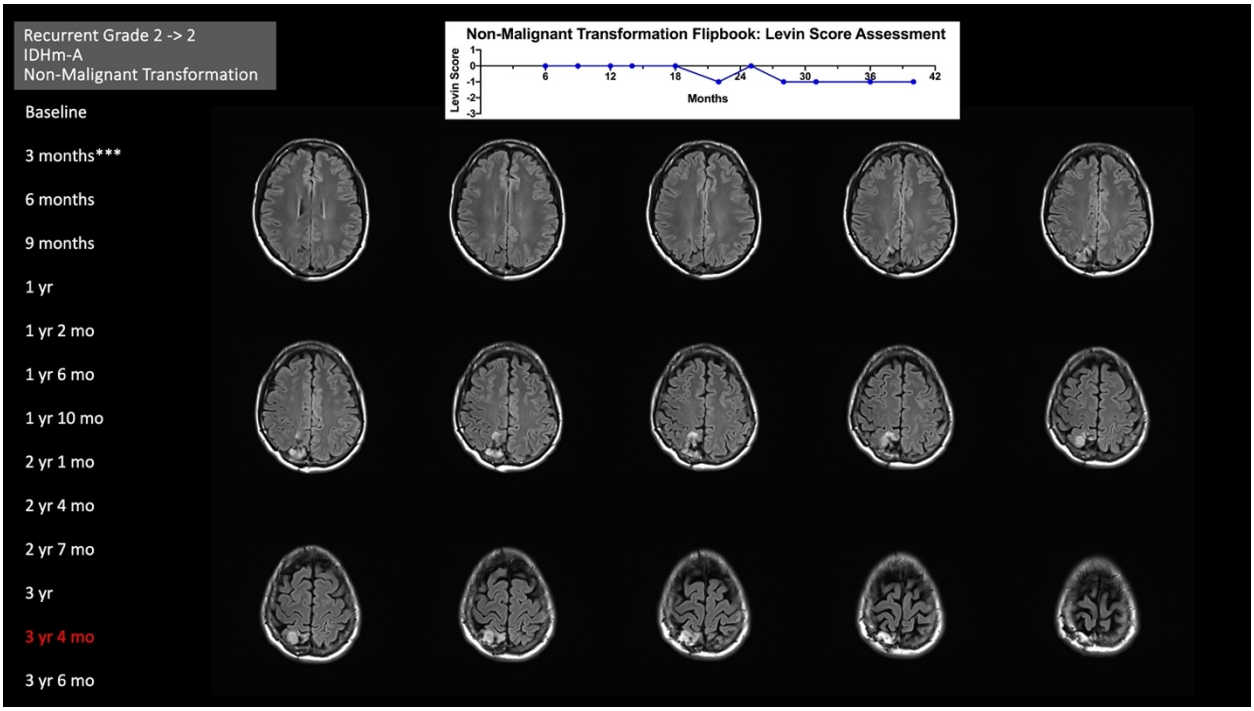
Recurrent Grade 2 -> 2
IDHm-A
Non-Malignant Transformation
Baseline
3 months***
6 months
9 months
1 yr
1 yr 2 mo
1 yr 6 mo
1 yr 10 mo
2 yr 1 mo
2 yr 4 mo
2 yr 7 mo
3 yr
3 yr 4 mo
3 yr 6 mo
Non-Malignant Transformation Flipbook: Levin Score Assessment
Levin Score
1
0
-1
-2
-3
6
12
18
24
30
36
42
Months

(Slide 14/14)

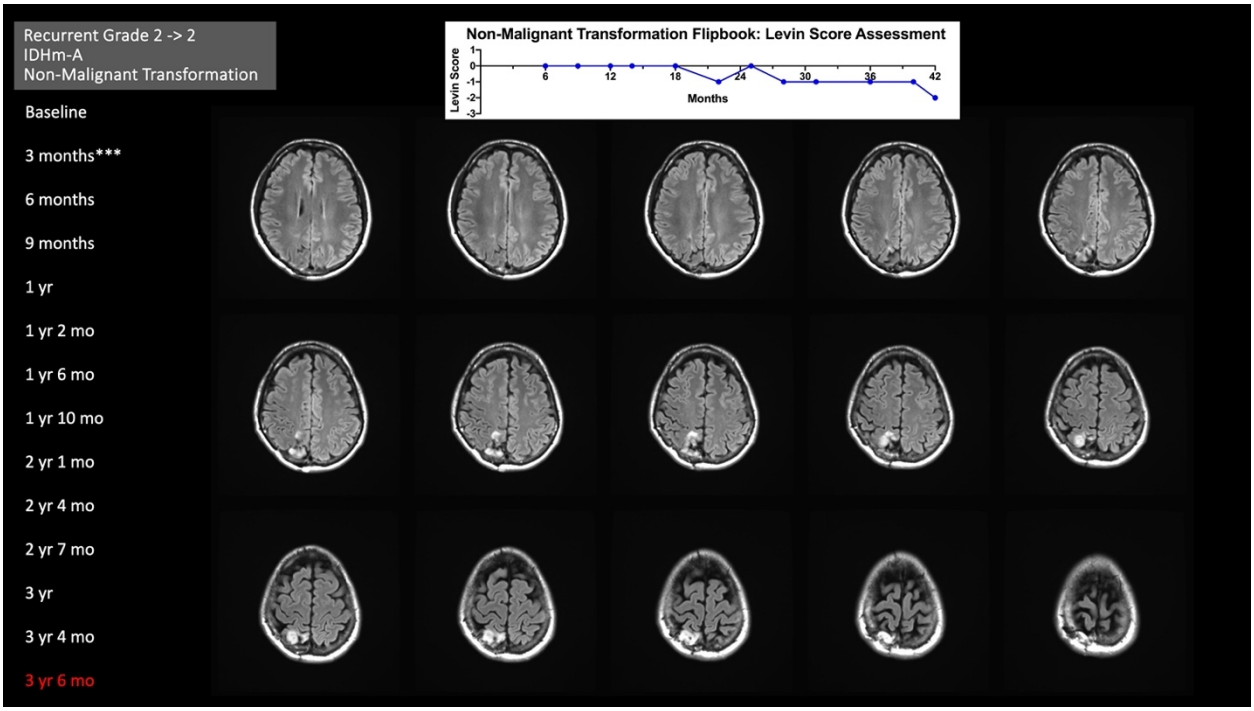
Recurrent Grade 2 -> 2
IDHm-A
Non-Malignant Transformation
Baseline
3 months***
6 months
9 months
1 yr
1 yr 2 mo
1 yr 6 mo
1 yr 10 mo
2 yr 1 mo
2 yr 4 mo
2 yr 7 mo
3 yr
3 yr 4 mo
3 yr 6 mo
Non-Malignant Transformation Flipbook: Levin Score Assessment
Levin Score
1
0
-1
-2
-3
6
12
18
24
30
36
42
Months

Slowly Growing Low-Grade IDH-Mutant Glioma: Mixed Response

There are also instances when only a portion of the tumor responds to therapy while other areas continue to grow. **Figure 8.4** (T2-weighted FLAIR MRI flipbook) shows a representative case of a 38-year-old female patient with recurrent grade 2 IDH-mutant non-enhancing astrocytoma involving the left frontal, temporal, and insular areas who received AG-120 IDH inhibitor therapy. During follow-up imaging, the tumor slowly shrank in the insular region while growing in the frontal and parietal lobe. This case showcases two advantages provided by flipbooks. First, tumor shrinkage (insula) and growth (frontal and parietal lobe) are slow-paced and easier to appreciate after superimposing multiple timepoints. Second, the "mixed" response (with one component progressing and one component responding to treatment) is easier to appreciate compared to quantitative measurements that may include the sum of the lesion sizes. Indeed, while the overall quantitative tumor burden may appear stable in mixed response cases, from a pathophysiological standpoint one of the lesions is clearly progressing and may require a change in clinical management (e.g., change of therapy, surgical resection, or radiation).

(Slide 1/8)

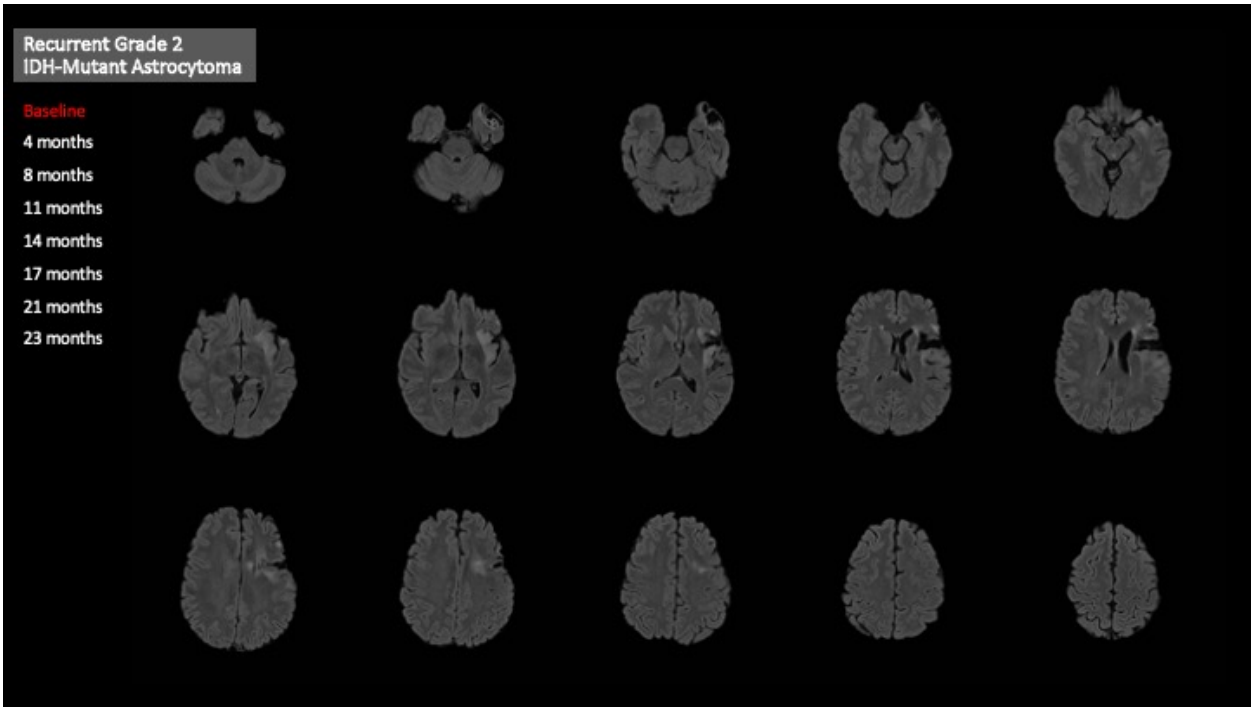

Figure 8.4. Representative Case of Using Flipbooks for Assessing Low-Grade IDH-Mutant Glioma with "Mixed Response" (T2-Weighted FLAIR MRI). Serial T2-weighted FLAIR images of a 38-year-old female patient with recurrent grade 2 IDH-mutant non-enhancing astrocytoma involving the left frontal, temporal, and insular areas who received AG-120 IDH inhibitor therapy. The lesion showed a mixed response to the treatments with progressive T2-hyperintensity and infiltrative growth in the parietal and posterior frontal regions as well as gradual shrinkage of the insular infiltrative component. **(Please view the flipbook in PDF format as "clickable" page view, not as "scroll" view.)**

(Slide 2/8)

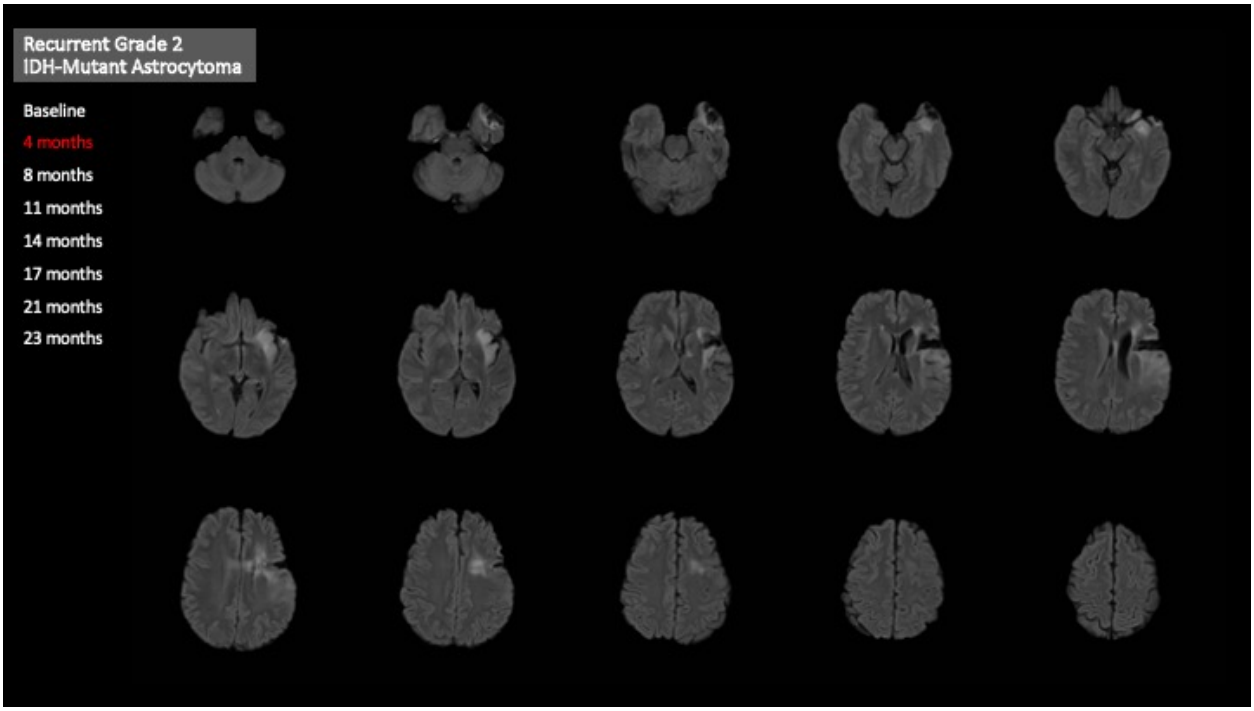
Recurrent Grade 2
IDH-Mutant Astrocytoma
Baseline
4 months
8 months
11 months
14 months
17 months
21 months
23 months

(Slide 3/8)

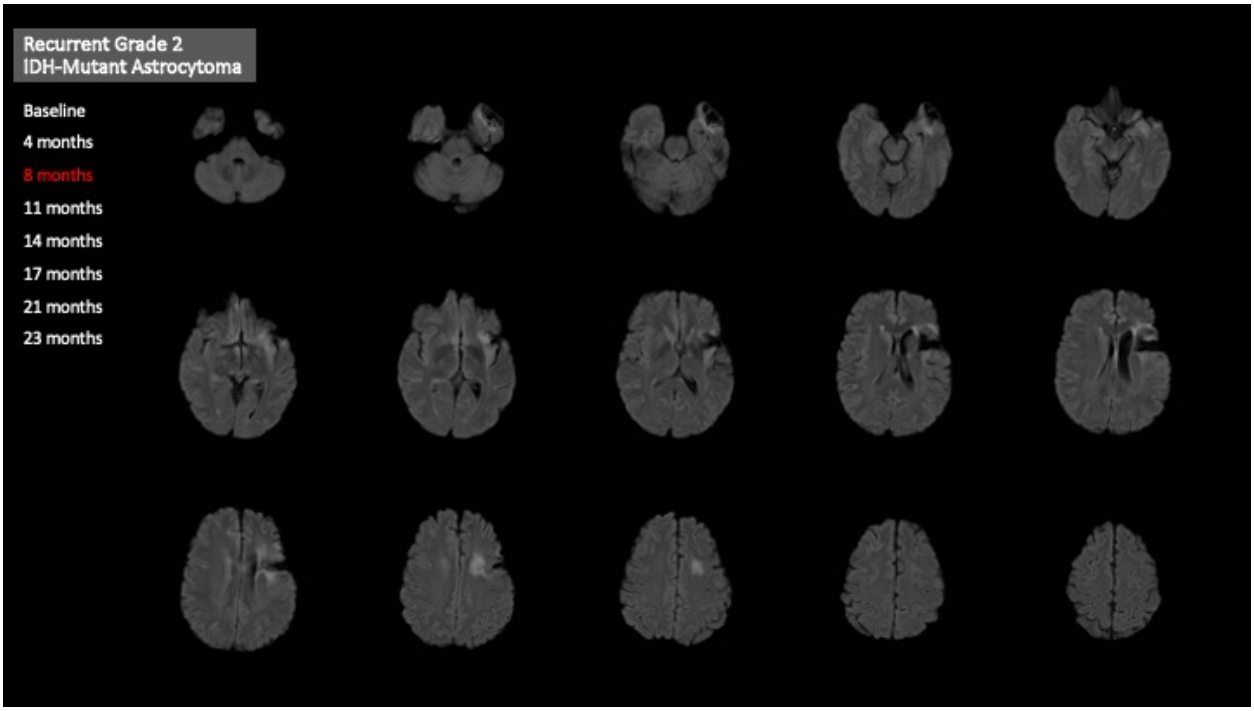
Recurrent Grade 2
IDH-Mutant Astrocytoma
Baseline
4 months
8 months
11 months
14 months
17 months
21 months
23 months

(Slide 4/8)

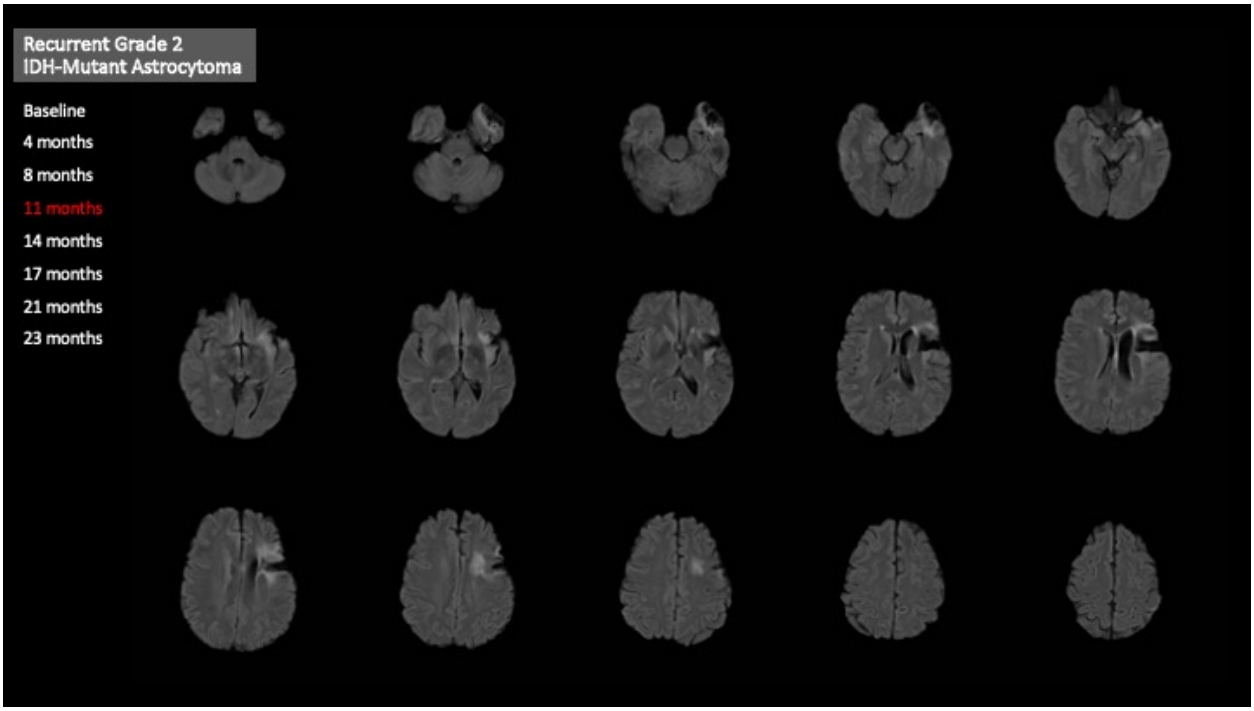
Recurrent Grade 2
IDH-Mutant Astrocytoma
Baseline
4 months
8 months
11 months
14 months
17 months
21 months
23 months

(Slide 5/8)

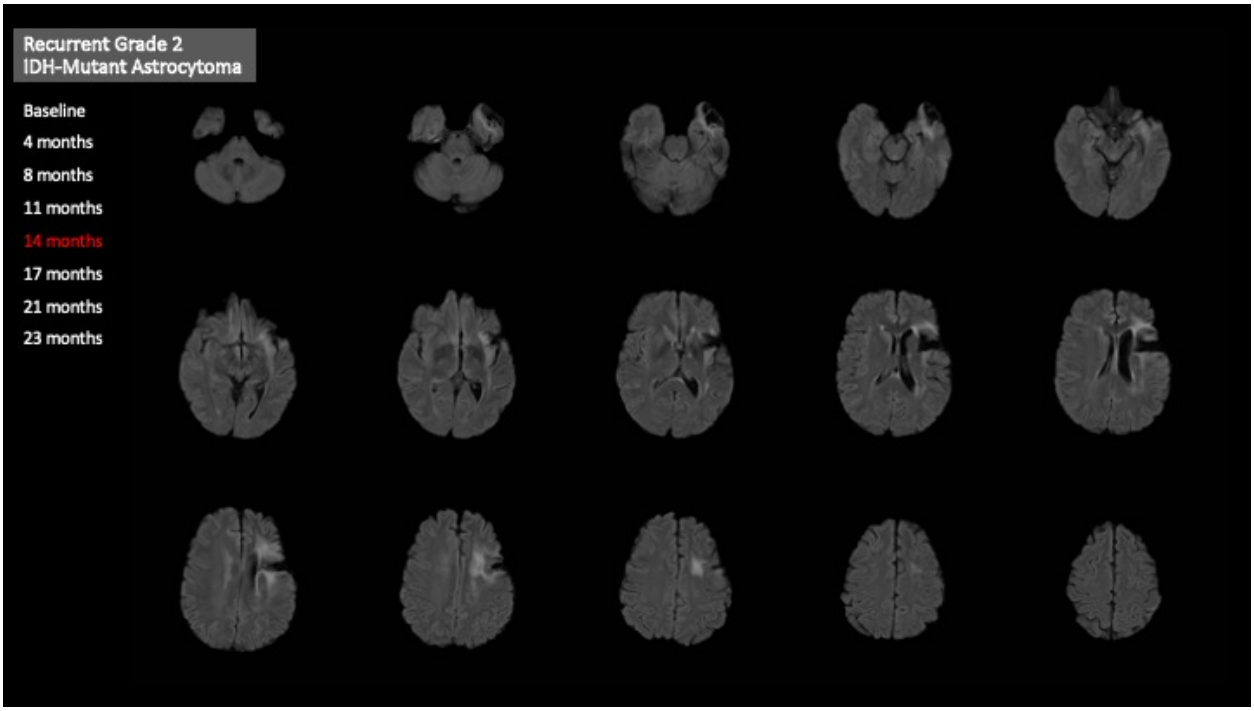
Recurrent Grade 2
IDH-Mutant Astrocytoma
Baseline
4 months
8 months
11 months
14 months
17 months
21 months
23 months

(Slide 6/8)

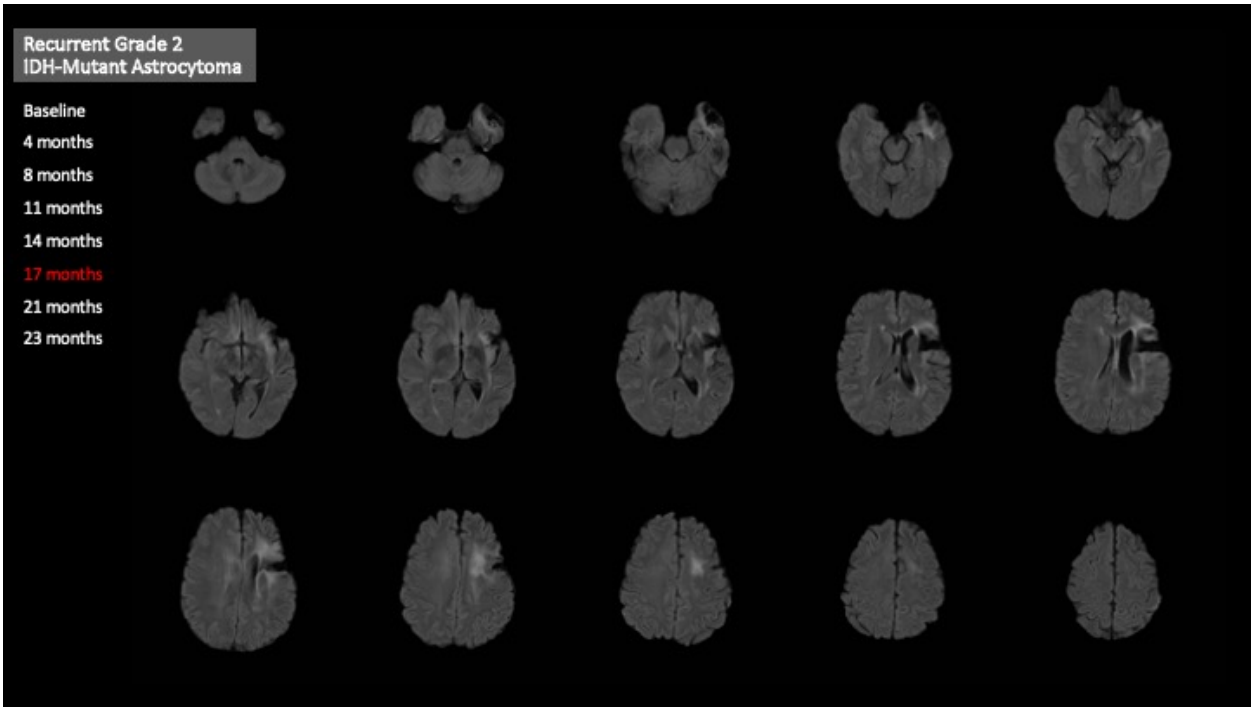
Recurrent Grade 2
IDH-Mutant Astrocytoma
Baseline
4 months
8 months
11 months
14 months
17 months
21 months
23 months

(Slide 7/8)

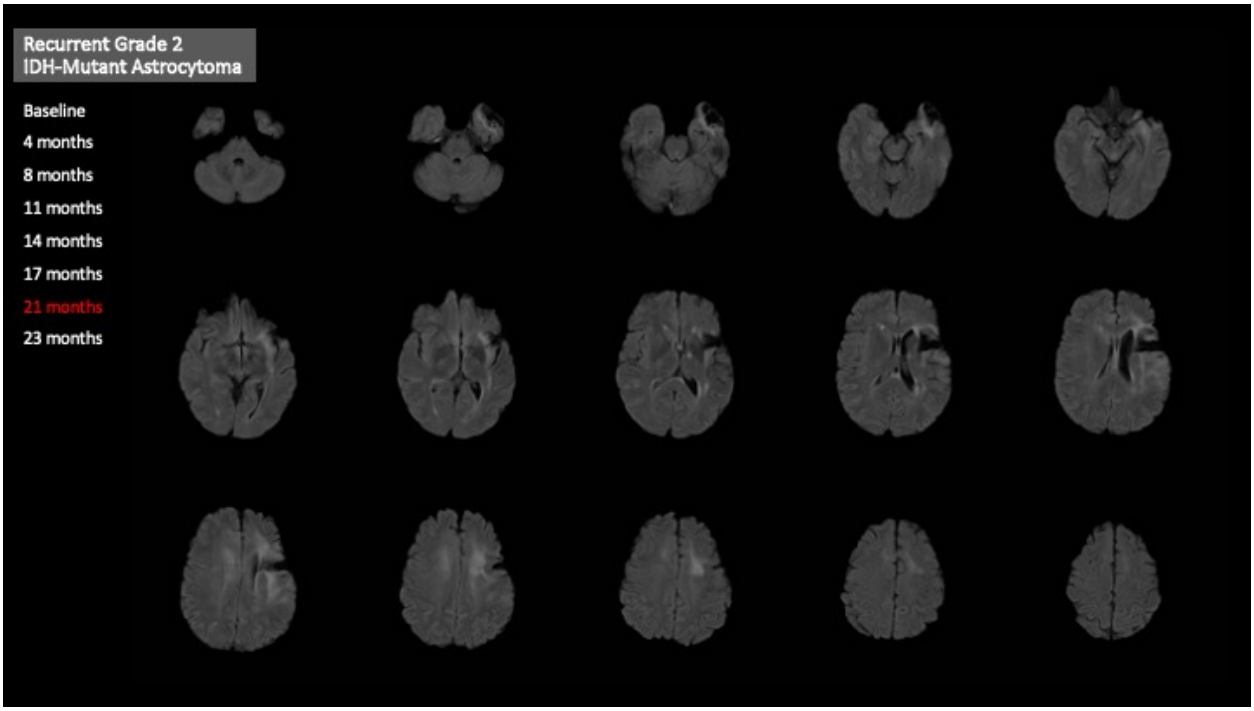
Recurrent Grade 2
IDH-Mutant Astrocytoma
Baseline
4 months
8 months
11 months
14 months
17 months
21 months
23 months

(Slide 8/8)

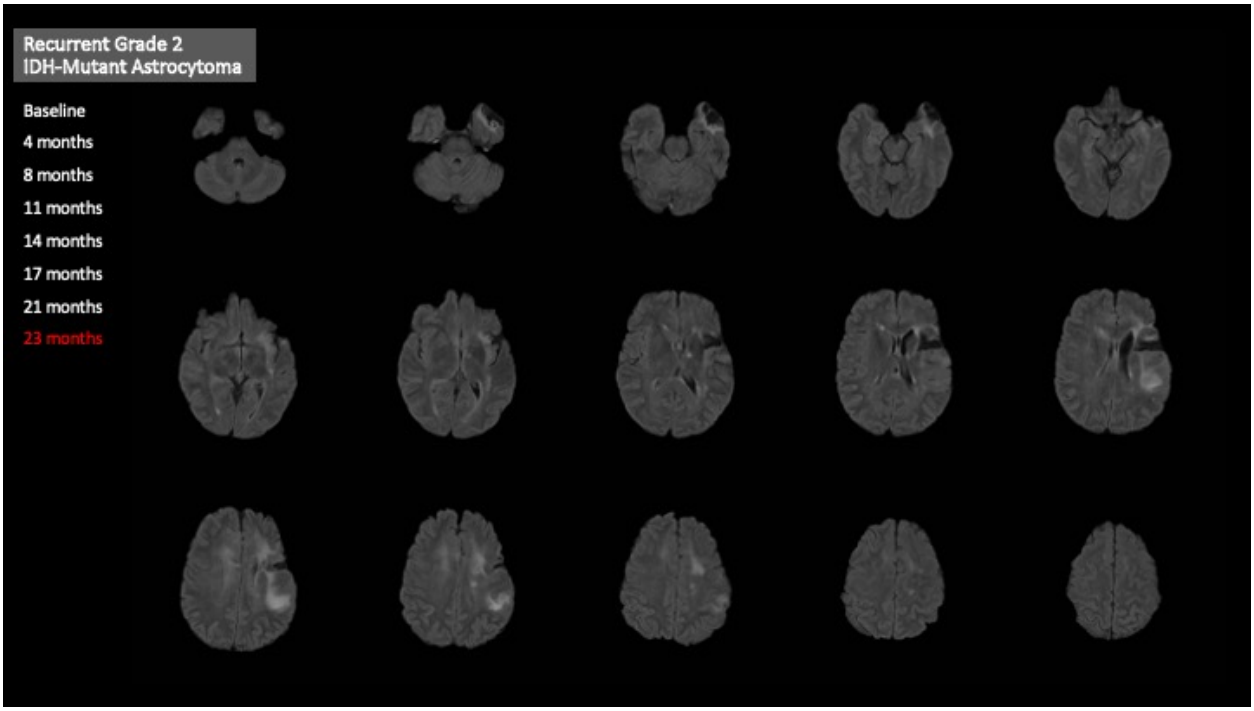
Recurrent Grade 2
IDH-Mutant Astrocytoma
Baseline
4 months
8 months
11 months
14 months
17 months
21 months
23 months

Post-Operative Peri-Cavitary Changes in Non-Enhancing Tumor

The assessment of T2/FLAIR changes over time in non-enhancing tumors is made difficult by the fact that T2/FLAIR hyperintense tissue may represent either neoplastic tissue (progressive disease) and/or non-neoplastic tissue, including vasogenic edema, surgery-induced gliosis, radiation-induced leukoencephalopathy, leukoaraiosis related to microangiopathic insults, and more. In particular, post-surgical changes can complicate the assessment of tumor progression or response because they can induce signal alterations in T2/FLAIR with a rate consistent with growth rates in lower grade gliomas, albeit often associated volume loss or stability. Peri-cavitary, post-surgical T2/FLAIR hyperintense alterations can be challenging to distinguish from residual neoplastic tissue. On contrast-enhanced T1-weighted images, surgery-induced non-neoplastic enhancement typically appears on the cavity border, possibly related to a blood-brain permeability increase due to devitalized tissue/necrosis, non-tumoral neovascularization, and reactive changes.[208, 209] This phenomenon is usually transitory and also occurs in patients undergoing resection for non-neoplastic conditions, such as epilepsy,[210] which confirms that these changes are induced by the surgery and not ascribable to tumor tissue. Indeed, recognizing non-neoplastic contrast-enhancement is crucial for a correct management of low-grade gliomas, since the appearance of contrast-enhancing tissue is typically concerning for disease progression with transformation in a higher grade ("malignant transformation"),[40, 176] which bears worse prognosis.

Digital flipbooks can be useful in the assessment of peri-cavitary radiographic findings. First, co-registering the pre- and post-surgical images allows to clearly identify peri-cavitary alterations that were present prior to surgery and to distinguish them from alterations appeared only after surgery. This is relevant because T2/FLAIR hyperintense tissue that is recognizable both before and after surgery possibly represents residual, unresected disease. Conversely, new areas of

peri-cavitary signal alterations that appear after surgery are likely ascribable to edema and reactive changes/gliosis. Second, the evaluation of multiple superimposed timepoints with flipbooks allows to appreciate the evolution of peri-cavitary alterations over time. Indeed, T2/FLAIR hyperintense tissue that grows and progressively causes mass effect probably represents residual/recurrent tumor, whereas post-surgical reactive changes typically appear stable or cause shrinkage over time. In more detail, post-surgical changes related to gliosis or scarring are typically associated with gradual tissue volume loss, expansion of the sulci, and ex vacuo enlargement of the ventricles that can last weeks[211] or many months when compounded with radiation-induced changes.[212-214] Conversely, signal alterations induced by tumor growth are associated with progressive gyral enlargement, sulcal effacement, and compression of the ventricles.

Figure 8.5 (T2-weighted FLAIR MRI & post-contrast T1-weighted flipbooks stacked) illustrate a representative case of post-surgical T2/FLAIR and T1-post-contrast alterations in a 33-year-old male patient diagnosed with recurrent grade 2 IDH-mutant oligodendroglioma in the right parietal lobe and temporo-parietal junction. After surgery, the follow-up scans showed the appearance of peri-cavitary non-enhancing alterations in the temporal lobe (post-surgical timepoint at month 5) and in the parietal lobe (month 6, corresponding to ~1 month after surgery), which were absent in the pre-surgical timepoint (pre-surgical timepoint at month 5). Additionally, peri-cavitary rim enhancement is noticed in the parietal lobe (month 6, corresponding to ~1 month after surgery). All these findings are ascribable to non-neoplastic post-surgical changes since they were absent on the pre-surgical timepoint, and because they demonstrated a typical evolution on follow-up imaging: the peri-cavitary enhancement gradually reduced, the parietal T2/FLAIR alteration showed stable appearance over time without mass effect, and the temporal T2/FLAIR

alteration shrank over time and was associated with tissue loss and ex vacuo dilation of the trigon of the lateral ventricle.

(Figure Legend Presented Before Figure due to Space Limitations)

Figure 8.5. Representative Case of Using Flipbooks for Assessing Post-Operative Glioma Changes (T2-Weighted FLAIR MRI and Post-Contrast T1-Weighted MRI). Serial T2-weighted FLAIR images (top) and post-contrast T1-weighted images (bottom) for a 33-year-old male patient diagnosed with recurrent grade 2 IDH-mutant oligodendroglioma in the right parietal lobe and temporo-parietal junction. The early post-surgical scan showed the appearance of a new area of peri-cavitary T2-hyperintensity (at 5 months, post-surgery). The following scan demonstrated additional peri-cavitary T2-hyperintense areas in the parietal lobe, accompanied by prominent peri-cavitary rim enhancement (month 6). These findings were compatible with non-neoplastic post-surgical changes, and the follow-up scans demonstrated a volumetric reduction of the T2-hyperintense areas and regression of the contrast-enhancement associated with overall tissue loss causing an ex vacuo dilation of the lateral ventricle. **(Please view the flipbook in PDF format as "clickable" page view, not as "scroll" view.)**

(Slide 1/16)

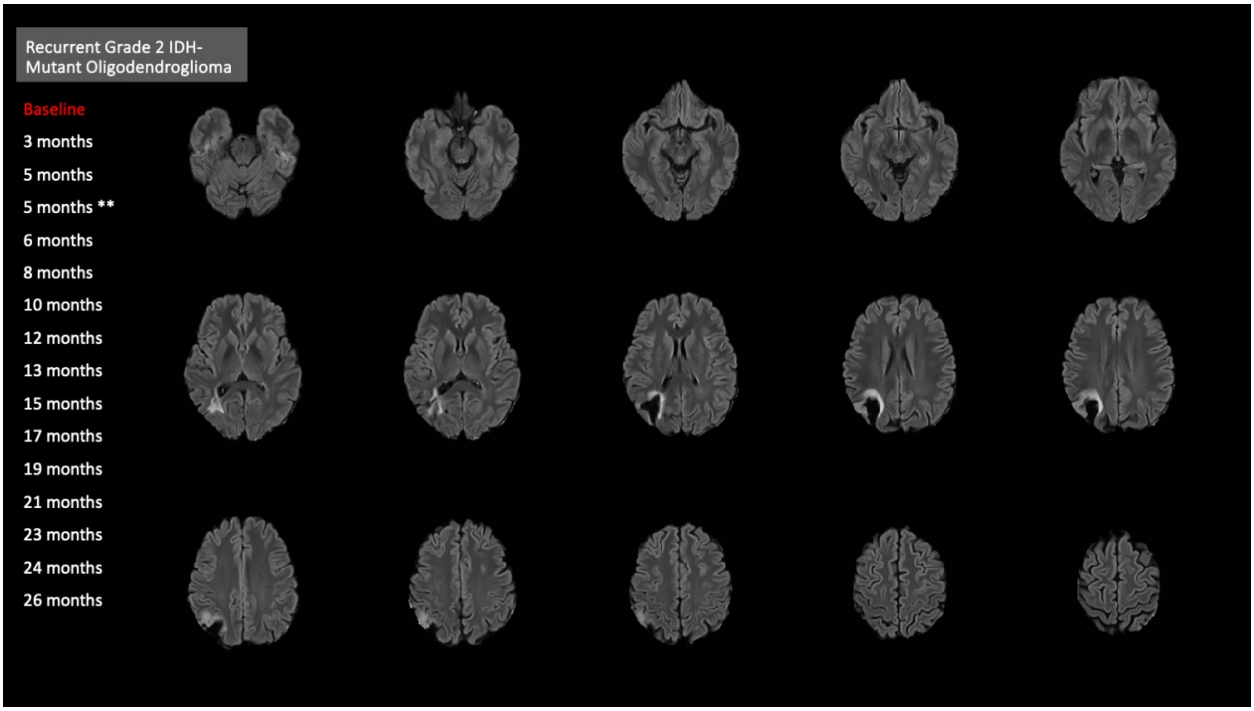
Recurrent Grade 2 IDH-Mutant Oligodendroglioma
Baseline
3 months
5 months
5 months **
6 months
8 months
10 months
12 months
13 months
15 months
17 months
19 months
21 months
23 months
24 months
26 months

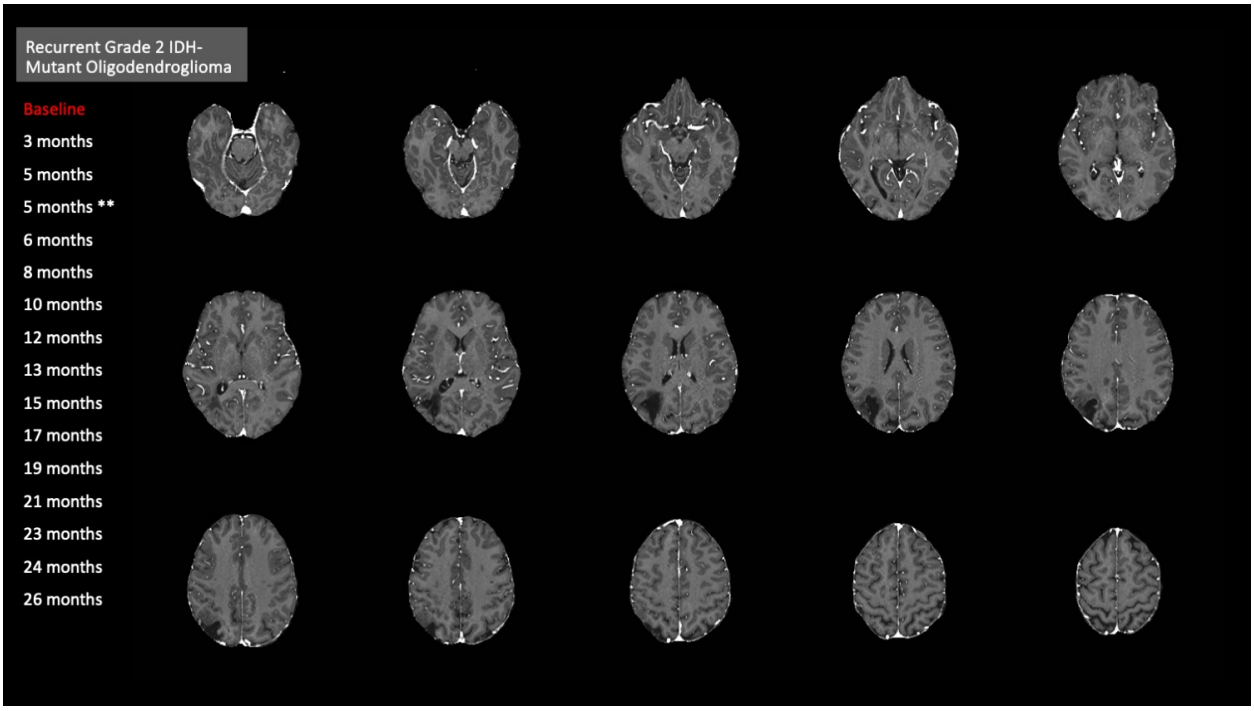
Recurrent Grade 2 IDH-Mutant Oligodendroglioma
Baseline
3 months
5 months
5 months **
6 months
8 months
10 months
12 months
13 months
15 months
17 months
19 months
21 months
23 months
24 months
26 months

(Slide 2/16)

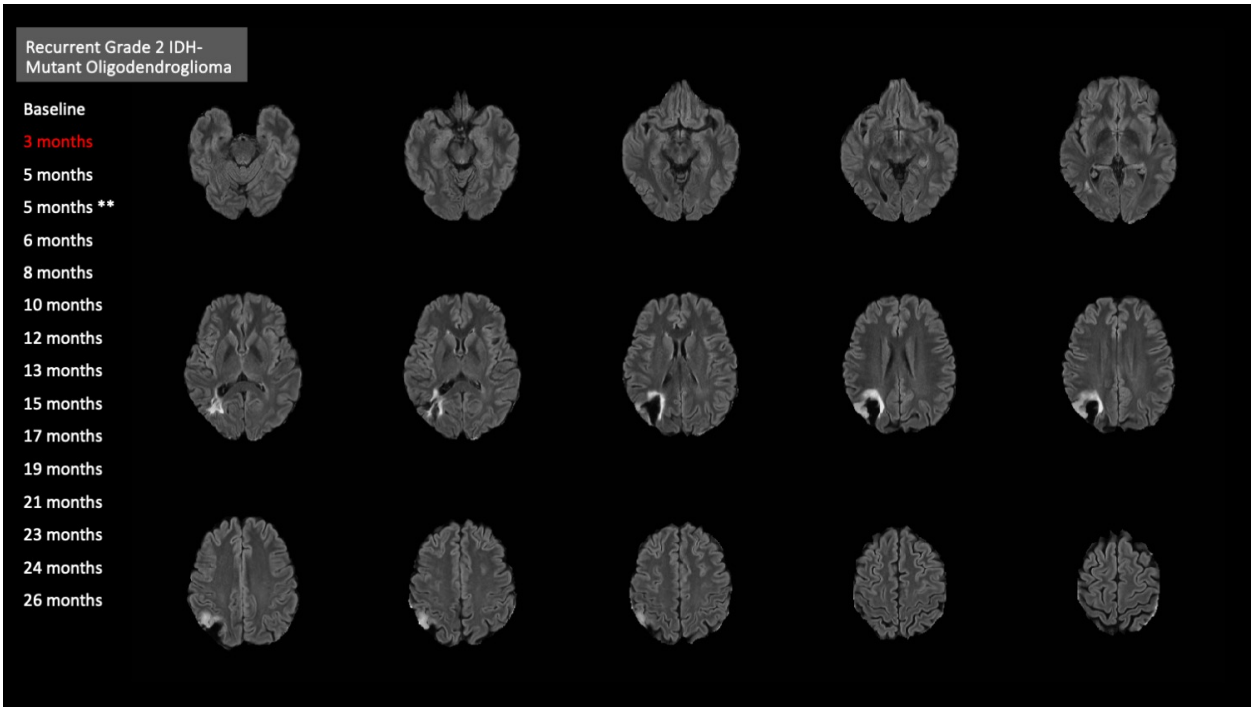
Recurrent Grade 2 IDH-Mutant Oligodendroglioma
Baseline
3 months
5 months
5 months **
6 months
8 months
10 months
12 months
13 months
15 months
17 months
19 months
21 months
23 months
24 months
26 months

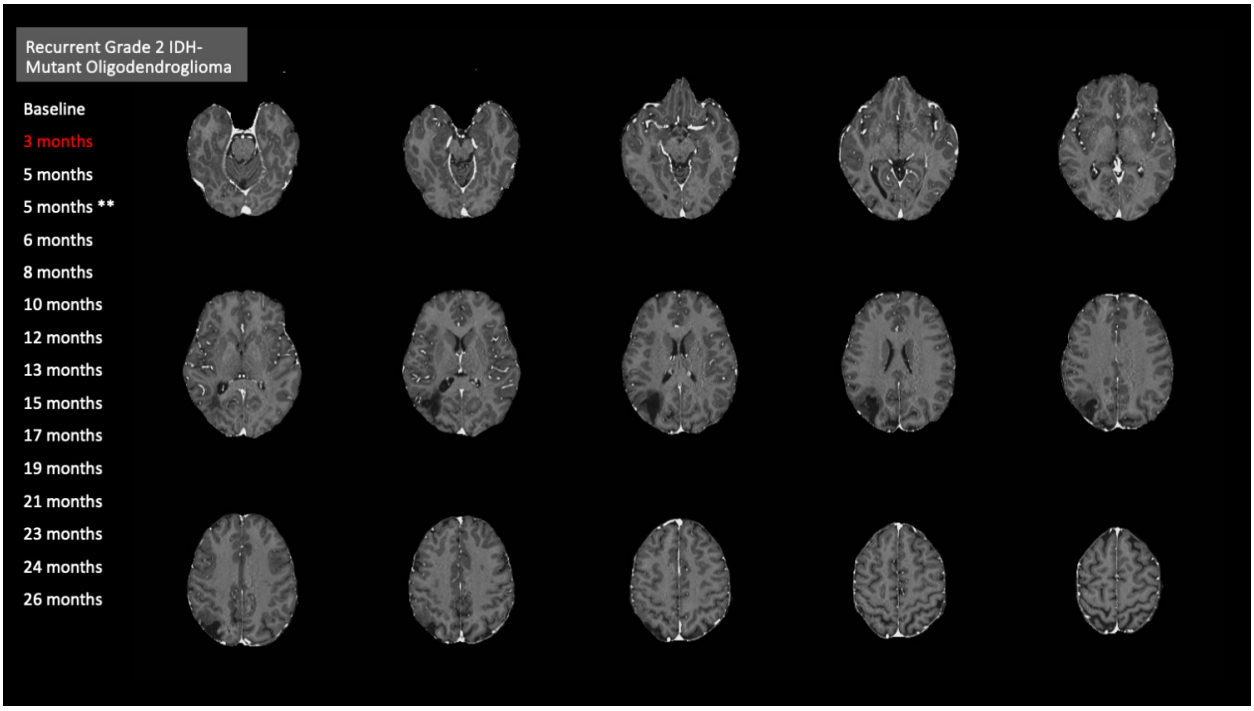
Recurrent Grade 2 IDH-Mutant Oligodendroglioma
Baseline
3 months
5 months
5 months **
6 months
8 months
10 months
12 months
13 months
15 months
17 months
19 months
21 months
23 months
24 months
26 months

(Slide 3/16)

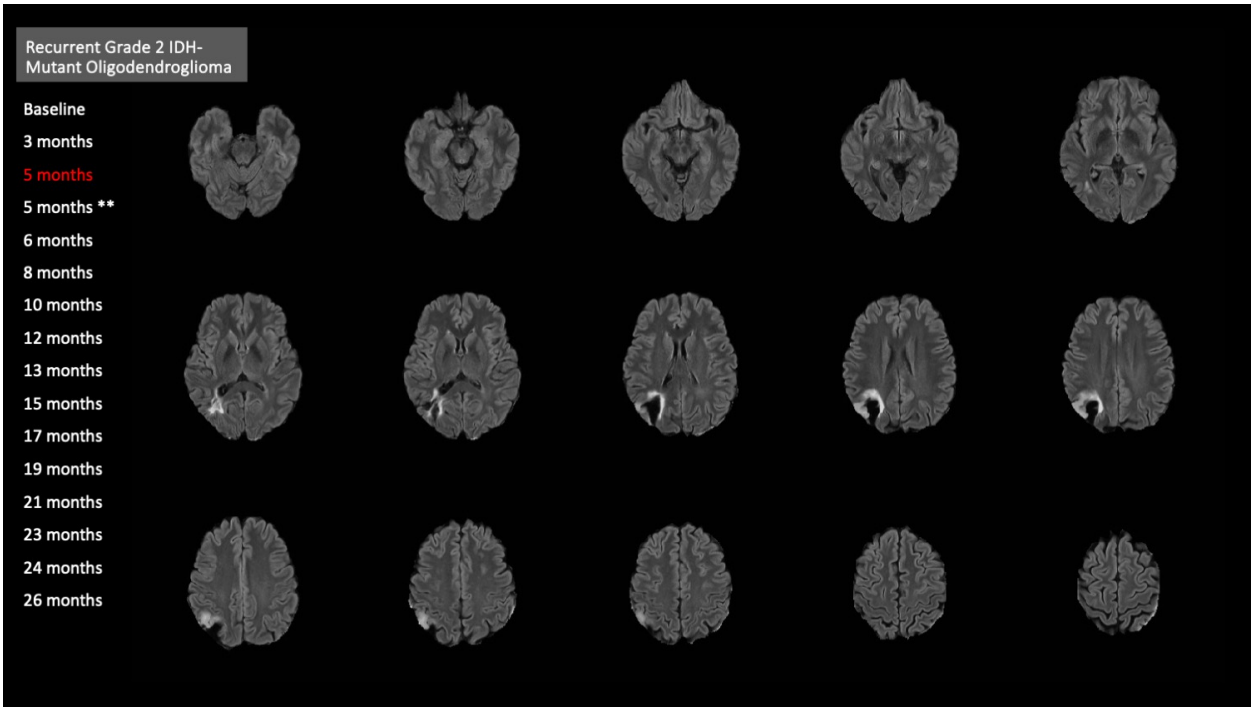
Recurrent Grade 2 IDH-Mutant Oligodendroglioma
Baseline
3 months
5 months
5 months **
6 months
8 months
10 months
12 months
13 months
15 months
17 months
19 months
21 months
23 months
24 months
26 months

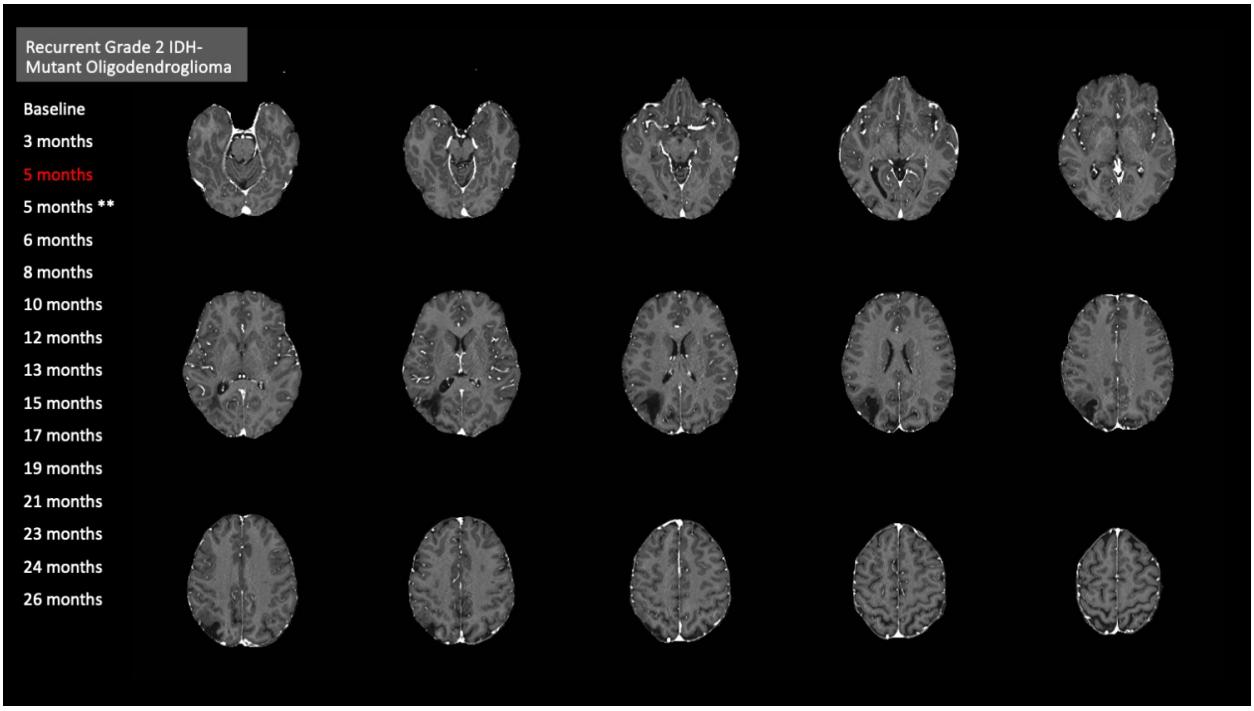
Recurrent Grade 2 IDH-Mutant Oligodendroglioma
Baseline
3 months
5 months
5 months **
6 months
8 months
10 months
12 months
13 months
15 months
17 months
19 months
21 months
23 months
24 months
26 months

(Slide 4/16)

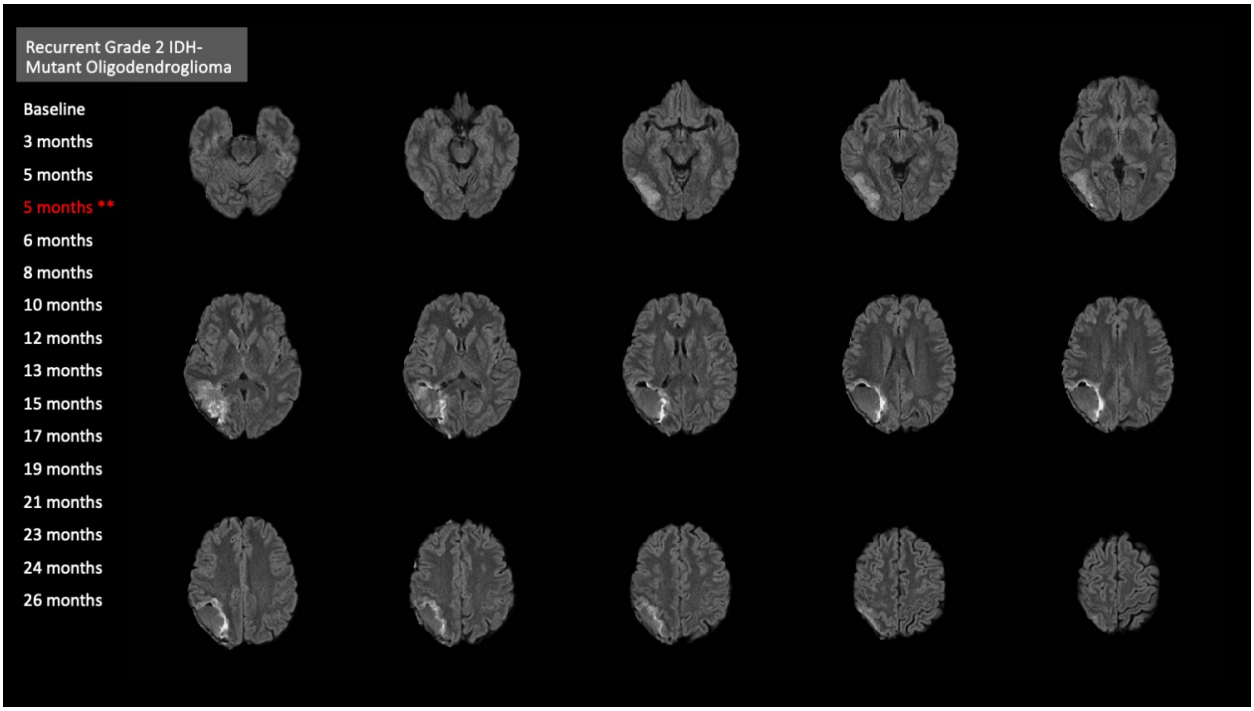
Recurrent Grade 2 IDH-Mutant Oligodendroglioma
Baseline
3 months
5 months
5 months **
6 months
8 months
10 months
12 months
13 months
15 months
17 months
19 months
21 months
23 months
24 months
26 months

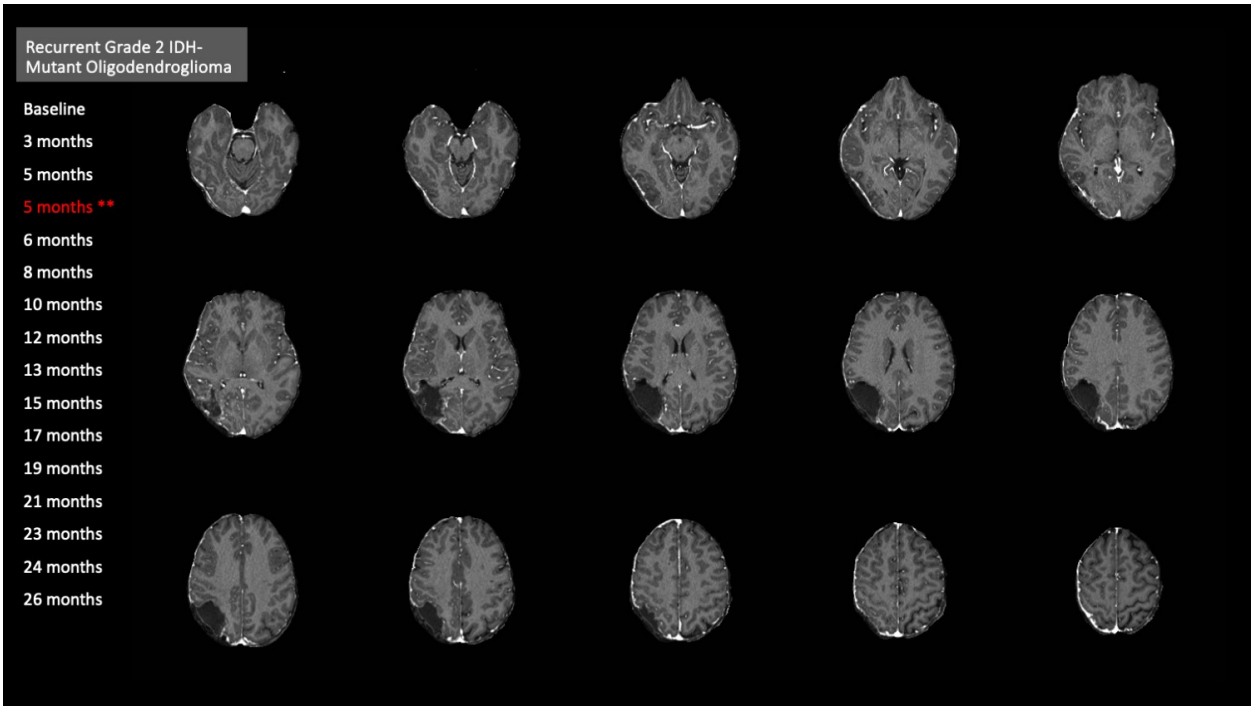
Recurrent Grade 2 IDH-Mutant Oligodendroglioma
Baseline
3 months
5 months
5 months **
6 months
8 months
10 months
12 months
13 months
15 months
17 months
19 months
21 months
23 months
24 months
26 months

(Slide 5/16)

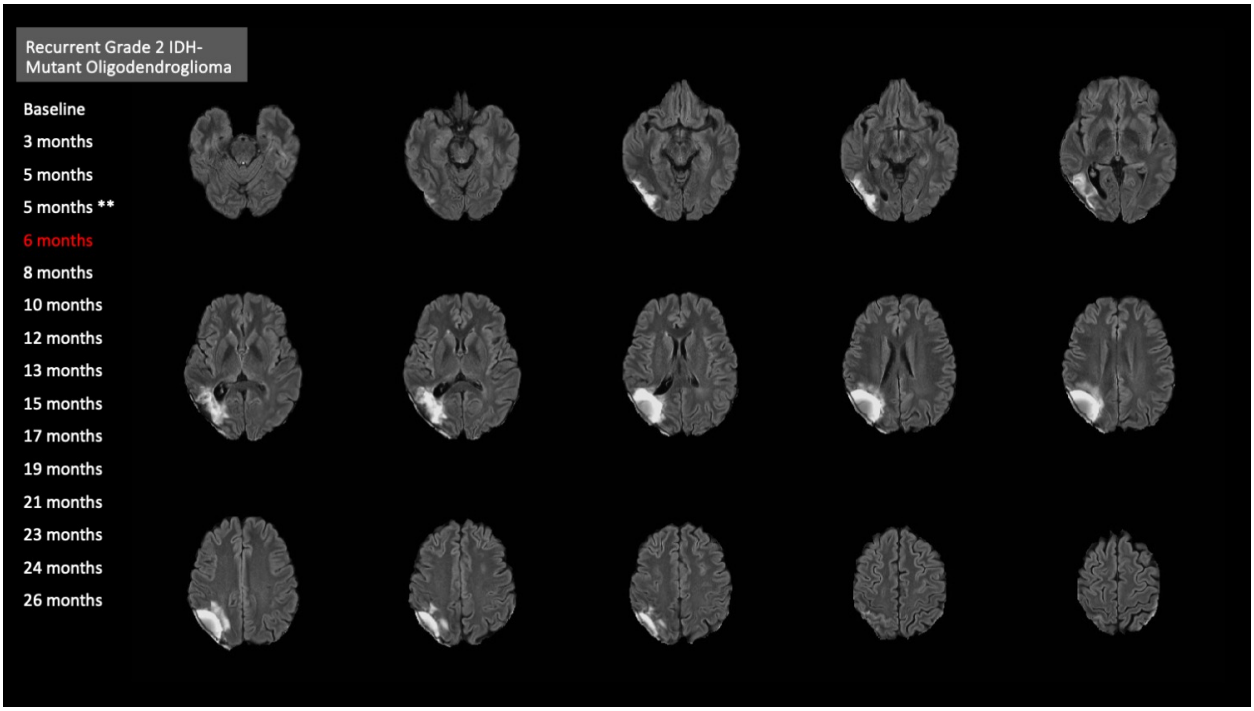
Recurrent Grade 2 IDH-Mutant Oligodendroglioma
Baseline
3 months
5 months
5 months **
6 months
8 months
10 months
12 months
13 months
15 months
17 months
19 months
21 months
23 months
24 months
26 months

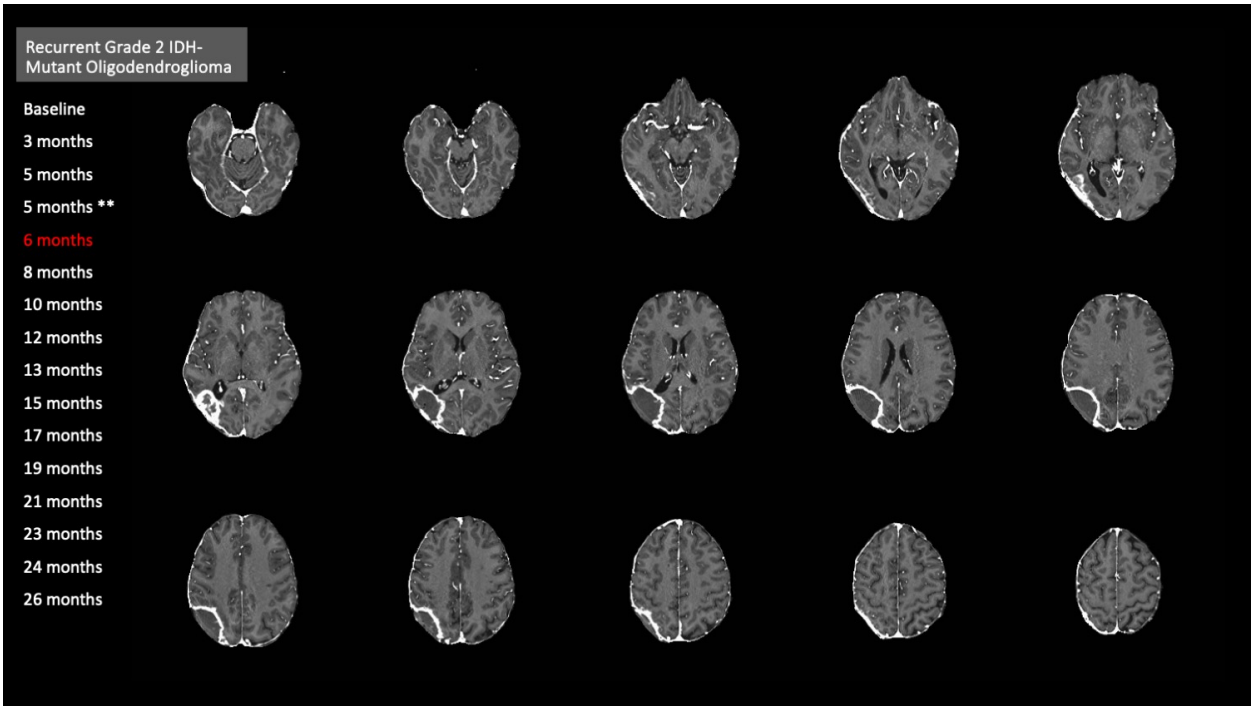
Recurrent Grade 2 IDH-Mutant Oligodendroglioma
Baseline
3 months
5 months
5 months **
6 months
8 months
10 months
12 months
13 months
15 months
17 months
19 months
21 months
23 months
24 months
26 months

(Slide 6/16)

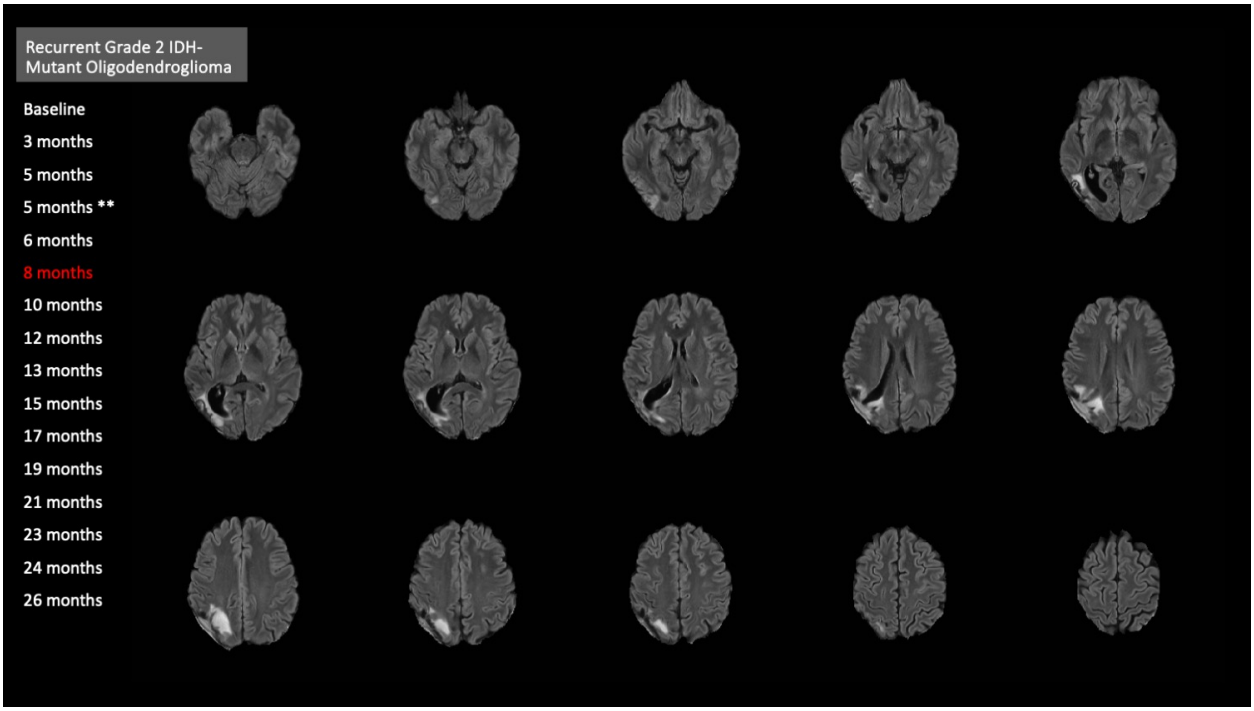
Recurrent Grade 2 IDH-Mutant Oligodendroglioma
Baseline
3 months
5 months
5 months **
6 months
8 months
10 months
12 months
13 months
15 months
17 months
19 months
21 months
23 months
24 months
26 months

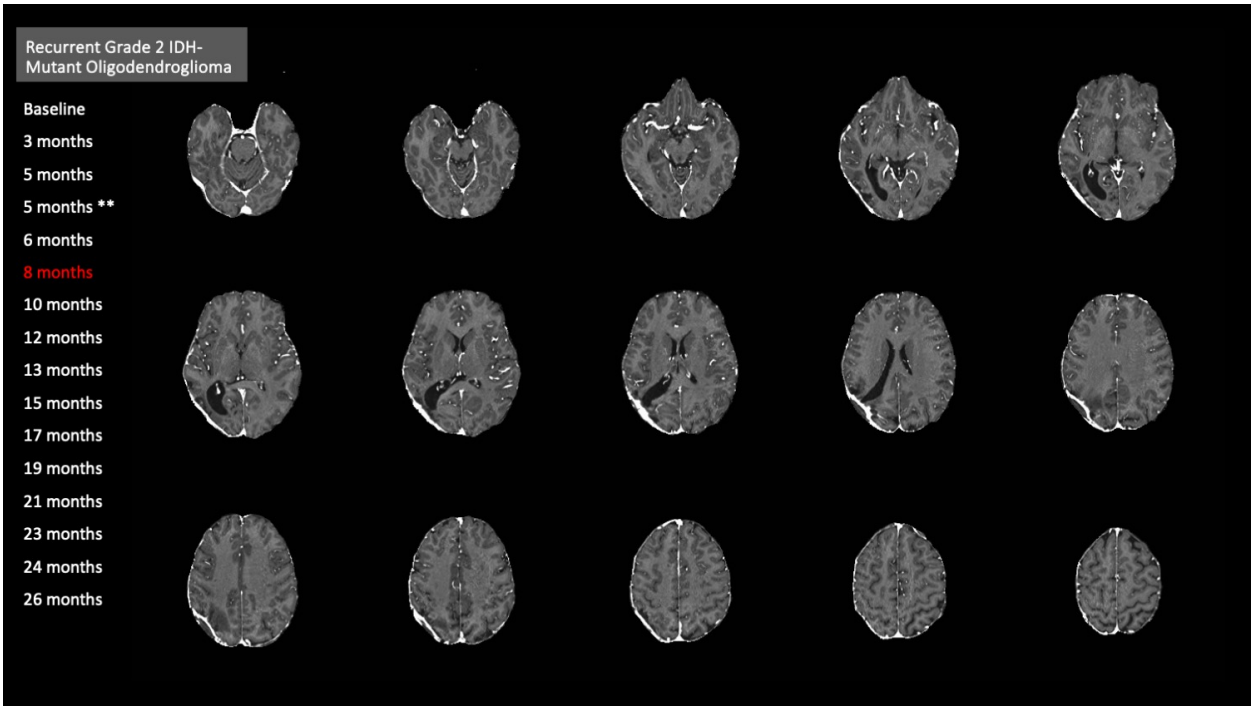
Recurrent Grade 2 IDH-Mutant Oligodendroglioma
Baseline
3 months
5 months
5 months **
6 months
8 months
10 months
12 months
13 months
15 months
17 months
19 months
21 months
23 months
24 months
26 months

(Slide 7/16)

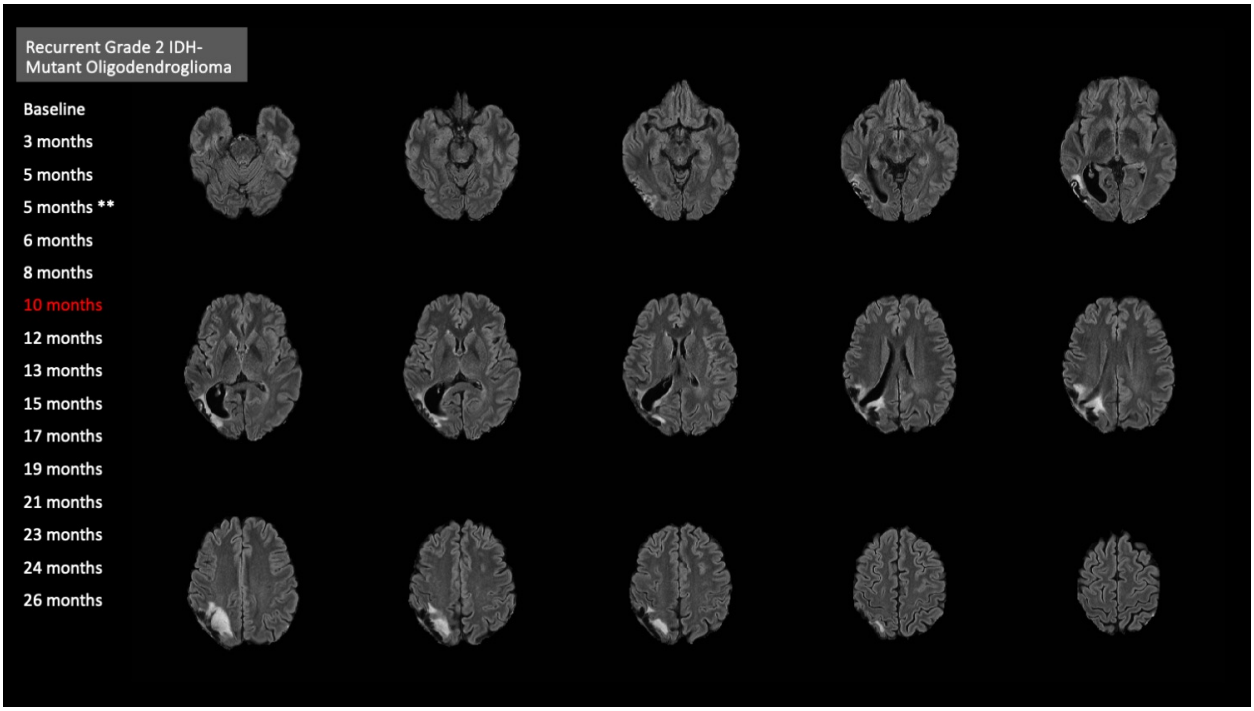
Recurrent Grade 2 IDH-Mutant Oligodendroglioma
Baseline
3 months
5 months
5 months **
6 months
8 months
10 months
12 months
13 months
15 months
17 months
19 months
21 months
23 months
24 months
26 months

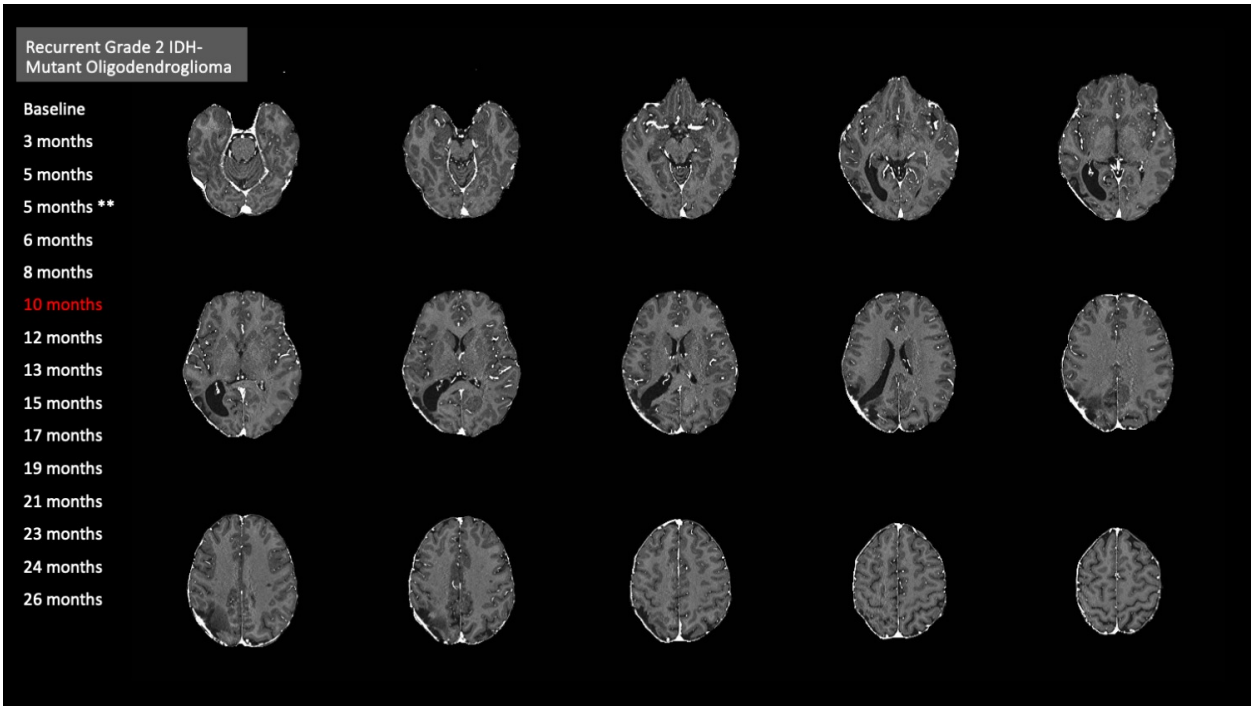
Recurrent Grade 2 IDH-Mutant Oligodendroglioma
Baseline
3 months
5 months
5 months **
6 months
8 months
10 months
12 months
13 months
15 months
17 months
19 months
21 months
23 months
24 months
26 months

(Slide 8/16)

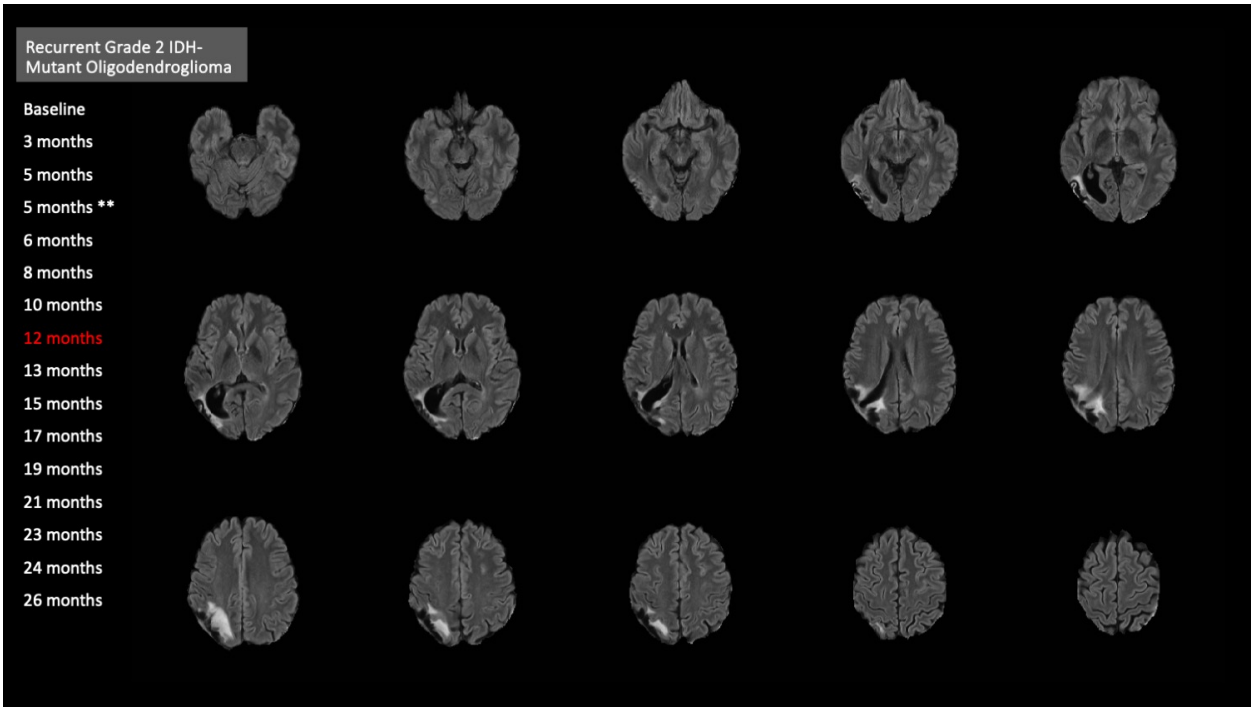
Recurrent Grade 2 IDH-Mutant Oligodendroglioma
Baseline
3 months
5 months
5 months **
6 months
8 months
10 months
12 months
13 months
15 months
17 months
19 months
21 months
23 months
24 months
26 months

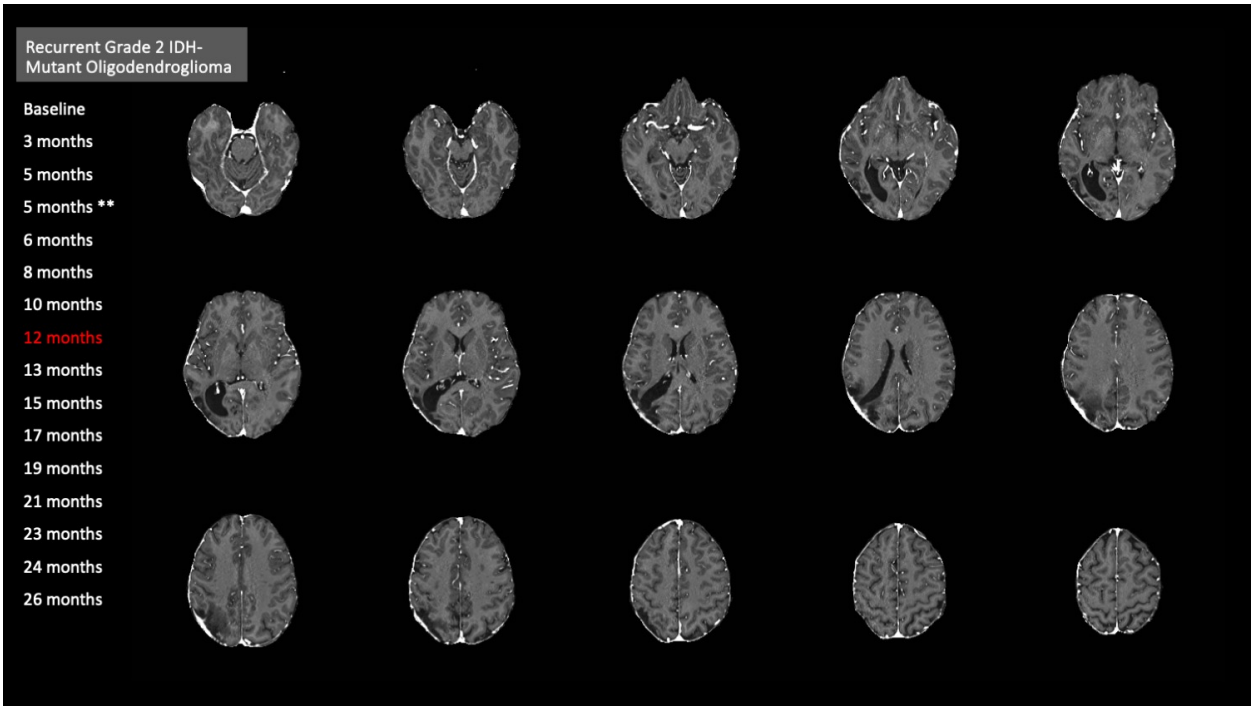
Recurrent Grade 2 IDH-Mutant Oligodendroglioma
Baseline
3 months
5 months
5 months **
6 months
8 months
10 months
12 months
13 months
15 months
17 months
19 months
21 months
23 months
24 months
26 months

(Slide 9/16)

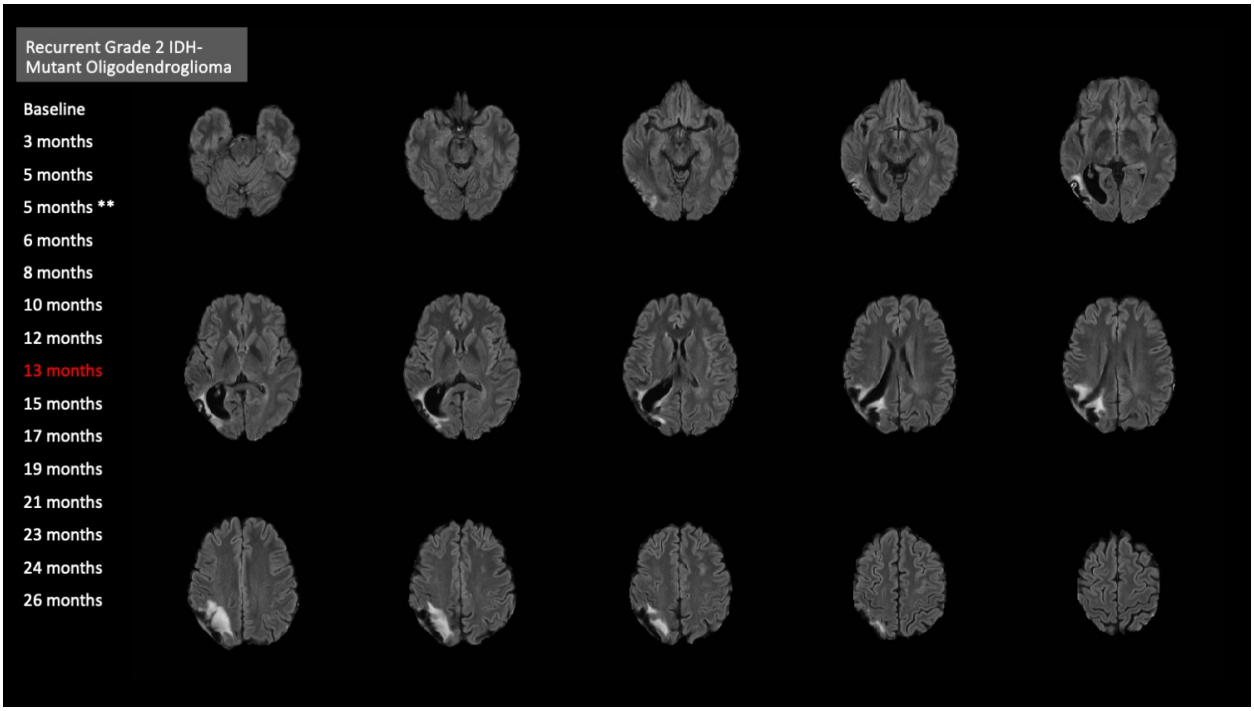
Recurrent Grade 2 IDH-Mutant Oligodendroglioma
Baseline
3 months
5 months
5 months **
6 months
8 months
10 months
12 months
13 months
15 months
17 months
19 months
21 months
23 months
24 months
26 months

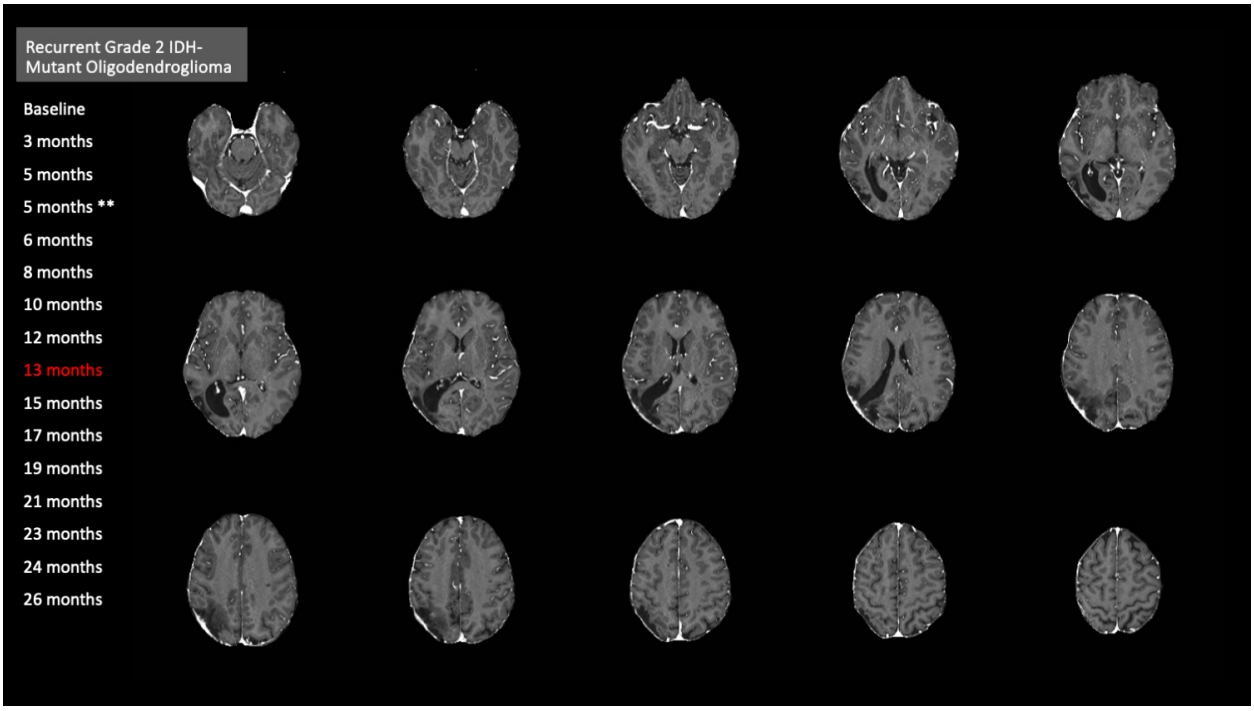
Recurrent Grade 2 IDH-Mutant Oligodendroglioma
Baseline
3 months
5 months
5 months **
6 months
8 months
10 months
12 months
13 months
15 months
17 months
19 months
21 months
23 months
24 months
26 months

(Slide 10/16)

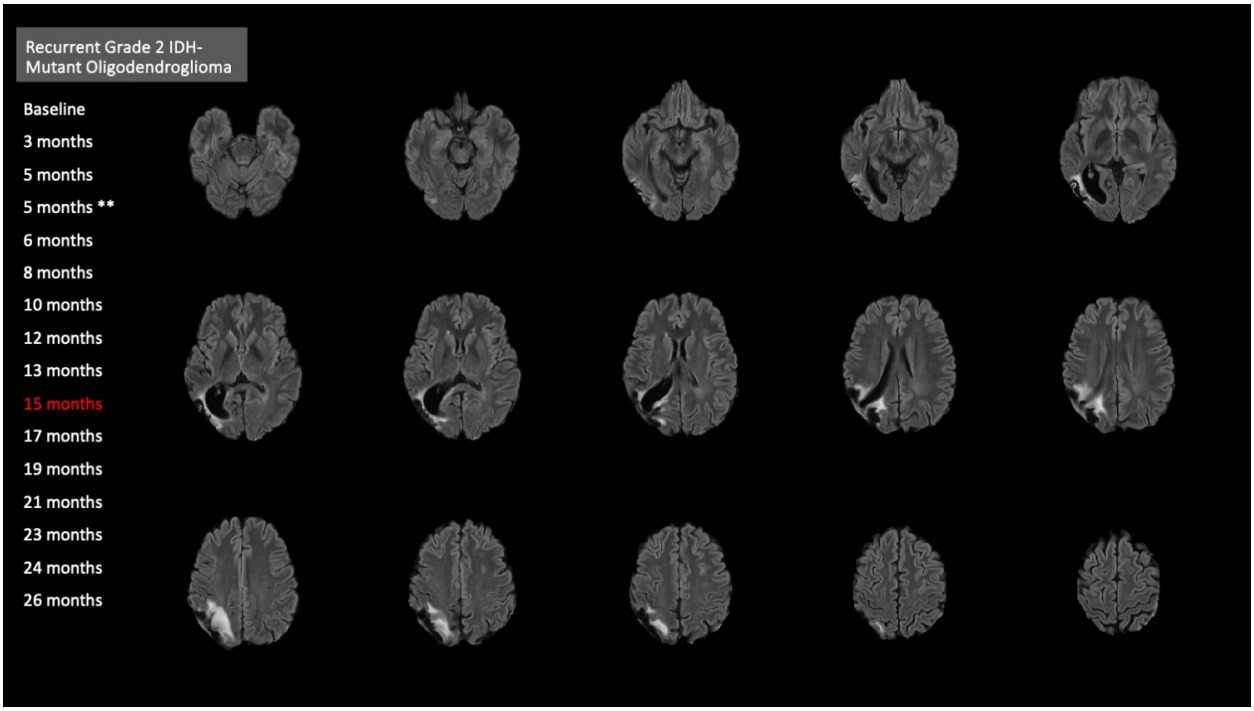
Recurrent Grade 2 IDH-Mutant Oligodendroglioma
Baseline
3 months
5 months
5 months **
6 months
8 months
10 months
12 months
13 months
15 months
17 months
19 months
21 months
23 months
24 months
26 months

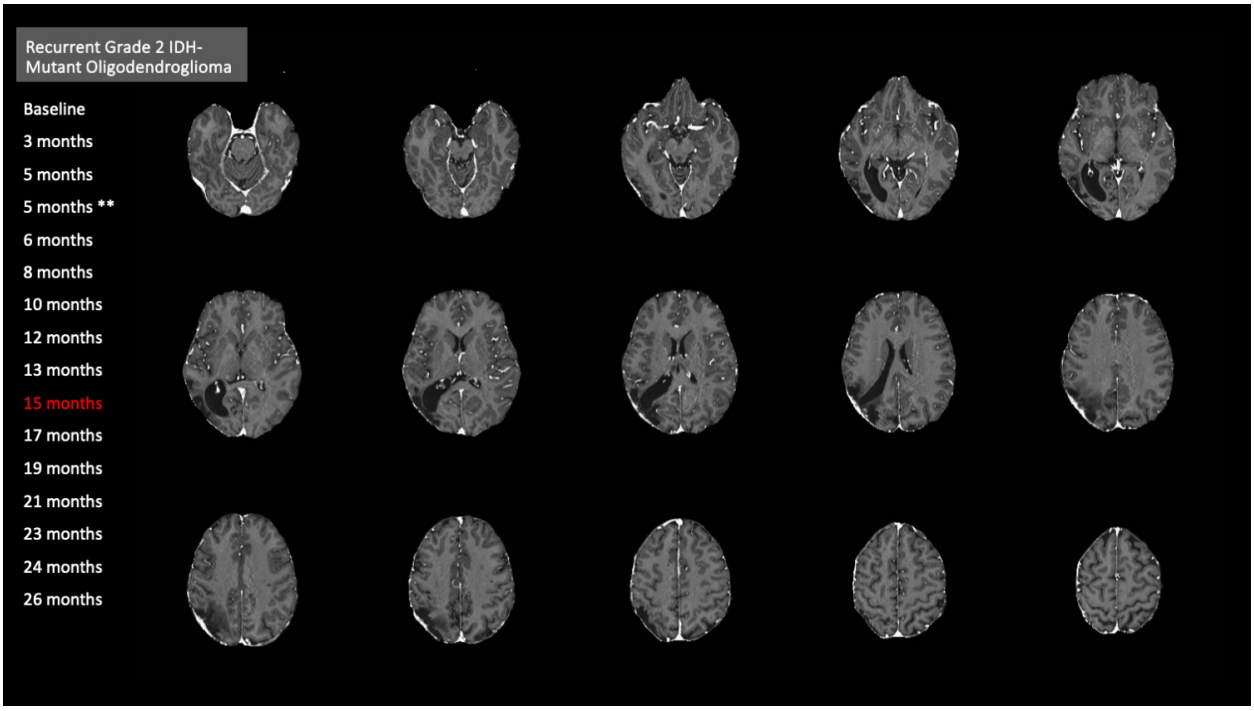
Recurrent Grade 2 IDH-Mutant Oligodendroglioma
Baseline
3 months
5 months
5 months **
6 months
8 months
10 months
12 months
13 months
15 months
17 months
19 months
21 months
23 months
24 months
26 months

(Slide 11/16)

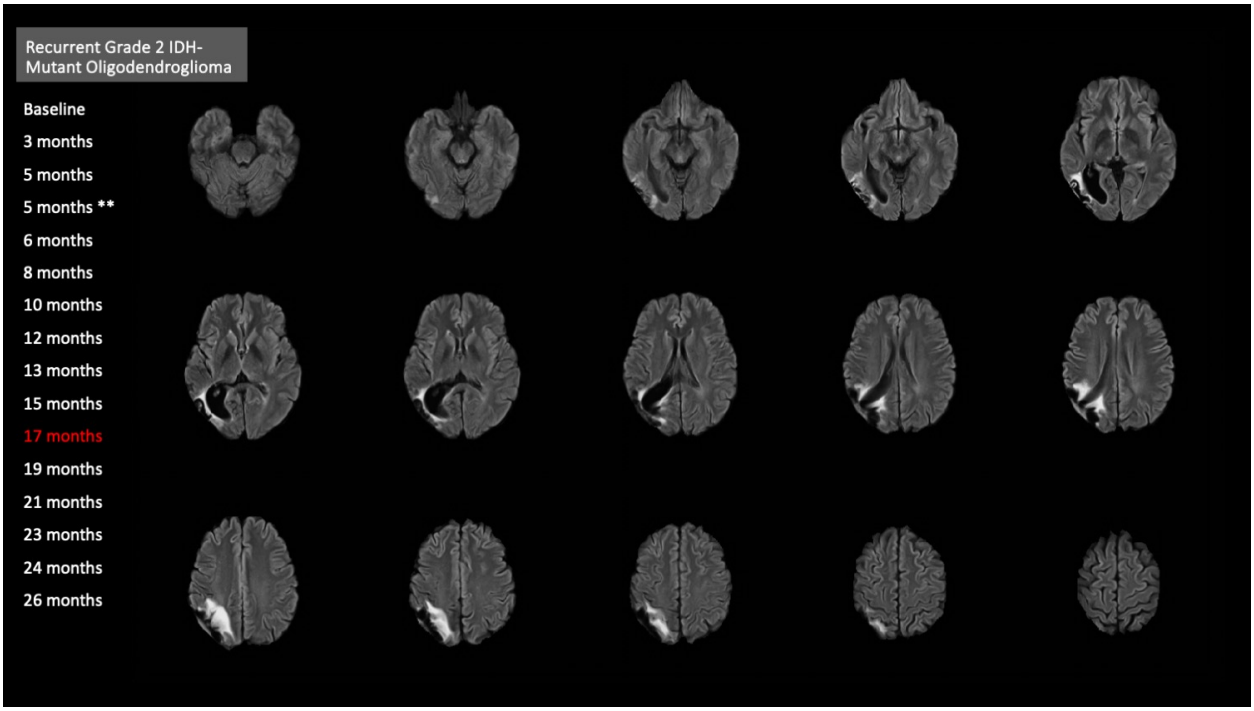
Recurrent Grade 2 IDH-Mutant Oligodendroglioma
Baseline
3 months
5 months
5 months **
6 months
8 months
10 months
12 months
13 months
15 months
17 months
19 months
21 months
23 months
24 months
26 months

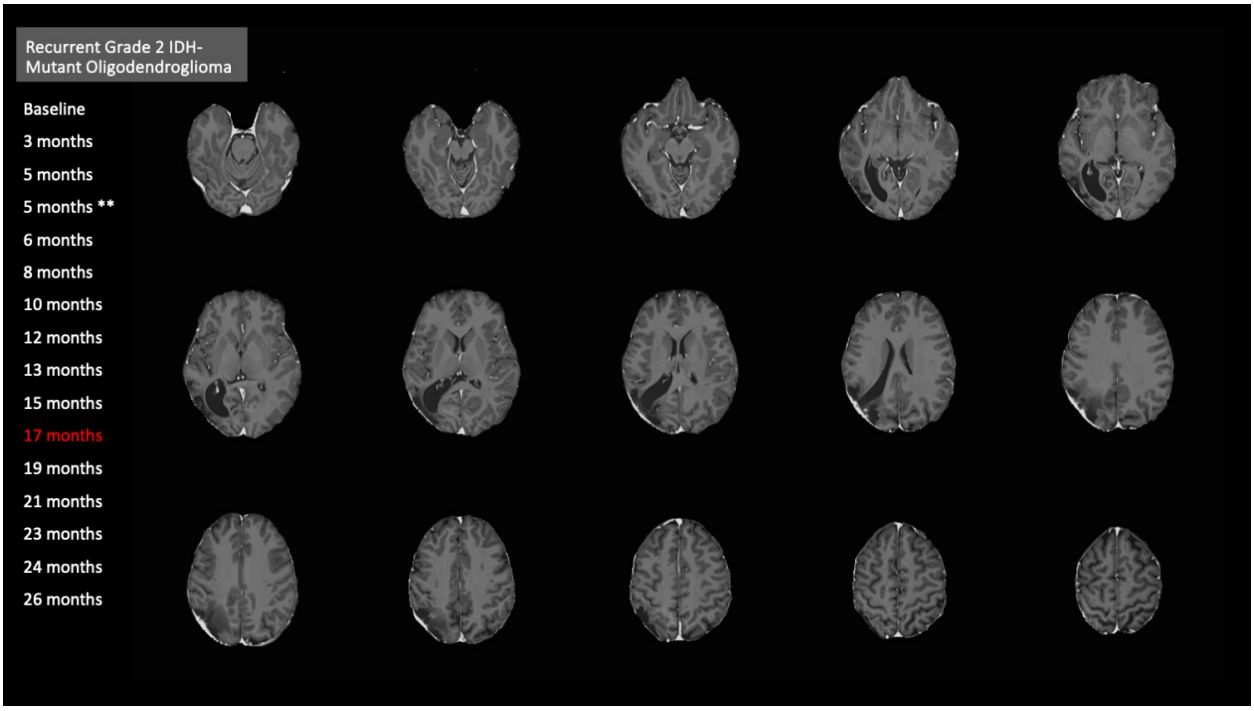
Recurrent Grade 2 IDH-Mutant Oligodendroglioma
Baseline
3 months
5 months
5 months **
6 months
8 months
10 months
12 months
13 months
15 months
17 months
19 months
21 months
23 months
24 months
26 months

(Slide 12/16)

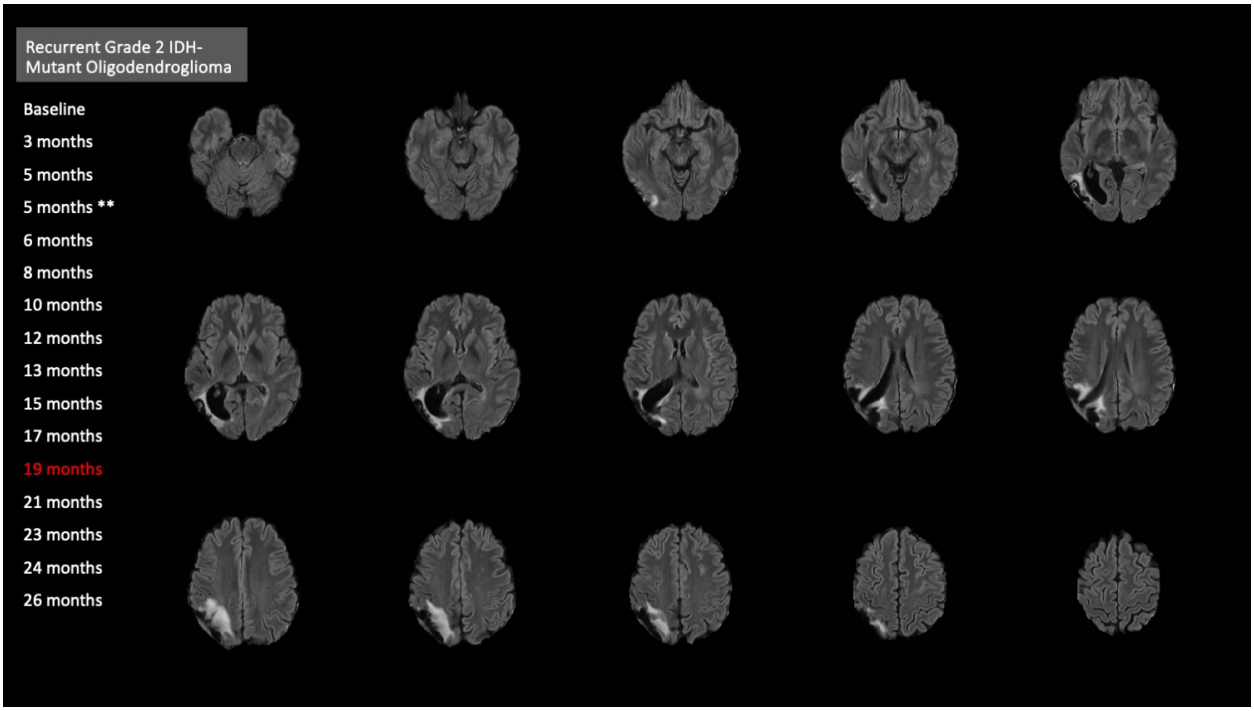
Recurrent Grade 2 IDH-Mutant Oligodendroglioma
Baseline
3 months
5 months
5 months **
6 months
8 months
10 months
12 months
13 months
15 months
17 months
19 months
21 months
23 months
24 months
26 months

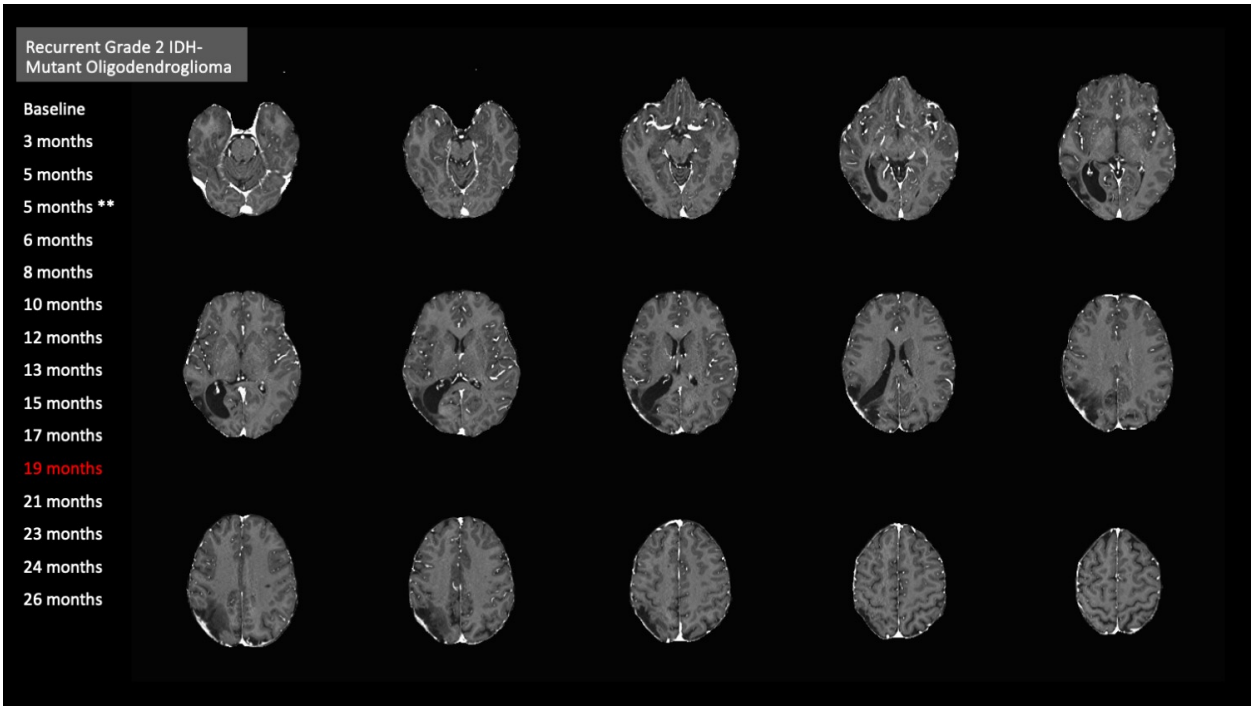
Recurrent Grade 2 IDH-Mutant Oligodendroglioma
Baseline
3 months
5 months
5 months **
6 months
8 months
10 months
12 months
13 months
15 months
17 months
19 months
21 months
23 months
24 months
26 months

(Slide 13/16)

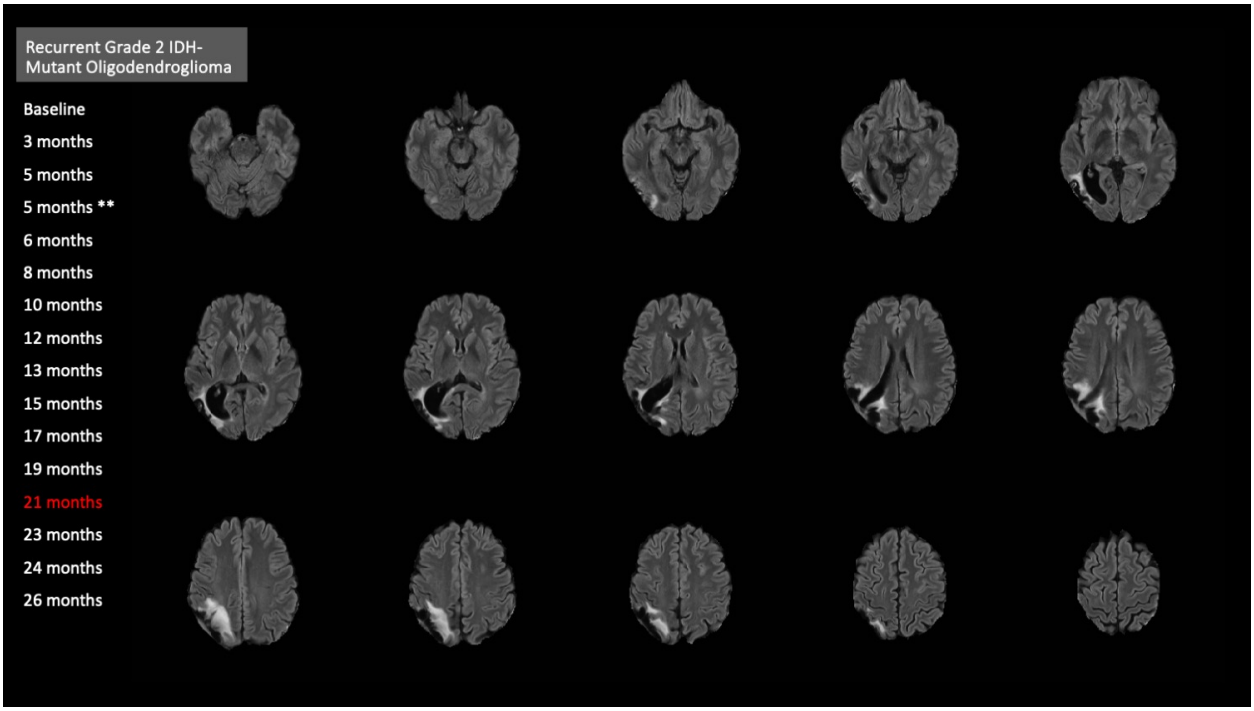
Recurrent Grade 2 IDH-Mutant Oligodendroglioma
Baseline
3 months
5 months
5 months **
6 months
8 months
10 months
12 months
13 months
15 months
17 months
19 months
21 months
23 months
24 months
26 months

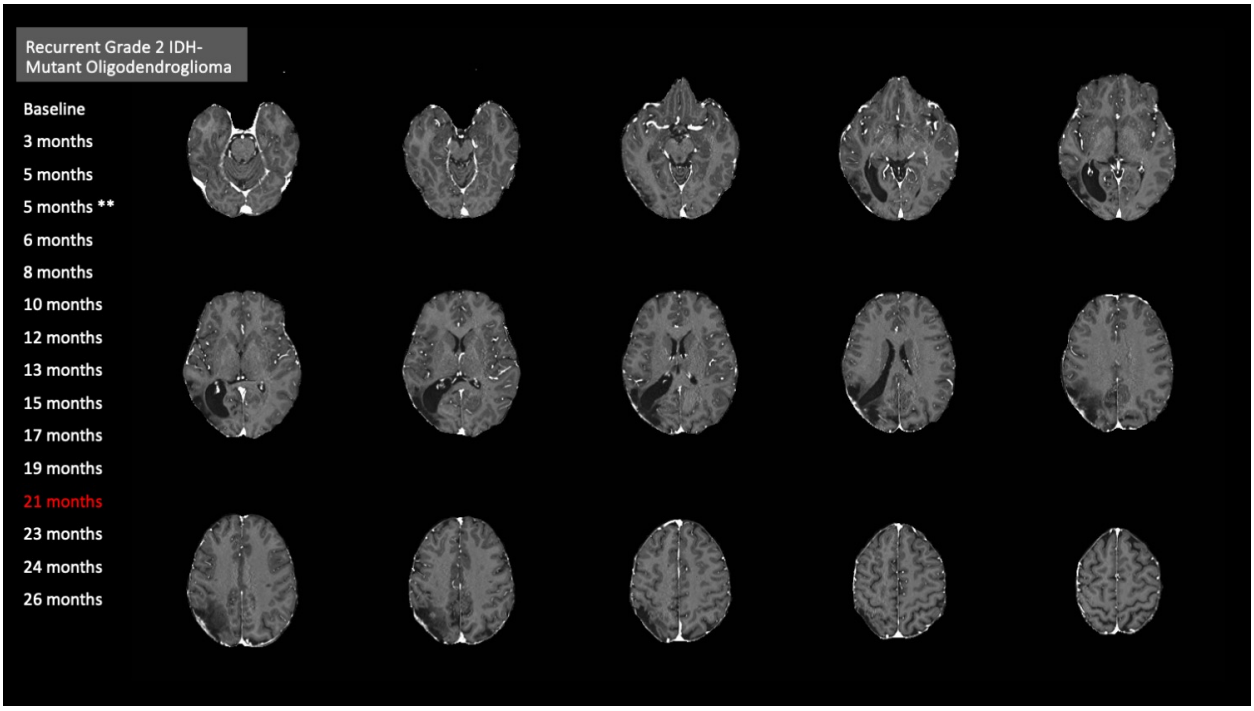
Recurrent Grade 2 IDH-Mutant Oligodendroglioma
Baseline
3 months
5 months
5 months **
6 months
8 months
10 months
12 months
13 months
15 months
17 months
19 months
21 months
23 months
24 months
26 months

(Slide 14/16)

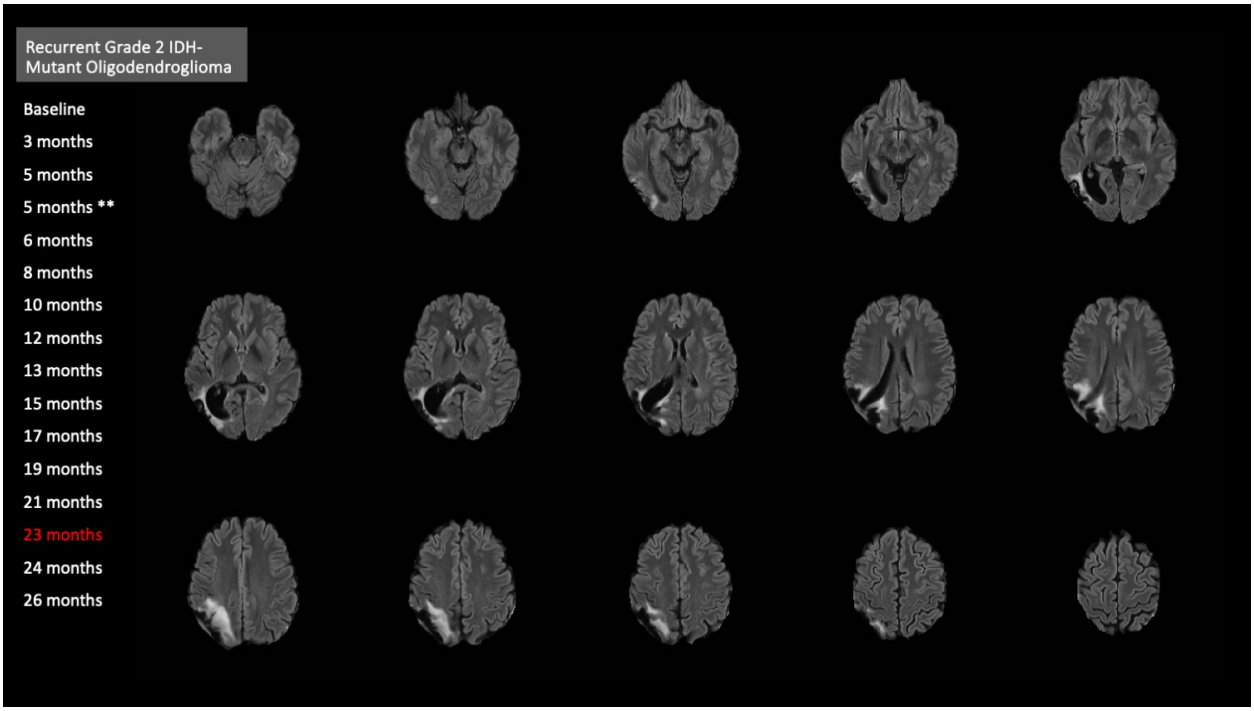
Recurrent Grade 2 IDH-Mutant Oligodendroglioma
Baseline
3 months
5 months
5 months **
6 months
8 months
10 months
12 months
13 months
15 months
17 months
19 months
21 months
23 months
24 months
26 months

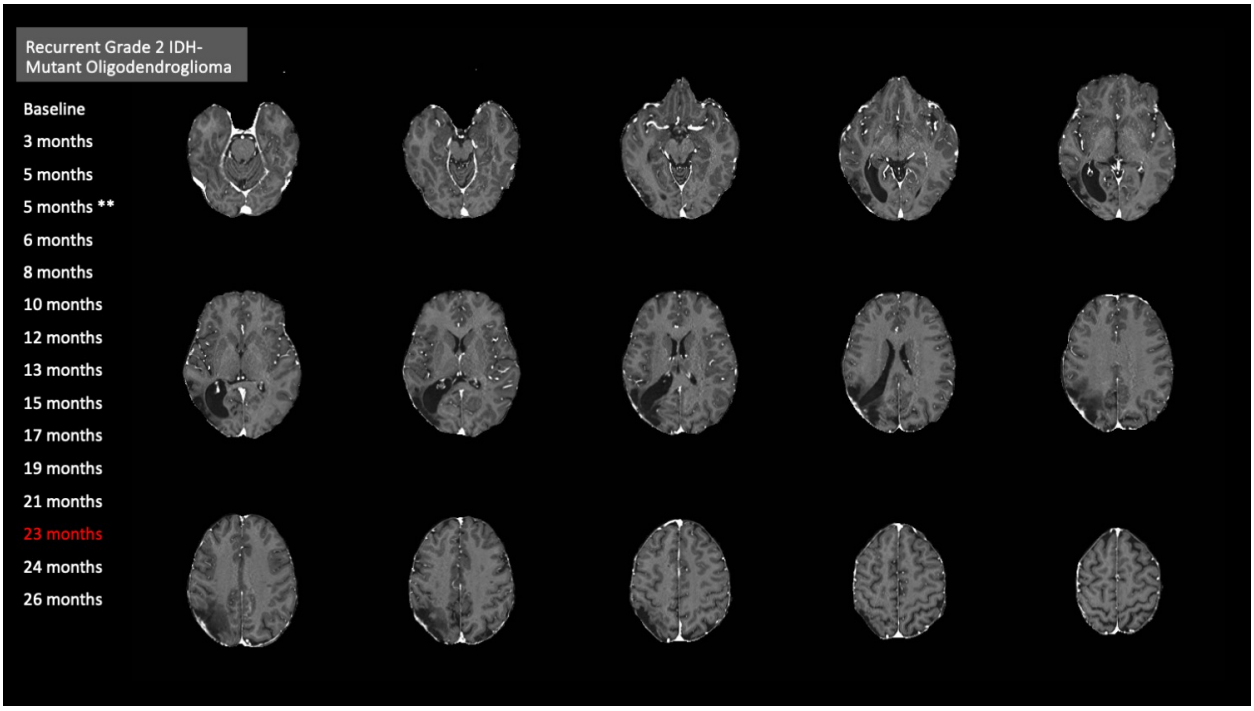
Recurrent Grade 2 IDH-Mutant Oligodendroglioma
Baseline
3 months
5 months
5 months **
6 months
8 months
10 months
12 months
13 months
15 months
17 months
19 months
21 months
23 months
24 months
26 months

(Slide 15/16)

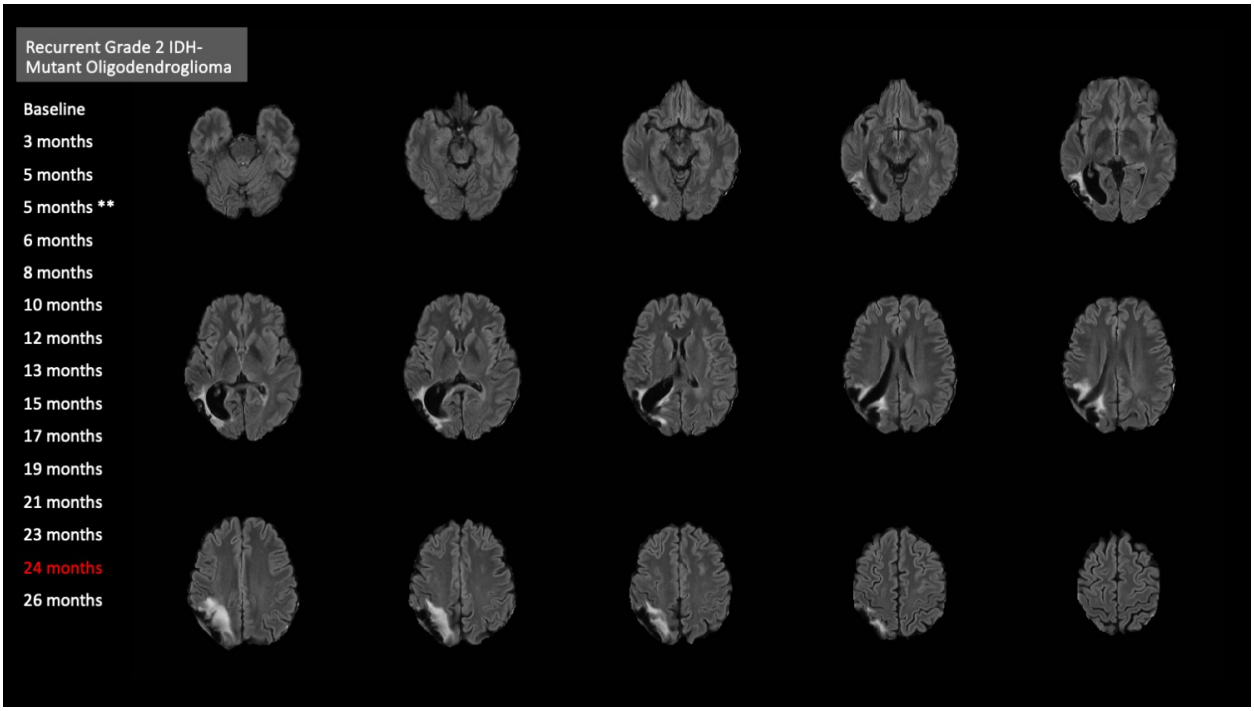
Recurrent Grade 2 IDH-Mutant Oligodendroglioma
Baseline
3 months
5 months
5 months **
6 months
8 months
10 months
12 months
13 months
15 months
17 months
19 months
21 months
23 months
24 months
26 months

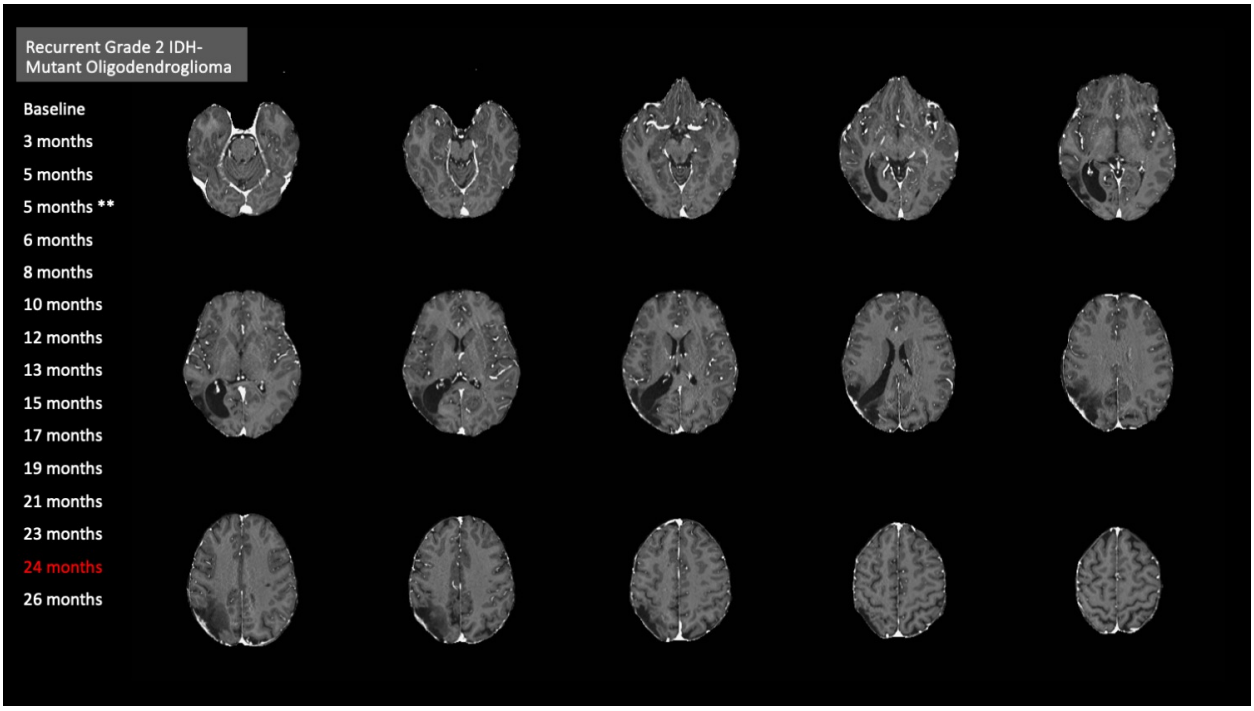
Recurrent Grade 2 IDH-Mutant Oligodendroglioma
Baseline
3 months
5 months
5 months **
6 months
8 months
10 months
12 months
13 months
15 months
17 months
19 months
21 months
23 months
24 months
26 months

(Slide 16/16)

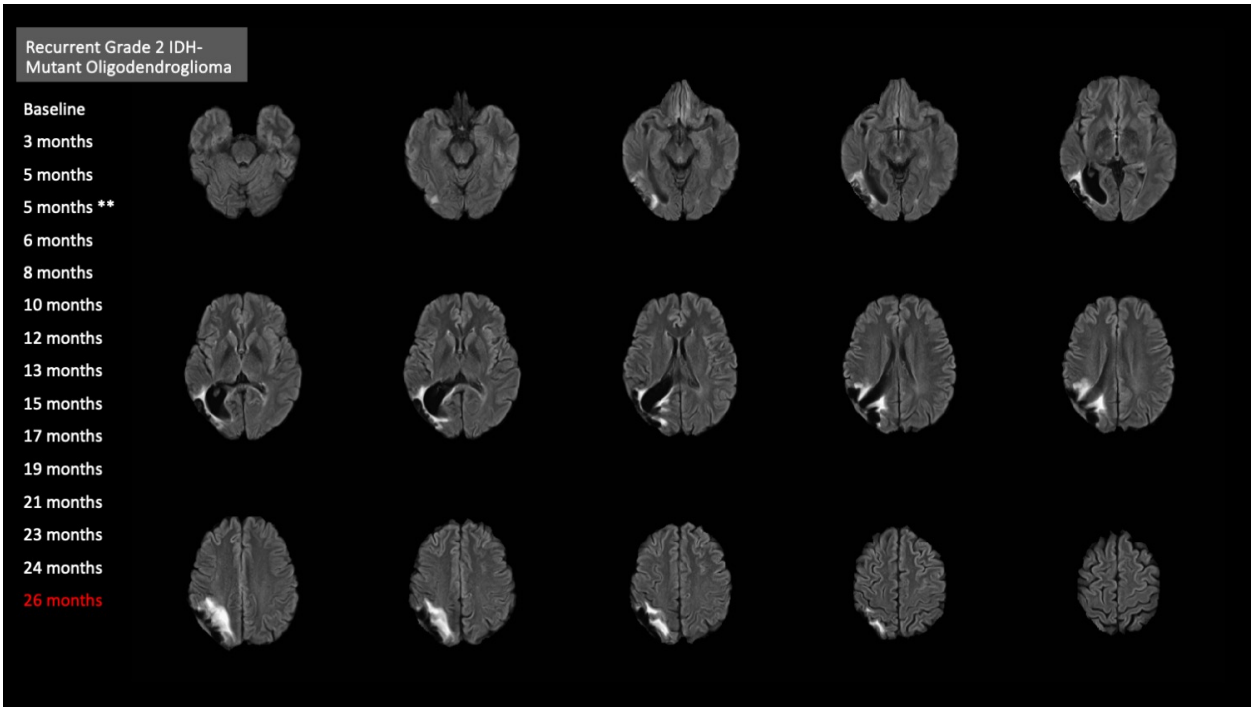
Recurrent Grade 2 IDH-Mutant Oligodendroglioma
Baseline
3 months
5 months
5 months **
6 months
8 months
10 months
12 months
13 months
15 months
17 months
19 months
21 months
23 months
24 months
26 months

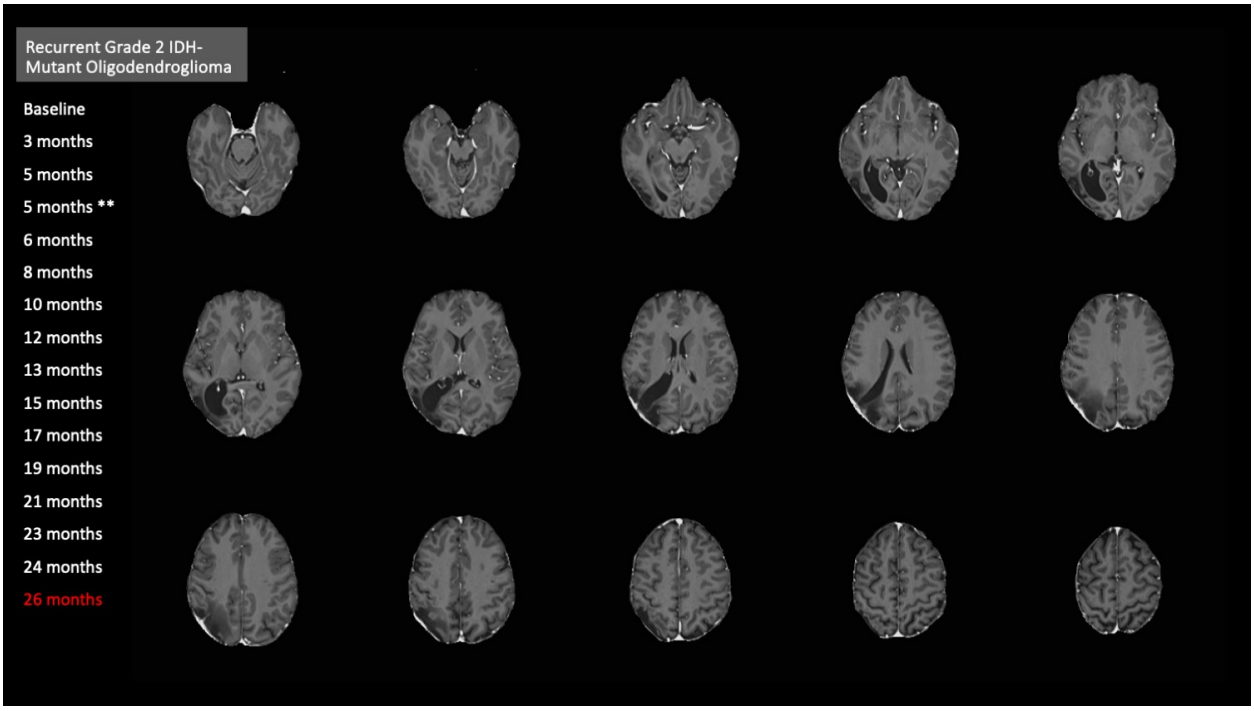
Recurrent Grade 2 IDH-Mutant Oligodendroglioma
Baseline
3 months
5 months
5 months **
6 months
8 months
10 months
12 months
13 months
15 months
17 months
19 months
21 months
23 months
24 months
26 months

Pseudoprogression in IDH-Mutant Gliomas

Pseudoprogression (PsP) is often defined as a worsening of radiographic findings, and specifically contrast-enhancement extension, which is *not* ascribable to an actual tumor recurrence/progression.[215] As per its classic definition, PsP appears on histology as gliosis and reactive changes, which are thought to lead to changes in vascular permeability as a consequence of radiation/chemoradiation.[215] A concept related to PsP is radiation necrosis (RN, i.e. the necrosis of non-neoplastic tissue within the radiation field), which may also mimic tumor progression on imaging.[216] However, on histology, RN shows geographic necrosis, which may co-localize with residual or quiescent tumor cells that are non-proliferative, while progressive/recurrent disease would demonstrate tumor cell proliferation. From a radiographic and RANO criteria standpoint, and particularly according to mRANO and RANO 2.0,[182, 200] "PsP" is a term that broadly applies to any radiographic worsening that is *not* followed by an additional worsening at the following timepoint (but rather stabilizes and then regresses over time), regardless of the underlying pathophysiology.[200] With some approximation, both histologic PsP and histologic RN generally show radiographic behavior that fit the definition of radiographic PsP. This definition also includes radiographic PsP observed following other therapies, such as immune checkpoint blockade, although the biological mechanism for immunotherapy-related PsP is thought to be different.[199]

The determination of PsP versus true progression remains a significant challenge in clinical settings and in clinical trials.[217] The false determination of true progression instead of PsP can lead to an unnecessary switch from an effective therapy and early removal from a clinical trial, while the false determination of PsP instead of true progression can lead to a delay in appropriate treatment.[217] Some general concepts can aid the interpretation of progressive or new contrast-enhancement. For instance, a new area of contrast-enhancement located outside of the high-dose

radiation field (e.g. >1 cm outside) should be more concerning for true progression. Nodular alterations with solid tissue should also be considered more suspicious for true progression, especially if they cause mass effect. Subependymal enhancement is a common location for both true progression and PsP in IDH-wildtype glioblastoma and in low-grade glioma.[218, 219] Distal ependymal enhancement (>1 cm away from the contrast-enhancing tumor) has previously been shown to be more likely to be true progression compared to PsP.[218] Thus, flipbooks can aid in differentiation of PsP from true progression through simultaneous consideration of lesion location, morphology, and growth dynamics.

Figure 8.6 (post-contrast T1-weighed MRI flipbook) shows an example of a 61-year-old male patient diagnosed with grade 3 IDH-mutant astrocytoma. After surgery and chemoradiation, follow-up imaging demonstrated linear ependymal/subependymal contrast enhancement on the wall of the left lateral ventricle (month 5). Over time, this linear enhancement appeared to "migrate" anteriorly and evolved into a rounder area involving the subependymal tissue and the centrum semiovale (month 11), and then eventually shrank and disappeared (month 35). Being self-limiting and since it resolved over time without treatment, this contrast-enhancement can be categorized as radiographic pseudoprogression.

(Slide 1/14)

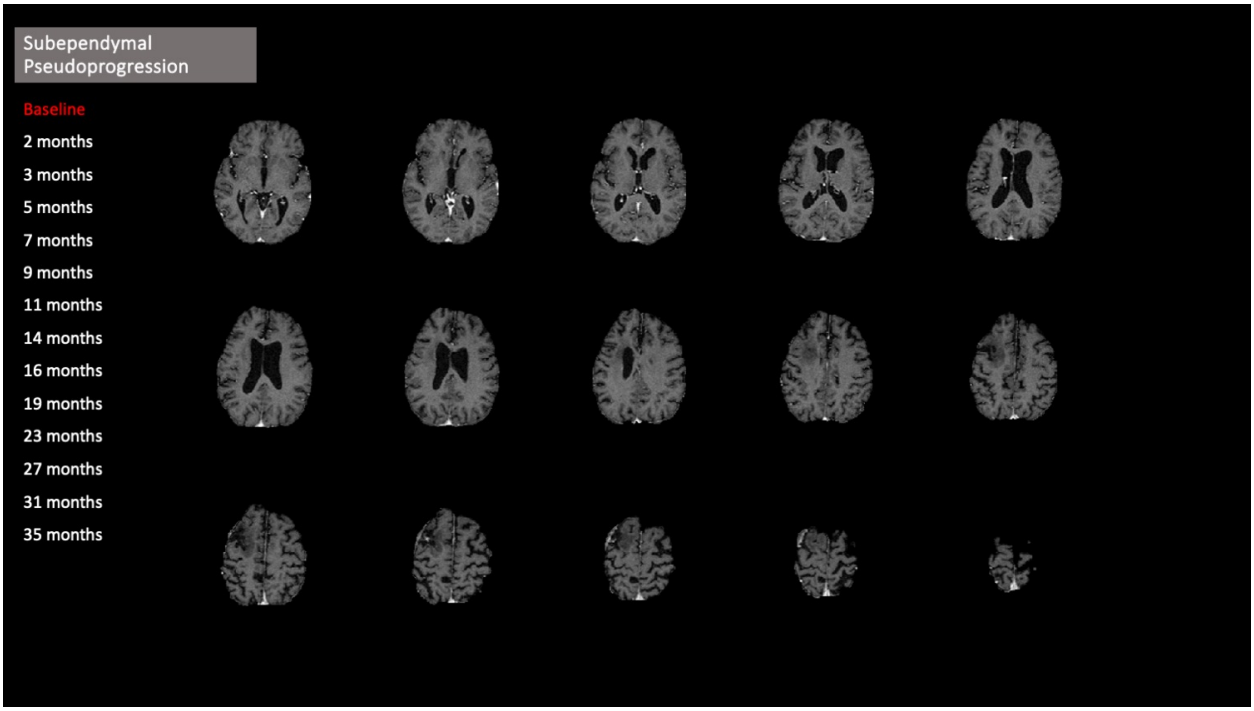

Figure 8.6. Representative Case of Using Flipbooks for Assessing Subependymal Pseudoprogression (Post-Contrast T1-Weighted MRI). Serial T1-post-contrast images for a 61-year-old male patient diagnosed with grade 3 IDH-mutant astrocytoma involving the right frontal lobe are shown. In this patient, ependymal/subependymal contrast-enhancement was noted (at 5 months) that appeared to migrate anteriorly at the following timepoints and form a nodule in the white matter, before shrinking and disappearing without treatment (pseudoprogression). **(Please view the flipbook in PDF format as "clickable" page view, not as "scroll" view.)**

(Slide 2/14)

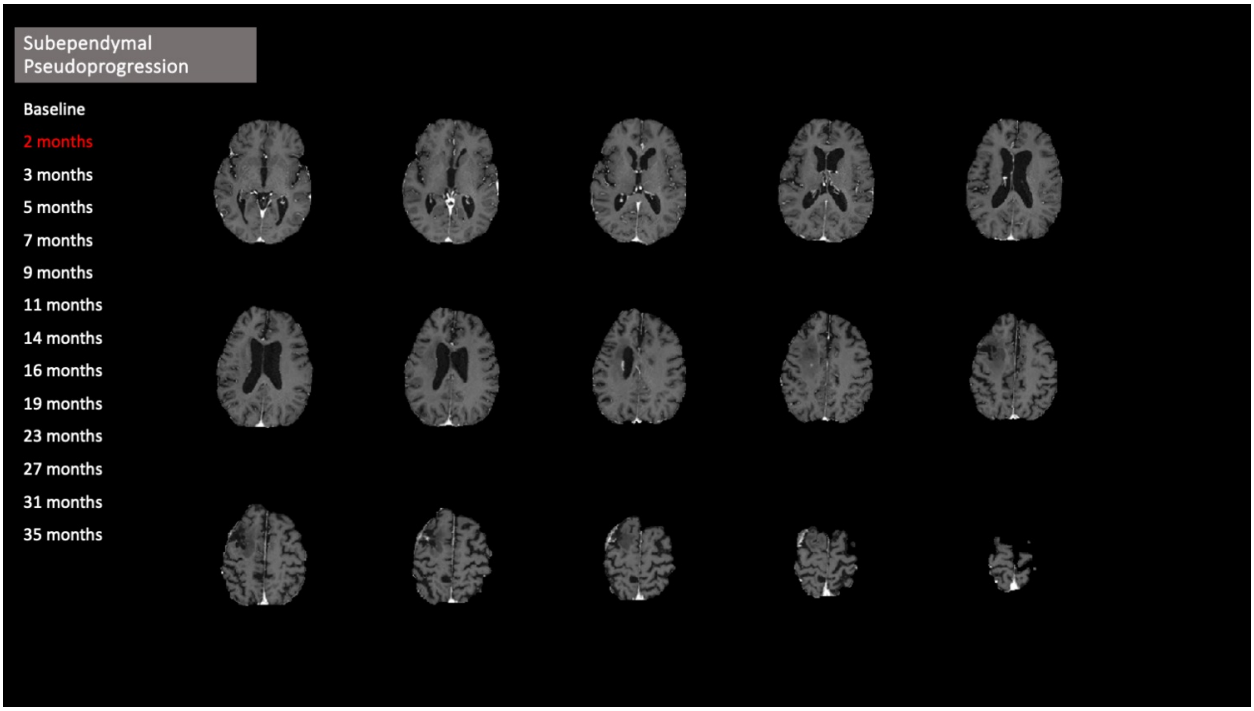
Subependymal
Pseudoprogression
Baseline
2 months
3 months
5 months
7 months
9 months
11 months
14 months
16 months
19 months
23 months
27 months
31 months
35 months

(Slide 3/14)

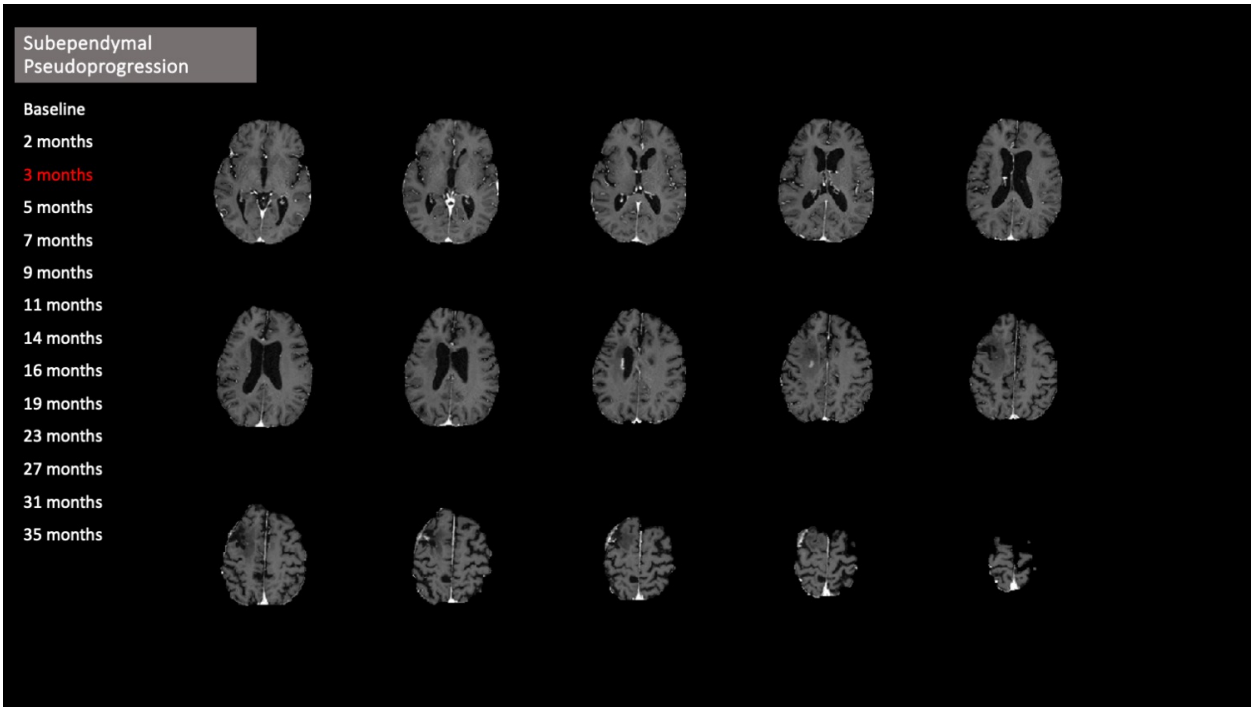
Subependymal
Pseudoprogression
Baseline
2 months
3 months
5 months
7 months
9 months
11 months
14 months
16 months
19 months
23 months
27 months
31 months
35 months

(Slide 4/14)

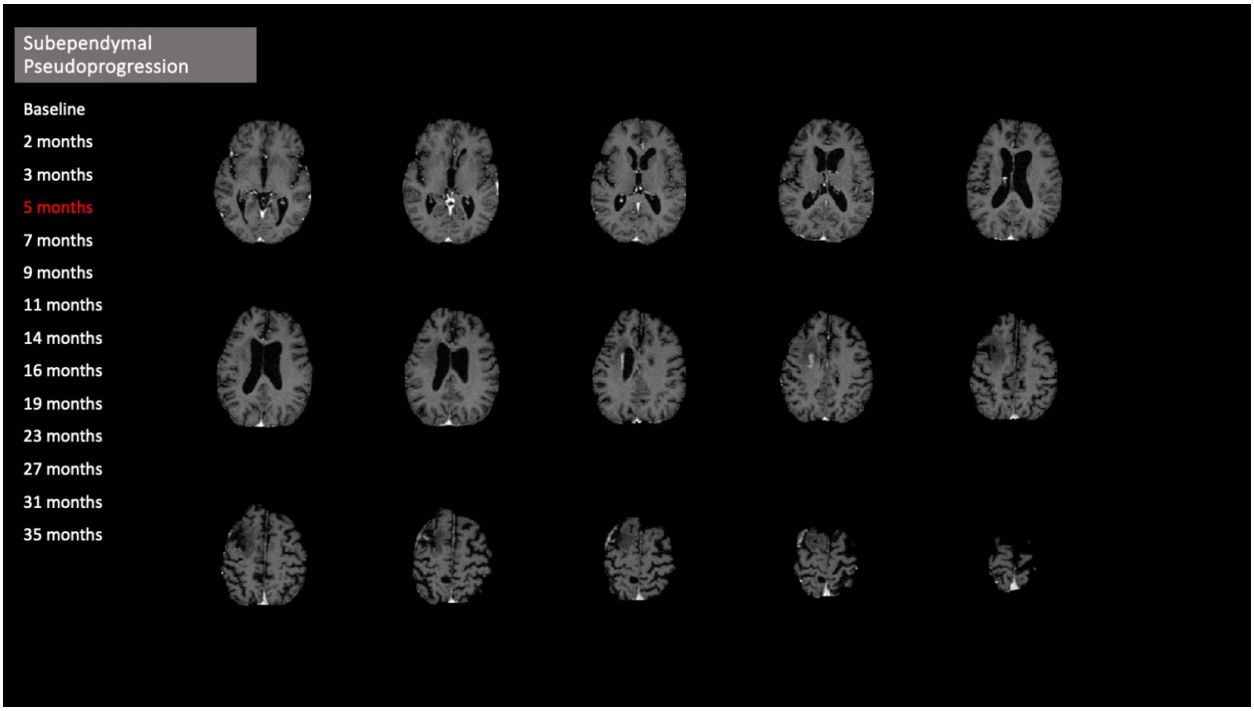
Subependymal
Pseudoprogression
Baseline
2 months
3 months
5 months
7 months
9 months
11 months
14 months
16 months
19 months
23 months
27 months
31 months
35 months

(Slide 5/14)

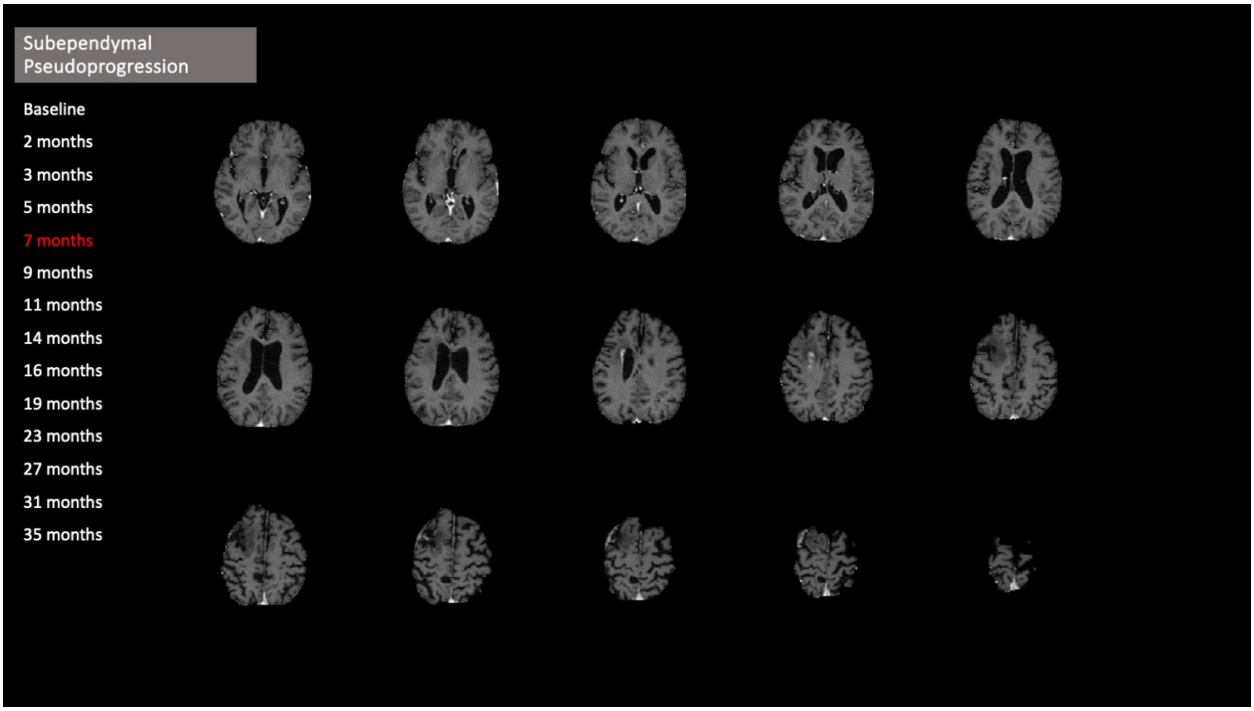
Subependymal
Pseudoprogression
Baseline
2 months
3 months
5 months
7 months
9 months
11 months
14 months
16 months
19 months
23 months
27 months
31 months
35 months

(Slide 6/14)

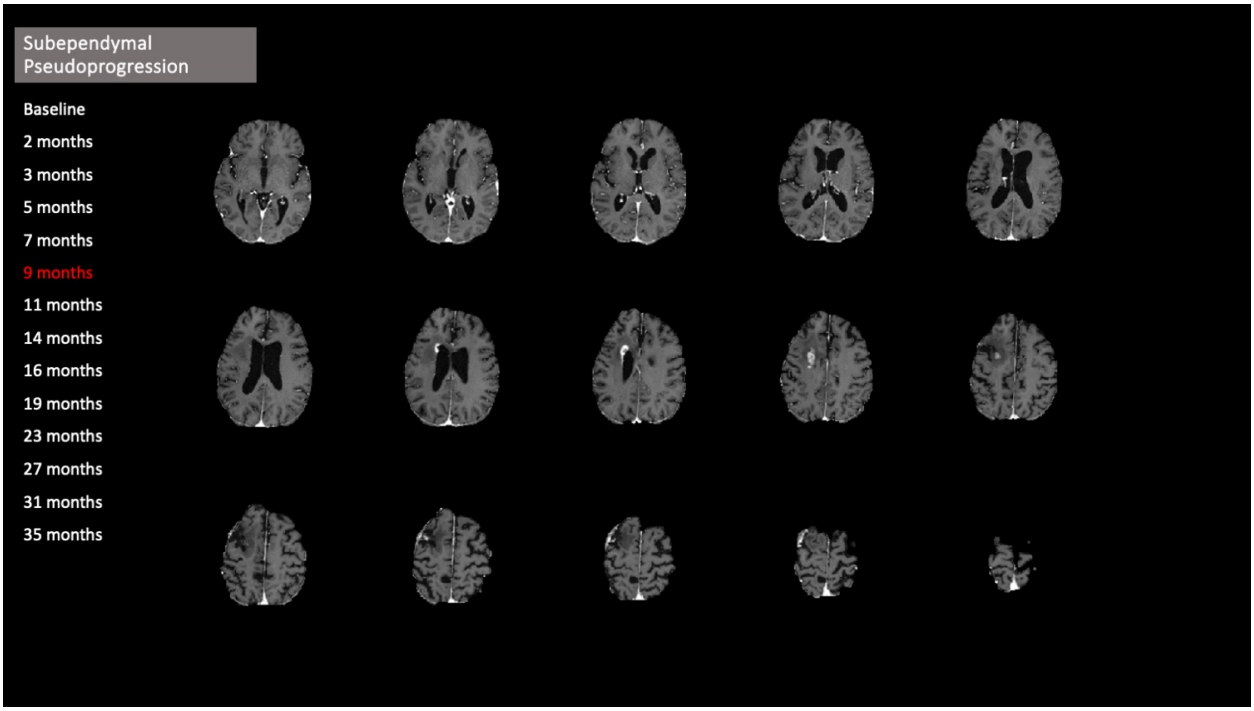
Subependymal
Pseudoprogression
Baseline
2 months
3 months
5 months
7 months
9 months
11 months
14 months
16 months
19 months
23 months
27 months
31 months
35 months

(Slide 7/14)

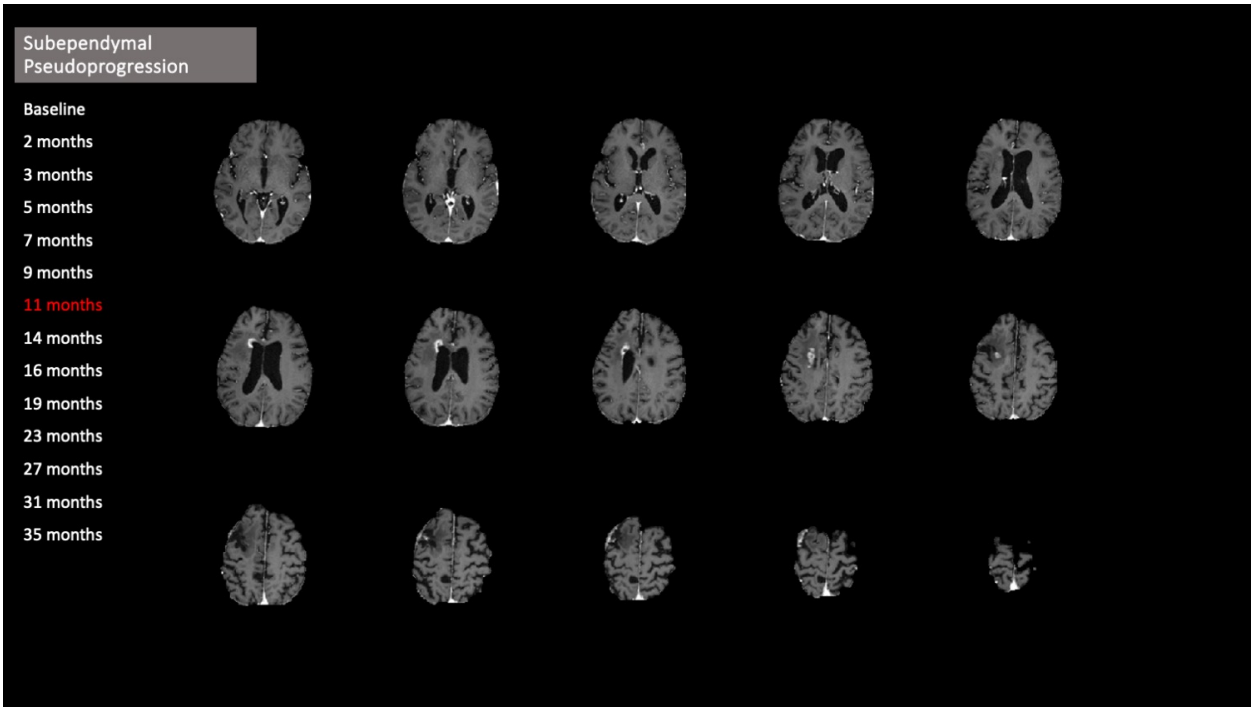
Subependymal Pseudoprogression
Baseline
2 months
3 months
5 months
7 months
9 months
11 months
14 months
16 months
19 months
23 months
27 months
31 months
35 months

(Slide 8/14)

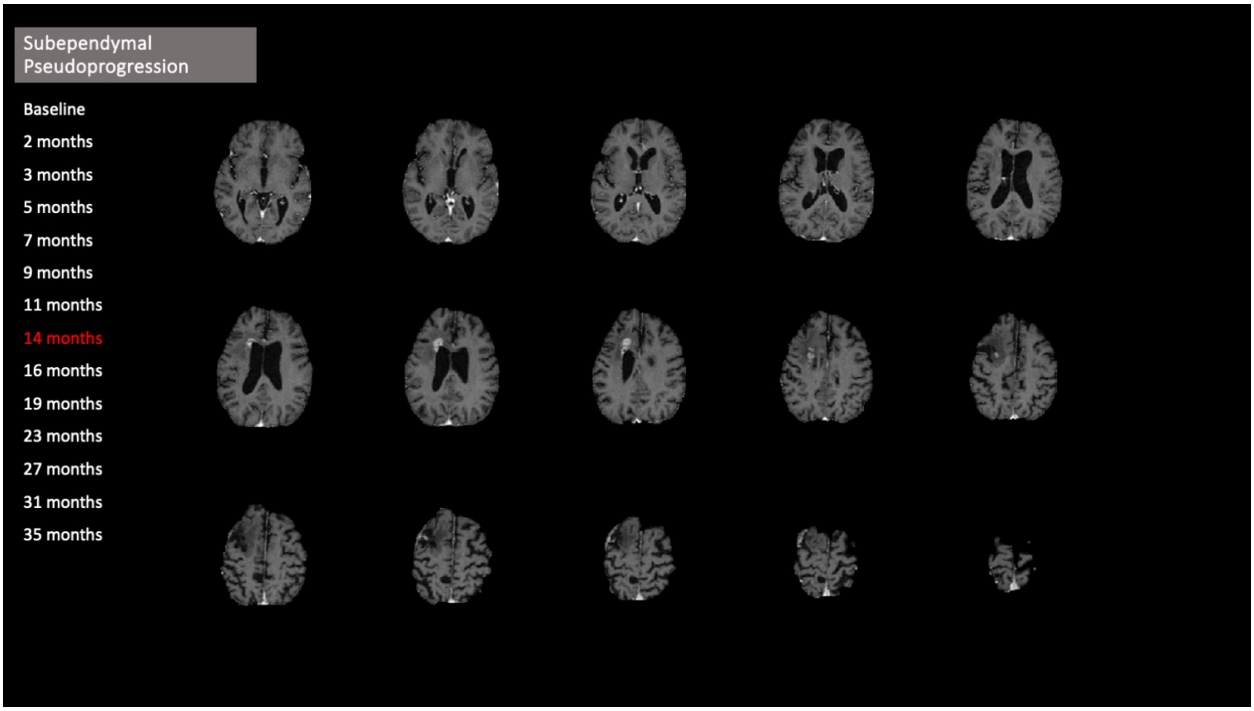
Subependymal
Pseudoprogression
Baseline
2 months
3 months
5 months
7 months
9 months
11 months
14 months
16 months
19 months
23 months
27 months
31 months
35 months

(Slide 9/14)

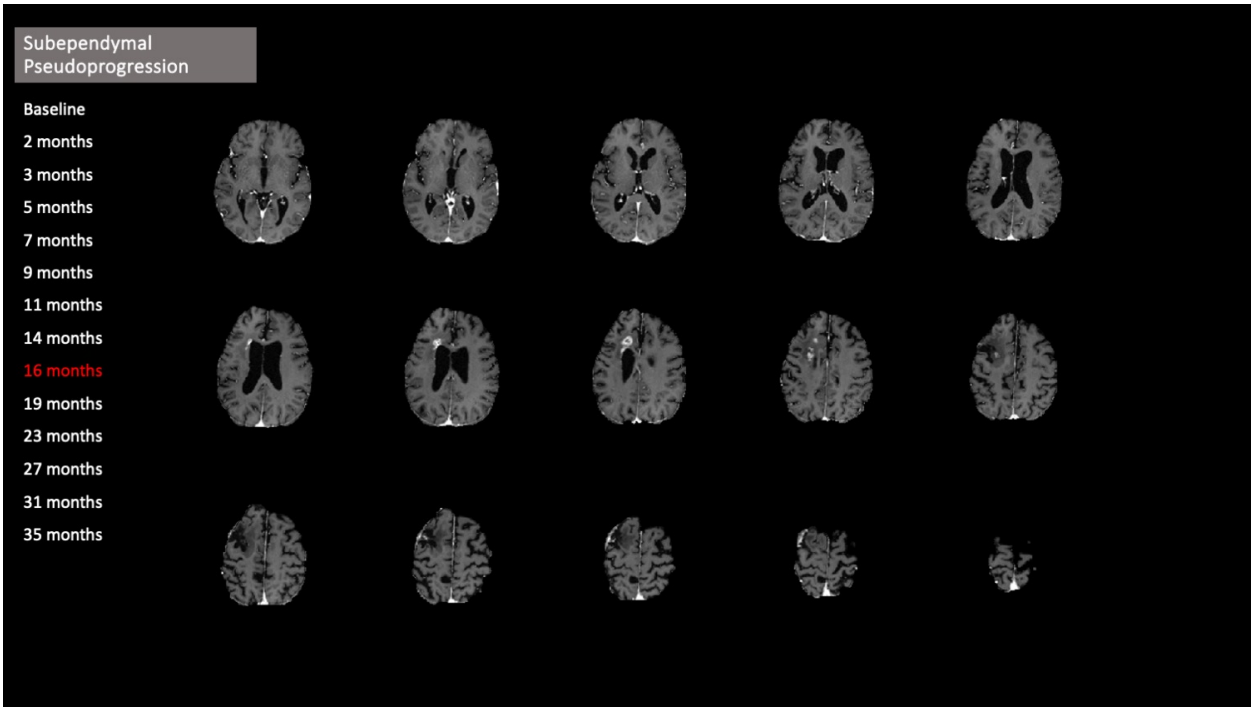
Subependymal
Pseudoprogression
Baseline
2 months
3 months
5 months
7 months
9 months
11 months
14 months
16 months
19 months
23 months
27 months
31 months
35 months

(Slide 10/14)

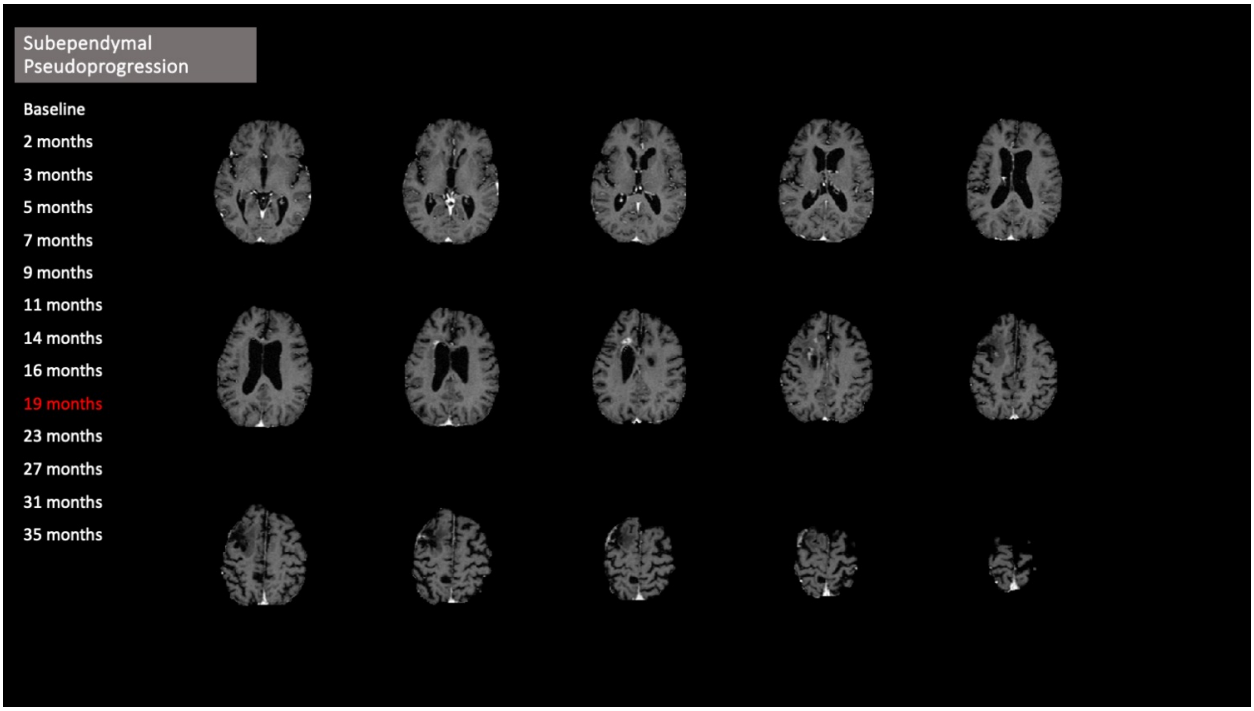
Subependymal
Pseudoprogression
Baseline
2 months
3 months
5 months
7 months
9 months
11 months
14 months
16 months
19 months
23 months
27 months
31 months
35 months

(Slide 11/14)

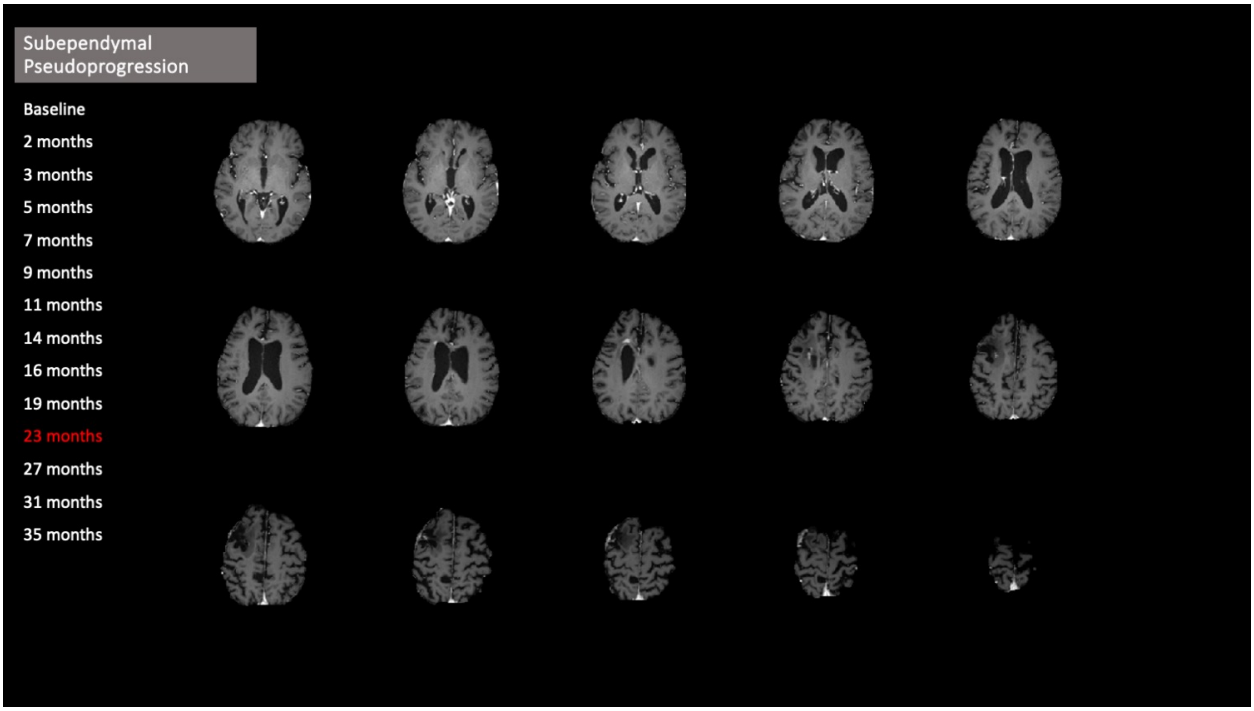
Subependymal
Pseudoprogression
Baseline
2 months
3 months
5 months
7 months
9 months
11 months
14 months
16 months
19 months
23 months
27 months
31 months
35 months

(Slide 12/14)

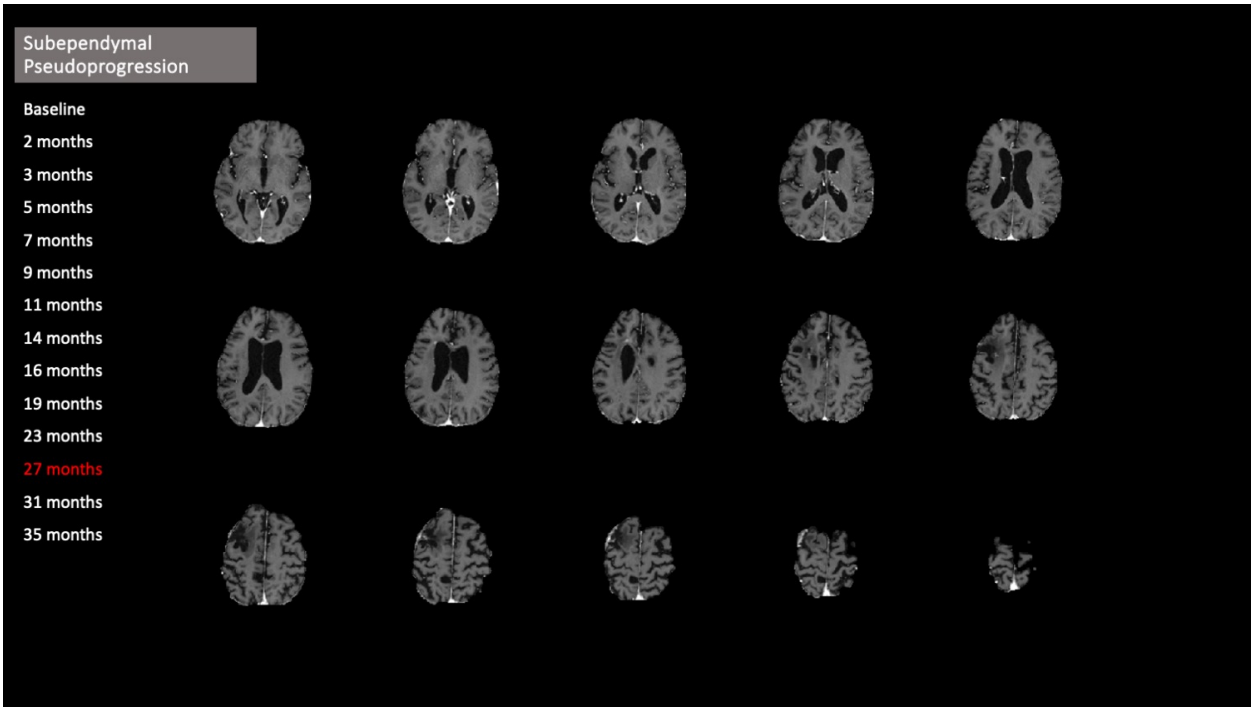
Subependymal Pseudoprogression
Baseline
2 months
3 months
5 months
7 months
9 months
11 months
14 months
16 months
19 months
23 months
27 months
31 months
35 months

(Slide 13/14)

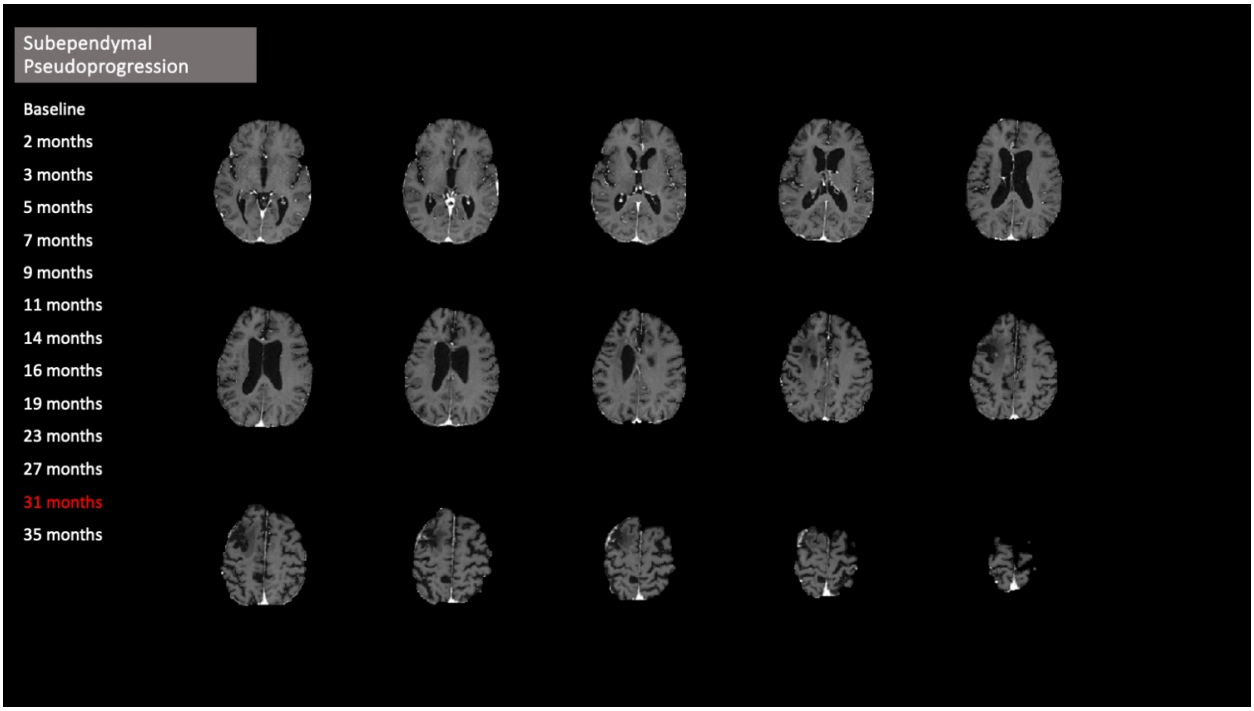
Subependymal
Pseudoprogression
Baseline
2 months
3 months
5 months
7 months
9 months
11 months
14 months
16 months
19 months
23 months
27 months
31 months
35 months

(Slide 14/14)

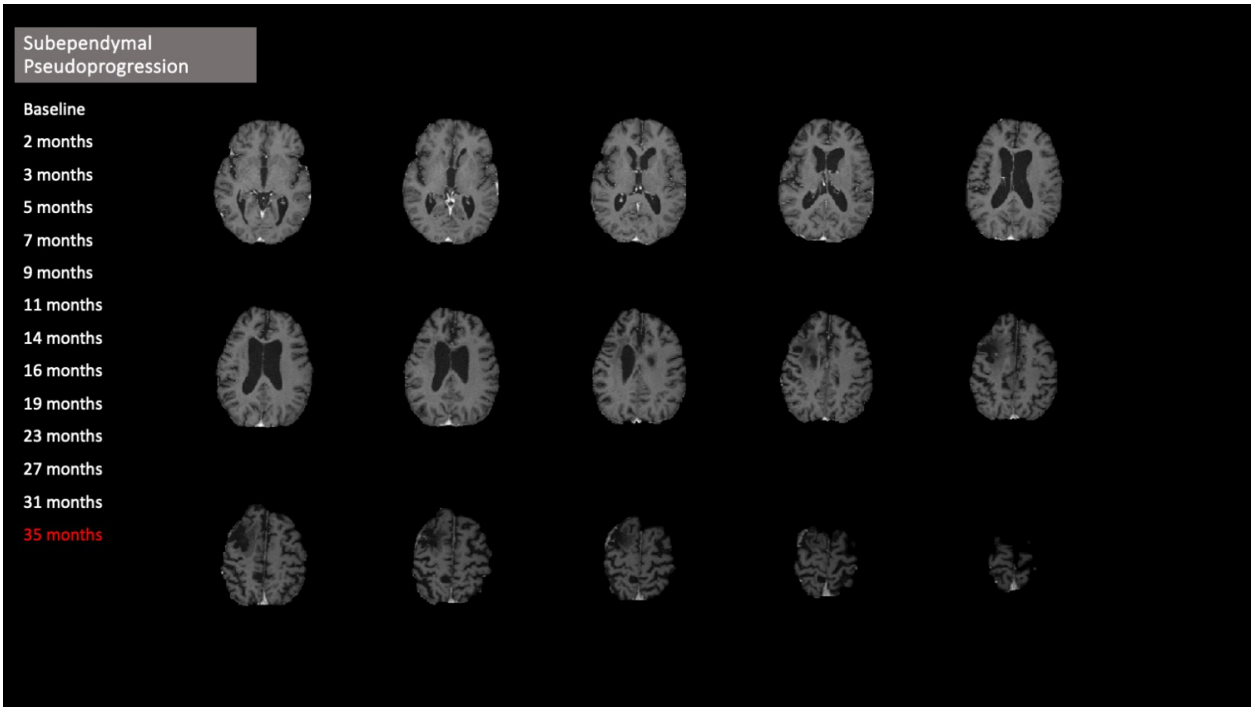
Subependymal
Pseudoprogression
Baseline
2 months
3 months
5 months
7 months
9 months
11 months
14 months
16 months
19 months
23 months
27 months
31 months
35 months

Limitations of Flipbooks

There are some limitations to the flipbooks concept that readers should be aware of when using this methodology for select cases in combination with qualitative clinical side-by-side reads. First, it is important to note that flipbooks work best if the image acquisition is standardized across time points within the same patient. Differences in acquisition parameters can lead to differences in contrast and challenges in windowing, thereby distracting from the ability to identify subtle changes. Also, it should be recognized that not all institutions may have the technical or personnel resources to create flipbooks. However, the proposed methodology has been optimized at our institution for utilizing minimally requisite image pre-processing steps and widely available software so that flipbooks can be made for patients on an as needed basis semi-regularly. Additionally, while the time for creating flipbooks may not be as quick as performing a real-time side-by-side read, flipbooks can be particularly appropriate for presentation at tumor boards where presentations are prepared for multi-disciplinary discussion on challenging cases when MRI scan interpretation and clinical decision making are non-trivial. Compared to a PACS workstation, the flipbooks also display each brain slice much smaller and with an artificial inter-slice gap to allow for whole-brain, mosaic view, which is optimal for an overview of tumor and tissue changes. Flipbooks are meant to be used in conjunction with PACS-based side-by-side reads and not as a replacement tool, so side-by-side reads must still be performed, especially for evaluating smaller details. Lastly, while this dissertation chapter summarizes a single-institution's perspective on the utility of flipbooks, a validation study would be valuable to systematically test the added value of flipbooks in relation to the time and effort involved in creating flipbooks for the clinical assessment of brain tumors.

Conclusions

Digital flipbooks derived from co-registered, longitudinal imaging exams may be advantageous for qualitative brain tumor evaluation to complement both RANO assessments and side-by-side reads in numerous clinical scenarios. Flipbooks can be created using freely available, open-source software with routine image pre-processing steps. Practicing physicians may consider creating flipbooks as needed for challenging cases to complement side-by-side reads across numerous timepoints, including for multi-disciplinary tumor board discussions. Future studies would be needed to assess the added value of flipbooks for clinical care upon wider adoption of the flipbooks concept.

Chapter 9. Conclusions and Future Directions

This dissertation focused on developing and utilizing new MRI tools to advance our understanding of human IDH-mutant gliomas. These tools and analyses methods have added to our field's knowledge of IDH-mutant glioma classification, cognitive impairment in patients, IDH inhibitor targeted therapy treatment response, malignant transformation, and longitudinal assessment. The conclusions and future directions of each study are presented below.

Aim 1. Development of Novel MRI Tools for IDH-Mutant Glioma Analyses

NAWM Normalization and T2-FLAIR Subtraction Maps

In **Chapter 2**, we developed an optimal NAWM normalization method for nrCBV values from DSC perfusion MRI and for nADC values from diffusion weighted MRI using a 3-spherical ROI method in the contralesional superior centrum semiovale.[41] The proposed method had excellent inter- and intra-reader agreement when assessed by 2 radiologists as well as the potential for time savings. In **Chapter 3**, we developed T2-FLAIR subtraction maps utilizing co-registered, z-score-normalized, NAWM-normalized (using the method developed in **Chapter 2**), and voxel-wise subtracted T2-weighted MRI and T2-weighted FLAIR MRI scans to quantitatively validate the visual T2-FLAIR mismatch sign.[42] The newly-developed metric percentage T2-FLAIR mismatch volume classified IDH-mutant astrocytomas with 100% specificity. Additionally, T2-FLAIR subtraction maps may be useful to characterize IDH-mutant astrocytomas, but there was no significant benefit in using T2-FLAIR subtraction maps for visual assessment of T2-FLAIR mismatch sign. In **Chapter 4**, we utilize T2-FLAIR subtraction maps to study the diffusion characteristics of IDH-mutant astrocytomas. We observe that T2-FLAIR subtraction map-defined

mismatched and non-mismatched IDH-mutant astrocytomas have different diffusion characteristics and that nADC is superior to percentage T2-FLAIR mismatch volume for classifying IDH-mutant astrocytomas amongst non-enhancing gliomas.

Future studies may consider exploring the biological correlates of T2-FLAIR subtraction map-defined mismatched and non-mismatched regions of the tumor to validate prior findings that mismatched subregions had greater microcysts and mTOR-pathway-related gene expression.[38] Molecular and histopathological correlates with T2-FLAIR subtraction map-guided biopsies in IDH-mutant astrocytoma would be valuable to better elucidate if mismatched IDH-mutant astrocytomas comprise a separate entity within IDH-mutant astrocytomas and/or the development of T2-FLAIR mismatch is characteristic of the development of some IDH-mutant astrocytomas. There may also be value in exploring T2-FLAIR subtraction maps within contrast-enhancing gliomas, especially given the recent discovery of a visual "partial" T2-FLAIR mismatch sign that can be used to identify grade 4 IDH-mutant astrocytomas with near-100% specificity.[93] Longitudinal analyses of T2-FLAIR mismatch[110] using T2-FLAIR subtraction maps (see representative case in **Figure 9.1**) would also be valuable to explore subregion growth dynamics and biological changes, including with other quantitative MRI sequences (diffusion, perfusion, and/or CEST MRI).

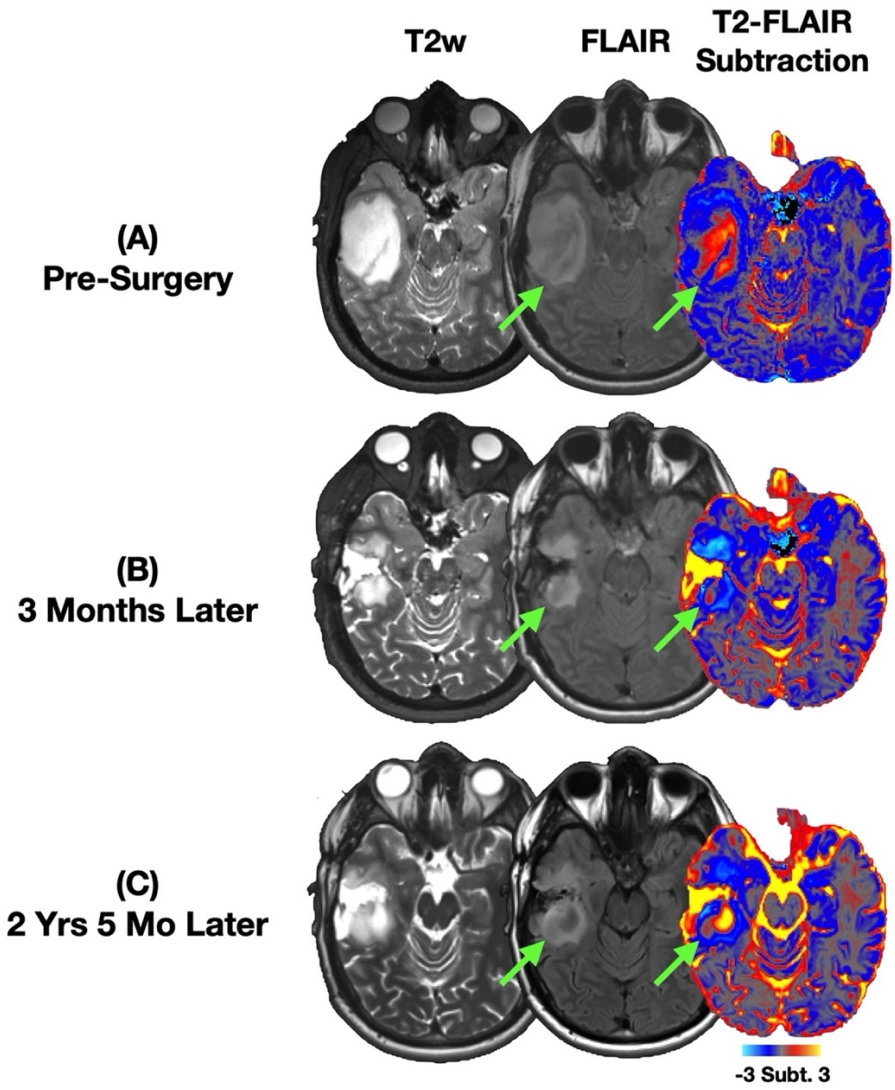

Figure 9.1 Representative Case of Visualizing Re-Development of T2-FLAIR Mismatch Post-Surgery Using T2-FLAIR Subtraction Maps. The patient is a 23-year-old male patient initially diagnosed with a grade 2 IDH-mutant astrocytoma. The glioma demonstrated T2-FLAIR mismatch sign at initial presentation (A) and re-developed T2-FLAIR mismatch areas (green arrows) after surgery.

Pseudo-Resting-State Functional MRI

In **Chapter 5**, we developed a novel MRI method called "pseudo-resting-state functional MRI" derived from DSC perfusion MRI (provisional patent filed). We conclude that this novel method can be readily employed by institutions around the world as a potential alternative to resting-state functional MRI for network mapping and functional connectivity analyses. Future studies using pseudo-resting-state functional MRI can expand upon prior resting-state functional MRI studies in patients with brain tumors by studying larger cohorts given the wide availability of DSC perfusion MRI. Studies related to patient cognition, brain reorganization, and pre-surgical planning utilizing the proposed pseudo-resting-state functional MRI would be valuable to demonstrate its potential clinical utility. Furthermore, novel functional connectivity analysis techniques such as graph theory[220] and BOLD asynchrony[154] (see **Chapter 7**) may be explored using pseudo-resting-state functional MRI to improve our understandings of cancer neuroscience and the brain tumor microenvironment. Pseudo-resting-state functional MRI should also be assessed in neurological conditions beyond brain tumors, including stroke, multiple sclerosis, Alzheimer's disease, epilepsy, and autism spectrum disorder. In the long-term, clinical integration of pseudo-resting-state functional MRI upon patent approval may also lead to a dedicated CPT code for functional connectivity analyses.

Aim 2. Contemporary Longitudinal Analyses of IDH-Mutant Gliomas

IDH Inhibitor Treatment and Malignant Transformation

In **Chapter 6**, we explored early volumetric, diffusion, and perfusion MRI changes in IDH-mutant gliomas upon IDH inhibitor therapy.[43] We conclude in this pilot study that the early ~1 month post-treatment timepoint (3–6 weeks) may reflect a combination of therapeutic effect and

continued tumor growth and that diffusion and perfusion metrics at the later 2–4 month timepoint may be more useful for IDH inhibitor treatment assessment. In **Chapter 7**, we explored volumetric, diffusion, and perfusion MRI biomarkers of IDH-mutant glioma malignant transformation. Future studies in these topics may want to utilize the pseudo-resting-state functional MRI technique to assess longitudinal brain functional connectivity and BOLD asynchrony changes in relation to therapy and/or tumor progression. Baseline predictors of successful IDH inhibitor therapy treatment or malignant transformation would also be valuable to improve IDH-mutant glioma patient management. The implementation of other advanced imaging techniques, such as pH-weighted CEST MRI,[187, 221, 222] may be valuable in the assessment of IDH inhibition and malignant transformation.

Flipbooks for Brain Tumor Assessment

Lastly, in **Chapter 8**, we introduced the concept of patient MRI flipbooks for improved visual assessment of IDH-mutant gliomas. We provide step-by-step methodology for clinicians and researchers at other institutions to develop flipbooks for brain tumor assessment. It is our hope that flipbooks become more readily utilized for neuro-oncological patient care. In the future, the development and implementation of automated MRI windowing methods would greatly expedite the flipbooks creation process and may improve the assessment of brain tumors using flipbooks.[223] Also, even though we readily use flipbooks at our institution, including for Brain Tumor Board multi-disciplinary discussions, a validation study would be valuable to assess the added value of flipbooks for brain tumor management.

In closing, the novel techniques and findings presented in this dissertation emphasize the need and possibilities for ongoing exploration into IDH-mutant gliomas. Expanded investigations

based on the ideas presented in this dissertation across larger cohorts and multiple institutions would be valuable to advance our knowledge of IDH-mutant gliomas and to improve the lives of patients with brain tumors.

References

1. Claus EB, Walsh KM, Wiencke JK, et al. Survival and low-grade glioma: the emergence of genetic information. *Neurosurg Focus* 2015;38:E6

2. Tran B, Rosenthal MA. Survival comparison between glioblastoma multiforme and other incurable cancers. *J Clin Neurosci* 2010;17:417-421

3. Louis DN, Perry A, Wesseling P, et al. The 2021 WHO Classification of Tumors of the Central Nervous System: a summary. *Neuro Oncol* 2021;23:1231-1251

4. Yan H, Parsons DW, Jin G, et al. IDH1 and IDH2 Mutations in Gliomas. *New England Journal of Medicine* 2009;360:765-773

5. Miller JJ, Gonzalez Castro LN, McBrayer S, et al. Isocitrate dehydrogenase (IDH) mutant gliomas: A Society for Neuro-Oncology (SNO) consensus review on diagnosis, management, and future directions. *Neuro-Oncology* 2023;25:4-25

6. Ostrom QT, Cioffi G, Waite K, et al. CBTRUS Statistical Report: Primary Brain and Other Central Nervous System Tumors Diagnosed in the United States in 2014-2018. *Neuro Oncol* 2021;23:iii1-iii105

7. Pekmezci M, Rice T, Molinaro AM, et al. Adult infiltrating gliomas with WHO 2016 integrated diagnosis: additional prognostic roles of ATRX and TERT. *Acta Neuropathol* 2017;133:1001-1016

8. Tork C, Atkinson C. Oligodendroglioma. *StatPearls*; 2023

9. Melhem JM, Detsky J, Lim-Fat MJ, et al. Updates in IDH-Wildtype Glioblastoma. *Neurotherapeutics* 2022;19:1705-1723

10. Suh CH, Kim HS, Jung SC, et al. Imaging prediction of isocitrate dehydrogenase (IDH) mutation in patients with glioma: a systemic review and meta-analysis. *European Radiology* 2019;29:745-758

11. Ellingson BM, Lai A, Harris RJ, et al. Probabilistic radiographic atlas of glioblastoma phenotypes. *AJNR Am J Neuroradiol* 2013;34:533-540

12. Mellinghoff IK, van den Bent MJ, Blumenthal DT, et al. Vorasidenib in IDH1- or IDH2-Mutant Low-Grade Glioma. *New England Journal of Medicine* 2023

13. Juratli TA, Kirsch M, Robel K, et al. IDH mutations as an early and consistent marker in low-grade astrocytomas WHO grade II and their consecutive secondary high-grade gliomas. *J Neurooncol* 2012;108:403-410

14. Gorovets D, Kannan K, Shen R, et al. IDH Mutation and Neuroglial Developmental Features Define Clinically Distinct Subclasses of Lower Grade Diffuse Astrocytic Glioma. *Clinical Cancer Research* 2012;18:2490-2501

15. Hartmann C, Meyer J, Balss J, et al. Type and frequency of IDH1 and IDH2 mutations are related to astrocytic and oligodendroglial differentiation and age: a study of 1,010 diffuse gliomas. *Acta Neuropathol* 2009;118:469-474

16. Dang L, White DW, Gross S, et al. Cancer-associated IDH1 mutations produce 2-hydroxyglutarate. *Nature* 2009;462:739-744

17. Yang H, Ye D, Guan K-L, et al. IDH1 and IDH2 mutations in tumorigenesis: mechanistic insights and clinical perspectives. *Clin Cancer Res* 2012;18:5562-5571

18. Xu W, Yang H, Liu Y, et al. Oncometabolite 2-hydroxyglutarate is a competitive inhibitor of α-ketoglutarate-dependent dioxygenases. *Cancer Cell* 2011;19:17-30

19. Turcan S, Rohle D, Goenka A, et al. IDH1 mutation is sufficient to establish the glioma hypermethylator phenotype. *Nature* 2012;483:479-483

20. Chesnelong C, Chaumeil MM, Blough MD, et al. Lactate dehydrogenase A silencing in IDH mutant gliomas. *Neuro Oncol* 2014;16:686-695

21. Kickingereder P, Sahm F, Radbruch A, et al. IDH mutation status is associated with a distinct hypoxia/angiogenesis transcriptome signature which is non-invasively predictable with rCBV imaging in human glioma. *Scientific Reports* 2015;5:16238

22. Molloy AR, Najac C, Viswanath P, et al. MR-detectable metabolic biomarkers of response to mutant IDH inhibition in low-grade glioma. *Theranostics* 2020;10:8757-8770

23. Rohle D, Popovici-Muller J, Palaskas N, et al. An Inhibitor of Mutant IDH1 Delays Growth and Promotes Differentiation of Glioma Cells. *Science* 2013;340:626-630

24. Mellinghoff IK, Ellingson BM, Touat M, et al. Ivosidenib in Isocitrate Dehydrogenase 1-Mutated Advanced Glioma. *J Clin Oncol* 2020;38:3398-3406

25. Mellinghoff IK, Penas-Prado M, Peters KB, et al. Vorasidenib, a Dual Inhibitor of Mutant IDH1/2, in Recurrent or Progressive Glioma; Results of a First-in-Human Phase I Trial. *Clin Cancer Res* 2021;27:4491-4499

26. Johannessen TA, Mukherjee J, Viswanath P, et al. Rapid Conversion of Mutant IDH1 from Driver to Passenger in a Model of Human Gliomagenesis. *Mol Cancer Res* 2016;14:976-983

27. Jalbert LE, Elkhaled A, Phillips JJ, et al. Metabolic Profiling of IDH Mutation and Malignant Progression in Infiltrating Glioma. *Sci Rep* 2017;7:44792

28. Noushmehr H, Weisenberger DJ, Diefes K, et al. Identification of a CpG island methylator phenotype that defines a distinct subgroup of glioma. *Cancer Cell* 2010;17:510-522

29. Park JW, Turcan Ş. Epigenetic Reprogramming for Targeting IDH-Mutant Malignant Gliomas. *Cancers (Basel)* 2019;11

30. Ruiz-Rodado V, Malta TM, Seki T, et al. Metabolic reprogramming associated with aggressiveness occurs in the G-CIMP-high molecular subtypes of IDH1mut lower grade gliomas. *Neuro Oncol* 2020;22:480-492

31. Mohamed E, Kumar A, Zhang Y, et al. PI3K/AKT/mTOR signaling pathway activity in IDH-mutant diffuse glioma and clinical implications. *Neuro-Oncology* 2022;24:1471-1481

32. Ellingson BM, Kim HJ, Woodworth DC, et al. Recurrent glioblastoma treated with bevacizumab: contrast-enhanced T1-weighted subtraction maps improve tumor delineation and aid prediction of survival in a multicenter clinical trial. *Radiology* 2014;271:200-210

33. Ellingson BM, Harris RJ, Woodworth DC, et al. Baseline pretreatment contrast enhancing tumor volume including central necrosis is a prognostic factor in recurrent glioblastoma: evidence from single and multicenter trials. *Neuro Oncol* 2017;19:89-98

34. Barajas RF, Hodgson JG, Chang JS, et al. Glioblastoma Multiforme Regional Genetic and Cellular Expression Patterns: Influence on Anatomic and Physiologic MR Imaging. *Radiology* 2010;254:564-576

35. Gupta RK, Cloughesy TF, Sinha U, et al. Relationships between choline magnetic resonance spectroscopy, apparent diffusion coefficient and quantitative histopathology in human glioma. *J Neurooncol* 2000;50:215-226

36. Chakhoyan A, Yao J, Leu K, et al. Validation of vessel size imaging (VSI) in high-grade human gliomas using magnetic resonance imaging, image-guided biopsies, and quantitative immunohistochemistry. *Scientific Reports* 2019;9:2846

37. Barajas RF, Chang JS, Segal MR, et al. Differentiation of Recurrent Glioblastoma Multiforme from Radiation Necrosis after External Beam Radiation Therapy with Dynamic Susceptibility-weighted Contrast-enhanced Perfusion MR Imaging. *Radiology* 2009;253:486-496

38. Patel SH, Poisson LM, Brat DJ, et al. T2–FLAIR Mismatch, an Imaging Biomarker for IDH and 1p/19q Status in Lower-grade Gliomas: A TCGA/TCIA Project. *Clinical Cancer Research* 2017;23:6078-6085

39. Cho NS, Sanvito F, Thakuria S, et al. Multi-nuclear sodium, diffusion, and perfusion MRI in human gliomas. *J Neurooncol* 2023;163:417-427

40. Rees J, Watt H, Jäger HR, et al. Volumes and growth rates of untreated adult low-grade gliomas indicate risk of early malignant transformation. *Eur J Radiol* 2009;72:54-64

41. Cho NS, Hagiwara A, Sanvito F, et al. A multi-reader comparison of normal-appearing white matter normalization techniques for perfusion and diffusion MRI in brain tumors. *Neuroradiology* 2023;65:559-568

42. Cho NS, Sanvito F, Le VL, et al. Quantification of T2-FLAIR Mismatch in Nonenhancing Diffuse Gliomas Using Digital Subtraction. *AJNR Am J Neuroradiol* 2024;45:188-197

43. Cho NS, Hagiwara A, Eldred BSC, et al. Early Volumetric, Perfusion, and Diffusion MRI Changes after Mutant Isocitrate Dehydrogenase (IDH) Inhibitor Treatment in IDH1-Mutant Gliomas. *Neuro-Oncology Advances* 2022:vdac124

44. Ellingson BM, Zaw T, Cloughesy TF, et al. Comparison between intensity normalization techniques for dynamic susceptibility contrast (DSC)-MRI estimates of cerebral blood volume (CBV) in human gliomas. *J Magn Reson Imaging* 2012;35:1472-1477

45. Thomsen H, Steffensen E, Larsson EM. Perfusion MRI (dynamic susceptibility contrast imaging) with different measurement approaches for the evaluation of blood flow and blood volume in human gliomas. *Acta Radiol* 2012;53:95-101

46. Quantitative Imaging Biomarkers Alliance Profile: Dynamic Susceptibility Contrast MRI (DSC-MRI). *Stage 2: Consensus Profile*; 2020

47. Sugahara T, Korogi Y, Tomiguchi S, et al. Posttherapeutic intraaxial brain tumor: the value of perfusion-sensitive contrast-enhanced MR imaging for differentiating tumor recurrence from nonneoplastic contrast-enhancing tissue. *AJNR Am J Neuroradiol* 2000;21:901-909

48. Matsusue E, Fink JR, Rockhill JK, et al. Distinction between glioma progression and post-radiation change by combined physiologic MR imaging. *Neuroradiology* 2010;52:297-306

49. Jiang J, Zhao L, Zhang Y, et al. Comparative analysis of arterial spin labeling and dynamic susceptibility contrast perfusion imaging for quantitative perfusion measurements of brain tumors. *Int J Clin Exp Pathol* 2014;7:2790-2799

50. Testud B, Brun G, Varoquaux A, et al. Perfusion-weighted techniques in MRI grading of pediatric cerebral tumors: efficiency of dynamic susceptibility contrast and arterial spin labeling. *Neuroradiology* 2021;63:1353-1366

51. Anzalone N, Castellano A, Cadioli M, et al. Brain Gliomas: Multicenter Standardized Assessment of Dynamic Contrast-enhanced and Dynamic Susceptibility Contrast MR Images. *Radiology* 2018;287:933-943

52. Conte GM, Castellano A, Altabella L, et al. Reproducibility of dynamic contrast-enhanced MRI and dynamic susceptibility contrast MRI in the study of brain gliomas: a comparison of data obtained using different commercial software. *Radiol Med* 2017;122:294-302

53. Smits M, Bendszus M, Collette S, et al. Repeatability and reproducibility of relative cerebral blood volume measurement of recurrent glioma in a multicentre trial setting. *European Journal of Cancer* 2019;114:89-96

54. Zhang H, Rödiger LA, Shen T, et al. Perfusion MR imaging for differentiation of benign and malignant meningiomas. *Neuroradiology* 2008;50:525-530

55. Hu LS, Baxter LC, Pinnaduwage DS, et al. Optimized Preload Leakage-Correction Methods to Improve the Diagnostic Accuracy of Dynamic Susceptibility-Weighted Contrast-Enhanced Perfusion MR Imaging in Posttreatment Gliomas. *American Journal of Neuroradiology* 2010;31:40

56. Bedekar D, Jensen T, Schmainda KM. Standardization of relative cerebral blood volume (rCBV) image maps for ease of both inter- and intrapatient comparisons. *Magn Reson Med* 2010;64:907-913

57. Prah MA, Stufflebeam SM, Paulson ES, et al. Repeatability of Standardized and Normalized Relative CBV in Patients with Newly Diagnosed Glioblastoma. *AJNR Am J Neuroradiol* 2015;36:1654-1661

58. Hoxworth JM, Eschbacher JM, Gonzales AC, et al. Performance of Standardized Relative CBV for Quantifying Regional Histologic Tumor Burden in Recurrent High-Grade Glioma: Comparison against Normalized Relative CBV Using Image-Localized Stereotactic Biopsies. *AJNR Am J Neuroradiol* 2020;41:408-415

59. Elson A, Bovi J, Siker M, et al. Evaluation of absolute and normalized apparent diffusion coefficient (ADC) values within the post-operative T2/FLAIR volume as adverse prognostic indicators in glioblastoma. *J Neurooncol* 2015;122:549-558

60. Hagiwara A, Oughourlian TC, Cho NS, et al. Diffusion MRI is an early biomarker of overall survival benefit in IDH wild-type recurrent glioblastoma treated with immune checkpoint inhibitors. *Neuro-Oncology* 2022;24:1020-1028

61. Thust SC, Hassanein S, Bisdas S, et al. Apparent diffusion coefficient for molecular subtyping of non-gadolinium-enhancing WHO grade II/III glioma: volumetric segmentation versus two-dimensional region of interest analysis. *European Radiology* 2018;28:3779-3788

62. Qin L, Li A, Qu J, et al. Normalization of ADC does not improve correlation with overall survival in patients with high-grade glioma (HGG). *Journal of neuro-oncology* 2018;137:313-319

63. Xing Z, Yang X, She D, et al. Noninvasive Assessment of IDH Mutational Status in World Health Organization Grade II and III Astrocytomas Using DWI and DSC-PWI Combined with Conventional MR Imaging. *AJNR Am J Neuroradiol* 2017;38:1138-1144

64. Kathrani N, Chauhan RS, Kotwal A, et al. Diffusion and perfusion imaging biomarkers of H3 K27M mutation status in diffuse midline gliomas. *Neuroradiology* 2022;64:1519-1528

65. Lin Y, Xing Z, She D, et al. IDH mutant and 1p/19q co-deleted oligodendrogliomas: tumor grade stratification using diffusion-, susceptibility-, and perfusion-weighted MRI. *Neuroradiology* 2017;59:555-562

66. Zonari P, Baraldi P, Crisi G. Multimodal MRI in the characterization of glial neoplasms: the combined role of single-voxel MR spectroscopy, diffusion imaging and echo-planar perfusion imaging. *Neuroradiology* 2007;49:795-803

67. Ellingson BM, Kim E, Woodworth DC, et al. Diffusion MRI quality control and functional diffusion map results in ACRIN 6677/RTOG 0625: a multicenter, randomized, phase II trial of bevacizumab and chemotherapy in recurrent glioblastoma. *Int J Oncol* 2015;46:1883-1892

68. Horváth A, Perlaki G, Tóth A, et al. Biexponential diffusion alterations in the normal-appearing white matter of glioma patients might indicate the presence of global vasogenic edema. *J Magn Reson Imaging* 2016;44:633-641

69. Leu K, Ott GA, Lai A, et al. Perfusion and diffusion MRI signatures in histologic and genetic subtypes of WHO grade II–III diffuse gliomas. *Journal of Neuro-Oncology* 2017;134:177-188

70. Lai A, Kharbanda S, Pope WB, et al. Evidence for sequenced molecular evolution of IDH1 mutant glioblastoma from a distinct cell of origin. *J Clin Oncol* 2011;29:4482-4490

71. Ellingson BM, Bendszus M, Boxerman J, et al. Consensus recommendations for a standardized Brain Tumor Imaging Protocol in clinical trials. *Neuro-Oncology* 2015;17:1188-1198

72. Boxerman JL, Quarles CC, Hu LS, et al. Consensus recommendations for a dynamic susceptibility contrast MRI protocol for use in high-grade gliomas. *Neuro-Oncology* 2020;22:1262-1275

73. Boxerman JL, Shiroishi MS, Ellingson BM, et al. Dynamic Susceptibility Contrast MR Imaging in Glioma: Review of Current Clinical Practice. *Magnetic Resonance Imaging Clinics of North America* 2016;24:649-670

74. Leu K, Boxerman JL, Cloughesy TF, et al. Improved Leakage Correction for Single-Echo Dynamic Susceptibility Contrast Perfusion MRI Estimates of Relative Cerebral Blood Volume in High-Grade Gliomas by Accounting for Bidirectional Contrast Agent Exchange. *AJNR American journal of neuroradiology* 2016;37:1440-1446

75. Yushkevich PA, Piven J, Hazlett HC, et al. User-guided 3D active contour segmentation of anatomical structures: significantly improved efficiency and reliability. *Neuroimage* 2006;31:1116-1128

76. Cox RW. AFNI: software for analysis and visualization of functional magnetic resonance neuroimages. *Comput Biomed Res* 1996;29:162-173

77. Koo TK, Li MY. A Guideline of Selecting and Reporting Intraclass Correlation Coefficients for Reliability Research. *J Chiropr Med* 2016;15:155-163

78. Bobak CA, Barr PJ, O'Malley AJ. Estimation of an inter-rater intra-class correlation coefficient that overcomes common assumption violations in the assessment of health measurement scales. *BMC Med Res Methodol* 2018;18:93

79. Shrot S, Salhov M, Dvorski N, et al. Application of MR morphologic, diffusion tensor, and perfusion imaging in the classification of brain tumors using machine learning scheme. *Neuroradiology* 2019;61:757-765

80. Park YW, Ahn SS, Kim EH, et al. Differentiation of recurrent diffuse glioma from treatment-induced change using amide proton transfer imaging: incremental value to diffusion and perfusion parameters. *Neuroradiology* 2021;63:363-372

81. Hu LS, Baxter LC, Smith KA, et al. Relative cerebral blood volume values to differentiate high-grade glioma recurrence from posttreatment radiation effect: direct correlation between image-guided tissue histopathology and localized dynamic susceptibility-weighted contrast-enhanced perfusion MR imaging measurements. *AJNR Am J Neuroradiol* 2009;30:552-558

82. Jenkinson MD, Smith TS, Joyce KA, et al. Cerebral blood volume, genotype and chemosensitivity in oligodendroglial tumours. *Neuroradiology* 2006;48:703-713

83. Kikuchi K, Hiwatashi A, Togao O, et al. Usefulness of perfusion- and diffusion-weighted imaging to differentiate between pilocytic astrocytomas and high-grade gliomas: a multicenter study in Japan. *Neuroradiology* 2018;60:391-401

84. Hagiwara A, Fujita S, Ohno Y, et al. Variability and Standardization of Quantitative Imaging: Monoparametric to Multiparametric Quantification, Radiomics, and Artificial Intelligence. *Invest Radiol* 2020;55:601-616

85. Broen MPG, Smits M, Wijnenga MMJ, et al. The T2-FLAIR mismatch sign as an imaging marker for non-enhancing IDH-mutant, 1p/19q-intact lower-grade glioma: a validation study. *Neuro Oncol* 2018;20:1393-1399

86. Lasocki A, Buckland ME, Drummond KJ, et al. Conventional MRI features can predict the molecular subtype of adult grade 2–3 intracranial diffuse gliomas. *Neuroradiology* 2022;64:2295-2305

87. Corell A, Ferreyra Vega S, Hoefling N, et al. The clinical significance of the T2-FLAIR mismatch sign in grade II and III gliomas: a population-based study. *BMC Cancer* 2020;20:450

88. Juratli TA, Tummala SS, Riedl A, et al. Radiographic assessment of contrast enhancement and T2/FLAIR mismatch sign in lower grade gliomas: correlation with molecular groups. *J Neurooncol* 2019;141:327-335

89. Kinoshita M, Arita H, Takahashi M, et al. Impact of Inversion Time for FLAIR Acquisition on the T2-FLAIR Mismatch Detectability for IDH-Mutant, Non-CODEL Astrocytomas. *Frontiers in Oncology* 2021;10

90. Deguchi S, Oishi T, Mitsuya K, et al. Clinicopathological analysis of T2-FLAIR mismatch sign in lower-grade gliomas. *Scientific Reports* 2020;10:10113

91. Jain R, Johnson DR, Patel SH, et al. “Real world” use of a highly reliable imaging sign: “T2-FLAIR mismatch” for identification of IDH mutant astrocytomas. *Neuro-Oncology* 2020;22:936-943

92. Li M, Ren X, Chen X, et al. Combining hyperintense FLAIR rim and radiological features in identifying IDH mutant 1p/19q non-codeleted lower-grade glioma. *European Radiology* 2022;32:3869-3879

93. Lee MD, Patel SH, Mohan S, et al. Association of partial T2-FLAIR mismatch sign and isocitrate dehydrogenase mutation in WHO grade 4 gliomas: results from the ReSPOND consortium. *Neuroradiology* 2023;65:1343-1352

94. Mohammed S, Ravikumar V, Warner E, et al. Quantifying T2-FLAIR Mismatch Using Geographically Weighted Regression and Predicting Molecular Status in Lower-Grade Gliomas. *AJNR Am J Neuroradiol* 2022;43:33-39

95. Lee MK, Park JE, Jo Y, et al. Advanced imaging parameters improve the prediction of diffuse lower-grade gliomas subtype, IDH mutant with no 1p19q codeletion: added value to the T2/FLAIR mismatch sign. *European Radiology* 2020;30:844-854

96. Yamashita S, Takeshima H, Kadota Y, et al. T2-fluid-attenuated inversion recovery mismatch sign in lower grade gliomas: correlation with pathological and molecular findings. *Brain Tumor Pathol* 2022;39:88-98

97. Calabrese E, Villanueva-Meyer JE, Rudie JD, et al. The University of California San Francisco Preoperative Diffuse Glioma MRI (UCSF-PDGM) (Version 4) [Dataset]. The Cancer Imaging Archive; 2022

98. Calabrese E, Villanueva-Meyer JE, Rudie JD, et al. The University of California San Francisco Preoperative Diffuse Glioma MRI Dataset. *Radiology: Artificial Intelligence* 2022;4:e220058

99. Clark K, Vendt B, Smith K, et al. The Cancer Imaging Archive (TCIA): Maintaining and Operating a Public Information Repository. *Journal of Digital Imaging* 2013;26:1045-1057

100. Kline CN, Joseph NM, Grenert JP, et al. Targeted next-generation sequencing of pediatric neuro-oncology patients improves diagnosis, identifies pathogenic germline mutations, and directs targeted therapy. *Neuro-Oncology* 2017;19:699-709

101. Fischl B. FreeSurfer. *Neuroimage* 2012;62:774-781

102. Smith SM, Jenkinson M, Woolrich MW, et al. Advances in functional and structural MR image analysis and implementation as FSL. *Neuroimage* 2004;23 Suppl 1:S208-219

103. Isensee F, Schell M, Pflueger I, et al. Automated brain extraction of multisequence MRI using artificial neural networks. *Human Brain Mapping* 2019;40:4952-4964

104. Cox RW. AFNI: Software for Analysis and Visualization of Functional Magnetic Resonance Neuroimages. *Computers and Biomedical Research* 1996;29:162-173

105. Ellingson BM, Harris RJ, Woodworth DC, et al. Baseline pretreatment contrast enhancing tumor volume including central necrosis is a prognostic factor in recurrent glioblastoma: evidence from single and multicenter trials. *Neuro-Oncology* 2017;19:89-98

106. Viera AJ, Garrett JM. Understanding interobserver agreement: the kappa statistic. *Fam Med* 2005;37:360-363

107. Foltyn M, Nieto Taborda KN, Neuberger U, et al. T2/FLAIR-mismatch sign for noninvasive detection of IDH-mutant 1p/19q non-codeleted gliomas: validity and pathophysiology. *Neuro-Oncology Advances* 2020;2:vdaa004

108. Wagner MW, Nobre L, Namdar K, et al. T2-FLAIR Mismatch Sign in Pediatric Low-Grade Glioma. *American Journal of Neuroradiology* 2023;44:841

109. Mancini L, Casagranda S, Gautier G, et al. CEST MRI provides amide/amine surrogate biomarkers for treatment-naïve glioma sub-typing. *Eur J Nucl Med Mol Imaging* 2022;49:2377-2391

110. van Garderen KA, Vallentgoed WR, Lavrova A, et al. Longitudinal characteristics of T2-FLAIR mismatch in IDH-mutant astrocytomas: Relation to grade, histopathology, and overall survival in the GLASS-NL cohort. *Neuro-Oncology Advances* 2023;5:vdad149

111. Ellingson BM, Malkin MG, Rand SD, et al. Validation of functional diffusion maps (fDMs) as a biomarker for human glioma cellularity. *J Magn Reson Imaging* 2010;31:538-548

112. Mecca C, Giambanco I, Donato R, et al. Targeting mTOR in Glioblastoma: Rationale and Preclinical/Clinical Evidence. *Dis Markers* 2018;2018:9230479

113. Ryskalin L, Lazzeri G, Flaibani M, et al. mTOR-Dependent Cell Proliferation in the Brain. *Biomed Res Int* 2017;2017:7082696

114. Karavaeva E, Harris RJ, Leu K, et al. Relationship Between [18F]FDOPA PET Uptake, Apparent Diffusion Coefficient (ADC), and Proliferation Rate in Recurrent Malignant Gliomas. *Mol Imaging Biol* 2015;17:434-442

115. Feraco P, Bacci A, Ferrazza P, et al. Magnetic Resonance Imaging Derived Biomarkers of IDH Mutation Status and Overall Survival in Grade III Astrocytomas. *Diagnostics*; 2020

116. Wu CC, Jain R, Radmanesh A, et al. Predicting Genotype and Survival in Glioma Using Standard Clinical MR Imaging Apparent Diffusion Coefficient Images: A Pilot Study from The Cancer Genome Atlas. *American Journal of Neuroradiology* 2018;39:1814

117. Carstam L, Corell A, Smits A, et al. WHO Grade Loses Its Prognostic Value in Molecularly Defined Diffuse Lower-Grade Gliomas. *Front Oncol* 2021;11:803975

118. Houillier C, Wang X, Kaloshi G, et al. IDH1 or IDH2 mutations predict longer survival and response to temozolomide in low-grade gliomas. *Neurology* 2010;75:1560-1566

119. Pasquini L, Peck KK, Jenabi M, et al. Functional MRI in Neuro-Oncology: State of the Art and Future Directions. *Radiology* 2023;308:e222028

120. Luna LP, Sherbaf FG, Sair HI, et al. Can Preoperative Mapping with Functional MRI Reduce Morbidity in Brain Tumor Resection? A Systematic Review and Meta-Analysis of 68 Observational Studies. *Radiology* 2021;300:338-349

121. Peck KK, Cho NS, Holodny AI. Methods of Analysis: Functional MRI for Presurgical Planning. *Neuroimaging Clin N Am* 2021;31:23-32

122. Biswal B, Yetkin FZ, Haughton VM, et al. Functional connectivity in the motor cortex of resting human brain using echo-planar MRI. *Magn Reson Med* 1995;34:537-541

123. Gohel S, Laino ME, Rajeev-Kumar G, et al. Resting-State Functional Connectivity of the Middle Frontal Gyrus Can Predict Language Lateralization in Patients with Brain Tumors. *American Journal of Neuroradiology* 2019;40:319

124. Kumar VA, Heiba IM, Prabhu SS, et al. The role of resting-state functional MRI for clinical preoperative language mapping. *Cancer Imaging* 2020;20:47

125. Leuthardt EC, Guzman G, Bandt SK, et al. Integration of resting state functional MRI into clinical practice - A large single institution experience. *PLOS ONE* 2018;13:e0198349

126. Sair HI, Yahyavi-Firouz-Abadi N, Calhoun VD, et al. Presurgical brain mapping of the language network in patients with brain tumors using resting-state fMRI: Comparison with task fMRI. *Human Brain Mapping* 2016;37:913-923

127. Tie Y, Rigolo L, Norton IH, et al. Defining language networks from resting-state fMRI for surgical planning—a feasibility study. *Human Brain Mapping* 2014;35:1018-1030

128. Greicius MD, Krasnow B, Reiss AL, et al. Functional connectivity in the resting brain: a network analysis of the default mode hypothesis. *Proc Natl Acad Sci U S A* 2003;100:253-258

129. Greicius MD, Supekar K, Menon V, et al. Resting-State Functional Connectivity Reflects Structural Connectivity in the Default Mode Network. *Cerebral Cortex* 2009;19:72-78

130. Huang Q, Zhang R, Hu X, et al. Disturbed small-world networks and neurocognitive function in frontal lobe low-grade glioma patients. *PLoS One* 2014;9:e94095

131. Kocher M, Jockwitz C, Caspers S, et al. Role of the default mode resting-state network for cognitive functioning in malignant glioma patients following multimodal treatment. *Neuroimage Clin* 2020;27:102287

132. Noll KR, Chen HS, Wefel JS, et al. Alterations in Functional Connectomics Associated With Neurocognitive Changes Following Glioma Resection. *Neurosurgery* 2021;88:544-551

133. Seitzman BA, Anandarajah H, Dworetsky A, et al. Cognitive deficits and altered functional brain network organization in pediatric brain tumor patients. *Brain Imaging Behav* 2023;17:689-701

134. Wang C, Van Dyk K, Cho N, et al. Characterization of cognitive function in survivors of diffuse gliomas using resting-state functional MRI (rs-fMRI). *Brain Imaging Behav* 2022;16:239-251

135. Nayak L, DeAngelis LM, Brandes AA, et al. The Neurologic Assessment in Neuro-Oncology (NANO) scale: a tool to assess neurologic function for integration into the Response Assessment in Neuro-Oncology (RANO) criteria. *Neuro Oncol* 2017;19:625-635

136. Correa DD. Neurocognitive function in brain tumors. *Curr Neurol Neurosci Rep* 2010;10:232-239

137. Fatterpekar GM, Galheigo D, Narayana A, et al. Treatment-Related Change Versus Tumor Recurrence in High-Grade Gliomas: A Diagnostic Conundrum—Use of Dynamic Susceptibility Contrast-Enhanced (DSC) Perfusion MRI. *American Journal of Roentgenology* 2012;198:19-26

138. Kim YH, Oh SW, Lim YJ, et al. Differentiating radiation necrosis from tumor recurrence in high-grade gliomas: Assessing the efficacy of 18F-FDG PET, 11C-methionine PET and perfusion MRI. *Clinical Neurology and Neurosurgery* 2010;112:758-765

139. Kumar VA, Lee J, Liu HL, et al. Recommended Resting-State fMRI Acquisition and Preprocessing Steps for Preoperative Mapping of Language and Motor and Visual Areas in Adult and Pediatric Patients with Brain Tumors and Epilepsy. *AJNR Am J Neuroradiol* 2024;45:139-148

140. Wefel JS, Vardy J, Ahles T, et al. International Cognition and Cancer Task Force recommendations to harmonise studies of cognitive function in patients with cancer. *Lancet Oncol* 2011;12:703-708

141. Reijneveld JC, Sitskoorn MM, Klein M, et al. Cognitive status and quality of life in patients with suspected versus proven low-grade gliomas. *Neurology* 2001;56:618-623

142. Ingraham LJ, Aiken CB. An empirical approach to determining criteria for abnormality in test batteries with multiple measures. *Neuropsychology* 1996;10:120-124

143. Whitfield-Gabrieli S, Nieto-Castanon A. Conn: a functional connectivity toolbox for correlated and anticorrelated brain networks. *Brain Connect* 2012;2:125-141

144. Jenkinson M, Beckmann CF, Behrens TEJ, et al. FSL. *NeuroImage* 2012;62:782-790

145. Otten ML, Mikell CB, Youngerman BE, et al. Motor deficits correlate with resting state motor network connectivity in patients with brain tumours. *Brain* 2012;135:1017-1026

146. Leu K, Boxerman JL, Cloughesy TF, et al. Improved Leakage Correction for Single-Echo Dynamic Susceptibility Contrast Perfusion MRI Estimates of Relative Cerebral Blood Volume in

High-Grade Gliomas by Accounting for Bidirectional Contrast Agent Exchange. *AJNR Am J Neuroradiol* 2016;37:1440-1446

147. Leu K, Boxerman JL, Lai A, et al. Bidirectional Contrast agent leakage correction of dynamic susceptibility contrast (DSC)-MRI improves cerebral blood volume estimation and survival prediction in recurrent glioblastoma treated with bevacizumab. *J Magn Reson Imaging* 2016;44:1229-1237

148. Hanley JA, McNeil BJ. A method of comparing the areas under receiver operating characteristic curves derived from the same cases. *Radiology* 1983;148:839-843

149. Rudie JD, Brown JA, Beck-Pancer D, et al. Altered functional and structural brain network organization in autism. *Neuroimage Clin* 2012;2:79-94

150. Tomasi D, Volkow ND. Aging and functional brain networks. *Mol Psychiatry* 2012;17:471, 549-458

151. Wang K, Liang M, Wang L, et al. Altered functional connectivity in early Alzheimer's disease: A resting-state fMRI study. *Human Brain Mapping* 2007;28:967-978

152. Park CH, Chang WH, Ohn SH, et al. Longitudinal changes of resting-state functional connectivity during motor recovery after stroke. *Stroke* 2011;42:1357-1362

153. Daniel AGS, Park KY, Roland JL, et al. Functional connectivity within glioblastoma impacts overall survival. *Neuro-Oncology* 2021;23:412-421

154. Petridis PD, Horenstein CI, Pereira B, et al. BOLD asynchrony elucidates tumor burden in IDH-mutated gliomas. *Neuro Oncol* 2022;24:78-87

155. Van Dijk KR, Hedden T, Venkataraman A, et al. Intrinsic functional connectivity as a tool for human connectomics: theory, properties, and optimization. *J Neurophysiol* 2010;103:297-321

156. Chakhoyan A, Leu K, Pope WB, et al. Improved Spatiotemporal Resolution of Dynamic Susceptibility Contrast Perfusion MRI in Brain Tumors Using Simultaneous Multi-Slice Echo-Planar Imaging. *AJNR Am J Neuroradiol* 2018;39:43-45

157. Bathla G, Gene MN, Peck KK, et al. Resting State Functional Connectivity of the Supplementary Motor Area to Motor and Language Networks in Patients with Brain Tumors. *J Neuroimaging* 2019;29:521-526

158. Cho NS, Peck KK, Gene MN, et al. Resting-state functional MRI language network connectivity differences in patients with brain tumors: exploration of the cerebellum and contralesional hemisphere. *Brain Imaging and Behavior* 2022;16:252-262

159. Stokes AM, Bergamino M, Alhilali L, et al. Evaluation of single bolus, dual-echo dynamic susceptibility contrast MRI protocols in brain tumor patients. *J Cereb Blood Flow Metab* 2021;41:3378-3390

160. Tordjman M, Madelin G, Gupta PK, et al. Functional connectivity of the default mode, dorsal attention and fronto-parietal executive control networks in glial tumor patients. *Journal of Neuro-Oncology* 2021;152:347-355

161. Gardini S, Venneri A, Sambataro F, et al. Increased functional connectivity in the default mode network in mild cognitive impairment: a maladaptive compensatory mechanism associated with poor semantic memory performance. *J Alzheimers Dis* 2015;45:457-470

162. Zhu S, Fang Z, Hu S, et al. Resting State Brain Function Analysis Using Concurrent BOLD in ASL Perfusion fMRI. *PLOS ONE* 2013;8:e65884

163. Cho N, Wang C, Raymond C, et al. Diffusion MRI changes in the anterior subventricular zone following chemoradiation in glioblastoma with posterior ventricular involvement. *J Neurooncol* 2020;147:643-652

164. Song J, Kadaba P, Kravitz A, et al. Multiparametric MRI for early identification of therapeutic response in recurrent glioblastoma treated with immune checkpoint inhibitors. *Neuro Oncol* 2020;22:1658-1666

165. Kickingereder P, Wiestler B, Burth S, et al. Relative cerebral blood volume is a potential predictive imaging biomarker of bevacizumab efficacy in recurrent glioblastoma. *Neuro-Oncology* 2015;17:1139-1147

166. Chang W, Pope WB, Harris RJ, et al. Diffusion MR Characteristics Following Concurrent Radiochemotherapy Predicts Progression-Free and Overall Survival in Newly Diagnosed Glioblastoma. *Tomography* 2015;1:37-43

167. van den Bent MJ, Wefel JS, Schiff D, et al. Response assessment in neuro-oncology (a report of the RANO group): assessment of outcome in trials of diffuse low-grade gliomas. *Lancet Oncol* 2011;12:583-593

168. Wen PY, Macdonald DR, Reardon DA, et al. Updated response assessment criteria for high-grade gliomas: response assessment in neuro-oncology working group. *J Clin Oncol* 2010;28:1963-1972

169. Pruis IJ, Koene SR, van der Voort SR, et al. Noninvasive differentiation of molecular subtypes of adult nonenhancing glioma using MRI perfusion and diffusion parameters. *Neurooncol Adv* 2022;4:vdac023

170. Tran AN, Lai A, Li S, et al. Increased sensitivity to radiochemotherapy in IDH1 mutant glioblastoma as demonstrated by serial quantitative MR volumetry. *Neuro-Oncology* 2014;16:414-420

171. Ellingson BM, Gerstner ER, Smits M, et al. Diffusion MRI Phenotypes Predict Overall Survival Benefit from Anti-VEGF Monotherapy in Recurrent Glioblastoma: Converging Evidence from Phase II Trials. *Clinical Cancer Research* 2017;23:5745

172. Zhao S, Lin Y, Xu W, et al. Glioma-derived mutations in IDH1 dominantly inhibit IDH1 catalytic activity and induce HIF-1alpha. *Science* 2009;324:261-265

173. Chenevert TL, Stegman LD, Taylor JMG, et al. Diffusion Magnetic Resonance Imaging: an Early Surrogate Marker of Therapeutic Efficacy in Brain Tumors. *JNCI: Journal of the National Cancer Institute* 2000;92:2029-2036

174. Stein E, Yen K. Targeted Differentiation Therapy with Mutant IDH Inhibitors: Early Experiences and Parallels with Other Differentiation Agents. *Annual Review of Cancer Biology* 2017;1:379-401

175. Anderson JR, Cain KC, Gelber RD. Analysis of survival by tumor response and other comparisons of time-to-event by outcome variables. *J Clin Oncol* 2008;26:3913-3915

176. Murphy ES, Leyrer CM, Parsons M, et al. Risk Factors for Malignant Transformation of Low-Grade Glioma. *Int J Radiat Oncol Biol Phys* 2018;100:965-971

177. Pierallini A, Bonamini M, Bozzao A, et al. Supratentorial diffuse astrocytic tumours: proposal of an MRI classification. *Eur Radiol* 1997;7:395-399

178. Scott JN, Brasher PMA, Sevick RJ, et al. How often are nonenhancing supratentorial gliomas malignant? A population study. *Neurology* 2002;59:947-949

179. Chen IE, Swinburne N, Tsankova NM, et al. Sequential Apparent Diffusion Coefficient for Assessment of Tumor Progression in Patients with Low-Grade Glioma. *AJNR Am J Neuroradiol* 2018;39:1039-1046

180. Danchaivijitr N, Waldman AD, Tozer DJ, et al. Low-grade gliomas: do changes in rCBV measurements at longitudinal perfusion-weighted MR imaging predict malignant transformation? *Radiology* 2008;247:170-178

181. Sanvito F, Telesca D, Cho NS, et al. Small pretreatment lesion size and high sphericity as favorable prognostic factors after laser interstitial thermal therapy in brain metastases. *J Neurosurg* 2024;140:338-349

182. Wen PY, van den Bent M, Youssef G, et al. RANO 2.0: Update to the Response Assessment in Neuro-Oncology Criteria for High- and Low-Grade Gliomas in Adults. *Journal of Clinical Oncology* 2023:JCO.23.01059

183. Arevalo-Perez J, Peck KK, Young RJ, et al. Dynamic Contrast-Enhanced Perfusion MRI and Diffusion-Weighted Imaging in Grading of Gliomas. *J Neuroimaging* 2015;25:792-798

184. Jensen RL. Brain tumor hypoxia: tumorigenesis, angiogenesis, imaging, pseudoprogression, and as a therapeutic target. *J Neurooncol* 2009;92:317-335

185. Sanghani P, Ti AB, Kam King NK, et al. Evaluation of tumor shape features for overall survival prognosis in glioblastoma multiforme patients. *Surg Oncol* 2019;29:178-183

186. Shidoh S, Savjani RR, Cho NS, et al. Relapse patterns and radiation dose exposure in IDH wild-type glioblastoma at first radiographic recurrence following chemoradiation. *J Neurooncol* 2022;160:115-125

187. Cho NS, Hagiwara A, Yao J, et al. Amine-weighted chemical exchange saturation transfer magnetic resonance imaging in brain tumors. *NMR Biomed* 2023;36:e4785

188. Avalos LN, Luks TL, Gleason T, et al. Longitudinal MR spectroscopy to detect progression in patients with lower-grade glioma in the surveillance phase. *Neurooncol Adv* 2022;4:vdac175

189. Villanueva-Meyer JE, Mabray MC, Cha S. Current Clinical Brain Tumor Imaging. *Neurosurgery* 2017;81:397-397

190. Thompson G, Lawrie TA, Kernohan A, et al. Interval brain imaging for adults with cerebral glioma. *The Cochrane Database of Systematic Reviews* 2019;2019

191. Ellingson BM, Brown MS, Boxerman JL, et al. Radiographic read paradigms and the roles of the central imaging laboratory in neuro-oncology clinical trials. *Neuro-Oncology* 2021;23:189-189

192. Reuter M, Gerstner ER, Rapalino O, et al. Impact of MRI head placement on glioma response assessment. *Journal of Neuro-Oncology* 2014;118:123-129

193. Ellingson BM, Bendszus M, Boxerman J, et al. Consensus recommendations for a standardized Brain Tumor Imaging Protocol in clinical trials. *Neuro-oncology* 2015;17:1188-1198

194. Sanvito F, Kaufmann TJ, Cloughesy TF, et al. Standardized brain tumor imaging protocols for clinical trials: current recommendations and tips for integration. *Frontiers in Radiology* 2023;3

195. Lin NU, Lee EQ, Aoyama H, et al. Response assessment criteria for brain metastases: proposal from the RANO group. *The Lancet Oncology* 2015;16:e270-e278

196. Huang RY, Bi WL, Weller M, et al. Proposed response assessment and endpoints for meningioma clinical trials: report from the Response Assessment in Neuro-Oncology Working Group. *Neuro Oncol* 2019;21:26-36

197. Chamberlain M, Junck L, Brandsma D, et al. Leptomeningeal metastases: a RANO proposal for response criteria. *Neuro Oncol* 2017;19:484-492

198. Erker C, Tamrazi B, Poussaint TY, et al. Response assessment in paediatric high-grade glioma: recommendations from the Response Assessment in Pediatric Neuro-Oncology (RAPNO) working group. *Lancet Oncol* 2020;21:e317-e329

199. Okada H, Weller M, Huang R, et al. Immunotherapy Response Assessment in Neuro-Oncology (iRANO): A Report of the RANO Working Group. *The Lancet Oncology* 2015;16:e534-e534

200. Ellingson BM, Wen PY, Cloughesy TF. Modified Criteria for Radiographic Response Assessment in Glioblastoma Clinical Trials. *Neurotherapeutics* 2017;14:307-320

201. Ellingson BM, Levin VA, Cloughesy TF. Radiographic Response Assessment Strategies for Early-Phase Brain Trials in Complex Tumor Types and Drug Combinations: from Digital "Flipbooks" to Control Systems Theory. *Neurotherapeutics* 2022;19:1855-1868

202. Hubel DH, Wiesel TN. Receptive fields of single neurones in the cat's striate cortex. *J Physiol* 1959;148:574-591

203. Hubel DH, Wiesel TN. Receptive fields and functional architecture of monkey striate cortex. *J Physiol* 1968;195:215-243

204. Gilaie-Dotan S, Saygin AP, Lorenzi LJ, et al. The role of human ventral visual cortex in motion perception. *Brain* 2013;136:2784-2798

205. Smith SM. Fast robust automated brain extraction. *Hum Brain Mapp* 2002;17:143-155

206. Isensee F, Schell M, Pflueger I, et al. Automated brain extraction of multisequence MRI using artificial neural networks. *Human Brain Mapping* 2019;40:4952-4964

207. Mandonnet E, Delattre JY, Tanguy ML, et al. Continuous growth of mean tumor diameter in a subset of grade II gliomas. *Ann Neurol* 2003;53:524-528

208. Wen PY, Macdonald DR, Reardon DA, et al. Updated response assessment criteria for high-grade gliomas: response assessment in neuro-oncology working group. *Journal of clinical oncology : official journal of the American Society of Clinical Oncology* 2010;28:1963-1972

209. Cairncross JG, Pexman JH, Rathbone MP, et al. Postoperative contrast enhancement in patients with brain tumor. *Ann Neurol* 1985;17:570-572

210. Sato N, Bronen RA, Sze G, et al. Postoperative changes in the brain: MR imaging findings in patients without neoplasms. *Radiology* 1997;204:839-846

211. McKeever PE. Chapter 20 - Immunohistology of the Nervous System. In: Dabbs DJ, ed. *Diagnostic Immunohistochemistry (Third Edition)*. Philadelphia: W.B. Saunders; 2010:820-889

212. Katsura M, Sato J, Akahane M, et al. Recognizing Radiation-induced Changes in the Central Nervous System: Where to Look and What to Look For. *RadioGraphics* 2020;41:224-248

213. Shah R, Vattoth S, Jacob R, et al. Radiation necrosis in the brain: imaging features and differentiation from tumor recurrence. *Radiographics* 2012;32:1343-1359

214. Walker AJ, Ruzevick J, Malayeri AA, et al. Postradiation imaging changes in the CNS: how can we differentiate between treatment effect and disease progression? *Future Oncol* 2014;10:1277-1297

215. Ellingson BM, Chung C, Pope WB, et al. Pseudoprogression, radionecrosis, inflammation or true tumor progression? challenges associated with glioblastoma response assessment in an evolving therapeutic landscape. *J Neurooncol* 2017;134:495-504

216. Ali FS, Arevalo O, Zorofchian S, et al. Cerebral Radiation Necrosis: Incidence, Pathogenesis, Diagnostic Challenges, and Future Opportunities. *Curr Oncol Rep* 2019;21:66

217. Thust SC, van den Bent MJ, Smits M. Pseudoprogression of brain tumors. *J Magn Reson Imaging* 2018;48:571-589

218. Yoo RE, Choi SH, Kim TM, et al. Independent Poor Prognostic Factors for True Progression after Radiation Therapy and Concomitant Temozolomide in Patients with Glioblastoma: Subependymal Enhancement and Low ADC Value. *AJNR Am J Neuroradiol* 2015;36:1846-1852

219. van West SE, de Bruin HG, van de Langerijt B, et al. Incidence of pseudoprogression in low-grade gliomas treated with radiotherapy. *Neuro-Oncology* 2017;19:719-725

220. Pasquini L, Peck KK, Tao A, et al. Longitudinal Evaluation of Brain Plasticity in Low-Grade Gliomas: fMRI and Graph-Theory Provide Insights on Language Reorganization. *Cancers (Basel)* 2023;15

221. Yao J, Chakhoyan A, Nathanson DA, et al. Metabolic characterization of human IDH mutant and wild type gliomas using simultaneous pH- and oxygen-sensitive molecular MRI. *Neuro Oncol* 2019;21:1184-1196

222. Yao J, Hagiwara A, Raymond C, et al. Human IDH mutant 1p/19q co-deleted gliomas have low tumor acidity as evidenced by molecular MRI and PET: a retrospective study. *Sci Rep* 2020;10:11922

223. Zhao X, Zhang T, Liu H, et al. Automatic Windowing for MRI With Convolutional Neural Network. *IEEE Access* 2019;7:68594-68606